Roughish ice, snow and turbulent heat fluxes on the Greenland ice sheet

Maurice van Tiggelen

Roughish ice, snow and turbulent heat fluxes on the Greenland ice sheet

Maurice van Tiggelen

Cover: Artistic impression of turbulent eddies in the atmospheric boundary layer over a rough ice surface at site S5, which is located in the lower ablation zone of the western Greenland ice sheet. At this location, the turbulent heat fluxes generated by the turbulent eddies explain a large part of the surface melt. The back-cover contains the eddy covariance station used in this thesis to measure the turbulent heat fluxes. Original lino print based on a photograph taken during fieldwork in September 2020. Cover art and design by Lotte Gerick.

Roughish ice, snow and turbulent heat fluxes on the Greenland ice sheet

Glace rugueuse, neige et flux de chaleur turbulents sur la calotte glaciaire du Groenland

(avec un résumé en Français)

Ruw ijs, sneeuw en turbulente warmtefluxen op de Groenlandse ijskap

(met een samenvatting in het Nederlands)

Proefschrift

ter verkrijging van de graad van doctor aan de
Universiteit Utrecht
op gezag van de
rector magnificus, prof.dr. H.R.B.M. Kummeling,
ingevolge het besluit van het college voor promoties
in het openbaar te verdedigen op
woensdag 17 mei 2023 des middags te 2.15 uur

door

Maurice van Tiggelen

geboren op 20 juli 1994
te Saint-Martin-d'Hères, Frankrijk

Contents

Summary

The mass loss of Earth's land ice, including glaciers, ice caps and ice sheets, has caused 114 mm of global sea-level rise between 1901-2018, or more than half of the total measured sea-level rise (202 mm) in that period. The remainder is explained by thermal expansion and changes in land water storage. The Greenland ice sheet and its peripheral glaciers contribute 40 mm to this sea-level rise, and are expected to continue to lose mass during the next century. Future projections of the mass loss of grounded ice, including the Greenland ice sheet (hereafter, the ice sheet), require robust projections of both surface, basal and calving processes.

Climate models are often used to calculate the surface mass balance of the ice sheet, defined as the precipitation minus the ablation at the surface. By far most of the ablation originates from the runoff of meltwater in the low-lying ablation zone, which covers only 10-16% of the ice sheet's surface. In the ablation zone, surface melt is mainly driven by the absorption of solar radiation and by the sensible heat flux (SHF). The latter is defined as the vertical turbulent exchange of sensible heat between the surface and the overlying atmosphere. This turbulent heat flux explains most of the surface melt variability, and can become the major source of energy during extreme melt events. However, very few direct observations of turbulent fluxes exist on the ice sheet, which makes the simulation of these fluxes in climate models uncertain. This thesis aims to better quantify and therewith reduce the uncertainty of modelling the SHF across the Greenland ice sheet.

In chapter 3, we address the issue of measuring the SHF on the ice sheet. The main challenge resides in measuring small-scale turbulent fluctuations over a long period of time, for which expensive, sensitive and energy-demanding instruments are normally employed. These are inadequate instruments for the remote measurement sites on the ice sheet that are typically visited once per year, and where they experience harsh climatic conditions. The vertical propeller eddy covariance (VPEC) method represents a simple alternative that can also be easily integrated in existing automatic weather station designs. The main drawback of the VPEC method is the large attenuation (up to 50%) of the turbulent flux due to the large response times of propeller anemometers. Fortunately, this attenuation can be accurately modelled, since both the response times and the spectral characteristics of the turbulent fluxes are known. An interesting outcome of our study is that the sampling time can be greatly reduced (down to 4s), since the higher frequency information is still present in the observations due to aliasing.

In chapter 4, we develop a novel method to map the surface aerodynamic roughness using either uncrewed aerial vehicles (UAV) or satellite laser altimetry (ICESat-2). A high roughness of the surface enhances the vertical mixing and leads to larger SHF values compared to a smooth surface. While it is known that parts of the ice sheet's bare ice surface are very rough due to the presence of ice hummocks and crevasses, a precise map of the aerodynamic roughness over the ice sheet for aiding the SHF calculations is still lacking. We find that a simplified model for obstacle height and drag is able to reproduce our in situ measurements. We apply this method to ICESat-2 data, which results in a map of surface aerodynamic roughness of the ice sheet. An important finding is the large horizontal variability in surface aerodynamic roughness across the

ice sheet. Our main conclusion is that on large spatial and temporal scales, the surface roughness mostly decreases with elevation, and seasonally during winter.

In chapter 5, we propose an updated model for the surface aerodynamic roughness based on the results from the previous chapter. Four locations in the ablation zone with simultaneous observations of the sensible heat flux and surface melt are used to test the model. We find that a more realistic description of the variation in the height of ice hummocks leads to a more accurate simulation of SHF, and therefore to a more accurate simulation of surface melt. An important finding comes from comparing several distinct datasets acquired over rough melting ice in both Greenland and Iceland over the last 25 years. All these flux measurements contain the same strong dependence of turbulent mixing scale (roughness length for heat) on the turbulence of flow (roughness Reynolds number).

In chapter 6, we finally address the last research question of this thesis, which is how accurately the SHF is modelled in climate models, and what the impact is of possible discrepancies on modelled surface melt. We build a database of surface energy balance fluxes from 25 automatic weather stations on the ice sheet, and we compare these measurements to the regional climate model RACMO2.3p2. We find that RACMO2.3p2 is underestimating the SHF during the melting season, with a larger underestimation at lower station elevations. We can partly explain the SHF underestimation by a lower wind speed in RACMO2.3p2 at the low-lying sites during summer. We implemented the updated roughness parameterizations from the previous chapter in RACMO. Currently, we are not able to explain this underestimation of wind speed by varying the surface roughness parameters in RACMO2.3p2.

We continue to monitor ice sheet surface processes with automatic weather stations, eddy covariance and surface mass balance observations. Together with remote sensing observations, these can be used as benchmarks for the development of future climate models. The continuous improvement of climate models allows for more accurate simulations of future ice sheet mass loss.

Samenvatting

Het massaverlies van het landijs in de wereld, oftewel gletsjers en ijskappen, heeft tussen 1901 en 2018 een mondiale zeespiegelstijging veroorzaakt van 114 mm. Dat is meer dan de helft van de gemeten mondiale zeespiegelstijging (202 mm). De rest kan worden verklaard door de thermische uitzetting van zeewater en door veranderingen in wateropslag op land. De Groenlandse ijskap en de omringende gletsjers droegen 40 mm bij aan deze zeespiegelstijging en zullen naar verwachting massa blijven verliezen in de nabije toekomst. De berekeningen van toekomstig massaverlies vereisen robuuste berekeningen van zowel oppervlakte-, basale als afkalvingsprocessen van gletsjers en ijskappen.

Klimaatmodellen worden vaak gebruikt om de oppervlakte massabalans te berekenen, welke is gedefinieerd als het nettoverschil tussen de accumulatie en de ablatie aan het oppervlak. Verreweg het grootste deel van de ablatie op de Groenlandse ijskap wordt veroorzaakt door afvoer van smeltwater in het zogeheten ablatiegebied, dat slechts 10-16% van het oppervlak van de hele ijskap bedekt. In het ablatiegebied wordt het afsmelten vooral veroorzaakt door absorptie van zonnestraling en door de voelbare warmteflux. Die laatste wordt ook wel 'sensible heat flux' genoemd (SHF). De SHF is gedefinieerd als de uitwisseling van voelbare warmte tussen het oppervlak en de atmosfeer door middel van turbulente wervelingen. Deze turbulente warmteflux verklaart een groot deel van de gemeten variabiliteit in oppervlakte smelt en kan de belangrijkste bron van warmte zijn tijdens dagen met een extreme hoeveelheid smelt. Er zijn echter weinig waarnemingen van turbulente warmtefluxen op de Groenlandse ijskap, waardoor de uitkomsten van de berekening van deze fluxen in klimaatmodellen nog onzeker zijn. Dit proefschrift heeft als doel om de onzekerheid van de SHF over de Groenlandse ijskap te kwantificeren en verminderen.

Hoofdstuk 3 begint met het meten van de SHF op de Groenlandse ijskap. Het is een grote uitdaging om kleinschalige turbulente fluctuaties te meten over een langere periode van tijd. Dit komt omdat hiervoor vaak dure en kwetsbare apparatuur gebruikt moet worden. Deze apparatuur is vaak niet geschikt voor de afgelegen en weerbarstige meetlocaties op de ijskap. Het feit dat deze locaties meestal niet meer dan één keer per jaar bezocht worden, maakt het onderzoek niet eenvoudiger. Toch moet een weerstation het hele jaar blijven werken in deze lastige weersomstandigheden. De 'vertical propeller eddy covariance' (VPEC) methode is een eenvoudig alternatief, met name omdat deze eenvoudig in bestaande automatische weerstations kan worden geïntegreerd. Het grootste nadeel van de VPEC methode is dat deze niet snel genoeg is om alle relevante turbulente wervelingen te meten. Een belangrijk resultaat van dit hoofdstuk is daarom dat de gemiddelde flux toch goed kan worden bepaald, omdat nauwkeurig berekend kan worden hoeveel wervelingen de VPEC methode gemiddeld mist. Daarnaast is een ander interessant resultaat dat er minder vaak gemeten hoeft te worden om gemiddeld een nauwkeurige turbulent flux te bepalen.

In hoofdstuk 4 wordt er een nieuwe methode gepresenteerd om de aerodynamische ruwheid van het oppervlak in kaart te brengen met behulp van onbemande luchtvaartuigen (UAV) of satellietmetingen (ICESat-2). Een verhoogde ruwheid van het oppervlak bevordert de turbulente menging met de atmosfeer, met als gevolg grotere SHF-

waarden, in vergelijking met een aerodynamisch glad oppervlak. Hoewel het bekend is dat het oppervlak van het ablatiegebied van de ijskap erg ruw is vanwege de aanwezigheid van ijsbulten en gletsjerspleten, bestaat er nog steeds geen kaart van de aerodynamische ruwheid over de ijskap die gebruikt kan worden voor SHF-berekeningen. In dit hoofdstuk wordt er een nieuwe methode gepresenteerd om de data van onze meetstations goed te kunnen reproduceren met een eenvoudig model voor de obstakelhoogte. Deze nieuwe methode is toegepast op de nieuwe laserhoogtemetingen van de ICESat-2 satelliet, wat uiteindelijk heeft geleid tot de eerste kaart van aerodynamische ruwheid van het oppervlak van de Groenlandse ijskap. Een belangrijke bevinding van dit hoofdstuk is de grote ruimtelijke variabiliteit van de ruwheid. Daarnaast neemt, gemiddeld genomen, de ruwheid van het oppervlak af met de hoogte.

Hoofdstuk 5 gaat dieper in op de aerodynamische oppervlakteruwheid. We hebben daartoe een model ontwikkeld om de verandering van deze aerodynamische oppervlakteruwheid te berekenen in de tijd. De metingen van vier locaties in het ablatiegebied, waar zowel SHF als smeltmetingen beschikbaar zijn, vormen de basis voor dit model. Een realistische beschrijving van de variatie in de hoogte van ijsheuvels leidt tot een betere bepaling van de voelbare warmteflux. Deze bepaling draagt uiteindelijk bij aan een betere berekening van de hoeveelheid oppervlaktesmelt. Dit kan worden gezien als een eerste belangrijk resultaat uit hoofdstuk 5. Een tweede belangrijk resultaat heeft betrekking op de SHF metingen. Alle SHF metingen die zijn vergeleken, kunnen worden gereduceerd tot eenzelfde verhouding. Deze verhouding is afhankelijk van de hoeveelheid turbulentie in de stroming, maar is theoretisch nog niet goed te verklaren.

Hoofdstuk 6 geeft antwoord op de laatste onderzoeksvraag van dit proefschrift: "Hoe nauwkeurig kan de SHF berekend worden in klimaatmodellen en wat is de impact van een meer realistische ruwheid op de gemodelleerde oppervlakte smelt?". Metingen van 25 weerstations zijn vergeleken met de berekeningen van het regionale klimaatmodel RACMO2.3p2. Een belangrijk resultaat heeft betrekking op de nauwkeurigheid van dit model: zowel de SHF als de hoeveelheid smelt worden gemiddeld genomen onderschat tijdens het smeltseizoen. De onderschatting van de SHF en hoeveelheid smelt blijkt het grootst bij de laaggelegen stations die dicht bij de rand van de ijskap staan. Deze onderschatting is, onder andere, te verklaren door een te lage windsnelheid berekend door RACMO2.3p2. Het beter modelleren van de ruwheid van het ijs in RACMO2.3p2 corrigeert deze onderschatting echter niet.

Ook in de toekomst zullen we de veranderingen van de Groenlandse ijskap blijven worden meten middels weerstations, flux- en massabalans metingen. Dit vormt, samen met satellietmetingen, een gedegen basis voor de doorontwikkeling van toekomstige klimaatmodellen. Deze doorlopende verbeteringen van bestaande klimaatmodellen, waar dit proefschrift een bijdrage aan heeft geleverd, maken het mogelijk om de toekomstige massaverliezen van ijskappen steeds nauwkeuriger te bepalen.

Résumé

La perte de masse de tous les glaciers et toutes les calottes glaciaires dans le monde a causé 114 mm d'élévation globale du niveau de la mer entre 1901 et 2018, soit plus de la moitié de l'élévation mesurée (202 mm) au cours de la même période. La dilatation thermique et la variation du stockage des eaux terrestres expliquent le reste. La calotte du Groenland et ses glaciers périphériques contribuent 40 mm à cette élévation, et vont continuer à perdre de la masse dans le future proche. Les futures projections de la perte de masse des glaciers et calottes, notamment de la calotte glaciaire du Groenland, nécessitent des modèles précis des processus de surface, de base et de vêlage des glaciers.

Des modèles climatiques sont utilisés afin de calculer le bilan de masse de surface sur la calotte glaciaire, défini comme l'accumulation moins l'ablation de surface. La majeure partie de l'ablation au Groenland est causée par le ruissellement de surface dans la zone d'ablation, qui ne couvre que 10 à 16% de la surface de la calotte du Groenland. Dans la zone d'ablation, la fonte de surface est principalement causée par l'absorption du rayonnement solaire et par le flux de chaleur sensible (SHF). Ce dernier est défini comme l'échange turbulent de chaleur sensible entre la surface et l'atmosphère. Ce flux de chaleur turbulent explique la majeure partie de la variabilité de la fonte en surface et peut devenir une source majeure d'énergie lors d'épisodes de fonte extrême. Cependant, il n'existe que très peu d'observations de flux turbulents sur la calotte, ce qui rend incertaine la simulation de ces flux dans les modèles climatiques. Cette thèse vise à quantifier et à réduire l'incertitude de la modélisation du SHF sur la calotte glaciaire du Groenland.

Dans le chapitre 3, nous commençons par mesurer le SHF. Le principal défi réside dans la mesure des rapides fluctuations turbulentes pendant une longue période. Des instruments coûteux, fragiles et consommateurs d'énergie sont souvent utilisés à ce but. Ceux-ci ne sont pas adaptés pour les sites de mesures sur la calotte, généralement visités une fois par an mais qui doivent tout de même fonctionner en permanence dans des conditions climatiques difficiles. La méthode du 'vertical propeller eddy covariance' (VPEC) est une simple alternative, notamment puisque ces instruments peuvent être directement intégrés sur des stations météorologiques existantes. Le principal inconvénient de cette méthode VPEC est la sous-estimation (jusqu'à 50%) du flux turbulent en raison du plus grand temps de réponse d'un anémomètre à hélice. Nous trouvons que cette atténuation peut tout de même être modélisée de manière précise, puisqu'à la fois les temps de réponse et les caractéristiques spectrales des flux turbulents sont connus. Un résultat intéressant de ce chapitre est que le temps d'échantillonnage peut être considérablement réduit (jusqu'à 4 s), puisque l'information à haute fréquence est toujours présente dans les observations grâce au repliement spectral.

Dans le chapitre 4, nous développons une nouvelle méthode permettant de cartographier la rugosité aérodynamique de la surface à l'aide d'aéronefs sans équipage (UAV) ou de satellites (ICESat-2). Une surface rugueuse améliore la diffusion turbulente et cause des valeurs de SHF plus élevées par rapport à une surface lisse. Bien qu'il soit connu que la surface de la calotte glaciaire peut être très rugueuse en raison de la présence de monticules de glace et de crevasses, une carte précise de la rugosité aérodynamique

sur la calotte glaciaire utilisable pour des calculs du SHF n'existe pas. Nous trouvons qu'un modèle simplifié pour la hauteur et la traînée des obstacles est capable de reproduire les mesures de terrain. Nous appliquons cette méthode aux nouvelles données du satellite ICESat-2, ce qui donne une première carte de la rugosité aérodynamique de surface. Une découverte importante de ce chapitre est la forte variabilité horizontale de la rugosité aérodynamique de surface sur la calotte. Notre principale conclusion est que la rugosité de surface diminue principalement avec l'altitude et pendant l'hiver.

Dans le chapitre 5, nous proposons un nouveau modèle pour la rugosité aérodynamique de surface. Nous testons le modèle à quatre endroits dans la zone d'ablation où nous avons à la fois des mesures de flux turbulents et de fonte de surface Nous trouvons qu'une description plus réaliste de la variation de la hauteur des obstacles à la surface permet une simulation plus précise de SHF, et donc une simulation plus précise de la fonte de surface. La comparaison de plusieurs données acquises sur des surface de glace rugueuses au Groenland et en Islande au cours des 25 dernières années aboutit à une découverte intéressante. Nous trouvons une même équation qui relie l'échange turbulent de chaleur à l'intensité de la turbulence proche de la surface.

Dans le chapitre 6, nous abordons la dernière question de cette thèse, qui est de savoir avec quelle précision le SHF est modélisé dans les modèles climatiques, et quel en est l'impact sur les calculs de fonte de surface. Nous assemblons une base de données avec des mesures météorologiques de 25 stations sur la calotte glaciaire, et nous comparons ces mesures au modèle climatique régional RACMO2.3p2. Nous constatons que RACMO2.3p2 sous-estime le SHF pendant la période de fonte. Cette sous-estimation semble la plus prononcée aux stations en basse altitude. Nous pouvons l'expliquer par une vitesse de vent trop faible dans RACMO 2.3p2. Nous ne sommes pas en mesure d'expliquer cette sous-estimation en variant les paramètres de rugosité de surface dans RACMO2.3p2.

Nous continuons de mesurer les processus de surface de l'inlandsis du Groenland avec des stations météorologiques, des mesures de flux turbulents et de mesures de de bilan de masse en surface. Utilisées en combinaison avec des observations de télédétection, elles servent de référence pour le développement des modèles climatiques. L'amélioration continue des modèles climatiques permet enfin des simulations précises de la future perte de masse de la calotte glaciaire.

Chapter 1

Introduction

The Greenland ice sheet is the focus of this thesis. This chapter introduces some meteorological and glaciological aspects of the ice sheet. A brief review of recent scientific progress is presented, which then leads to the research questions addressed in the remainder of this thesis.

1.1 Historical context

Driven by a need for adventure stories, it was in the late 19th century that the first expeditions to the Greenland ice sheet took place, with the first attempts of Nordenskiöld in 1883 (Nordenskjöld, 1883) and Peary in 1886 (Peary, 1887) to reach its interior. But it was not until 1888, notably the first crossing by Fridtjof Nansen of the ice sheet (Nansen, 1890, Figure 1.1a), that it became clear that the ice sheet is in fact one large and connected ice mass (Figure 1.2). The first scientific explorations quickly followed. In 1893, Erich von Drygalski and his team performed the first glaciological survey on Store Glacier, near the Greenlandic town of Uummannaq. This later inspired Swiss meteorologist Alfred de Quervain to set up a research expedition, which eventually led to the crossing of the ice sheet during the Swiss Greenland Expedition in 1912 (Barr, 2015). Together with the Greenland expedition of the University of Michigan in 1926-1927, and the first overwintering on the inland ice during the Alfred Wegener's German Greenland Expedition in 1930 (Georgi et al., 1935), the first datasets of meteorological observations on the ice sheet became available.

   After WWII, both the technological progress and the development of air bases by the US Army in Greenland allowed for a significant modernisation of the expeditions. In 1952, both the Paul-Emile Victor's expedition (France) and the British North Greenland Expedition were among the first to make use of modern techniques, trading the dog sleds for tracked vehicles, planes and helicopters. Several years later, in 1957, the first International Glaciological Greenland Expedition (EGIG) took place at the start of the International Geophysical Year (Finsterwalder, 1959), which was repeated ten years later in 1967. Measurements from these two expeditions allowed for a first quantification of, among other aspects, the vertical wind profile characteristics (Ambach, 1960,
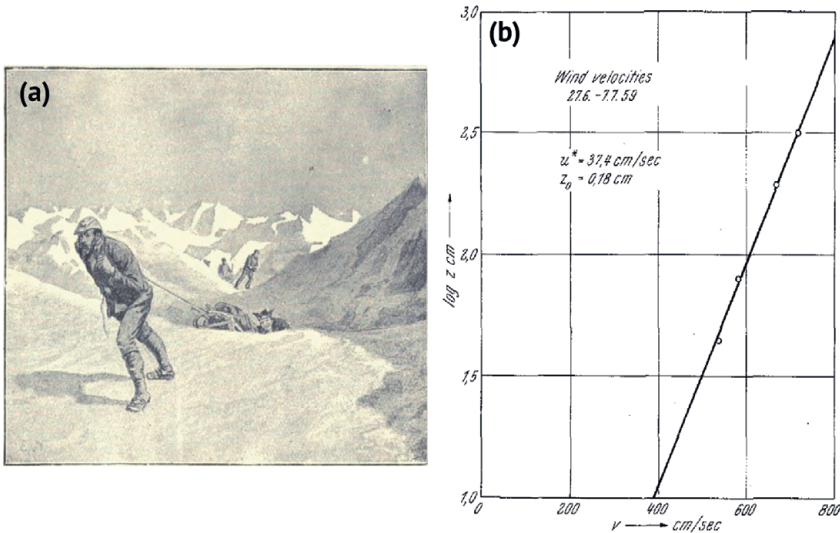
Figure 1.1: (a) "Roughish ice", on 23 September 1888 in West Greenland. By E. Nielsen from *The First Crossing of Greenland* (Nansen, 1890). (b) Observed vertical profile of horizontal wind speed during EGIG at Camp IV between 27 June and 7 July 1959 (Ambach, 1960).

Figure 1.1b), and the total mass balance of the Greenland ice sheet (Bauer, 1955, 1967; Loewe, 1964). At that time, the ice sheet was estimated to be in approximate balance, meaning that the total mass gained by snow accumulation was estimated to balance the combined mass loss due to surface runoff and due to solid ice discharge from calving glaciers. However, the uncertainties in these calculations were considerable, due to the lack of sufficient long-term, and spatially distributed data. The early 1960s also mark the start of deep ice drilling in Greenland at Camp Century (Jouzel, 2013).

In the 1970s and 1980s, the Grønlands Geologiske Undersøgelse (GGU), predecessor of the current Geological Survey of Denmark and Greenland (GEUS), performed several meteorological and surface mass balance measurements, mostly on local glaciers for hydropower applications (Olesen, 1986; Braithwaite, 1986). They produced an improved understanding of ice sheet surface processes, yet not any published field study before the 1990s produced a surface mass balance record longer than 10 years (Machguth et al., 2016).

In the early 1990s, several coordinated research expeditions took place, including the Greenland Ice Margin Experiment (GIMEX) organised by the University of Utrecht and Free University of Amsterdam (Oerlemans and Vugts, 1993), the Swiss ETH Zurich Greenland expedition (Ohmura et al., 1994), and the start of the Greenland Climate network (GC-Net), a network of automated weather stations (AWS) mostly located in the accumulation zone of the ice sheet (Steffen and Box, 2001). The main focus of these studies was the investigation of the sensitivity of the Greenland ice sheet mass balance

to global warming. These studies were also the first to make use of sonic anemometers to measure turbulent heat fluxes in the ablation area of the ice sheet, as presented in e.g. Henneken et al. (1994); Forrer and Rotach (1997); Box and Steffen (2001). In 2008, the PROMICE network was started (Ahlstrøm et al., 2008), which is a network of AWS and mass balance observations in the ablation area across the entire ice sheet, operated by GEUS. In 2020, GEUS also took over the operation of GC-Net. At present, many of the measurement sites from GIMEX are still continued along the so called K-transect (Smeets et al., 2018). In combination with GC-Net and PROMICE stations, the IMAU stations are currently one of the longest time series of in-situ meteorological and surface mass balance data on the Greenland ice sheet (Figure 1.2).

1.2 Greenland ice sheet characteristics and climate

Since the first scientific measurements before the 1950s, our knowledge about the state of the Greenland ice sheet has considerably evolved. The ice sheet, including its surrounding glaciers and ice caps, covers an area of 1.78×10^6 km^2 with an average thickness of 1.68 km, meaning that there is 2.99×10^6 km^3 of ice volume stored, or 2.74×10^{18} kg (2.74×10^6 Gt, 1 Gt $= 10^{12}$ kg) of total ice mass assuming an average density of 916.17 kg m^{-3}. This makes it the second largest ice mass on Earth. Once removed, this would be enough water to rise the global mean sea-level by 7.42 m (Morlighem et al., 2017). In contrast, the Antarctic ice sheet holds a potential rise of 57.9 m (Morlighem et al., 2020), while all other glaciers and ice sheets together have a global sea-level potential rise of 0.32 m (Farinotti et al., 2019). The Greenland ice sheet as we know it today was most likely formed during the late Pliocene (between 5 - 2.58 million years ago, Lunt et al. 2008), a period during which the accumulation of snow would have exceeded mass losses due to ablation for a period long enough for the ice sheet to form. Over millennial time scales and beyond, the ice sheet's evolution is partly driven by oscillations in insolation due to changes in the Earth's orbit, also known as Milankovitch cycles, and by long-term changes in atmospheric CO_2 concentrations. The response of the ice sheets to this forcing is nonlinear, due to feedback processes between the ice sheet and global climate (Oerlemans, 1991). At present, the ice sheet is a dome of ice with an average elevation of 2109 m, with the highest point located at 3238 m above sea level. Between 2001 to 2016, the maximum bare ice extent, that is the surface not covered by snow during the melting season, ranged in between 10 to 16% of the total ice sheet area, with a maximum snowline elevation ranging between 1300 - 1700 m elevation (Ryan et al., 2019).

Near surface air temperature   The 2m air temperature on the ice sheet is mainly determined by elevation due to adiabatic cooling, and the latitude and the day of year that determine the insolation. The yearly averaged observed lapse rate equals 6.0±0.7 °C/km, with smaller lapse rates usually observed during summer (Fausto et al., 2009). The lowest temperatures are typically observed in February, with the absolute recorded minimum being -69.9 °C on 22 December 1991 near the ice sheet summit (Weidner et al., 2021). In the ablation zone during summer, the air temperatures can exceed 10 °C, especially during extreme melt events as was the case in south Greenland
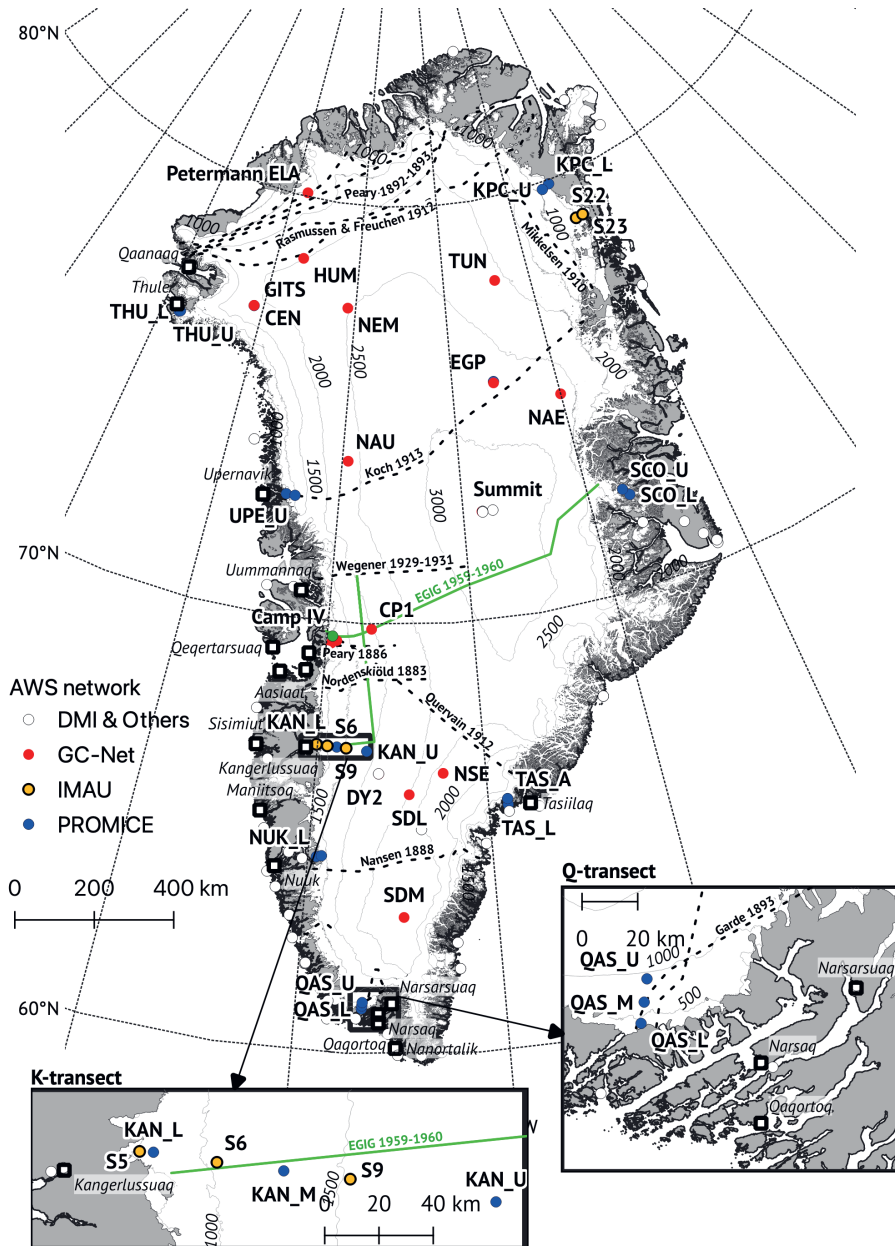
Figure 1.2: Location of Automated Weather Stations (AWS) from the DMI, GC-Net, IMAU and PROMICE networks. Major settlements in Greenland are shown, together with the approximate tracks of historical expeditions on the inland ice in dashed lines and solid green line. The insets detail the K-transect and Q-transect. Elevation contours are taken from the GIMP DEM (Howat et al., 2014) and shown in 500 m intervals, in m a.s.l.

in July 2012 (Fausto et al., 2016a).

Wind speed The near-surface wind regime on the ice sheet is dominated by the katabatic forcing, which forces the wind downslope due to buoyancy forces, deviated to the right (in the northern hemisphere) due to the Coriolis force. The katabatic forcing, caused by a combination of strong surface cooling and sloping topography, is most pronounced near the margins, during winter and on the east side, due to the presence of larger temperature gradients and steeper slopes (Van Angelen et al., 2011). The convergence of the flow due to the local topography, in combination with the presence of nearby mesocyclones, can locally cause extreme near-surface wind speeds, also called Piteraq winds (Klein and Heinemann, 2002). During summer, the katabatic forcing is less pronounced due the smaller temperature gradient. Between the warmer tundra and the ice sheet, a thermal gradient is typically present. In combination with the large scale pressure gradient, these can generate barrier winds which interact with katabatic winds and increases the near surface wind speed on the ice sheet (Van den Broeke and Gallée, 1996). The climatology of the near-surface wind speed and air temperature explain the sensible heat flux climatology on the Greenland ice sheet, which is the main focus of this thesis.

Large-scale meteorology On a large scale, the near surface temperature fluctuations in Greenland are correlated with the Greenland Blocking Index (GBI), defined as the averaged 500 hPa geopotential height over Greenland (Hanna et al., 2021). A high GBI is associated with a blocking event, which typically occurs during Rossby wave breaking (Barnes and Hartmann, 2012), and stimulates the advection to the ice sheet of southerly warmer and more humid air. Another characteristic synoptic feature in Greenland are the narrow stripes of warm, cloudy and more humid air, often referred to as Atmospheric Rivers (ARs). ARs can be linked to breaking Rossby waves (Liu and Barnes, 2015), and also enhance poleward heat and moisture transport. ARs have a strong impact on Greenland surface mass balance through increased precipitation and surface melt (Mattingly et al., 2018).

1.3   Mass balance and surface energy balance

The total mass balance (MB) of the grounded part of the Greenland ice sheet is defined over one year as the surface mass balance (SMB) minus the ice discharge (D) and basal mass balance (BMB):

$$MB = SMB - D - BMB \quad \text{(kg s}^{-1} \text{ or Gt year}^{-1}\text{)}, \tag{1.1}$$

The BMB contains the ice melt at the base of the ice sheet due to either geothermal heating, frictional heating, or viscous heat dissipation (Karlsson et al., 2021). The MB can be converted to global sea-level equivalent in mm/year by dividing by the surface of the oceans ($362.5 \times 10^6 \text{km}^2$), meaning that 362.5 Gt of land ice loss corresponds to 1 mm of global averaged sea-level rise. The focus of this thesis is to study the specific SMB (SSMB), which is the sum of all the mass fluxes at the surface-atmosphere interface
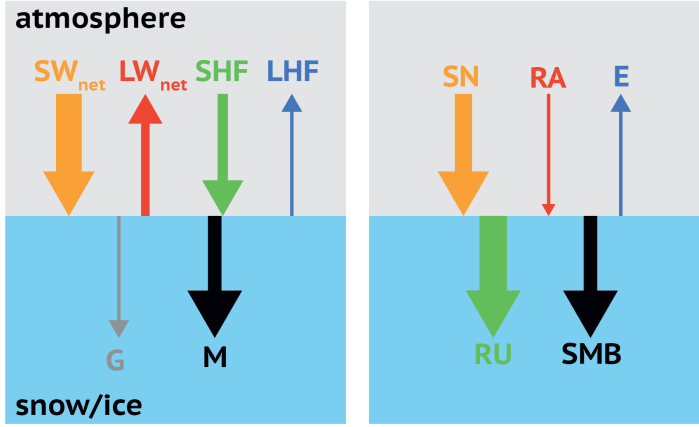
Figure 1.3: Surface energy balance (SEB, left) and surface mass balance (SMB, right) fluxes typical over a melting snow/ice surface in the ablation zone of the Greenland ice sheet. Abbreviations of each flux are defined in the text.

per unit area (Figure 1.3) :

$$SSMB = SN + RA - RU - E - ER \quad \text{(kg m}^{-2}\text{ s}^{-1}), \qquad (1.2)$$

with SN the solid precipitation, RA the rainfall, RU the liquid water runoff, E the sublimation/evaporation from the surface and ER the erosion due to drifting snow (deposition/scour). The runoff is determined through the liquid water balance:

$$RU = M_m + RA + C - RF - RE \quad \text{(kg m}^{-2}\text{ s}^{-1}), \qquad (1.3)$$

with M_m the surface melt expressed as a mass flux, RA the rainfall, C the condensation, RF the refreezing of liquid water and RE the retention of liquid water.

At the interface between any surface and the atmosphere, four main energy fluxes always compete: (1) radiative fluxes, (2) turbulent heat fluxes, (3) subsurface conductive heat flux, and (4) energy fluxes corresponding to phase changes happening at the surface (melt, refreezing, evaporation/sublimation, condensation/deposition). In addition, heat may be added/extracted from the surface by rain if the temperature of the rain droplets differs from the temperature of the surface. Conservation of energy states that all these fluxes must always be in balance. This balance is defined as the surface energy balance (SEB, Figure 1.3):

$$M = R_{net} + SHF + LHF + G + E_r \quad \text{(W m}^{-2}), \qquad (1.4)$$

with M the surface melt, expressed here in terms of flux of energy and defined in this thesis as positive if melting occurs. M can be converted from M_m (Box 1). R_{net} is the net absorbed radiation at the surface, SHF is the turbulent sensible heat flux, LHF is the turbulent latent heat flux, G is the subsurface conductive heat flux and E_r the energy added/removed by rain. In the remainder we will neglect E_r, although it can

be a limited source of energy during ARs (Box et al., 2022). All the fluxes are defined positive if they are directed towards the surface, unless stated otherwise. It is practical, for both modelling and measurements, to separate R_{net} into a downward and an upward component, and into two different spectral bands :

$$M = SW_d - SW_u + LW_d - LW_u + SHF + LHF + G \quad (\text{W m}^{-2}), \tag{1.5}$$

with SW_d, SW_u the downward and upward components of shortwave radiation chosen in the wavelength interval $[0.15 - 3]$ μm. We do not explicitly take into account the penetration of shortwave radiation below the surface. LW_d, LW_u are the downward and upward components of longwave radiation chosen in the thermal infrared wavelength interval $[3 - 100]$ μm. In this definition all four radiation components are positive, while the SHF, LHF en G are defined positive when directed towards the surface.
The SEB constitutes the lower boundary condition for atmospheric models. The SEB is also used to compute surface melt, either using measurements from an automatic weather station, or by coupling with an atmospheric model.

1.4   Greenland ice sheet zones

The Greenland ice sheet can be separated into four different climate zones, each with contrasting SEB/SMB patterns (Figure 1.4). The highest zone is the dry-snow zone. This area is permanently covered by firn, which is dense snow that has accumulated during the previous years. Surface melting very rarely occurs in the dry-snow zone due to the low air temperatures and the high snow albedo, defined as the shortwave reflectivity. At lower elevations, surface melting occurs during summer, yet the meltwater is retained in the available pore spaces of the firn. This area is defined as the percolation zone. Moving to even lower elevations, we find the wet-snow zone, which is the area where the surface melt exceeds the capacity of the snow to retain water, therefore surface runoff occurs. When taken over one year, snow accumulation in the wet-snow zone still exceeds the runoff, therefore the SMB is still positive. The surface meltwater often refreezes, forming either impermeable ice lenses in the snow, or superimposed ice on top of the snow or ice. Finally, moving further down, we enter the ablation zone, where surface runoff exceeds snowfall on an annual basis, meaning that the SMB is negative. During the melting season, this zone is mostly covered by bare ice and is often rougher and darker than the other zones (Nolin and Payne, 2007). The surface meltwater creates an organised network of streams which eventually drain into moulins, which are deep holes formed in the ice by the meltwater runoff, or crevasses, which are cracks in the ice formed by the lateral movement of the ice. The ice can also be very dark due to the presence of impurities like black carbon or algae. In the lowest part of the ablation zone, surface meltwater is often not even visible at the surface since it directly drains into the sub-glacial drainage network. Due to the contemporary warming, the ablation zone is expanding, which is discernible in the recent increase of the snowline elevation and increase of bare ice extent (Smith et al., 2019; Tedstone and Machguth, 2022).
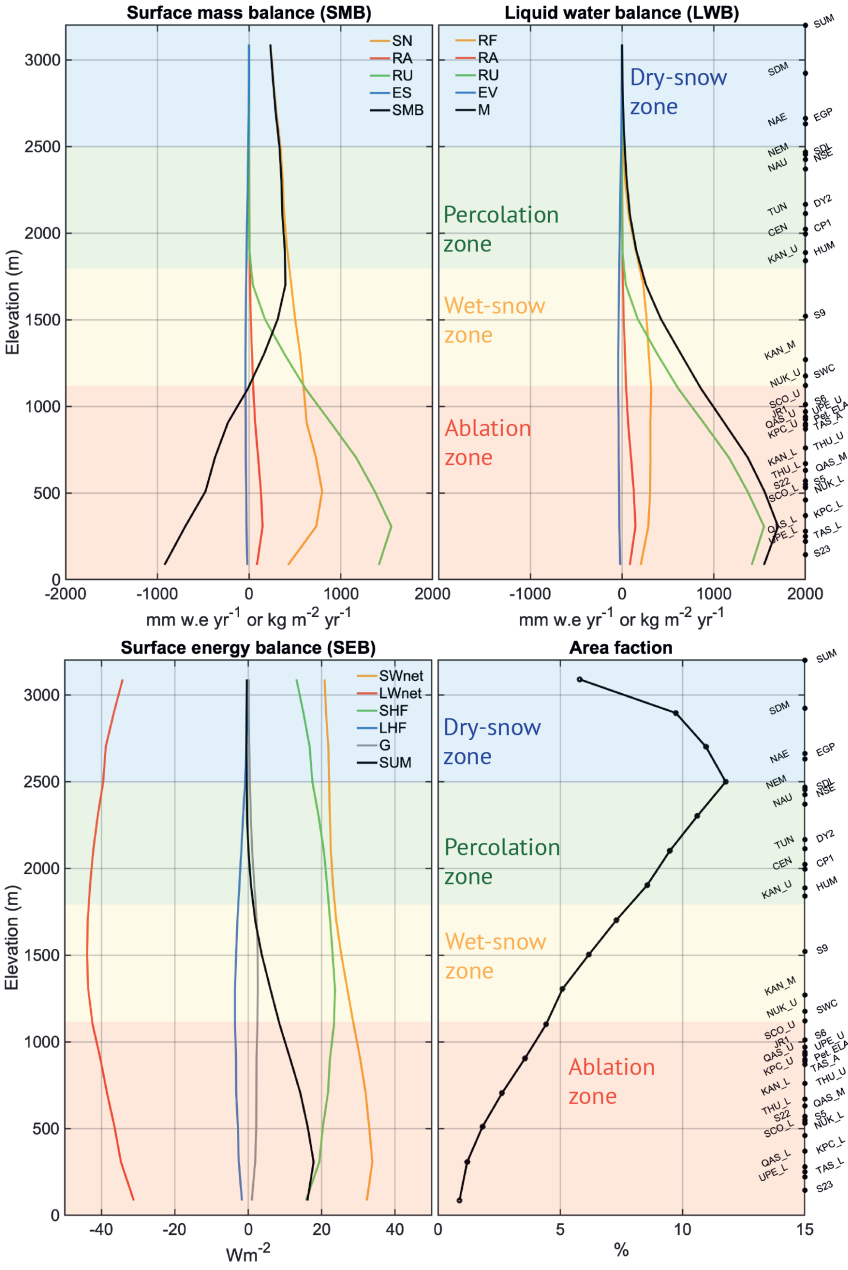
Figure 1.4: Yearly averaged components of the surface mass balance (SMB), liquid water balance (LWB) and surface energy balance (SEB) on the Greenland ice sheet as function of elevation, in the period 1990-2020, modelled by RACMO2.3p2 at 5.5 km resolution (data from Noël et al. (2021)). The area fraction per elevation is shown in the bottom right panel. A rough delineation of each climate zone is given. Elevations of the AWS used in this thesis are also shown.

1.5 Contemporary knowledge on Greenland mass balance

In 1990, the first report of the Intergovernmental Panel on Climate Change (IPCC) published a synthesis of the sensitivity of the ice sheet to global warming. Based on EGIG data and on SEB modelling, the sensitivity of the ice sheet was estimated to be equivalent to 0.3 ± 0.2 mm/year of global mean sea-level rise per degree of warming (IPCC, 1990). At the time, this sensitivity explained 0.23 ± 0.16 mm/year of global sea-level rise between 1880 and 1980, or approximately 15% of the observed value of 1-2 mm/year of global mean sea-level in the same period. These values remained uncertain, due to the lack of long-term measurements on the ice sheet, and the lack of robust satellite measurements at the time.

Box 1: Converting surface melt units

Surface melt is typically expressed as a mass flux (M_m) across a surface area of 1m^2 in SI units [kg m^{-2} s^{-1}], which is equivalent to [mm water equivalent s^{-1}], or [mm w.e. s^{-1}]. The conversion to an energy flux (M) in SI units [W m^{-2}] is :

$$M = L_m M_m \quad [\text{W m}^{-2}] \tag{1.6}$$

with $L_m = 3.34 \times 10^5$ J kg^{-1} the latent heat of fusion at $0°C$.

Surface melt is typically measured by lowering of the melting snow/ice surface. Assuming that the measured lowering is caused by surface melt only (and not by sublimation or snow densification), the height change Δh in a time period Δt can be converted to a melt energy flux:

$$M = \rho_{i,s} L_m \frac{\Delta h}{\Delta t} \quad [\text{W m}^{-2}] \tag{1.7}$$

with $\rho_{i,s}$ the density of ice or snow. Taking a typical value for $\rho_i = 916$ kg m^{-3}, we find that a melt energy flux of $M = 100$ W m^{-2} is equivalent to a lowering of the ice surface of 2.82 cm per day. Also, a yearly averaged energy available for melting of $M = 10$ W m^{-2} corresponds to a mass flux of $M_m = 944$ kg m^{-2} yr^{-1}.

From \ To	Mass flux	Energy flux	Height change
Mass flux	1	L_m	$\Delta t / \rho_{i,s}$
Energy flux	$1/L_m$	1	$\Delta t / (\rho_{i,s} L_m)$
Height change	$\rho_{i,s}/\Delta t$	$\rho_{i,s} L_m / \Delta t$	1

Multiplication factors for converting between surface melt units

---

Between the 1990s and present, much progress has been made in terms of observations and modelling of the Greenland ice sheet mass balance. For instance, the satellites from the Gravity Recovery and Climate Experiment (GRACE, and its successor GRACE-FO) directly measure total mass change of the Greenland ice sheet by gravimetry, i.e. by

measuring changes in gravity anomalies (e.g. Wouters et al., 2008; Groh and Horwath, 2021). Satellite altimeters, such as CryoSat-2 (McMillan et al., 2016; Nilsson et al., 2016; Gourmelen et al., 2018), ICESat (Sørensen et al., 2011; Csatho et al., 2014; Felikson et al., 2017), and ICESat-2 (Smith et al., 2020) allow for a direct measure of height (and volume) change, which can be converted to mass changes if the surface density is known (Box 1). Furthermore, regional climate models (RCM), such as RACMO (Ettema et al., 2010; Van Angelen et al., 2014; Noël et al., 2018; Van Dalum et al., 2020), MAR (Fettweis et al., 2013), HIRHAM (Lucas-Picher et al., 2012) and NHM-SMAP (Niwano et al., 2018) have greatly improved and now allow for complete and realistic simulation of Greenland's climate and SMB. In order to close the mass budget of the ice sheet, ice discharge can be independently estimated by differencing SMD and D, i.e. the input-output method, which combines the estimated ice velocity from remote sensing with the measured ice thickness (Andersen et al., 2015; Colgan et al., 2019; Mouginot et al., 2019; Mankoff et al., 2020). Combining all these datasets provides a complete picture of Greenland MB during the satellite era (1990s-present). This reference period is then used to reconstruct the SMB and MB back in time using historical data (Box, 2013; Kjeldsen et al., 2015; Mankoff et al., 2021). This reference period is also used to estimate future mass loss, either using ice sheet models forced with climate model data as was done in the Ice Sheet Model Intercomparison Project for CMIP6 (Goelzer et al., 2020, ISMIP6,), or by using a statistical emulator calibrated on ice sheet model output (Edwards et al., 2021).
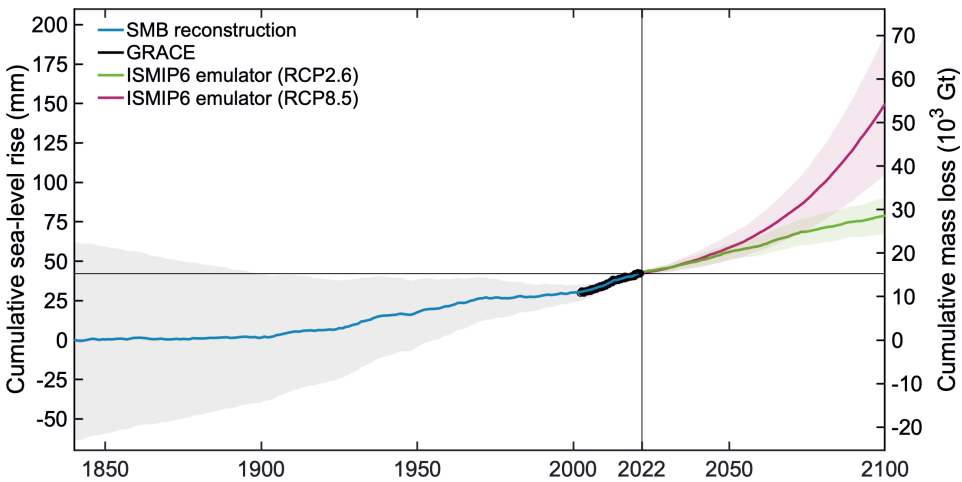
Figure 1.5: Relative change in cumulative Greenland ice sheet mass balance between 1840 and 2100. The 1840-2022 reconstruction is from Mankoff et al. (2021). The 2002-2022 Gravity Recovery and Climate Experiment (GRACE) data is from ESA-CCI using the methods of Groh and Horwath (2021). The two 2016-2100 projections are from IPCC (2021) for two different future emission scenarios (RCP2.6 and RCP8.5), which is based on an emulator of ISMPI6 data from Edwards et al. (2021) (see also Goelzer et al. (2020)). It is assumed that 362.5 Gt of mass loss is equivalent to 1 mm global seal-level rise. Shaded areas denote the 1-σ uncertainty reported in each dataset, shown as cumulative starting from present-day.

In 2019, the Ice Sheet Mass Balance Intercomparison Exercise (IMBIE) published a state of the art synthesis on the Greenland ice sheet mass budget (Shepherd et al., 2020), which combined all the techniques mentioned above. The Greenland ice sheet was found to have lost 3902 ± 342 Gt between 1992 and 2018, thereby contributing 0.43 ± 0.075 mm/year to global sea-level rise (Figure 1.5). This estimate was part of the most recent 6th assessment report of the IPCC (IPCC, 2021). Climate models show the SMB sensitivity to global warming to be non-linear, which prevents us to carry out a simple linear regression with air temperature into the future (Fettweis et al., 2013; Noël et al., 2021).
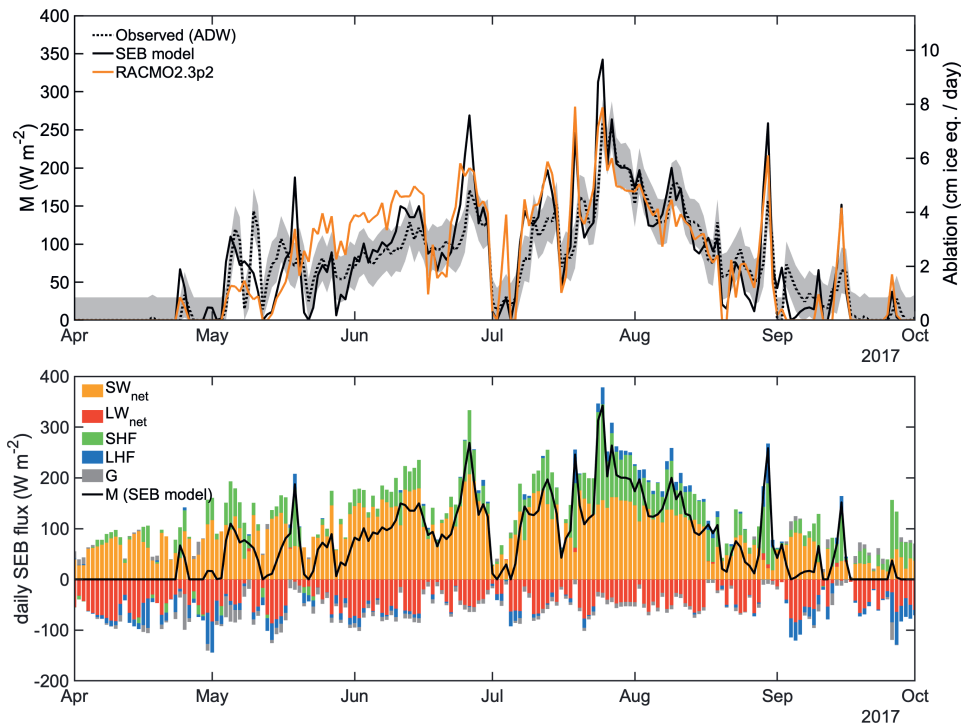
Figure 1.6: Top: Daily observed surface ablation from an ablation draw wire (ADW), and modelled surface melt with a surface energy balance (SEB) model and with the regional climate model (RACMO2.3p2) at site S5 in 2017. The shaded area denotes the uncertainty in daily ablation measurement of 1 cm ice equivalent. The energy fluxes are converted to metres ice equivalent lowering assuming an ice density of 917 kgm^{-3} (Box 1). Bottom: Observed radiative heat fluxes (SW_{net}, LW_{net}) and modelled turbulent heat flux using a SEB model (SHF, LHF), subsurface heat flux (G) and surface melt (M) at S5.

1.6   This thesis

In its latest assessment report (AR6), the first working group of the IPCC (IPCC, 2021) states that there is "medium confidence in the ability of climate models to simulate changes in Greenland SMB" (chapter 9.4.1.2). This is mainly "[...] due to deficiencies in an accurate model representation of the ablation zone extent and processes related to surface melt and runoff [...]". This statement is based on a recent inter-comparison project (Fettweis et al., 2020), in which a large spread in SMB in climate models became evident. An efficient way to improve the modelled SMB in climate models is to apply statistical downscaling (Noël et al., 2016, e.g.). This process corrects for the limited horizontal resolution of a climate model, and for known biases. Another way is to increase the horizontal resolution of climate models (Van de Berg et al., 2020, e.g.), which may yield a more accurate representation of the SEB components and therefore SMB. The motivation of this thesis is to improve our understanding of the physics of the glacier and ice sheet surface melt and runoff, with the main objective to eventually improve the SMB in climate models.

As shown in the SEB equation above (Eq. 1.5), the accurate modelling of surface melt requires the accurate modelling of all the components of both radiative and turbulent heat fluxes. Several recent studies focus on ways to improve the modelled radiative fluxes over the Greenland ice sheet. For instance, one recent work quantifies the effect of biological activity on surface albedo (Tedstone et al., 2020), another explicitly includes the spectral properties of surface albedo into a climate model (Van Dalum et al., 2021). On the other side, the turbulent heat fluxes have received a relatively less scientific attention. Some recent studies suggest that the SHF is underestimated by climate models in the ablation area (Fausto et al., 2016b; Noël et al., 2018). However, it is still not clear how large this underestimation is, and where it originates.

For illustration, we show times series of measured radiative fluxes, modelled turbulent heat fluxes and modelled surface melt using a SEB model during 2017 at site S5, which is located at roughly 550 m elevation on the K-transect (Figure 1.6). The modelled daily energy available for surface melt (M) ranges up to 350 W m^{-2}, which is equivalent to 9.87 cm of ice ablation per day (assuming an ice density of 917 kg m^{-3}, Box 1). From April until mid-July, most of the melt can be explained by the net absorbed shortwave radiation (SW_{net}). After mid July, the SHF starts to contribute to around one third of the average melt, and the LHF, while still small (around 10 W m^{-2}), changes sign and now starts to contribute as well. We also show the modelled surface melt from the regional climate model RACMO2.3p2 (top panel, orange line) and observed lowering with an ablation draw wire (top panel, dashed black line). Despite the large day-to-day discrepancies, both models are able to reproduce the overall variation in surface lowering as measured by the ablation draw wire (top panel, dashed line). Interestingly, the largest deviations are found during periods with the largest modelled SHF values. Both the SHF and LHF clearly explain the maxima in surface melt (bottom panel), yet these two models find very different values during these periods of extreme melt rates. Unfortunately, before the start of this thesis, no continuous SHF measurements were available at S5, or anywhere else in the ablation zone, which prevents the direct evaluation of

modelled SHF and LHF. Therefore, the modelled SHF and LHF remain uncertain.

A physical process related to turbulent exchange that is not yet included in climate models is the variability in time and space in aerodynamic roughness (z_{0m}) throughout the ablation area. A rough surface consisting of hummocks and crevasses is found not only at site S5 but across the entire ablation area, which enhances the turbulent mixing between the surface and the atmosphere. Based on previous model evaluations over glaciers (Munro, 1989; Conway and Cullen, 2013; Fitzpatrick et al., 2017), an accurate knowledge of the surface roughness in models is expected to improve the SHF and LHF. Another possible shortcoming is that the assumptions implemented in the current models to calculate turbulent fluxes, e.g. Monin-Obukhov Similarity Theory (MOST), do not hold for the ablation area due to typical boundary layer conditions (Radić et al., 2017). To test these hypotheses and improve on all these uncertainties and shortcomings we need a robust, long-term dataset of turbulent heat flux measurements.

The research questions (RQs) addressed in this thesis are the following:

1. Is it possible to accurately measure the sensible heat flux (SHF) and surface aerodynamic roughness (z_{0m}) in the Greenland ice sheet ablation zone over longer periods of time using a simple and robust vertical propeller eddy covariance (VPEC) system ? (chapter 3)

2. How accurately can we derive spatial information about z_{0m} over the ice sheet from satellite remote sensing ? (chapter 4)

3. How can we use our improved knowledge of SHF and LHF, and therefore surface melt, to improve modelling the SEB components over the ice sheet ? (chapter 5)

4. How accurate is the modelling of SHF in regional climate models (RCMs) such as RACMO across the ice sheet, and where do the discrepancies originate from ? Can we improve RCMs by improving the description of surface aerodynamic roughness ? (chapter 6)

1.7   Outline

The different chapters in this thesis aim to answer these research questions (RQs). In chapter 2, a detailed description is given of the surface turbulent heat fluxes: what is their origin, how are they modelled and measured. Additionally we describe how the radiative fluxes and surface lowering are measured. RQ1 is addressed in chapter 3, in which a vertical propeller eddy covariance (VPEC) method is described that provides continuous turbulent heat flux measurements, for longer periods of time without regular maintenance and no additional energy consumption. We have applied the VPEC method for the first time in the ablation of the Greenland ice sheet. This yields year-round SHF measurements in Greenland's ablation zone. RQ2 is addressed in chapter 4, in which a novel method is validated that enables mapping of surface roughness values from ICESat-2 satellite laser altimeter data. For this purpose, data from direct turbulence measurements obtained at two locations and high-resolution elevation models from uncrewed aerial systems (UAV) are used. This yields the first quantitative map of the spatial variability of the surface aerodynamic roughness across an extended area of

the Greenland ice sheet. In chapter 5 we focus on RQ3 by combining both long-term field measurements and surface aerodynamic roughness maps derived from ICESat-2 data to develop a new, simple yet physically based model for the aerodynamic roughness of the surface. The new models are implemented in a SEB model to determine the surface melt for different locations in the ablation zone. Two case studies are presented which demonstrate the important contribution of the turbulent heat fluxes during large melt events. Finally, in chapter 6, RQ4 is addressed in which regional climate model RACMO2.3p2 is tested with the newly developed roughness models implemented. The modelled SEB and SBM components from short simulations (2016-2021) are compared to both IMAU & PROMICE measurements, in order to provide a robust estimate of possible biases in RACMO2.3p2. This chapter also presents a sensitivity analysis of RCM surface melt on surface roughness. Finally in chapter 7, we present an outlook for future research directions.

Chapter 2

Turbulent heat fluxes

This chapter provides an overview of the existing mathematical expressions that describe the turbulent heat fluxes, followed by a description of the closure model mostly used in regional climate models. The measurement methods, their limitations and instrumental corrections for the eddy covariance method and all other energy balance measurements as applied throughout this thesis are also presented.

2.1 Governing equations

The general conservation of mass, momentum, heat and moisture for moist and incompressible atmospheric flows is expressed in Einstein summation notation as (Stull, 1988, e.g. p.78):

$$\frac{\partial u_j}{\partial x_j} = 0, \tag{2.1}$$

$$\frac{\partial u_i}{\partial t} + u_j \frac{\partial u_i}{\partial x_j} = -\delta_{i3}g + f\epsilon_{ij3}u_j - \frac{1}{\rho_a}\frac{\partial p}{\partial x_i} + \nu\frac{\partial^2 u_i}{\partial x_j^2}, \tag{2.2}$$

$$\frac{\partial \theta}{\partial t} + u_j \frac{\partial \theta}{\partial x_j} = \nu_\theta \frac{\partial^2 \theta}{\partial x_j^2} - \frac{1}{\rho_a C_p}\frac{\partial Q_j^*}{\partial x_j} - \frac{L_p E}{\rho_a C_p}, \tag{2.3}$$

$$\frac{\partial q}{\partial t} + u_j \frac{\partial q}{\partial x_j} = \nu_q \frac{\partial^2 q}{\partial x_j^2} + \frac{S_q}{\rho_a}, \tag{2.4}$$

in which the conserved variables are the velocity vector components ($u_i = u, v, w$), the potential temperature (θ, Box 2), and the specific humidity (q, Box 2). The air density is written as ρ_a. These equations contain storage, advection, the influence of gravity through the gravitational acceleration (g), earth's rotation through the Coriolis parameter (f), the pressure-gradient forces and viscous stresses through molecular diffusivities for momentum, temperature and humidity (ν, ν_θ and ν_q). The heat conservation equation also includes two source/sink terms expressed by the divergence of net radiation ($Q*$) or generated by the heat released by phase changes (E), such as evaporation. These

equations do not take into account the air liquid water content.

It is common for a turbulent flow to separate each conserved quantity into an average and a fluctuating part, with the Reynolds decomposition:

$$u_i = \overline{u_i} + u'_i, \tag{2.5}$$

$$\theta = \overline{\theta} + \theta', \tag{2.6}$$

$$q = \overline{q} + q', \tag{2.7}$$

for which the following Reynolds averaging rules are defined for any quantity a and b :

$$\overline{a + b} = \overline{a} + \overline{b}, \tag{2.8}$$

$$\overline{\overline{a}} = \overline{a}, \tag{2.9}$$

$$\overline{a'} = 0, \tag{2.10}$$

$$\overline{\frac{\partial a}{\partial x_i}} = \frac{\partial \overline{a}}{\partial x_i}. \tag{2.11}$$

Substituting the conserved variables into the conservation equations 2.1-2.4, applying ensemble averaging and the Reynolds averaging rules (Equations 2.9-2.12), and removing the negligibly small terms yields the following equations for the averages:

$$\frac{\partial \overline{u_j}}{\partial x_j} = 0, \tag{2.12}$$

$$\frac{\partial \overline{u_i}}{\partial t} + \overline{u_j} \frac{\partial \overline{u_i}}{\partial x_j} = -\delta_{i3}g + f\,\epsilon_{ij3}\overline{u_j} - \frac{1}{\overline{\rho_a}}\frac{\partial \overline{p}}{\partial x_i} + \nu \frac{\partial^2 \overline{u_i}}{\partial x_j^2} - \frac{\partial(\overline{u'_i u'_j})}{\partial x_j}, \tag{2.13}$$

$$\frac{\partial \overline{\theta}}{\partial t} + \overline{u_j} \frac{\partial \overline{\theta}}{\partial x_j} = \nu_\theta \frac{\partial^2 \overline{\theta}}{\partial x_j^2} - \frac{1}{\overline{\rho_a}C_p}\frac{\partial \overline{Q_j^*}}{\partial x_j} - \frac{L_p E}{\overline{\rho_a}C_p} - \frac{\partial(\overline{u'_j \theta'})}{\partial x_j}, \tag{2.14}$$

$$\frac{\partial \overline{q}}{\partial t} + \overline{u_j} \frac{\partial \overline{q}}{\partial x_j} = \nu_q \frac{\partial^2 \overline{q}}{\partial x_j^2} + \frac{S_q}{\overline{\rho_a}} - \frac{\partial(\overline{u'_j q'})}{\partial x_j}. \tag{2.15}$$

It becomes clear that the set of equations after Reynolds averaging is nearly identical to the general conservation equations that we started with, except for the appearance of a new divergence term on the r.h.s of Eqs. 2.13-2.15, which incorporates the effect of the fluctuations and turbulence on the mean flow. These are the covariances of velocity fluctuation components with themselves, or with temperature and humidity, and behave as fluxes of momentum, heat and moisture in the conservation equations. These covariances, or fluxes, need to be modelled in order to predict the average evolution of the flow.

Box 2: Conversion between temperature and humidity variables:
Potential temperature is defined as:

$$\theta = T \exp\left(\frac{p_0}{p}\right)^{R_d/C_p} \tag{2.16}$$

with T the temperature, $R_d = 287.05$ J kg^{-1} K^{-1} the gas constant for dry air, $C_p = 1004.7$ J kg^{-1} K^{-1} the specific heat capacity of dry air at constant pressure, p the air pressure and $p_0 = 10^5$ Pa the reference pressure. The virtual temperature and potential virtual temperature are then defined as:

$$T_v = T\left(1 + (R_v/R_d - 1)q\right) \tag{2.17}$$
$$\theta_v = \theta\left(1 + (R_v/R_d - 1)q\right) \tag{2.18}$$

with $R_v = 461.5$ J kg^{-1} K^{-1} the gas constant for water vapour, and q specific humidity (in unit kg kg^{-1}). The air density can then be estimated using the ideal gas law:

$$\rho_a = \frac{p}{R_d T_v} \tag{2.19}$$

Specific humidity is related to relative humidity (RH) by:

$$q = \frac{RH}{100}q_{sat} \tag{2.20}$$

where the saturation specific humidity is defined as:

$$q_{sat} = \frac{R_d}{R_v} \frac{e_{sat}}{p + e_{sat}\left(\frac{R_d}{R_v} - 1\right)} \tag{2.21}$$

with e_{sat} the water vapour pressure at saturation with respect to ice or liquid water, which is a function of air temperature following the Clausius-Clapeyron relation (Murphy and Koop, 2005).

2.2 Modelling the turbulent heat fluxes: Monin-Obukhov similarity theory

The separation of the conserved quantities into a mean and a fluctuating part results in a set of equations that contains more unknowns than equations, due to the appearance of covariances in the conservation equations. It is possible to develop additional prognostic equations for the variances and covariances, which will lead to more unknown (co)-variances. Therefore a "closure" model for the turbulent fluxes becomes necessary. Commonly, near the surface, *First-order closure*, or *K-theory* is used to model the vertical

fluxes using the mean vertical gradients of u, θ and q:

$$\overline{u'w'} = -K_m \frac{\partial \overline{u}}{\partial z}, \tag{2.22}$$

$$\overline{w'\theta'} = -K_h \frac{\partial \overline{\theta}}{\partial z}, \tag{2.23}$$

$$\overline{w'q'} = -K_q \frac{\partial \overline{q}}{\partial z}, \tag{2.24}$$

in which K_m, K_h and K_q are defined as the turbulent diffusion coefficients for momentum, heat and moisture. Parameterizing the quantities K_m, K_h and K_q as a function of wind speed, and integration with respect to z gives the solutions of u, θ and q with height. Often the mixing length parameterization is used, which was derived nearly a century ago by Prandtl (1925). One main challenge resides in incorporating the effect of thermal stratification on the turbulent diffusion coefficients. Monin-Obukhov Similarity Theory (MOST) postulates that five parameters exist that fully describe turbulence above a flat and horizontally homogeneous surface. These are the height above the surface (z), the friction velocity (u_*), the buoyancy flux at the surface ($\overline{w'\theta_v'}$), the surface flux of any conserved scalar, such as specific humidity ($\overline{w'q'}$), and the buoyancy (g/θ_v). Then, using the *Buckingham Pi Theorem*, a new dimensionless parameter may be defined:

$$\zeta = \frac{z}{L}, \tag{2.25}$$

called the stability parameter, with L a characteristic length scale defined as:

$$L = -\frac{u_*^3 \theta_v}{\kappa g \overline{w'\theta_v'}} \tag{2.26}$$

called the Obukhov length, with $\kappa = 0.4$ the von Kármán constant. Furthermore, fluxes and gradients are combined in non dimensional groups:

$$\frac{\partial \overline{u}}{\partial z} \frac{\kappa z}{u_*}, \frac{\partial \overline{\theta}}{\partial z} \frac{\kappa z}{\theta_*}, \frac{\partial \overline{q}}{\partial z} \frac{\kappa z}{q_*}, \tag{2.27}$$

with $u_* = (\overline{u'w'}^2 + \overline{v'w'}^2)^{1/4}$ the friction velocity, $\theta_* = -\overline{w'T'}/u_*$ the temperature scale and $q* = -\overline{w'q'}/u_*$ the humidity scale. Using MOST and the *Buckingham Pi Theorem*, the non dimensional groups are written as universal functions of the stability parameter:

$$\frac{\partial \overline{u}}{\partial z} \frac{\kappa z}{u_*} = \phi_m(\zeta), \tag{2.28}$$

$$\frac{\partial \overline{\theta}}{\partial z} \frac{\kappa z}{\theta_*} = \phi_h(\zeta), \tag{2.29}$$

$$\frac{\partial \overline{q}}{\partial z} \frac{\kappa z}{q_*} = \phi_q(\zeta). \tag{2.30}$$

When comparing these set of equations with the 'K-theory' equations (Equations 2.23-2.26), it becomes clear that MOST in fact models the turbulent diffusion coefficients for
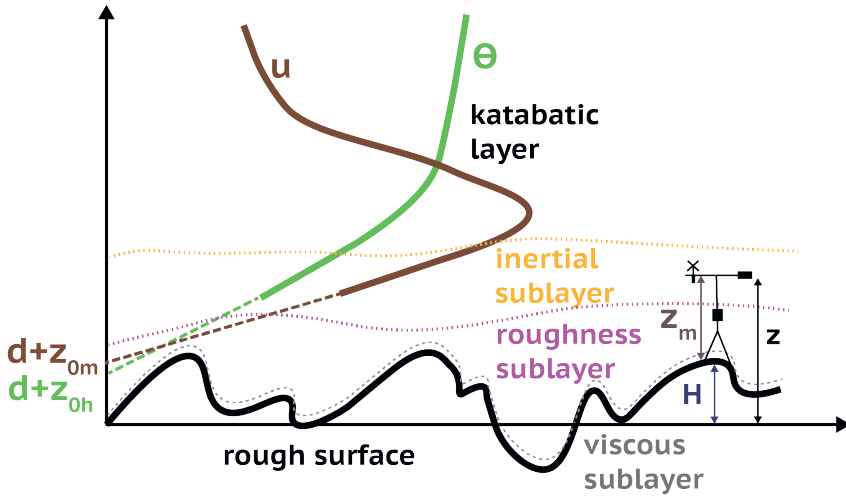
Figure 2.1: Schematic representation of a typical vertical profile of potential temperature (θ) and horizontal wind speed (u) in a katabatic wind regime over a rough surface. The extrapolation of the vertical profiles within the inertial sublayer down to surface values at the height above the displacement height (d) of the roughness lengths (z_{0m}, z_{0h}) is also shown. H denotes the height of the ice obstacle, z_m denotes the height of the instruments above the local surface, and z is the height of the instruments above the surface relevant for flux calculations. The different layers in the atmospheric boundary layer are shown with horizontal dotted lines.

momentum, heat and moisture as a function of atmospheric stability via the functions ϕ_m, ϕ_h and ϕ_q. The main assumptions of MOST are that the mean turbulent quantities (1) do not change in time (stationarity), (2) do not change in the x, y direction (horizontal homogeneity) and (3) are not influenced by exchange mechanisms outside of the surface layer, which is defined as the lower 10% of the atmospheric boundary layer.

The inertial sublayer is defined as the layer within the surface layer in which MOST is assumed to be valid, i.e. where the mean conserved quantities are not influenced by external processes. Therefore, the inertial layer is the layer where the vertical profiles of wind and temperature must vary logarithmically with height, as was found during EGIG at Camp IV by Ambach (1960) (Figure 1.1). For a rough surface in a katabatic wind regime this layer may not exist (or very shallow) due to the presence of a roughness sublayer below (Garratt, 1980) and a nearby katabatic wind speed maximum (Denby, 1999) (see Figure 2.1). Assumption (3) may in this case not hold, which would prevent us from using Equations 2.28-2.30 to compute the fluxes from the gradients. A main assumption in this thesis is that all the turbulent flux measurements are taken above the roughness sublayer and well below the katabatic wind maximum, i.e $z_{0m} \ll z \ll z_{u,max}$, with z_{0m} the roughness length for momentum, z the measurement height and $z_{u,max}$ the height of the katabatic wind maximum. One very common application of MOST is to

estimate the fluxes using the gradients. For instance, integrating between two levels z_1 and z_2 above the surface yields (Moene and van Dam, 2014, p.110):

$$\overline{u}(z_2) - \overline{u}(z_1) = \frac{u_*}{\kappa} \left[\ln\left(\frac{z_2}{z_1}\right) - \Psi_m\left(\frac{z_2}{L}\right) + \Psi_m\left(\frac{z_1}{L}\right) \right] \tag{2.31}$$

$$\overline{\theta}(z_2) - \overline{\theta}(z_1) = \frac{\theta_*}{\kappa} \left[\ln\left(\frac{z_2}{z_1}\right) - \Psi_h\left(\frac{z_2}{L}\right) + \Psi_h\left(\frac{z_1}{L}\right) \right] \tag{2.32}$$

$$\overline{q}(z_2) - \overline{q}(z_1) = \frac{q_*}{\kappa} \left[\ln\left(\frac{z_2}{z_1}\right) - \Psi_q\left(\frac{z_2}{L}\right) + \Psi_q\left(\frac{z_1}{L}\right) \right], \tag{2.33}$$

where Ψ_m, Ψ_m and Ψ_m are the integrated flux gradient relationships for momentum, heat and moisture, and are parameterized based on empirical data. These equations form the basis of the so-called *gradient method* for estimating the turbulent fluxes based on measurements taken at different heights in the inertial sublayer. In this thesis MOST, is applied using the so-called *bulk method* for estimating fluxes based on single level data. The latter results from an integration of the MOST flux-profile relationships between one level in the atmosphere (z) and one near the surface where the conserved quantities reach their surface values (denoted z_{0m}, z_{0h} and z_{0q}), which equals to zero for $\overline{u}$:

$$\overline{u}(z) = \frac{u_*}{\kappa} \left[\ln\left(\frac{z}{z_{0m}}\right) - \Psi_m\left(\frac{z}{L}\right) + \Psi_m\left(\frac{z_{0m}}{L}\right) \right] \tag{2.34}$$

$$\overline{\theta}(z) - \overline{\theta}_s = \frac{\theta_*}{\kappa} \left[\ln\left(\frac{z}{z_{0h}}\right) - \Psi_h\left(\frac{z}{L}\right) + \Psi_h\left(\frac{z_{0h}}{L}\right) \right] \tag{2.35}$$

$$\overline{q}(z) - \overline{q}_s = \frac{q_*}{\kappa} \left[\ln\left(\frac{z}{z_{0q}}\right) - \Psi_q\left(\frac{z}{L}\right) + \Psi_q\left(\frac{z_{0q}}{L}\right) \right]. \tag{2.36}$$

The quantities z_{0m}, z_{0h} and z_{0q} are the roughness lengths for momentum, heat and moisture. Physically, these are the heights above the flat surface where wind speed, potential temperature and specific humidity reach their surface values (Figure 2.1). Mathematically, these quantities are a consequence of integrating the MOST flux-profile relations down to the surface. They must therefore be regarded as necessary parameters for extrapolating the whole vertical profiles in the inertial sublayer. In practice, the roughness length cannot be measured directly, since the assumptions of MOST do not hold very close to the surface at $z = z_0$. Therefore the roughness lengths are either modelled or indirectly estimated using turbulent flux or profile observations.

Computing fluxes from gradients in the surface layer requires the knowledge of the Obukhov length (L), which depends on the fluxes (u_* and $\overline{w'\theta_v'}$) and are thus not known a priori. An iteration procedure is necessary. A possible procedure is given in Algorithm 1, which is used when single level measurements are used to estimate the turbulent fluxes.

Algorithm 1 Estimating Obukhov length (L) from single level AWS data

---

Compute air and surface virtual potential temperature :

$$\theta_v = \theta(1 + (R_v/R_d - 1)q_v) \tag{2.37}$$

$$\theta_{v,s} = \theta_s(1 + (R_v/R_d - 1)q_{v,s}) \tag{2.38}$$

Compute bulk Richardson number $Ri_b = (g/\theta_{v,s})z(\theta_v - \theta_{v,s})/u^2$

Initialise Obukhov length : $L = \text{sign}(Ri_b) \times 0.01$ and set δ_L to a large value

while $\delta_L > 0.001$ **do**

   Calculate drag coefficient for momentum:

$$C_m = \frac{\kappa^2}{(\ln(z/z_{0m}) - \Psi_m(z/L) + \Psi_m(z_{0m}/L))^2} \tag{2.39}$$

   Define aerodynamic resistance and friction velocity:

$$r_a = \frac{1}{C_m U}, \quad u_* = \frac{U}{r_a} \tag{2.40}$$

   Get scalar roughness length from empirical parameterization:

$$z_{0h,q} = f(Re_* = u_* z_{0m}/\nu) \tag{2.41}$$

   Evaluate function to minimise at L:

$$f(L) = Ri_b - z/L \frac{\ln(z/z_{0h}) - \Psi_h(z/L) + \Psi_h(z_{0h}/L)}{(\ln(z/z_{0m}) - \Psi_m(z/L) + \Psi_m(z_{0m}/L))^2} \tag{2.42}$$

   Evaluate derivative of function to minimise at L between $L^- = L - 0.001$ and $L^+ = L + 0.001$:

$$f'(L) = \frac{f(L^-) - f(L^+)}{L^- - L^+} \tag{2.43}$$

   Get updated estimate for Obukhov length:

$$L_{new} = L - \frac{f(L)}{f'(L)} \tag{2.44}$$

   Compute convergence criterion:

$$\delta_L = \frac{L_{new} - L}{L_{new}} \tag{2.45}$$

end while
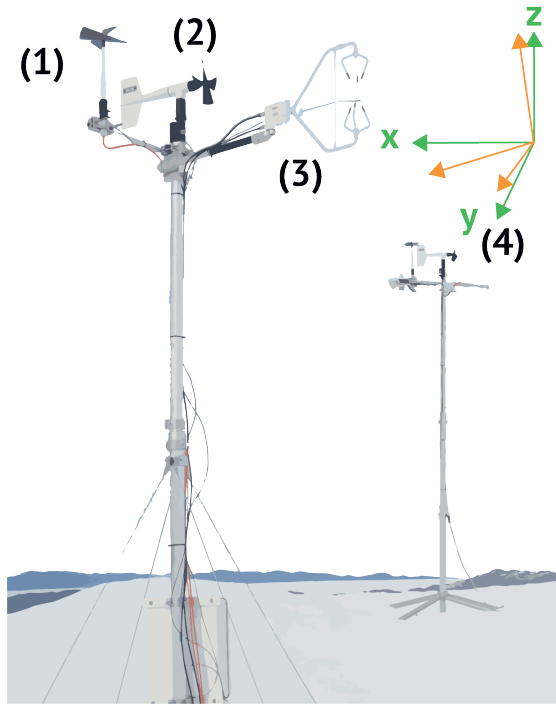
Figure 2.2: Site S5 on 9 September 2020, taken from a photograph. (1) Vertical wind propeller anemometer, (2) horizontal wind vane anemometer, (3) sonic anemometer with thermocouple, (4) IMAU automatic weather station (AWS). The coordinate system of the sonic anemometer is shown in orange, while the coordinate system after rotation is shown in green.

2.3 Measuring the turbulent heat fluxes: eddy covariance method

Modelling turbulent heat fluxes using single-level observations not only requires expressions for the stability functions (Ψ), but also values for the roughness lengths (z_0), which are not necessarily known a priori. The eddy covariance technique uses the simultaneous measurement of fast sampled wind speed components, temperature and humidity, which allows to directly estimate their covariances. This section aims to give a concise description of the technique and methods. A complete and detailed description of the eddy covariance method is given by e.g. Aubinet et al. (2000); Lee et al. (2004) and Foken (2008). The technique typically employs sonic anemometers to measure the fluctuations of u, v, w and T in the atmospheric boundary layer via measuring time delays between opposing acoustic transducers. The use of an additional gas analyser allows for the measurement of fluctuations of scalar concentrations, such as specific humidity (q), carbon dioxide (CO_2) or methane (CH_4). The eddy covariance method requires a coordinate rotation, since it assumes that the coordinate system is rotated in

the average wind direction ($\overline{v} = 0$, $\overline{w} = 0$). The mathematical formulation to rotate into the appropriate reference frame is given in Box 3.

Box 3: Rotation of eddy covariance data in the mean flow direction

The velocity vector is measured in the coordinate system of the eddy covariance sensor (e.g. a sonic anemometer). The following coordinate rotation is applied to write the wind vector in the coordinate system of the average flow:

$$\begin{pmatrix} \overline{u} \\ \overline{v} \\ \overline{w} \end{pmatrix} = A \begin{pmatrix} \overline{u}_m \\ \overline{v}_m \\ \overline{w}_m \end{pmatrix}, \tag{2.46}$$

with $A = \begin{pmatrix} \cos\gamma & -\sin\gamma & 0 \\ \sin\gamma & \cos\gamma & 0 \\ 0 & 0 & 1 \end{pmatrix} \begin{pmatrix} \cos\alpha & 0 & -\sin\alpha \\ 0 & 1 & 0 \\ \sin\alpha & 0 & \cos\alpha \end{pmatrix} \begin{pmatrix} 1 & 0 & 0 \\ 0 & \cos\beta & \sin\beta \\ 0 & -\sin\beta & \cos\beta \end{pmatrix} \tag{2.47}$

with γ, α, β the yaw, pitch and roll angles, respectively. The subscript 'm' denotes the measured quantity in the reference frame of the sonic anemometer. Several methods exist for estimating these three angles. The planar-fit method (Wilczak et al., 2001) applies a least-squares regression on the entire dataset and assumes that $\overline{w} = 0$. The double rotation also assumes $\overline{w} = 0$ yet calculates new angles for each averaging period. Using the double rotation method we first estimate a yaw angle:

$$\gamma = \tan^{-1}\left(\frac{\overline{v}_m}{\overline{u}_m}\right), \tag{2.48}$$

then we estimate the pitch angle on the yaw-corrected data, and neglect the roll angle:

$$\alpha = \tan^{-1}\left(\frac{\widehat{\overline{w}_m}}{\widehat{\overline{u}_m}}\right), \quad \beta = 0 \tag{2.49}$$

with $\widehat{\overline{u}_m}$ and $\widehat{\overline{w}_m}$ the yaw-corrected velocity components. The coordinate rotation can be applied to the high-frequency measurements, but it can also be applied to the averages and (co)variances in case high-frequency data is not available:

$$\begin{pmatrix} \overline{u'T'} \\ \overline{v'T'} \\ \overline{w'T'} \end{pmatrix} = A \begin{pmatrix} \overline{u'_m T'} \\ \overline{v'_m T'} \\ \overline{w'_m T'} \end{pmatrix}, \quad \begin{pmatrix} \overline{u'u'} & \overline{u'v'} & \overline{u'w'} \\ \overline{v'u'} & \overline{v'v'} & \overline{v'w'} \\ \overline{w'u'} & \overline{w'v'} & \overline{w'w'} \end{pmatrix} = A \begin{pmatrix} \overline{u'_m u'_m} & \overline{u'_m v'_m} & \overline{u'_m w'_m} \\ \overline{v'_m u'_m} & \overline{v'_m v'_m} & \overline{v'_m w'_m} \\ \overline{w'_m u'_m} & \overline{w'_m v'_m} & \overline{w'_m w'_m} \end{pmatrix} A^T$$

$$\tag{2.50}$$

A major assumption of this method is stationarity, which allows to interpret the time-averaged observations as the ensemble averaged turbulent fluxes in the conservation equations resulting from Reynolds decomposition (Eqs 2.13-2.15). Furthermore, measurements must be taken over horizontally homogeneous surfaces during steady-state conditions within the surface layer, such that the measured covariance at a certain height can be directly interpreted as the turbulent flux at the surface, i.e. $\left(\overline{w'\theta'}\right)_s \approx$

$\overline{w'\theta'} \approx \overline{w'T'}$. Hence, in the remainder of this thesis we will compute the sensible heat flux (SHF) from eddy covariance measurements as:

$$SHF = -\rho_a C_p \overline{w'T'},\tag{2.51}$$

with ρ_a the air density and C_p the air specific heat at constant pressure. We will assume that all the heat storage and source/sink terms between the surface and the height of instruments, including the divergence of radiation, are negligibly small.

The covariance between w and a quantity χ is estimated as :

$$\overline{w'\chi'} = \frac{1}{N-1} \sum_{k=0}^{N-1} [(w_k - \overline{w_k})(\chi_k - \overline{\chi_k})]\tag{2.52}$$

where N is the amount of samples in the time interval Δt. The time interval should be carefully chosen, such that it is long enough to capture all relevant scales of the turbulent fluctuations, i.e. all time scales during which the fluctuations of vertical velocity and conserved quantities remain correlated. Too short averaging periods will miss the long time correlation in the turbulent flux information, while too long periods are contaminated by large scale fluctuations not directly related to the fluxes close to the surface (Finnigan et al., 2003). Furthermore, since the fluctuations of conserved quantities are usually correlated over several time scales, the sampling frequency must be high enough such that all the relevant scales are measured (Bosveld and Beljaars, 2001). Using empirical data such as from the Kansas 1968 experiment (Kaimal et al., 1972), the size of the turbulent eddies mixing the conserved quantities is found to depend on the height of the sensor (z), the wind speed (u) and stability parameter (ζ). Modelling both the spectral distribution of turbulent flux information and the frequency characteristics of the sensor allows to estimate the flux attenuation (Horst, 1997). We define the cospectrum $S_{w\chi}(f)$ of two time series w' and χ' as the real part of the cross-spectrum, with f the frequency:

$$S_{w\chi}(f) = \mathcal{R}\left[\mathcal{F}_w(f) \cdot \mathcal{F}_\chi^*(f)\right],\tag{2.53}$$

where $\mathcal{F}_\chi^*(f)$ is the complex conjugate of the Fourier transform $\mathcal{F}_\chi(f)$ of the signal $\chi'(t)$, defined as:

$$\mathcal{F}_\chi(f) = \frac{1}{\sqrt{2}} \int_{-\infty}^{+\infty} \chi'(t) e^{ift} \mathrm{dt}.\tag{2.54}$$

An interesting property of the cospectrum is that it describes how the turbulent flux information is distributed in the frequency space:

$$\overline{w'\chi'} = \int_0^{+\infty} S_{w\chi}(f) \mathrm{df}.\tag{2.55}$$

Based on measurements of the Kansas 1968 experiment (Kaimal et al., 1972), the following empirical expressions were derived for the momentum and heat flux cospectra under stable conditions:

$$\frac{f S_{w\chi}}{\overline{w'\chi'}} = \frac{n}{A_{w\chi} + B_{w\chi} n^{2.1}},\tag{2.56}$$

where $n = fz/u$ is the normalised frequency and with $A_{w\chi}$ and $B_{w\chi}$ defined as :

$$A_{uw} = 0.124(1 + 7.9\zeta)^{3/4} \tag{2.57}$$

$$A_{wT} = 0.284(1 + 6.4\zeta)^{3/4} \tag{2.58}$$

$$B_{w\chi} = 2.34 A_{w\chi}^{-1.1}. \tag{2.59}$$

These expressions allow to estimate the required sampling frequency such that nearly all the relevant spectral information is located at lower frequencies than the so-called Nyquist frequency, defined as half the sampling frequency. For practical applications in the lowest part of atmospheric boundary layer, the sampling frequency should be at least 10 Hz to capture most of the relevant high frequency eddies. Conversely, these equations can be used to our advantage, i.e. to estimate the loss of information, or flux attenuation, if slow-response instruments are used. The estimated attenuation factor $(A_{w'\chi'})$ is:

$$A_{w'\chi'} \equiv \frac{\overline{w'\chi'}_m}{\overline{w'\chi'}} = \frac{\int_0^{+\infty} S_{w\chi}(f) T_{w\chi}(f) \mathrm{d}f}{\int_0^{+\infty} S_{w\chi}(f) \mathrm{d}f}. \tag{2.60}$$

where $\overline{w'\chi'}_m$ is the measured covariance that differs from the real covariance $(\overline{w'\chi'})$ because of the frequency filtering described by $T_{w\chi}(f)$, the total transfer function of the measuring system. The latter contains the effects of slow response sensors, spatial averaging, sensor separation, time averaging, and must be individually modelled for each time interval and acquisition system (Moore, 1986; Horst, 2000). In practice, measuring $\overline{u'w'}$ and $\overline{w'\theta'}$ with a modern sonic anemometer such as the CSAT3 at 10 Hz sampling frequency results in 1% flux attenuation. However, this attenuation can exceed 50% when using two slow-response sensors under stable conditions as will be shown in chapter 3. The processing steps used in this thesis before analysing the eddy covariance data are given in Algorithm 2.

The first step in analysing the eddy covariance data is the data selection strategy. Sonic anemometers suffer from flow distortion due to transducer shadowing (Frank et al., 2015; Horst et al., 2015). This translates into an undesired dependence of measured wind and temperature averages and fluctuations, on wind direction (Figure 2.3). This dependence is minimised by selecting data in a narrow interval of wind directions, which is for a CSAT3 instrument typically ±45° from the orientation of the transducer heads. The wind directional dependency of quantities $|\overline{v'w'}/\overline{u'w'}|$ and σ_w/u_* are robust indicators of flow distortion (Figure 2.3). An additional limitation of data from sonic anemometers is the presence of large spikes, which are present during either blowing snow conditions, fog, or rain events. A limited amount of spikes can be filtered out using a moving median filter (Mauder et al., 2013). Periods with too much noise can be identified by using thresholds on measured u_* and σ_T quantities.

Transducer shadowing and the presence of spikes greatly reduce the percentage of data that can be used for further interpretation. Furthermore, a sonic anemometer or a fast hygrometer operating in remote polar regions can sometimes be switched off for part of the time when the temperatures are very low e.g. to save battery capacity. These
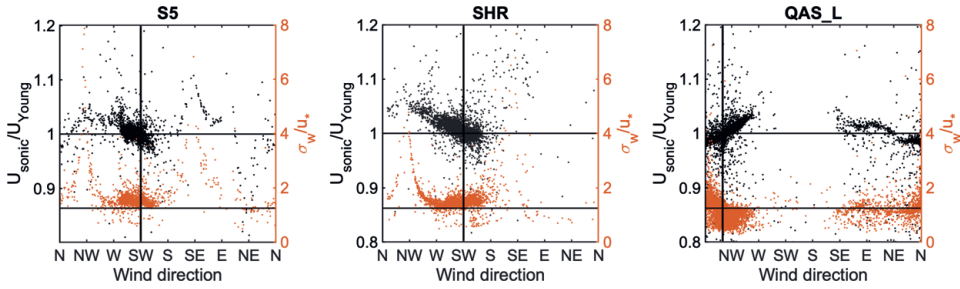
Figure 2.3: Ratio of measured wind speed with a CSAT3 sonic anemometer and a Young anemometer (black) and the standard deviation of vertical wind speed normalised with the friction velocity (orange) as a function of wind direction for eddy covariance systems at three different sites in the ablation zone of the Greenland ice sheet. The vertical line denotes the orientation of the transducers heads, and the horizontal lines denote the expected value under neutral conditions.

limitations are not present when using vertical and horizontal propellers and thermo-couples to measure fluxes instead. The drawback of such a vertical propeller eddy covariance (VPEC) system is the larger attenuation due to the higher response-time of these instruments. This will be investigated in chapter 3.

2.4 Measuring the surface energy balance and ablation

This section describes the measurements that are required for estimating surface melt, either by closing the SEB or by directly measuring the lowering of the surface. The four components of net radiation at the surface are measured with a net radiometer. This instrument incorporates a pair of pyranometers to measure incoming and reflected shortwave radiation, and a pair of pyrgeometers to measure incoming and outgoing longwave radiation. For IMAU stations, a CNR1 was used before 2016 and a CNR4 after (both from Kipp & Zonen, Delft, the Netherlands). A detailed description of the IMAU AWS measurements can be found in Smeets et al. (2018) and Kuipers Munneke et al. (2018b), while the PROMICE stations are described by Fausto et al. (2021). The corrections applied to the radiometer are the following:

- Correction of the calibration coefficients (or sensitivity) of the sensors, possibly including a sensitivity dependence on temperature

- Excess window heating offset of the pyrgeometer due to absorbed shortwave radiation (Smeets et al., 2018)

- Correction of zero-offset in pyranometer caused by cooling of the dome due to infrared radiation (so called Zero offset A, Behrens (2021))

- Tilt correction after Van den Broeke et al. (2004), or similar to Fausto et al. (2021) when inclinometer data are available

Overall, the reported accuracy by the manufacturer of daily averaged radiation components measured by a CNR4 is $< 10\%$ for the pyrgenometer and $< 5\%$ for the pyranometer. The zero-offset can cause a bias of up to 10 W m^{-2} in both shortwave components (Behrens, 2021). The average tilt correction for PROMICE data can reach up to 8 W m^{-2} (Fausto et al., 2021). The measured tilt angles for stations S5 and S6 are shown in Figure 2.4. The tilt angle and direction were converted from the measured pitc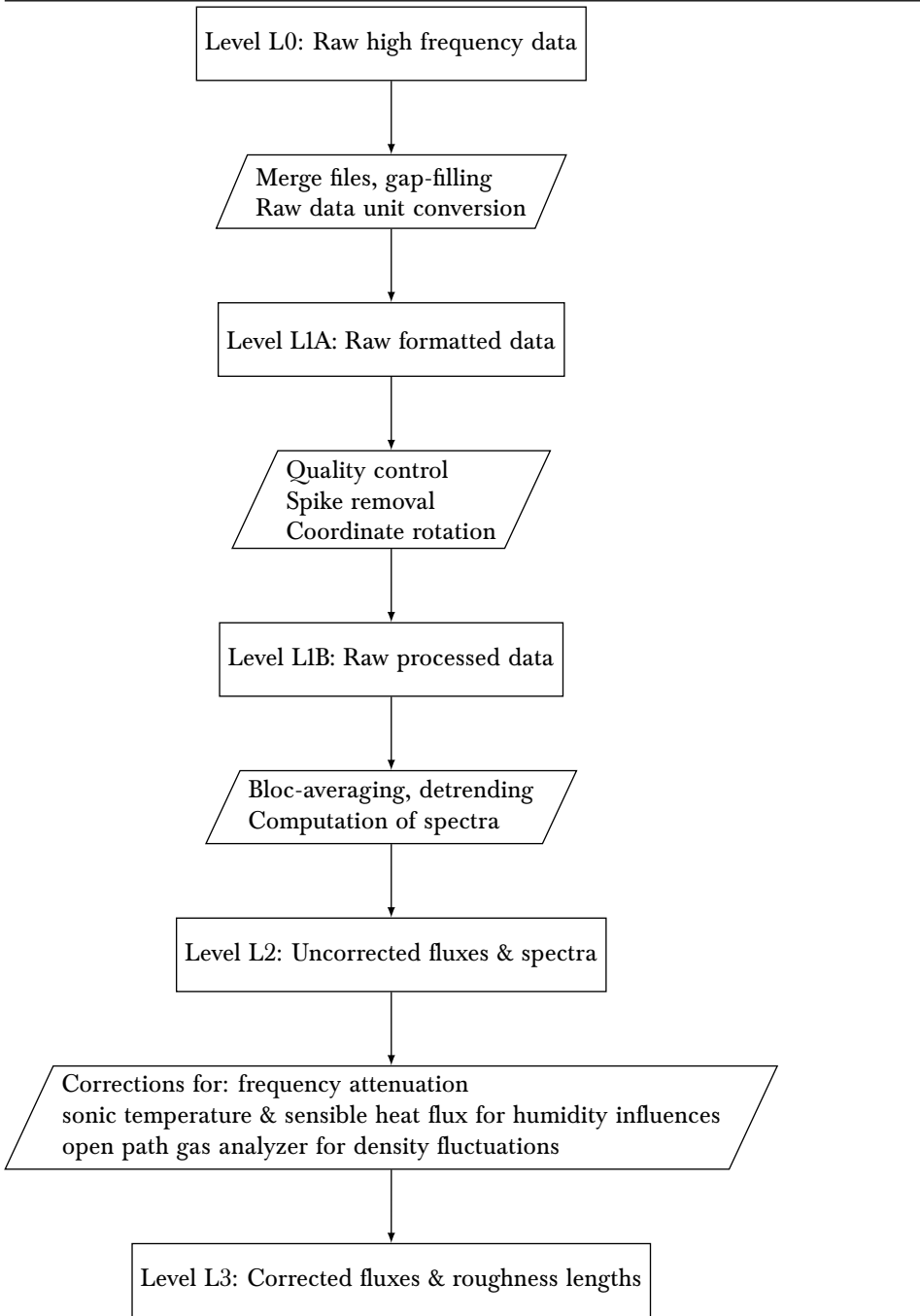h, roll and yaw angle (Box 4). The tilt angle of the mast shows a random behaviour during the melting season, due to heterogeneous ice ablation under the feet of the mast. On rare occasions this angle can become as large as 10°, as was the case at S5 during the summer of 2020 (Figure 2.4). The tilt angle determines the amplitude of the correction, and the tilt direction determines the sign and the phase shift of the correction. A radiometer, in the Northern hemisphere, that is tilted towards South overestimates the downward radiation over a planar surface. And if it is tilted to the West, the maximum observed downward shortwave radiation with respect to the local solar maximum will be delayed.

Algorithm 2 Eddy covariance data processing flowchart

Level L0: Raw high frequency data

Merge files, gap-filling
Raw data unit conversion

Level L1A: Raw formatted data

Quality control
Spike removal
Coordinate rotation

Level L1B: Raw processed data

Bloc-averaging, detrending
Computation of spectra

Level L2: Uncorrected fluxes & spectra

Corrections for: frequency attenuation
sonic temperature & sensible heat flux for humidity influences
open path gas analyzer for density fluctuations

Level L3: Corrected fluxes & roughness lengths

Figure 2.4: Measured tilt angles of AWS S5 and S6 in the period 2016-2022. Black crosses denotes the orientation after each yearly visit.

Box 4: **Conversion of measured inclinometer angles**

The mast tilt azimuth orientation (a_w,clockwise with respect to true North), and the mast tilt angle (b) are defined by:

$$b = \pi/2 - \tan^{-1}\left(\frac{Y_2}{\sqrt{Y_0^2 + Y_1^2}}\right) \tag{2.61}$$

$$a_w = \tan^{-1}\left(\frac{Y_1}{Y_0}\right) + \gamma \tag{2.62}$$

where γ is the yaw angle, i.e. the azimuth angle of the horizontal boom on which the inclinometer is installed, and $Y = [Y_0, Y_1, Y_2]$ is the true mast position vector in the local (x,y,z) cartesian reference frame. This position is obtained after applying a pitch and roll rotation to a perfectly vertical mast :

$$Y = A_\alpha A_\beta X \tag{2.63}$$

where $X = [0, 0, 1]$ is the position vector of a perfectly vertical mast. The roll and pitch rotation matrices are defined as:

$$A_\beta = \begin{pmatrix} 1 & 0 & 0 \\ 0 & \cos\beta & \sin\beta \\ 0 & -\sin\beta & \cos\beta \end{pmatrix} \tag{2.64}$$

$$A_\alpha = \begin{pmatrix} \cos\alpha & 0 & -\sin\alpha \\ 0 & 1 & 0 \\ \sin\alpha & 0 & \cos\alpha \end{pmatrix} \tag{2.65}$$

with α the pitch angle and β the roll angle measured by the inclinometer.

The computation of turbulent heat fluxes from automatic weather station data is often performed using the bulk method. This requires knowledge of the air potential temperature (θ), surface potential temperature (θ_s), wind speed (u), air specific humidity (q) and surface specific humidity (q_s). When an unventilated temperature sensor is used, as is the case for IMAU stations, the air temperature must be corrected for excess heating of the sensor body due to shortwave radiation (Smeets et al., 2018). The surface temperature is computed using the Stefan-Boltzmann equation, excluding the reflection of incoming longwave radiation at the surface:

$$T_s = \left(\frac{LW_u - (1-\epsilon)LW_d}{\sigma\epsilon} \right)^{1/4} \tag{2.66}$$

with $\sigma = 5.67 \times 10^{-8}$ W m^{-2} K^{-4} the Stefan-Boltzmann constant and ϵ the emissivity of the surface. For snow and ice, ϵ ranges between 0.95 and 1.00 (Hori et al., 2006). Horizontal wind speed is measured by a propeller vane, with an accuracy of ± 0.3 m s^{-1}. Specific humidity is converted from air pressure and relative humidity (Box 2), which is measured with a typical uncertainty of 2% with respect to the saturation humidity of liquid water. Therefore a correction is required for temperature below the freezing point in order to estimate the humidity relative to the saturation of ice. The surface is always assumed to be at saturation, i.e. $q_s = q_{sat}(T_s)$.

The surface lowering is measured in-situ using four different methods: (1) manual annual stake observations, (2) ablation draw wire (ADW), (3) pressure transducer assembly (PTA) and (4) sonic height ranger on a stake (SR). The manual stake observations are considered as the reference, yet they only provide one measurement per visit (typically annually) at one very specific location, and suffer from random sampling errors of around 5 mm w.e. (Braithwaite et al., 1998). The ADW and PTA measurements provide sub-daily measurement of surface lowering, and are well-suited for areas with large ablation rates (> 3 m/year), or for monitoring over longer periods without the need of annual maintenance. The drawback of the PTA is the unknown variability in the output due to either an imperfect sealing of the hose containing the liquid, causing changes in fluid pressure (Fausto et al., 2012), or the horizontal movement of the station with respect to the borehole. The ADW eliminates the practical complication of using a liquid (Hulth, 2010), nevertheless it also needs to be corrected for lateral movement with respect to the borehole. The SR is the only measurement capable of detecting both snow accumulation, snow melt and ice ablation, but it is contaminated by large spikes caused by secondary reflections, or drifts due to the bending of the stake over areas with large ablation. Apart from the instrumental limitations, the spatial variability in surface lowering also causes differences between adjacent measurements. Furthermore, the depth of the anchor point (the point on which the instruments are fixed) of the PTA and ADW instruments (tripod feet) determines how much the measurement will be delayed in capturing the melt that occurs directly at the surface. A photograph of site QAS_L in South Greenland where these four techniques have been employed is shown in Figure 2.5.

A typical workflow for processing AWS data is shown in Algorithm 3. Most of these steps can be programmed, which facilitates an almost real-time and consistent treat-

ment of a large network of AWS. These processing steps are used to process AWS data used in all the following chapters.
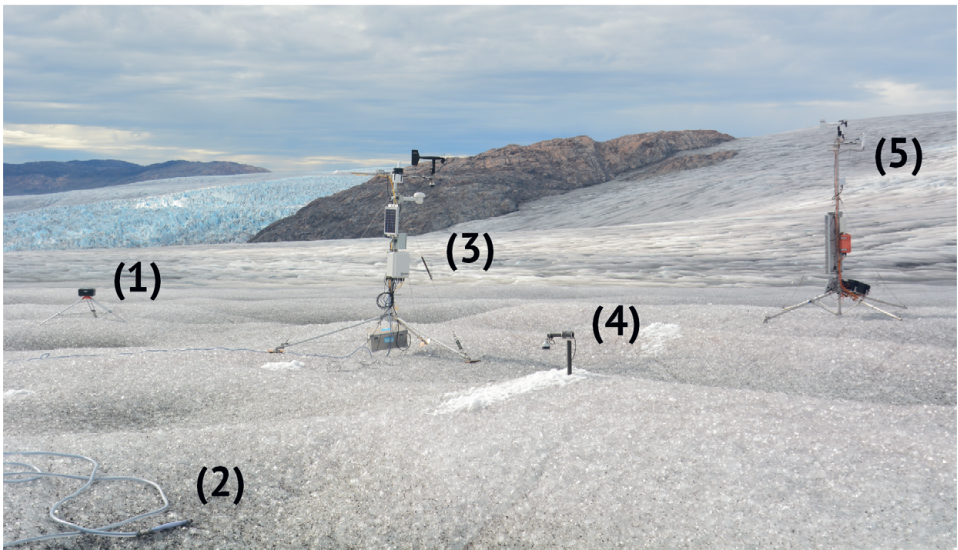
Figure 2.5: Site QAS_L after maintenance on 29 August 2020. (1) Ablation draw wire (ADW), (2) pressure transducer assembly (PTA), (3) PROMICE automatic weather station (AWS), (4) sonic height ranger on a stake (SR) and (5) eddy covariance station.

Algorithm 3 Automatic weather station (AWS) data processing flowchart

Level L0: Raw logger data

Gap-filling
Raw data unit conversion

Level L1A: Uncorrected formatted data

Import metadata
Quality control
T & RH corrections
Radiometer corrections
Filtering sonic ranger data
Compute derived variables:
(q_v, θ, T_s, T_v, θ_s, q_s, ρ_a, albedo, solar angles)
Compute cumulative change in surface level

Level L1B: Corrected data $\rightarrow$ SEB model forcing

Compute SHF & LHF using the bulk method

Level L2: Corrected AWS data & turbulent heat fluxes

Merge with level L3 eddy covariance data

Level L3B: Corrected AWS data & eddy covariance data

Chapter 3

Measuring turbulent fluxes with the Vertical Propeller Eddy-Covariance Method

Summary

On the Greenland ice sheet, the sensible heat flux is the second largest source of energy for surface melt. Yet in atmospheric models, the surface turbulent heat fluxes are always indirectly estimated using a bulk turbulence parametrization, which needs to be constrained by long-term and continuous observations. Unfortunately, such observations are challenging to obtain in remote polar environments, especially over ablating ice surfaces. We therefore test a classical eddy-covariance method, based on propeller anemometers and thermocouple measurements, to estimate the momentum and sensible heat fluxes on the Greenland ice sheet. To correct for the high-frequency attenuation, we experimentally derive the sensor frequency-response characteristics and evaluate the universal turbulence spectra on the ice sheet. We show that the corrected fluxes are accurate and that the sampling interval can be reduced to 4 s to increase the system's autonomy. To illustrate its potential, we apply the correction to one year of vertical propeller eddy-covariance measurements in the western ablation area of the ice sheet, and quantify the seasonal variability of the sensible heat flux and of the aerodynamic roughness length.

3.1 Introduction

The total mass balance of the Greenland ice sheet, defined as the integrated surface mass balance minus the calving of ice at marine-terminating glaciers, is a primary component of the global sea-level budget. Between 2012 and 2016, the ice sheet lost on average 247 Gt yr^{-1} of mass ($\approx$ 0.7 mm yr^{-1} sea-level equivalent), which accounts for 37% of all the land-ice contribution to global sea-level rise (Bamber et al., 2018). This recent strong mass imbalance of the ice sheet has been linked to a significant increase in

surface melt (Van den Broeke et al., 2016), which is either measured in-situ or calculated by closing the surface energy balance[1],

$$M = R_{net} - H - LE + G, \tag{3.1}$$

where M is the surface melt, R_{net} is the net absorbed radiation by the surface, H is the sensible heat flux, LE the latent heat flux, and G the ground heat flux. Here we define H, LE, and G positive upwards and express them in W m^{-2}. On the ice sheet, a positive R_{net} drives most of the surface melt, while LE and G are an order of magnitude smaller (Kuipers Munneke et al., 2018b). The sensible heat flux H, however, is an important source of energy for the melt of seasonal snow in mountain regions (Mott et al., 2011) and in the Arctic tundra (Pohl et al., 2006), but also for the melt of Arctic sea ice (Tjernström et al., 2015) and at the surface of Antarctic ice shelves (Kuipers Munneke et al., 2018a).

Despite efforts to measure the various components of the surface energy balance on the ice sheet (Steffen and Box, 2001; Van As et al., 2011; Kuipers Munneke et al., 2018b), direct measurements of turbulent heat fluxes are still limited. Instead, an indirect bulk method is typically used to estimate the turbulent surface fluxes from measurements made by single-level automatic weather stations. This has revealed that the sensible heat flux is also an important source of energy for surface melt on the ice sheet, both in the western ablation area (Kuipers Munneke et al., 2018b) and the southern ablation area (Fausto et al., 2016a). However, the modelled sensible heat flux using these methods can be highly uncertain, either due to underlying assumptions (Radić et al., 2017) or due to physical parameters that are not well constrained in time and space, such as the aerodynamic roughness length (Smeets and Van den Broeke, 2008a).

One way to directly measure the turbulent surface fluxes uses the sonic eddy-covariance (SEC) method, based on fast measurements of the three-dimensional wind vector and temperature acquired with sonic anemometers. Such instruments are costly, require a continuous and significant power supply, and do not function under drifting snow conditions or precipitation. This makes them less than practical for long-term experiments in remote polar areas. Yet several experimental campaigns have successfully measured the turbulent surface fluxes with sonic anemometers on the ice sheet (Henneken et al., 1994; Forrer and Rotach, 1997; Box and Steffen, 2001; Smeets and Van den Broeke, 2008a; Miller et al., 2017; Madsen et al., 2019). Unfortunately these datasets rarely span more than several weeks, and are not always representative of areas with the highest surface melt rates.

A more feasible alternative to measuring turbulent fluxes on the ice sheet is the vertical propeller eddy-covariance (VPEC) method, which relies on propeller anemometers and thermocouples (Blanford and Gay, 1992). One then faces two practical obstacles: the icing of the instruments, and their limited frequency response (Horst, 1997). Conveniently, icing is not a frequently occurring problem in the katabatic wind zone, where the air is usually undersaturated (Smeets et al., 2018). This paper aims to provide a solution to the second challenge: the high-frequency attenuation of the measured fluxes due to the limited frequency response of the propeller anemometers and thermocouples.

---

[1]Note that this notation and sign convention differs from the other chapters in this thesis to comply with the journal requirements
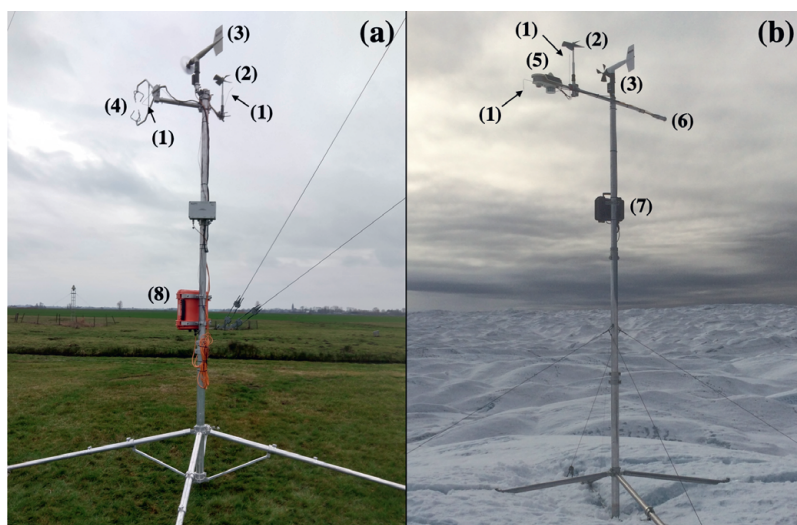
Figure 3.1: Experimental set-up used during Experiments 1 and 2 (a), and during Experiment 4 (b). The set-up of Experiment 3 is not shown here but can be found in Lenaerts et al. (2014). The numbers indicate different instruments: (1) Fine-wire thermocouples (also indicated by arrows), (2) Gill vertical propeller anemometer, (3) Young horizontal propeller anemometer, (4) CSAT3 sonic anemometer, (5) Intelligent weather station and logger, (6) CNR4 net radiation sensor, (7) Ablation draw-wire sensor, (8) CR1000 data-logger.

Although the high-frequency attenuation of the measured fluxes has received quite some attention, the latest developments mainly focus on experimental set-ups that use a slow-response sensor in combination with a fast sensor to measure fluxes of atmospheric gases, such as carbon dioxide and water vapour (Ibrom et al., 2007), or methane (Peltola et al., 2013). We focus on the high-frequency attenuation of momentum and sensible heat fluxes caused by applying a combination of two slow-response sensors. Our aim is to accurately model this attenuation, in particular under the stable conditions commonly observed in the atmospheric boundary layer over the ice sheet.

The paper is organized as follows: in Sect. 3.2 we give an overview of the field experiments and the instruments, in Sect. 3.3 we give a detailed description of the model that is used to correct for the high-frequency attenuation of the fluxes. In Sect. 3.4 we then evaluate the model and the corrected VPEC fluxes against SEC fluxes, and we quantify the influence of a reduced sampling rate. Finally, we apply the high-frequency correction to one year of VPEC measurements made in the western ablation area of the ice sheet in Sect. 3.5, and quantify the temporal variability of the fluxes.

3.2 Methods: Description of the Datasets

3.2.1 Instrumental Set-up

In the following experiments, we test the vertical propeller eddy-covariance (VPEC) method. For the horizontal wind measurement we use a Young wind vane anemometer (model 05103-L, R.M. Young Company, Traverse City, Michigan, USA) fitted either with polypropylene or carbon fiber thermoplastic blades. For the measurement of the vertical wind speed we use a Gill vertical propeller fitted with expanded polystyrene blades (model 27106, R.M. Young Company, Traverse City, Michigan, USA). An alternative instrument for the VPEC method is the K-Gill propeller vane (Ataktürk and Katsaros, 1989), which has a higher sensitivity to wind fluctuations. Unfortunately, this sensor requires sensitive material for both the propellers, which makes it unsuitable for long-term studies in polar conditions. Besides, it is more convenient to install a vertical Gill propeller next to the Young wind vanes that are already used on many existing weather stations.

The temperature is measured by a 76.2 µm diameter, type E, fine-wire thermocouple (model FW3, Campbell Scientific, Logan, USA). The propellers are positioned at the same height above the surface, and the centres of the blades are separated by 0.50 m. The fine-wire thermocouple referred to hereafter is fitted just below the blades of the vertical propeller.

As a reference, we apply the sonic eddy-covariance (SEC) method with a non-orthogonal sonic anemometer (CSAT3, Campbell Scientific, Logan, USA) sampling at a rate of 10 Hz. The sonic anemometer is positioned at 0.50 m distance from the Young wind vane anemometer and at the same height as the centre of the propeller blades.

When mentioned, net absorbed radiation by the surface is measured by a net radiometer (model CNR4, Kipp & Zonen, Delft, the Netherlands) and ice ablation is measured by a draw-wire (model FD115 – 15000, Althen, Leidschendam, the Netherlands). For the measurements presented below, the draw-wire sensor is positioned on the same mast as the other instruments, at a height of 3.08 m (see Fig. 3.1). A weight is attached to the tip of the draw-wire, which is drilled 10 m into the ice. The cumulative ablation of the ice surface causes the wire to roll around a spring-loaded spool, and the wire's linear extension is then measured every 30 min with a potentiometer (Hulth, 2010).

3.2.2 Description of the Experiments

We use measurements from four separate field experiments, two of which were performed on the Greenland ice sheet. The characteristics of each experiment are summarized in Table 3.1 and are further detailed below.

Experiments 1 and 2: CESAR Site in 2011 and 2019

The full set-up consisting of both the VPEC and SEC instruments was tested twice at the Cabauw experimental site for atmospheric research (CESAR, e.g. Monna and Bosveld, 2013), located on a flat grassland in the Netherlands (51.970°N, 4.927°W,−0.8 m a.s.l.).

Table 3.1: Instrumental set-up during the four different field experiments, performed at the Cabauw Experimental Site for Atmospheric Research (CESAR) located in the Netherlands (NL), and at two sites on the Greenland ice sheet (GrIS). z_m denotes the measurement height above the local surface, d is the displacement height and H is the height of the local surface above the surrounding average topography, L_u is the response length of the horizontal anemometer, A_w is the calibration constant of the vertical anemometer, and τ_T is the response time of the fine-wire thermocouple, which were used to correct for high-frequency attenuation and are defined in the body of the paper. Their measurement uncertainty is given in the brackets. Propeller types used are identified as follows: PP: polypropylene, CFT: carbon fiber thermoplastic, EPS: expanded polystyrene.

Experiment	1	2	3	4
Location	CESAR NL	CESAR NL	S10 GrIS	S5 GrIS
z_m (m)	4.45	3.9	[4.2;4.9]	[3.7;4.0]
d (m)	0	0	0	0.5
H (m)	0	0	0	1.5
$F_{s,VPEC}$ (Hz)	10	2	1 (not used)	0.25
$F_{s,SEC}$ (Hz)	10	5	10	none
Unobstructed Wind directions	[200;250]	[130;220]	[70;130]	[40;180]
$L_u(\Delta L_u)$ (m)	1.78 (0.2)	3.15 (0.2)	not used	3.15 (0.2)
$A_w(\Delta A_w)$ (m)	0.45 (0.1)	0.45 (0.1)	not used	0.45 (0.1)
$\tau_T(\Delta \tau_T)$ (s)	0.13 (0.04)	0.13 (0.04)	not used	0.13 (0.04)
Horizontal (Vertical) propeller material	CFT (EPS)	PP (EPS)	not used	PP (EPS)
Sonic orientation	209°	195°	165°	none
Selected fluxes	577	279	not used	11300
Selected variance spectra	283	137	not used	not used
Selected cospectra	not used	not used	30	not used
Total 30-min data	1967 (41 days)	674 (14 days)	661 (14 days)	16889 (352 days)

The first experiment took place during August and September 2011, while the second experiment took place during February 2019.

In the first experiment, all the time series were sampled at 10 Hz. In the second experiment, however, the sampling rate of the VPEC system was reduced to 2 Hz in order to test a different sampling of the horizontal wind speed. Differences between the two experiments also comprise the height and the orientation of the sensors, as well as the material of the horizontal propeller. All information can be found in Table 3.1.

Experiment 3: Site S10 in 2012

This experiment took place at site S10 of the K-transect (67.00°N,47.02°W, 1850 m a.s.l), which is a transect of automatic weather stations and mass balance observations located in the ablation area of the western Greenland ice sheet. It spans from the ice edge up to 1850 m elevation and has been operated by the Institute for Marine and Atmospheric research Utrecht since 1993. Further details about the K-transect can be found in Smeets et al. (2018) and Kuipers Munneke et al. (2018b). The measurements for this specific experiment are documented by Lenaerts et al. (2014) and are used to test the validity of the Kaimal et al. (1972) turbulence spectra on the ice sheet. We use the raw SEC time series, which were recorded four hours per day between August and October 2012. The comparison between SEC and VPEC fluxes cannot be done with this experiment, as there was no Young anemometer adjacent to the Gill vertical propeller. Furthermore the sensible heat fluxes are small, with an average of 20 W m^{-2}, and the frequency of both riming and blowing-snow events reduces the amount of valid data for comparison.

The snow surface at this site is very homogeneous, and slopes downward from east to west with a slope angle of about 0.4 degrees. This gives rise to south-easterly katabatic flow more than 70 percent of the time (Smeets et al., 2018). The height of the SEC instruments was recorded every 30 min by a sonic height ranger, and decreased from 4.9 m in August to 4.2 m in the end of October due to snowfall.

Experiment 4: Site S5 in 2016–2017

To illustrate the potential of the method, the VPEC instruments without a sonic anemometer have also been operated on the K-transect for a longer period of time. The measurements were made at site S5 of the K-transect (67.09°N, 50.06°W, 540 m a.s.l) between September 2016 and August 2017. All the instruments are connected to a low power logger which continuously records the time series at an interval of 4 s.

The local ice surface is composed of rough hummocks and domes, interlaced by melt-water streams. The station is located on the top of an ice dome, and the dome itself is located approximately 1.5 m above the average surrounding topography, denoted H. The effective measurement height is thus:

$$z = z_m + H - d, \tag{3.2}$$

where z_m is the height of the sensors above the local surface, which was recorded every 30 min by a sonic height ranger and ranges between 3.7 m and 4.0 m during the

measurement period. The displacement height d, and the height of the local surface above the average surrounding topography H are assumed constant and equal to 0.5 m and 1.5 m, respectively, after Smeets and Van den Broeke (2008a).

3.2.3   Notations

We work with the measured time series of the horizontal wind speed vector $\mathbf{U} = (u, v)$, vertical wind speed w, and air temperature T, where u and v are the along-wind and cross-wind components of $\mathbf{U}$, respectively, and w is the wind component normal to the local surface slope. The 30-min average of x is written as $\overline{x}$, while the 30-min covariance between the fluctuations of x and y is written as $\overline{x'y'}$. The temperature flux is thus $\overline{w'T'}$, and the along-wind momentum flux is $\overline{u'w'}$. Hereafter we write the 30-min average of $\|\mathbf{U}\|$ as U.

3.2.4   Preliminary Corrections

The raw time series of each experiment are first screened for non-physical values, and the measured vertical wind speed from the vertical propeller anemometer is multiplied by a factor 1.25, in order to account for the non-cosine response of propeller anemometers at high angles of attack (Gill, 1975). Then multiple iterations of a median absolute difference threshold filter (Mauder et al., 2013) are performed to remove individual spikes in the raw time series. The latter filter proved unnecessary for the propeller and thermocouple measurements, due to the very small amount of spikes in these time series. The raw time series are block-averaged in 30-min windows, linearly de-trended, and windows with more than 5% missing data are flagged. Furthermore, block-averaged time windows with wind directions that are suspected to contain flow distortion are also flagged.

For both the VPEC and the SEC instruments, a yaw rotation followed by a pitch rotation, or double rotation (Kaimal and Finnigan, 1994), is used to rotate the raw measured wind vector in the local horizontal reference frame, thereby correcting for the flux biases induced by tilted sensors. This rotation method was chosen over the planar fit method (Wilczak et al., 2001), as the tilt angles of the weather station in the ablation area of the ice sheet change over time due to melt. Besides, only a narrow band of downslope wind directions are available for analysis in the katabatic zone of the ice sheet. The final step of the preliminary processing involves the calculation of the raw turbulence (co)spectra, which are smoothed with an averaging window that exponentially expands with frequency (Kaimal and Finnigan, 1994).

During Experiments 1 and 2, the buoyancy flux measured by the sonic anemometer is corrected for humidity influences according to Schotanus et al. (1983), using the latent heat flux measured at a nearby location by the Royal Netherlands Meteorological Institute (KNMI) at the CESAR observatory. Finally the SEC fluxes are corrected for path averaging after Moore (1986), using a path length of 0.12 m.

The downward shortwave radiation measured during Experiment 4 is corrected for the pitch and roll of the net radiometer. For this we use the tilt angles measured by the inclinometer located in the station logger, and the geometrical equations found in, e.g.,

Wang et al. (2016). The tilt angle of the weather station varied between 4° and 6° towards the west over one year. This tilt orientation means that the correction mostly shifts the phase of the measured shortwave incoming radiation, which affects the daily averaged radiation by less than 2 W m^{-2}. The ablation draw wire measurement is not corrected for the movement of the station, as the horizontal displacement of the station with respect to the borehole was less than 0.5 m after one year. This offset results in an error in yearly ice ablation of less than 0.04 m, which is also the difference with the manual ablation measurement at a nearby stake and $\approx$ 1% of the total yearly ablation. The ice ablation is converted to an energy flux using a latent heat of melting of 334 $\times$ 10^3 J kg^{-1} and a constant ice density of 916 kg m^{-3}.

3.2.5 Data Selection Strategy

Fluxes

When analyzing the fluxes measured during all four experiments, we minimize the influence of flow obstruction and propeller stalling at low wind velocities by applying the following data selection criteria:

(i) $\overline{WD} \in$ Unobstructed wind directions,

(ii) $U > 3$ m s^{-1},

(iii)   Flag = 0,

where $\overline{WD}$ is the wind direction of the 30 min-averaged wind vector and 'Flag' is the quality flag of the preliminary flux corrections. The interval of unobstructed wind directions is determined a priori by the design of the mast and the relative location of each instrument. It is then adjusted iteratively until an optimal trade-off between VPEC and SEC flux agreement and data quantity is found. The final chosen intervals for each experiment are given in Table 3.1. We do not include any filter related to the error in the cross-momentum flux $\overline{v'w'}$, as we assume that the same error is present in both the SEC and the VPEC fluxes.

Variance Spectra

For the analysis of the variance spectra measured at the CESAR site during Experiments 1 and 2, we remove the ill-defined spectra in terms of signal-to-noise ratio, and thus extend the previous data selection with the following criteria:

(iv) $\dfrac{z}{L_O} < 0.2$,

(v) $\overline{w'^2} > 0.01$ m^2 s^{-2},

(vi) $\overline{u'^2} > 0.01$ m^2 s^{-2},

(vii) $\overline{T'^2} > 0.04$ K^2 ,

where $L_O \approx -\dfrac{u_*^3 \overline{T}}{\kappa g \overline{w'T'}}$ is the Obukhov length, $u_* = \left(\overline{u'w'}^2 + \overline{v'w'}^2 \right)^{1/4}$ is the friction

velocity, $\kappa = 0.4$ is the von Kármán constant, and $g = 9.81$ m s^{-2} is the acceleration due to gravity.

Covariance Spectra

Finally, when analyzing the turbulence cospectra measured at site S10 on the ice sheet during Experiment 3, we limit the influence of drifting snow and apply a very strict near-neutral stability range:

(viii) $\; 0 < \dfrac{z}{L_O} < 0.2,$

(ix) $\;\; 0.1 < u_* < 0.5$ m s$^{-1},$

(x) $\;\; \overline{w'T'} > 0.005$ K m s$^{-1}.$

The resulting selected fluxes and spectra for each experiment are summarized in Table 3.1.

3.3 Methods: High-frequency Attenuation Correction

When used to measure turbulent fluxes, propeller anemometers have the following limitations : (1) a limited frequency response, (2) a non-linear directional sensitivity, and (3) a threshold starting wind speed (Wyngaard, 1981). In this section we provide a spectral correction for the limited frequency response. The data selection criteria are used to mitigate for limitations (2) and (3).

The measured (co)variance between atmospheric quantities x and y, denoted $\overline{x'y'}$, is a fraction A_{xy} of the true (co)variance. We calculate the attenuation coefficient A_{xy} after Moore (1986),

$$A_{xy} \equiv \frac{\overline{x'y'}_m}{\overline{x'y'}} = \frac{\displaystyle\int_0^{+\infty} S_{xy}(f)T_{xy}(f)\,\mathrm{d}f}{\displaystyle\int_0^{+\infty} S_{xy}(f)\,\mathrm{d}f}, \qquad x,y \in \{u,w,T\}, \tag{3.3}$$

where $\overline{x'y'}_m$ is the measured (attenuated) (co)variance between atmospheric variables x and y, and f is the frequency (Hz). With this definition, the attenuation of the flux is equal to $1 - A_{xy}$. This method thus requires an expression for the reference turbulence (co)spectrum S_{xy} and the total transfer function of the system T_{xy} .

3.3.1 Sensor Transfer Function

Model

The sensor transfer functions T_{xy} are the product of both the low-pass and the high-pass filters,

$$T_{xx}(f) = T_D \, T_p(p_x) G_x^2(f), \tag{3.4a}$$

$$T_{xy}(f) = T_D \sqrt{T_p(p_x) T_p(p_y)} \, T_s(f, s_{xy}) G_{xy}(f), \tag{3.4b}$$

where T_D denotes the high-pass filter caused by the block-averaging procedure, T_p is the low-pass filter associated to the averaging of the x measurement along a path length p_x. The latter filter is not used for the VPEC system. In the above, G_x is the frequency response function of the x sensor, T_s denotes the low-pass filter caused by the spatial separation of the x and y sensors by a distance s_{xy}, and G_{xy} is the frequency response of the covariance $\overline{x'y'}$. For T_s and T_p we use the exponential expressions from Moore (1986). For T_D we use the analytical expression from Moncrieff et al. (2005).

The frequency response of a propeller anemometer or a thermocouple is approximated as a first-order gain function, with a response time of τ_x (Wyngaard, 1981),

$$G_x(f) = \sqrt{\frac{1}{1 + (2\pi f \tau_x)^2}}. \tag{3.5}$$

With this definition of τ_x, the cut-off frequency is $f_c = 1/(2\pi\tau_x)$, such that $G_x^2(f_c) = 1/2$. The a priori response time of a sensor is not known, but we will assume that the response time of a horizontal propeller anemometer is inversely proportional to the horizontal wind speed (MacCready Jr. and Jex, 1964),

$$\tau_u = \frac{L_u}{U}, \tag{3.6}$$

where we define L_u as a response length (or distance constant), which only depends on the physical sensor characteristics.

We assume that the response time of the vertical propeller also depends on the angle of attack, which is defined as the angle of the instantaneous wind vector with the plane of rotation of the propeller (Fichtl and Kumar, 1974),

$$\tau_w = \frac{A_w}{U} \left(\frac{\sigma_w}{U} \right)^{-2/3}, \tag{3.7}$$

where A_w is an empirical calibration constant depending on the propeller type, and σ_w is the standard deviation of the vertical wind speed. Assuming that the phase difference between x and y is small and independent of frequency, the transfer function of the covariance is then written as (Horst, 1997),

$$G_{xy}(f) = \frac{\left(1 + (2\pi f)^2 \tau_x \tau_y\right)}{\left(1 + (2\pi f)^2 \tau_x^2\right)\left(1 + (2\pi f)^2 \tau_y^2\right)}. \tag{3.8}$$
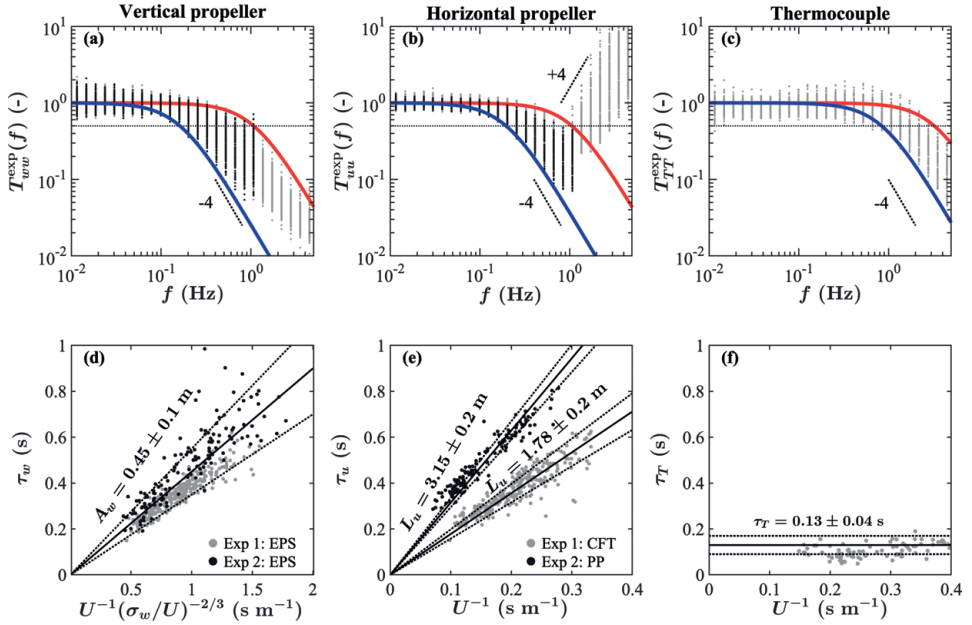
Figure 3.2: Top panels: experimental transfer functions measured during Experiment 1 (grey dots) and Experiment 2 (black dots) of the vertical propeller anemometer (a), of the horizontal propeller anemometer (b) and the fine-wire thermocouple (c). The horizontal lines mark the cut-off frequency, where $T_{xx}^{exp}(1/(2\pi\tau_x)) = 0.5$. The red and blue lines denote the whole range of fitted first-order functions. The '- 4' ('+ 4') dashed lines denote the 6 dB per octave decrease (increase) with increasing frequency related to first-order roll-off and instrumental noise, respectively. Bottom panels: Corresponding estimated response times of the vertical propeller anemometer (d), the horizontal propeller anemometer (e) and the fine-wire thermocouple (f). The linear regression of the response time characteristics is denoted by the solid line, and the chosen uncertainty interval by the dashed lines.

Experimental Derivation of Sensor Response Times

We derive the response times of the propeller anemometers and the thermocouples using the measurements acquired at the CESAR site during Experiments 1 and 2. This is done by fitting the square of a first-order gain function, $G_x^2(f)$, to the experimental transfer functions using the non-linear least-squares Levenberg–Marquardt algorithm. The experimental transfer functions are defined as,

$$T_{xx}^{\text{exp}}(f) = N \frac{S_{xx}^{VPEC}(f)}{S_{xx}^{SEC}(f)}, \tag{3.9a}$$

$$\text{with } N = \frac{\int_0^{f'} S_{xx}^{SEC}(f)\,\mathrm{d}f}{\int_0^{f'} S_{xx}^{VPEC}(f)\,\mathrm{d}f}, \tag{3.9b}$$

where S_{xx}^{VPEC} is the variance spectrum measured by the slower instruments and S_{xx}^{SEC} is the simultaneous spectrum measured by the sonic anemometer. We include a normalization coefficient N to force the lower-frequency part of the transfer function to be equal to one. The limit frequency f' is chosen such that the normalization coefficient is not affected by high-frequency attenuation (Aubinet et al., 2000). To reduce the influence of noise and aliasing, we only fit $T_{xx}^{\text{exp}}(f)$ to $G_x^2(f)$ in the $[0.01; 0.5]$ (Hz) frequency range. Finally, we reject half the estimated response times that yield the poorest fit residuals, with the aim of rejecting spectra with poor signal-to-noise ratios that result in non-physical response times. The resulting estimated response times are shown in Fig. 3.2. The associated error bar is taken differently for each instrument. For the vertical propeller the error bar is taken as the interval containing 80% of the estimated response times, while for the horizontal propeller it is taken as the interval containing 80% of the estimated values for wind speeds below 5 m s^{-1}. The thermocouple response time is assumed constant and taken as the average estimated response time after three weeks of operation in the field.

The heavier material of the propeller blades increases the response length of the horizontal anemometer from $L_u = 1.78 \pm 0.2$ m for carbon fiber thermoplastic to $L_u = 3.15 \pm 0.2$ m for polypropylene. These values differ significantly from the values reported by the manufacturer (2.2 m and 2.7 m, respectively). During Experiment 1, the horizontal wind speed was sampled at 10 Hz by counting the amount of revolutions of the horizontal propeller every 100 ms. This sampling method results in violet noise in the S_{uu} spectrum, or noise increasing as f^2, which is visible in Fig. 3.2b at frequencies above 1 Hz. During Experiment 2, the horizontal wind speed was sampled differently from Experiment 1 by averaging the time between all the propeller revolutions every 200 ms. This removes the noise and results in more well-defined first-order spectra. However, with the latter method, wind speeds less than one propeller revolution within a 200-ms interval cannot be measured. For the type of propellers used in this study this corresponds to wind speeds of less than 2 m s^{-1}.

For the vertical anemometer, only expanded polystyrene blades were tested, and the average response constant is equal to $A_w = 0.45 \pm 0.1$ m. In the surface layer, σ_w/U typically ranges between 0.02 and 0.2, depending on stability and surface roughness. This means that the effective response distance of the vertical anemometer $L_w \equiv \tau_w U$ can range from 1.3 m to 6.1 m (see Eq. 3.7), depending on the average angle of attack. This is a known result (Fichtl and Kumar, 1974; Garratt, 1975), and partly explains why different wind-tunnel (McBean, 1972; Hicks, 1972; Gill, 1975) and field experiments (Horst, 1973) find a different value for L_w. The drawback of applying Eq. 3.7 to estimate the τ_w in time is that it requires a priori knowledge of σ_w, which is underestimated by a propeller anemometer. As such, we simply assume that $\sigma_w = 2 \times \sigma_{w,VPEC}$ in Eq. 3.7, where $\sigma_{w,VPEC}$ is the uncorrected standard deviation of the vertical wind speed, measured by the vertical propeller anemometer. Conveniently, the spectra of the vertical anemometer do not contain high-frequency noise, as the vertical wind speed is sampled by measuring a voltage that is directly proportional to the propeller revolution speed.

The fine-wire thermocouple response could only be estimated during the first experiment because of the higher sampling rate. The response time does not show any significant variation with wind speed. It does however show an increase in time, from 0.08 s to 0.14 s after 6 weeks of operation in the field, which we attribute to accretion of material on the fine wires due to air pollution and rain. In the remainder of the paper we will assume τ_T to be constant and equal to 0.13 ± 0.04 s.

3.3.2 Reference Turbulence Cospectra

Model

We assume that the normalized turbulence spectra follow the functions experimentally derived by Kaimal et al. (1972). Under stable stratification, i.e., $z/L_O > 0$, these functions are written as,

$$\frac{f S_{wx}(f)}{\overline{w'x'}} = \frac{n}{A_{wx} + B_{wx} n^{2.1}}, \tag{3.10a}$$

$$A_{uw} = 0.124 \left(1 + 7.9 \frac{z}{L_O}\right)^{0.75}$$

$$A_{wT} = 0.284 \left(1 + 6.4 \frac{z}{L_O}\right)^{0.75} \tag{3.10b}$$

$$B_{wx} = 2.34 \, A_{wx}^{-1.1},$$

where $n = f z/U$ is the normalized frequency. A more general relation is given by Horst et al. (2004) and by Massman and Clement (2005),

$$f S_{xy}(f) = A_0 \frac{f/f_m}{\left(1 + m \left(f/f_m\right)^{2\mu}\right)^{\frac{1}{2\mu}\left(\frac{m+1}{m}\right)}}, \tag{3.11}$$

where A_0 is a normalization coefficient, μ a broadness parameter and $m = 3/4$ for the cospectra. The spectral peak frequency f_m is then parametrized as an increasing
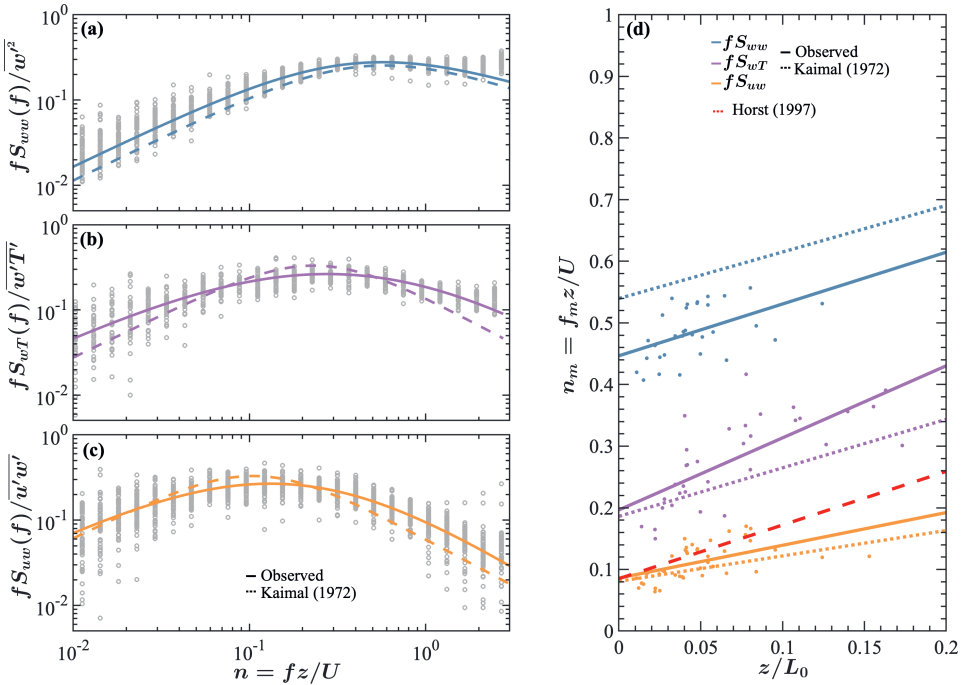
Figure 3.3: Observed normalized turbulence (co)spectra during Experiment 3 (grey dots) at site S10 on the Greenland ice sheet (a): Vertical wind speed variance spectra, (b) Sensible heat flux cospectra, (c) Momentum flux cospectra, and (d) estimated normalized spectral peak frequency as function of stability. The dashed lines in (a)-(b)-(c) are the turbulence spectra from Kaimal et al. (1972) and the solid lines are the optimal fit of Eq. 3.11 on the average spectra. The solid (resp. dashed) lines in (d) denote the linear regression of the measured (resp. Kaimal) spectra. The red dashed line is the simplified function given by Horst (1997).

function of the atmospheric stability z/L_0. Equation 3.11 is used to experimentally estimate an expression for $fS_{xy}(f)$, which we then compare to the Kaimal et al. (1972) spectra (Eq. 3.10).

Experimental Verification of Turbulence Cospectra Models

Virtually all high-frequency attenuation corrections are based on Moore (1986), Horst (1997), or Massman (2000), which assume that the Kaimal et al. (1972) spectra are valid (Eq. 3.10). This assumption does not have a notable effect on the high-frequency correction, as long as the response time of the sensors falls within the well-defined inertial subrange. For a VPEC system, the response time is of the order of ≈ 1 s. This means that the system also misses a small fraction of the flux in the lower frequency part of the turbulence spectrum, which is not necessarily well defined, as demonstrated by Smeets et al. (1998) for katabatic flow due to the influence of large-scale flow. As such, we test the validity of the Kaimal et al. (1972) spectra in a katabatic flow regime

with measurements from Experiment 3.

We first estimate a fixed shape parameter μ by fitting the average turbulence (co)spectra to Eq. 3.11. We then estimate the spectral peak frequency f_m by fitting each individual (co)spectrum. The results are plotted as function of atmospheric stability in Fig. 3.3. The observed peak frequency shows significant scatter, but its increase with stability is well visible and roughly follows the relation derived by Kaimal et al. (1972). Furthermore, the observed averaged spectra appear wider than the Kaimal et al. (1972) spectra. Finally, our data suggest that the vertical wind speed spectra are slightly shifted to lower frequencies, although the limited sampling rate makes it difficult to fit these spectra due to aliasing. It must also be noted that the relation by Horst (1997) is a reasonable approximation for the momentum cospectra under near-neutral circumstances, i.e., $z/L_0 < 0.1$ (see Fig. 3.3).

3.3.3 Analytical Model

Several analytical models of Eq. 3.3 have been derived (Horst, 1997; Massman, 2000). These present an analytical function for both the normalized turbulence cospectra S_{xy} and the sensor transfer functions T_{xy} such that the attenuation coefficient in Eq. 3.3 can be integrated analytically. In the general case of two slow-response sensors, and assuming that the phase difference between x and y is small and independent of frequency, Horst (1997) writes the attenuation coefficient of the covariance $\overline{x'y'}$ as,

$$A_{xy} = \frac{2\pi f_m \tau_x + 2\pi f_m \tau_y + 2(2\pi f_m)^2 \tau_x \tau_y}{(1 + 2\pi f_m \tau_x)(1 + 2\pi f_m \tau_y)(2\pi f_m \tau_x + 2\pi f_m \tau_y)}, \tag{3.12}$$

where the following model for the cospectral peak frequency is used,

$$f_m = \frac{U}{z}\left(2.0 - \frac{1.915}{1 + 0.5\dfrac{z}{L_0}}\right). \tag{3.13}$$

However, both our measured cospectra during Experiment 3 and the peak frequency of the spectra derived by Kaimal et al. (1972) suggest that the following models are more accurate in the $z/L_0 \in [0; 0.2]$ range,

$$\text{momentum flux } fS_{uw}:$$

$$f_m = \frac{U}{z}\left(0.08 + 0.41\frac{z}{L_0}\right), \tag{3.14a}$$

$$\text{sensible heat flux } fS_{wT}:$$

$$f_m = \frac{U}{z}\left(0.19 + 0.8\frac{z}{L_0}\right). \tag{3.14b}$$

The modelled attenuation coefficient based on Eq. 3.12 and Eq. 3.3 using the experimentally derived expressions for τ_x, τ_y and f_m agree within 1%. This difference is mostly due to the high-pass filter T_D that is not taken into account in Eq. 3.12. Hereafter we will numerically calculate the integral in Eq. 3.3 to estimate the attenuation factor.

3.3.4   Summary: Model Parameters

The model described in the previous section used to estimate the attenuation of the (co)variance $\overline{x'y'}$ is thus entirely described by the following parameters:

- L_u : response length (or distance constant) of the horizontal propeller anemometer (m)

- A_w : calibration constant of the vertical propeller anemometer (m)

- τ_T: response time of the thermocouple (s)

- p_x: path averaging length of the x sensor, set to zero for a VPEC system (m)

- s_{xy}: spatial separation between the two sensors (m)

- U: average horizontal wind speed (m s^{-1})

- σ_w: standard deviation of the vertical wind speed (m s^{-1})

- z: measurement height (m)

- L_O: Obukhov length (m)

3.4   Results: Evaluation of the Correction for the High-Frequency Attenuation (Experiments 1 and 2)

We apply the correction for the high-frequency attenuation to the measured vertical propeller eddy covariance (VPEC) fluxes. We then compare these corrected fluxes to the simultaneously measured sonic eddy covariance (SEC) fluxes during Experiments 1 and 2. The sensible heat flux is converted to an energy flux according to $H = \rho_a C_p \overline{w'T'}$, where the air density ρ_a and air heat capacity C_p are calculated using the 2 m air temperature, the 2 m air specific humidity and the surface pressure measured by the KNMI at the CESAR tower.

3.4.1   Accuracy of the High-Frequency Correction

The comparison of VPEC and SEC fluxes is shown in Fig. 3.4, where we have used the response times derived in Sect. 3.3 and written in Table 3.1. Both the corrected VPEC momentum and sensible heat fluxes show a small bias and root-mean-square error (RMSE) when compared to the SEC fluxes. The bias, which we define as the average of the difference between the two time series, is for the friction velocity equal or smaller than 0.01 m s^{-1} for both experiments. The RMSE value is 0.03 m s^{-1} and 0.05 m s^{-1} for Experiments 1 and 2, respectively. The sensible heat flux is slightly overestimated by the VPEC system compared to the SEC system: 6.3 W m^{-2} during Experiment 1 and 4.4 W m^{-2} during Experiment 2. This small bias is also present when comparing the sensible heat fluxes obtained with the sonic temperature and with the thermocouple attached to the SEC system. Hence the bias is not related to the vertical propeller but to the sensitivity of the thermocouples.

The RMSE value of the sensible heat flux is 12.4 W m^{-2} and 11.9 W m^{-2} during the two experiments. The difference between the VPEC fluxes and SEC fluxes is of similar magnitude as the difference obtained when measuring fluxes with two adjacent sonic anemometers (Mauder and Zeeman, 2018).

The only adjustable parameters in the correction for the high-frequency attenuation are the response times of the instruments. In order to quantify the sensitivity of the correction to these input parameters, the same comparison as presented above is done using perturbed response times. The optimal response parameters of the vertical anemometer, horizontal anemometer, and thermocouple are perturbed by $\pm \Delta A_w$, $\pm \Delta L_u$ and $\pm \Delta\tau_T$ respectively. These error bars are derived from the calibration procedure (see Fig. 3.2 and Table 3.2), and result in three combinations of sensor response times that we denote τ_x^-, τ_x^{ref}, and τ_x^+. The bias and RMSE value of the corrected fluxes for each parameter set are presented in Table 3.2. The comparison with the SEC fluxes shows that changing the input parameters within the defined range does not affect the RMSE value of the fluxes, neither does it significantly affect the bias of the correct friction velocity. It does, however, slightly (< 1 W m^{-2}) affect the bias of the corrected sensible heat flux.

3.4.2 Influence of the Sampling Rate

The power supply and memory usage are the most important limiting factors when considering the sampling rate of an automatic weather station, denoted F_s, deployed in remote polar areas. As such we test whether the sampling rate can be decreased without significantly increasing the bias and RMSE value of the measured fluxes, as presented by Bosveld and Beljaars (2001). For this purpose, the measured VPEC time series from Experiments 1 and 2 are artificially downsampled from the initial sampling interval to sampling intervals of 1 s and 4 s. This is done by taking the first sample in each sampling interval. We then apply the processing steps and high-frequency correction from Sect. 3.3 to the downsampled time series, and compare the corrected and VPEC fluxes to the SEC fluxes. The resulting bias and RMSE value of the fluxes calculated with the downsampled time series are shown in Table 3.2.

Increasing the sampling interval from 0.1 s to 4 s increases the RMSE value of the sensible heat flux and the friction velocity by ≈ 1 W m^{-2} and ≈ 0.01 m s^{-1}, respectively. This is of the same order of magnitude as the uncertainty related to the response time of the sensors shown in the previous paragraph. Furthermore, the downsampling does not significantly affect the bias, as expected from Bosveld and Beljaars (2001).

We conclude from these comparisons that the overall precision and accuracy of the corrected VPEC fluxes are neither dominated by the high-frequency correction, nor by the sampling rate. After correcting for their limited dynamical response, VPEC instruments sampling at an interval of 4 s are able to measure the sensible heat flux during the first two experiments with a typical bias of 6.3 W m^{-2} and a RMSE value of 13.4 W m^{-2} (Table 3.2). For the friction velocity the bias is less than 0.01 m s^{-1}, and the RMSE value of the order of 0.05 m s^{-1}. Overall, this means that a corrected VPEC system measures the turbulent surface fluxes with an accuracy similar to the deviation between two adjacent sonic anemometers (Frank et al., 2015; Mauder and
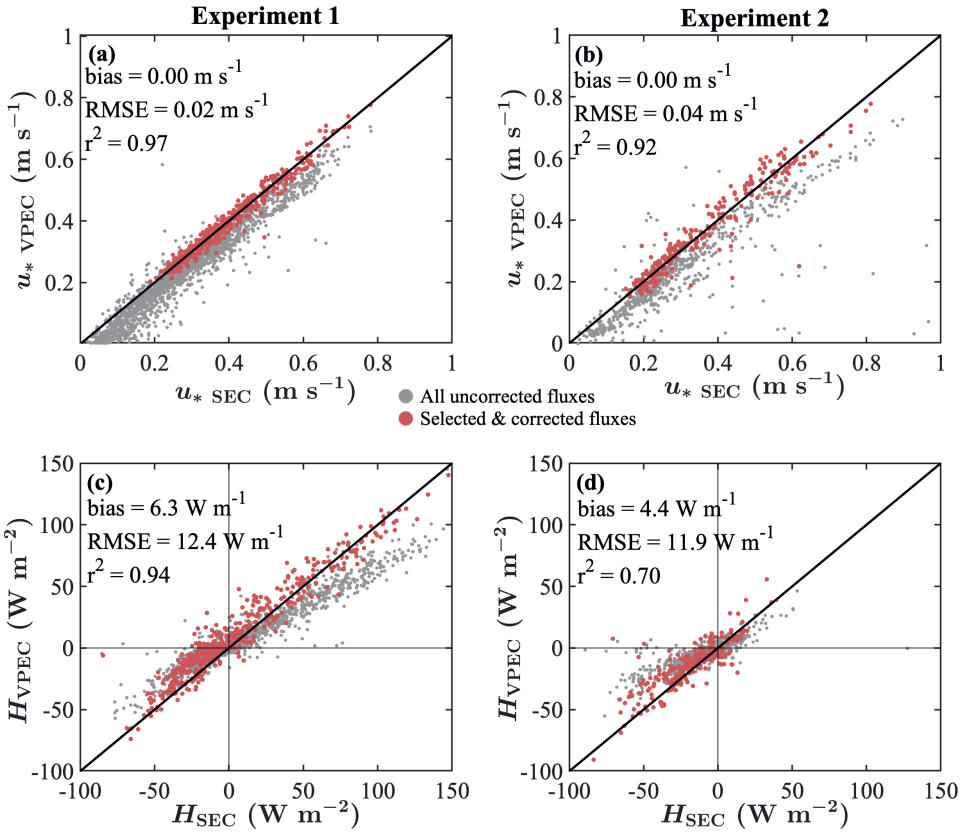
Figure 3.4: Comparison of the friction velocity (a), (b) and sensible heat flux (c), (d) measured by sonic anemometer eddy-covariance (SEC) and by vertical propeller eddy-covariance (VPEC) at the CESAR site. The left panels (a) and (c) are during Experiment 1, while the right panels (b) and (d) are during Experiment 2

Table 3.2: Bias and root mean square error (RMSE) of corrected vertical propeller eddy-covariance (VPEC) fluxes compared to sonic eddy-covariance (SEC) fluxes during Experiments 1 and 2. The experiments are described in detail in Sect. 3.2 and in Table 3.1. The bias is written in bold and the RMSE value is given in the brackets. Three different sampling rates F_s of the VPEC system are compared. For each experiment, three different parameter sets used to model the instrument response times τ_x have been applied, based on the uncertainty when deriving these parameters experimentally. The values for the optimal set τ_x^{ref} and the two perturbed sets τ_x^- and τ_x^+ are given in Table 3.1.

Bias	F_s	10 Hz			1 Hz			0.25 Hz		
(RMSE)		τ_x^-	τ_x^{ref}	τ_x^+	τ_x^-	τ_x^{ref}	τ_x^+	τ_x^-	τ_x^{ref}	τ_x^+
H	Exp.1	**5.9**	**6.3**	**6.6**	**6.1**	**6.4**	**6.8**	**5.9**	**6.3**	**6.6**
(W m^{-2})		(12.6)	(12.4)	(12.4)	(13.3)	(13.1)	(13.1)	(13.5)	(13.4)	(13.6)
	Exp.2	-	-	-	**5.7**	**4.4**	**3.1**	**5.5**	**4.1**	**2.7**
					(12.3)	(11.9)	(11.8)	(12.7)	(12.4)	(12.4)
u_*	Exp.1	**-0.01**	**0.00**	**0.00**	**-0.01**	**0.00**	**0.00**	**0.00**	**0.00**	**0.01**
(m s^{-1})		(0.02)	(0.02)	(0.02)	(0.02)	(0.02)	(0.02)	(0.03)	(0.03)	(0.03)
	Exp.2	-	-	-	**-0.01**	**0.00**	**0.01**	**0.00**	**0.00**	**0.01**
					(0.04)	(0.04)	(0.04)	(0.05)	(0.05)	(0.05)

Zeeman, 2018). Yet the main advantage of the VPEC system is its simplicity, which allows for longer periods of unattended operation in remote polar areas.

3.5 Results: One Year of Turbulent Fluxes in the Western Ablation Area of the Greenland Ice Sheet (Experiment 4)

To demonstrate its potential, we apply the correction for the high-frequency attenuation of the fluxes to one year of VPEC measurements at site S5 on the Greenland ice sheet (Experiment 4). The values for A_w, L_u, and τ_T are found in Table 3.1 and are based on the calibration of identical sensors during the first two experiments.

3.5.1 Corrected Turbulent Fluxes

The time series of both the corrected turbulent fluxes and of the modelled attenuation coefficients are presented in Fig. 3.5. Over the course of one year, the attenuation factor A_{xy} of both fluxes remains in the $[0.6 - 0.8]$ range, which is the same interval of modelled corrections during the first two experiments. At this location, katabatic winds continuously generate turbulent mixing despite the stable stratification. This means that near-neutral conditions are nearly always observed close to the surface (i.e., $z/L_0 < 0.2$), thereby keeping the spectral peak to lower frequencies (Fig. 3.3). On the other hand, the high wind speeds shift the spectral peak to higher frequencies, but this effect is compensated by the simultaneous decrease in the response time of the propeller anemometers (see Eqs. 3.6 and 3.7 and Fig. 3.2). The highest flux attenuation factor

of 0.5 is modelled in winter, during short periods with low wind speeds and increasing stability (Fig. 3.5). During such periods, the propeller anemometers become slower while the most energetic turbulent fluctuations become smaller, which results in high flux attenuation. Only one period with probable propeller freezing was identified in January (Fig. 3.5c1), which results in a gap of several days in the measurements. The smallest attenuation factor of 0.8 is modelled in summer, during periods with high wind speed and near-neutral stability. These are also the periods when the highest fluxes are measured: sensible heat fluxes up to -300 W m^{-2} and friction velocities up to 1 m s^{-1}.

3.5.2 Error Caused by the Uncertainty in Response Times

For the first two experiments, the uncertainty in the response times propagates in an uncertainty of $\pm$ 0.4 W m^{-2} in the corrected VPEC sensible heat flux and less than 0.01 m s^{-1} for the corrected friction velocity (Table 3.2). However, the measured fluxes during the first two experiments were smaller, so these error intervals are not representative of the fluxes measured during Experiment 4. As such, the same response time perturbation exercise as in Sect. 3.4 is performed for Experiment 4.

The different corrected fluxes show a maximal deviation of $\pm$ 10% for the sensible heat flux and $\pm$ 1.5% for the friction velocity (not shown in Fig. 3.5). The uncertainty of the corrected flux depends on the flux, and reaches up to 30 W m^{-2} for measured sensible heat fluxes of -300 W m^{-2}. These intervals must be interpreted as the widest interval of all possible corrected fluxes, using the response times derived in Fig. 3.2. It is often smaller, for instance for higher wind speeds and more neutral conditions. This maximum difference interval can only be reduced further if the response times are known with greater accuracy.

3.5.3 Contribution of the Sensible Heat Flux to Surface Ablation

In Fig. 3.5 we compare the measured sensible heat flux with the other measured components of the surface energy balance. During winter, the surface cools due to net emission of longwave radiation, which is on average compensated by the downwards sensible heat flux. The net imbalance between the two fluxes then contributes to either warming or cooling of the surface, which rarely exceeds the melting point during winter. During summer, both a net absorbed radiation by the surface and a downward sensible heat flux warm the surface. The excess energy supplied when the surface is already at the melting point results in enhanced melt.

During the first half of the melting season (May–June), the measured ice ablation closely follows R_{net}. Then, after several consecutive warm events in July, the daily ice ablation is on average 100 W m^{-2} larger than R_{net} (Fig. 3.5d1). This additional energy flux can for the most part be explained by the measured sensible heat flux (Fig. 3.5a1, d1). It must be noted that we did not measure the latent heat flux and the ground heat flux, which are also an important part of the surface energy balance. In fact during winter, important temperature gradients in the ice will compensate for the difference between the emitted radiation and the sensible heat flux. During summer, the ice is mostly at the constant melting temperature, which makes the ground heat flux negligible, but will enhance latent heat fluxes due to important vertical gradients in specific humidity.
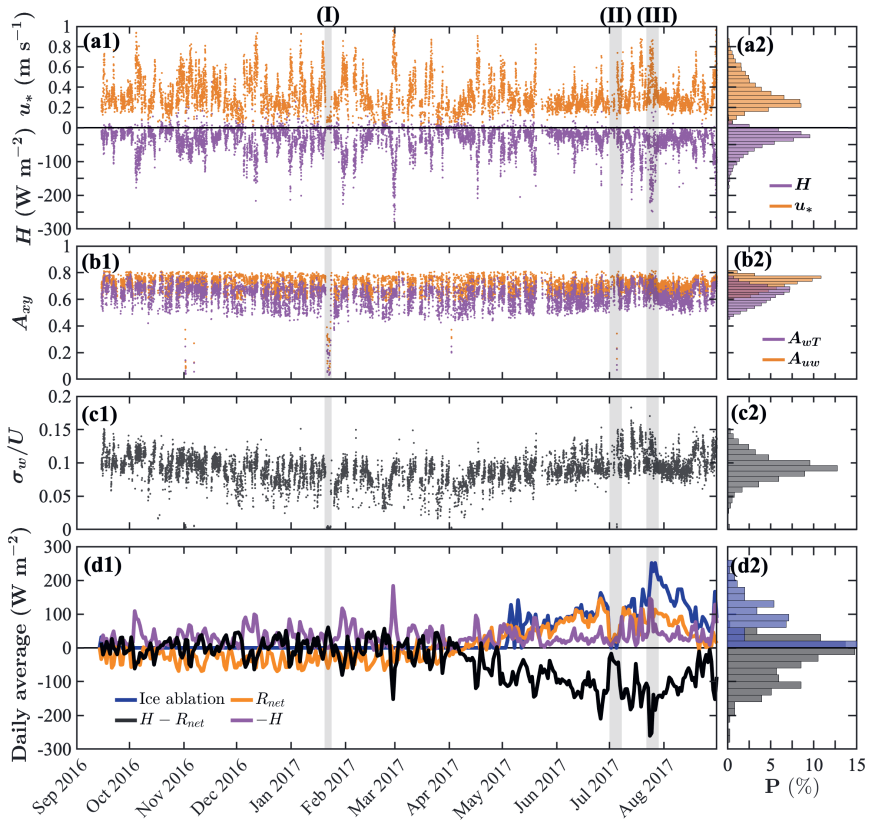
Figure 3.5: Time series of selected measurements from the vertical propeller eddy-covariance (VPEC) system during Experiment 4 at site S5, located in the western ablation area of the Greenland ice sheet. From top to bottom: (a1) friction velocity (u_*) and sensible heat flux (H), (b1) modelled attenuation coefficients A_{xy}, (c1) standard deviation of the vertical wind speed σ_w divided by the horizontal wind wind speed (U), (d1) daily averaged ice ablation, net absorbed radiation by the surface (R_{net}) and sensible heat flux (H). The panels on the right are the probability histograms for each variable calculated for the whole measurement period. Three notable periods are shaded as follows: (I) A period with a rimed or stalling vertical propeller, (II) a period in the middle of the melting season without observed ablation, and (III) an extreme warm summer event when the strongest ablation is observed. A daily average of 100 W m^{-2} in panel (d1) corresponds to a cumulative daily ice ablation of 2.82 cm, assuming a latent heat of melting of 334×10^3 J kg^{-1} and a constant ice density of 916 kg m^{-3}.

Furthermore, small snowfall events during summer (as is the case during event (II) in Fig. 3.5) will also absorb a large part of the total melt energy during the consecutive days. Finally, the footprint of the sensible heat flux is not necessarily representative of the area in direct vicinity of the weather station. Especially after several warm events, the melt water will accumulate in the surrounding narrow channels and melt ponds, which remain invisible to the ablation and radiation sensors as they are located on top of an ice hummock.

3.5.4   Variability of the Aerodynamic Roughness Length

When the sensible heat flux and the friction velocity are calculated using a bulk turbulence model, the aerodynamic roughness length (z_{0m}) is often unknown and becomes an adjustable parameter. Assuming Monin–Obukhov similarity, the aerodynamic roughness length is defined as the height where the logarithmic wind profile extrapolates to zero. Here we evaluate the value of this parameter by extrapolating the measured wind speed to the surface using the measured momentum flux at the same height, according to:

$$\frac{\kappa U}{u_*} = \ln\left(\frac{z}{z_{0m}}\right) - \Psi_m\left(\frac{z}{L_O}\right) + \Psi_m\left(\frac{z_{0m}}{L_O}\right), \tag{3.15}$$

where we use the expression of Holtslag and De Bruin (1988) for the integrated stability functions for momentum Ψ_m. We only select the measurements when $z/L_O < 0.2$, and we assume that the last term on the right-hand side of Eq. 3.15 is negligible and thus set it to zero. The estimated aerodynamic roughness length is then shown as function of both time of year and wind direction in Fig. 3.6.

The aerodynamic roughness length z_{0m} shows a very significant variability over the course of one year, and ranges between 10^{-4} m in winter to nearly 10^{-1} m in summer, which is consistent with the two-level wind profile and sonic anemometer measurements by Smeets and Van den Broeke (2008a) at the same location. The reduction of z_{0m} from September to February (Fig. 3.6a) is mainly attributed to the accumulation of snow that gradually reduces the size of the ice hummocks. Furthermore, winter time sublimation smoothens the top of the hummocks, which explains that the smallest values of z_{0m} are observed in March and April. From May onwards, the melting of the snow increases the amplitude of the ice hummocks. The resulting rapid increase of z_{0m} from March to August (Fig 3.6b) is further enhanced by the differential melting of the ice hummocks.

The roughness length z_{0m} shows a remarkable dependency on the wind direction as well, with minimal values found in summer at $95°$ and in winter at $115°$. The maximum values of z_{0m} are found for the most southerly wind directions, independently of the season. We attribute this strong directional dependency to changes in the effective obstacle area, which is most likely a direct consequence of the complex geometry and spacing of the ice hummocks (Miles et al., 2017; Fitzpatrick et al., 2019). A detailed topographical survey is required to property quantify this effect at this location.

Remarkably, the southerly wind directions are also the directions when the warmer and more turbulent air masses generate the highest sensible heat fluxes (Fig. 3.6). The southerly wind directions are most likely caused by the interaction between katabatic
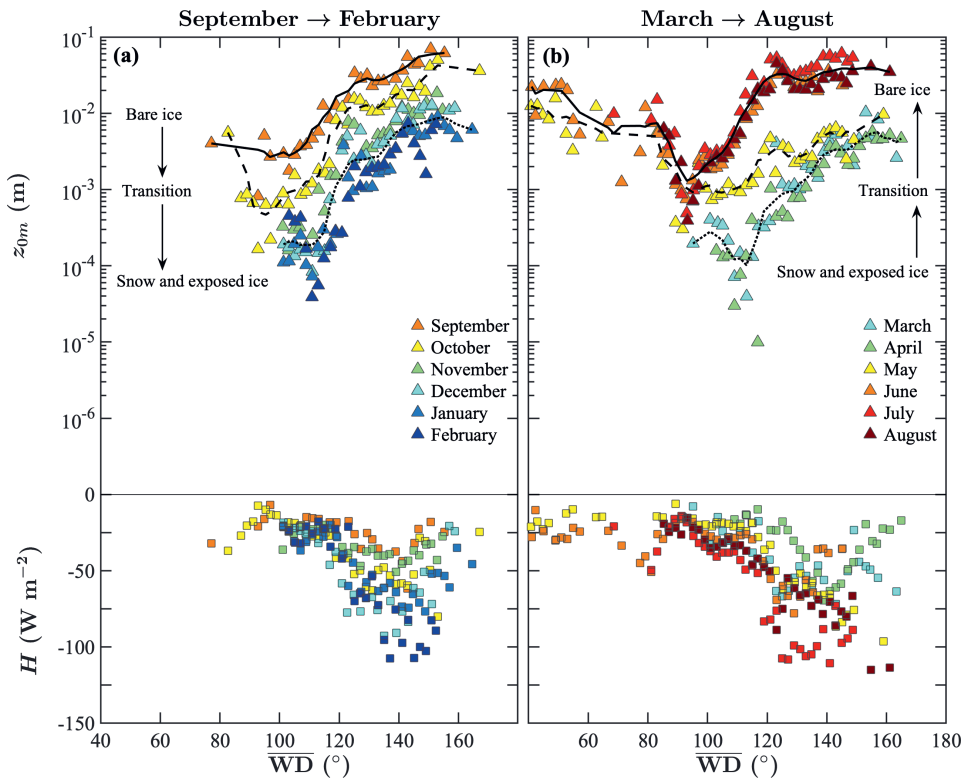
Figure 3.6: Averaged aerodynamic roughness length z_{0m} (triangles, upper panels) and sensible heat flux H (squares, bottom panels) as function of month and wind direction. The measurements are from corrected vertical propeller eddy-covariance (VPEC) observations made during Experiment 4 at site S5 (see Sect. 3.2). The data have been subjected to the $z/L_O < 0.2$ filter and to the additional selection procedures described in Sect. 3.3. The black lines in the upper panel are the moving average roughness during winter (snow and exposed ice), October and May (transition) and summer (bare ice).

winds and barrier winds (Van den Broeke and Gallée, 1996), although this interaction remains to be investigated in more detail.

The results from this experiment confirm even more that using a constant value for z_{0m} over snow and ice surfaces is not recommended, as shown by similar experiments at other locations (e.g. Miles et al., 2017; Vignon et al., 2017; Fitzpatrick et al., 2019). This is especially the case at this location on the western ablation area of the Greenland ice sheet, where a shift in wind direction is often associated with fast changes in air mass properties. This raises the question of the parametrization of turbulent heat fluxes in climate models, and of the possible feedback between surface roughness and surface ablation through turbulent heat exchange.

3.6 Conclusions

Motivated by the important contribution of turbulent heat fluxes to surface ablation on the Greenland ice sheet, we tested a vertical propeller eddy-covariance (VPEC) system, which is capable of continuously measuring the surface turbulent fluxes for longer periods without regular maintenance. By comparing the VPEC system to a sonic eddy-covariance (SEC) system, we found that the frequency responses of propeller anemometers and thermocouples may accurately be approximated as first-order functions, with typical response times of less than 1 s. We have shown that the resulting flux attenuation can be accurately modelled, as long as the normalized turbulence cospectra are known. Furthermore, the sampling interval can be reduced to 4 s to increase the system's autonomy even further in terms of power supply and data storage.

We presented one year of measured VPEC turbulent sensible heat and momentum fluxes at site S5 of the K-transect, located in the western ablation area of the ice sheet. Near the margins of the ice sheet, persistent density-driven katabatic winds are the main source for near-surface turbulence. Such a forcing results in quasi-continuous stable but near-neutral conditions. These are very favourable conditions for a VPEC system and keeps the attenuation factor of the fluxes above 0.6 (e.g., the attenuation below 40%).

This long-term and continuous dataset of turbulent fluxes is invaluable for the evaluation of atmospheric models, but also for the fundamental understanding of processes and drivers of surface ablation. At this location, downward sensible heat fluxes as large as 300 W m^{-2} have been measured, both during winter and during summer. Such values are similar or even more important than the surface net absorbed radiation, which makes them an essential part of the surface energy balance. Furthermore, we have shown that the aerodynamic roughness length is very variable in time and space, and that the highest roughness length of nearly 10^{-1} m is estimated when the sensible heat fluxes are also at their maximum.

Chapter 4

Mapping the aerodynamic roughness of the Greenland Ice Sheet surface using ICESat-2: evaluation over the K-transect

Summary

The aerodynamic roughness of heat, moisture and momentum of a natural surface is an important parameter in atmospheric models, as it co-determines the intensity of turbulent transfer between the atmosphere and the surface. Unfortunately, this parameter is often poorly known, especially in remote areas where neither high-resolution elevation models nor eddy-covariance measurements are available. In this study we adapt a bulk drag partitioning model to estimate the aerodynamic roughness length (z_{0m}) such that it can be applied to 1D (i.e. unidirectional) elevation profiles, typically measured by laser altimeters. We apply the model to a rough ice surface on the K-transect (west Greenland Ice Sheet) using UAV photogrammetry, and evaluate the modelled roughness against in situ eddy-covariance observations. We then present a method to estimate the topography at 1 m horizontal resolution using the ICESat-2 satellite laser altimeter, and demonstrate the high precision of the satellite elevation profiles against UAV photogrammetry. The currently available satellite profiles are used to map the aerodynamic roughness during different time periods along the K-transect, that is compared to an extensive dataset of in situ observations. We find a considerable spatio-temporal variability in z_{0m}, ranging between 10^{-4} m for a smooth snow surface over 10^{-1} m for rough crevassed areas, which confirms the need to incorporate a variable aerodynamic roughness in atmospheric models over ice sheets.

4.1   Introduction

Between 1992 and 2018, the mass loss of the Greenland Ice Sheet (GrIS) contributed 10.8 ± 0.9 mm to global mean sea-level rise (Shepherd et al., 2020). This mass loss is caused in approximately equal parts by an increase in ice discharge (Mouginot et al., 2019; King et al., 2020), and an increase in surface meltwater runoff (Noël et al., 2019). Runoff occurs mostly in the low-lying ablation area of the GrIS, where bare ice is exposed to on-average positive air temperatures throughout summer (Smeets et al., 2018; Fausto et al., 2021). As a consequence, the downward turbulent mixing of warmer air towards the bare ice, the sensible heat flux, is an important driver of GrIS mass loss next to radiative fluxes (Fausto et al., 2016a; Kuipers Munneke et al., 2018b; Van Tiggelen et al., 2020).

Although the strong vertical temperature gradient provides the required source of energy, it is the persistent katabatic winds that generate the turbulent mixing through wind shear (Forrer and Rotach, 1997; Heinemann, 1999). Additionally, the surface of the GrIS close to the ice edge is very rough (Yi et al., 2005; Smeets and Van den Broeke, 2008a). It is composed of closely spaced obstacles, such as ice hummocks, crevasses, melt streams and moulins. Due to the effect of form drag (or pressure drag) τ_r, the magnitude of the turbulent fluxes increases with surface roughness (e.g. Garratt, 1992), thereby enhancing surface melt (Van den Broeke, 1996; Herzfeld et al., 2006). As of today, the effect of form drag on the sensible heat flux over the GrIS, and therefore its impact on surface runoff, remains poorly known.

The first challenge in modelling this turbulent mixing resides in accurately modelling the surface shear stress, without the need to calculate the detailed air pressure distribution around each individual surface obstacle. Such bulk drag models have been developed by e.g. Arya (1975) to estimate the drag caused by pressure ridges on Arctic pack ice. This model was extended by Hanssen-Bauer and Gjessing (1988) for varying sea-ice concentrations. A more general drag model was proposed by Raupach (1992), that was extended by Andreas (1995) for sastrugi, by Smeets et al. (1999) for rough ice and by Shao and Yang (2008) for surfaces with higher obstacle density, such as urban areas. Lüpkes et al. (2012) and Lüpkes and Gryanik (2015) developed a bulk drag model for sea-ice that is used in multiple atmospheric models. Over glaciers, semi-empirical approaches based on Lettau (1969) are often used, such as by Munro (1989), Fitzpatrick et al. (2019) and Chambers et al. (2019).

The second challenge is the application of such models in weather and climate models, which requires mapping small-scale obstacles over large areas, e.g. an entire glacier or ice sheet. Historically, the surveying of rough ice was spatially limited to areas accessible for instrument deployment, possibly introducing a bias when it comes to quantifying the overall roughness of a glacier. The recent development of airborne techniques, such as uncrewed aerial vehicle (UAV) photogrammetry and airborne LiDAR, opened up new possibilities for mapping surface roughness properties. While these techniques enable the high resolution mapping of roughness obstacles, they often only cover portions of a glacier or ice sheet. On the other hand, satellite altimetry provides the means to cover entire ice sheets, though the horizontal resolution remains a limiting factor when mapping all the obstacles that contribute to form drag. Depending on the type of

surface, parameterizations using available satellite products are possible, as presented for Arctic sea-ice by Lüpkes et al. (2013), Petty et al. (2017), and Nolin and Mar (2019).

The third and final challenge is the experimental validation of bulk drag models over remote rough ice areas, which either requires in situ eddy-covariance or multi-level wind and temperature measurements. Long-term and continuous datasets remain scarce on the GrIS, although simplifying in situ methods can be applied for long-term monitoring of turbulent fluxes T20 (Van Tiggelen et al., 2020).

In this paper, we address the first two challenges by applying the model of Raupach (1992) to 1 m resolution elevation profiles measured over the western GrIS by the ICESat-2 laser altimeter. We apply the bulk drag model to roughness information from UAV photogrammetry, and address the third challenge by evaluating the modelled aerodynamic roughness against in situ eddy-covariance measurements. We then evaluate the ICESat-2 elevation profiles against UAV photogrammetry, and finally apply the bulk drag model to the ICESat-2 profiles obtained over an extended area and during different time periods.

This paper is organised as follows. In Sect. 4.2 we describe the modifications in the bulk drag model, and in Sect. 4.3 we describe the elevation datasets used to force the model. We then evaluate the bulk drag model for one site in Sect. 4.4.1, and the roughness statistics derived from ICESat-2 at multiple sites in Sect. 4.4.3. In Sect. 4.4.4 we apply the model to map the aerodynamic roughness length (z_{0m}) along the K-transect, on the western GrIS.

4.2 Model

4.2.1 Definition of the aerodynamic roughness length (z_{0m})

Atmospheric models assume that the lowest grid point above the surface is located in the inertial sublayer (or surface layer). In this layer, the eddy diffusivity for momentum increases linearly with height and decreases with atmospheric stability, which yields the semi-logarithmic vertical profile of horizontal wind speed. Over a rough surface, the pressure drag force on the obstacles acts as an additional sink of momentum, next to skin friction. Furthermore, the turbulent wakes generated by the flow separation enhance turbulent mixing. This may be approximated by an increase of the eddy diffusivity in the roughness sublayer (Garratt, 1992; Raupach, 1992; Harman and Finnigan, 2007). As such, the vertical profile of horizontal wind speed ($u(z)$) over a rough surface can be written as:

$$u(z) = \frac{u_*}{\kappa}\left[\ln\left(\frac{z-d}{z_{0m}}\right) - \Psi_m\left(\frac{z-d}{L_o}\right) + \Psi_m\left(\frac{z_{0m}}{L_o}\right) + \widehat{\Psi_m}(z)\right], \tag{4.1}$$

where z is the height above the surface, $u_* = \left(\dfrac{\tau}{\rho}\right)^{0.5}$ is the friction velocity, ρ the air density, $\kappa = 0.4$ is the von Kármán constant, τ the total surface shear stress and z_{0m} is the roughness length for momentum. The average wind profile in Eq. (4.1) is shifted upwards by a displacement height d, which is defined as the centroid of the drag force
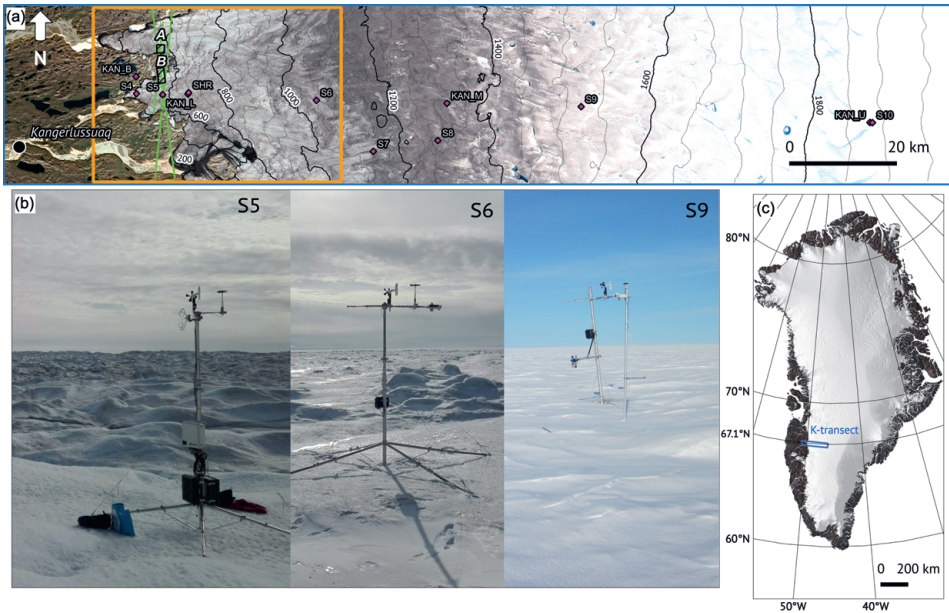
Figure 4.1: (a) Map of the K-transect, with the location of the automatic weather stations and mass balance sites indicated by the pink diamonds. The black boxes A and B delineate the areas mapped by UAV photogrammetry. The large orange box indicates the area covered in Figs. 4.6 and 4.9. The background image was taken by the MSI instrument (ESA, Sentinel-2) on 12-08-2019. Pixel intensity is manually adjusted over the ice sheet for increased contrast. The green solid lines denote the ICESat-2 laser tracks that are compared to the UAV surveys (Table 4.2). (b) Sites S5 (06 Sep 2019), S6 (06 Sep 2019) and S9 (03 Sep 2019) taken during the yearly maintenance. Note that no data from the AWS shown at S9 are used in this study. (c) Location of the K-transect on the Greenland Ice Sheet.

profile on the roughness elements (Jackson, 1981). z_{0m} is thus defined as the height above d where $u(z) = 0$. The dependency of the eddy diffusivity for momentum on the diabatic stability and on the turbulent wake diffusion are described as $\Psi_m\left(\dfrac{z-d}{L_o}\right)$ and $\widehat{\Psi_m(z)}$, respectively, where L_o is the Obukhov length. The hat notation is used for the roughness layer quantities, as in Harman and Finnigan (2007). Above the roughness sublayer, $\widehat{\Psi_m(z)} = 0$.

The problem we address is the estimation of z_{0m}. Rewriting Eq. (4.1) and assuming neutral conditions (i.e. $\Psi_m = 0$), yields :

$$z_{0m} = (z-d)\left[\exp\left(\kappa\frac{u(z)}{u_*} - \widehat{\Psi_m(z)})\right)\right]^{-1}. \tag{4.2}$$

Hence, the process of finding z_{0m} is equivalent to finding d, $\dfrac{u(z)}{u_*}$ and $\widehat{\Psi_m(z)}$ simultaneously.

4.2.2   Bulk drag model of z_{0m}

The main task is to model the total surface shear stress $\tau = \rho u_*^2$, which for a rough surface is the sum of both form drag τ_r and skin friction τ_s:

$$\tau = \tau_r + \tau_s. \tag{4.3}$$

Both τ_r and τ_s are parameters of the flow, but can be related to the geometry of the roughness obstacles using a bulk drag model. Two important parameters of the roughness obstacles are their height (H) and their frontal area index (λ), defined as:

$$\lambda = \frac{A_f}{A_l}, \tag{4.4}$$

with A_f the frontal area of the roughness obstacles perpendicular to the flow, and A_l the total horizontal area.

At this point, we will differ from the model by Shao and Yang (2008), who add an extra term in Eq.(4.3) in order to separate the skin friction at the roughness elements and the underlying surface. We also differ from the models by Lüpkes et al. (2012) and Lüpkes and Gryanik (2015), where skin friction over sea-ice is separated between a component over open water, and a component over ice floes. In the case of a rough land ice surface, there is no clear distinction between the obstacles and the underlying surface. Therefore, we follow the model of R92 (Raupach, 1992), which is designed for surfaces with a moderate frontal area index ($\lambda < 0.2$). As we will see in the next sections, the ice surfaces considered here do not exceed $\lambda = 0.2$. As a comparison we will also consider the models from L69 (Lettau, 1969) and M98 (Macdonald et al., 1998). The detailed equations of the bulk drag models can be found in Appendix 1.
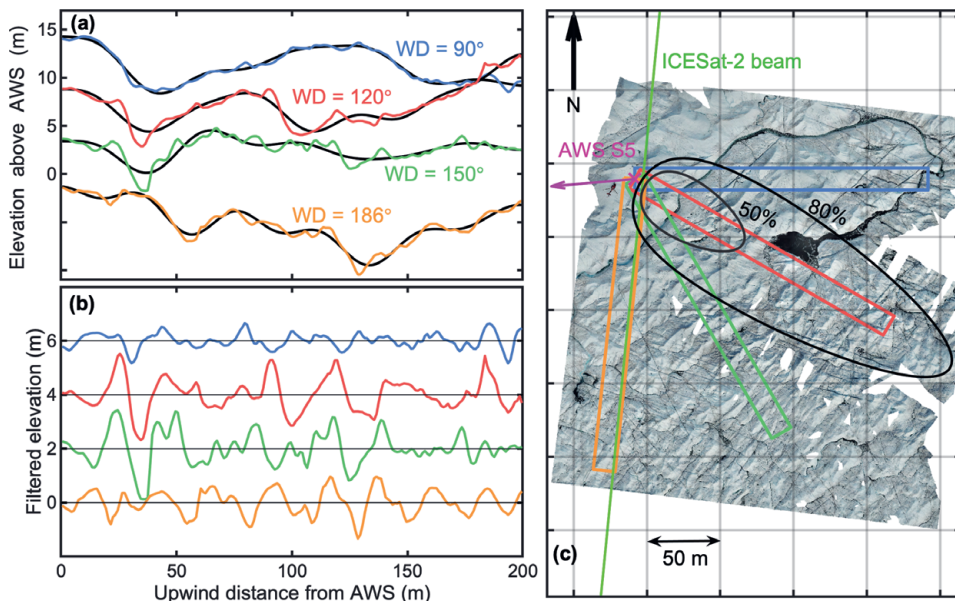
Figure 4.2: (a) Measured elevation profiles for four different wind directions upwind of AWS S5, (b) Filtered elevation profiles and (c) orthomosaic true-color image of AWS S5 and surroundings taken by UAV photogrammetry on 6 September 2019. The different coloured rectangles in (c) indicate the profiles shown in panel (a). The profiles have been vertically offset by 5 m in (a) and by 2 m in (b) for clarity. The black line in (a) denotes the low-frequency contribution of the profiles for a cut-off wavelength $\Lambda = 35$ m. The pink arrow in (c) denotes the displacement vector of the AWS between the ICESat-2 overpass on 14 March 2019 and the UAV imagery on 6 September 2019. The estimated extent of the 50% and 80% fetch footprints for the data in September 2019 in wind directions $\in [179; 181]°$ is shown by the black ovals.

4.2.3 Definition of the height (H) and frontal area index (λ) over a rough ice surface

Here we introduce the type of surfaces that we are considering. Our aim is to model the aerodynamic roughness of a rough ice surface, including its dependence on wind direction (Van Tiggelen et al., 2020). We will consider rectangular elevation profiles of length $L = 200$ m, measured upwind from a point of interest (e.g. an automatic weather station, or AWS). This geometry is a strong simplification of the true fetch footprint, which is calculated for a specific wind direction at S5 in Fig. 4.2, after Kljun et al. (2015). Yet this simplification allows us to use 1D elevation datasets, such as profiles from the ICESat-2 satellite laser altimeter. Besides, the true fetch footprint depends on flow parameters such as the friction velocity (u_*) and the boundary-layer height (Kljun et al., 2015), which are not known a priori.

Four measured elevation profiles, and a high-resolution orthomosaic image are shown in Fig. 4.2. These were measured on 6 September 2019 at site S5 (67.094°N, 50.069°W,
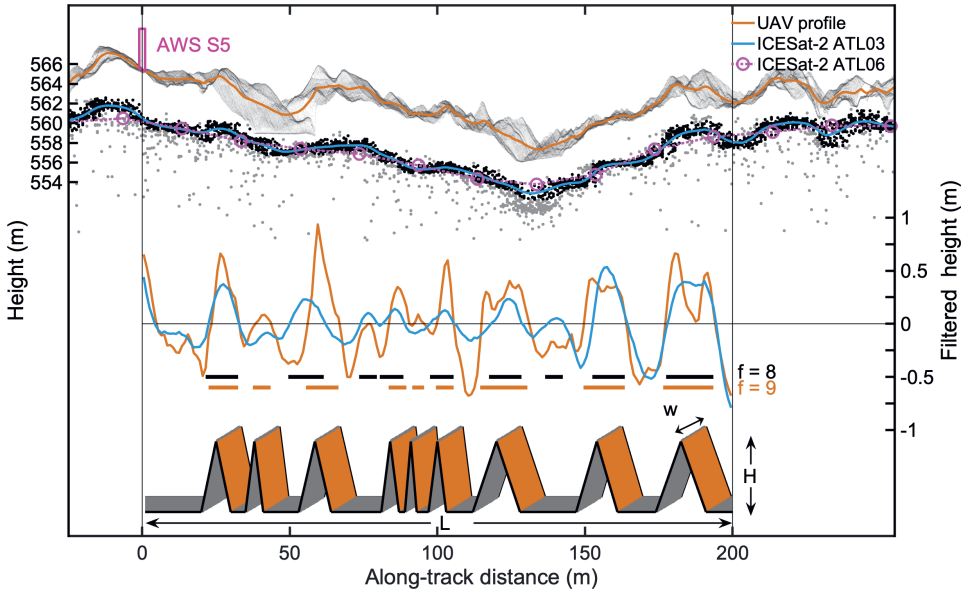
Figure 4.3: Steps in converting a measured digital elevation model to the modelled topography, where L is the length of the profile, f the number of obstacles, H the height of the obstacles and w the width of the elevation profile. The location and height of AWS S5 is shown on top of the UAV elevation profile. The grey dots denote all the ATL03 photons, while the black dots denote the selected photons for the kriging procedure. The solid blue line denotes the 1 m resolution interpolated profile for ATL03 data, and the pink dots denote the 20 m resolution ATL06 signal.

560 m a.s.l.) in the locally prevailing wind directions, using UAV photogrammetry, of which the details will be given in Sect. 4.3. At this site, pyramidal ice hummocks with heights between 0.5 m to 1.5 m are superimposed on larger domes of more than 50 m in diameter (see also Fig. 4.1b). The elevation profiles for different fetch directions illustrate three important issues: (1) the zero-referencing of the surface, (2) the identification of distinct roughness obstacles and (3) the important variability of the surrounding topography, depending on the fetch direction. The obstacles being anisotropic, the surface appears rougher in the southerly directions than in the easterly directions. Besides, the ice ridges and troughs have variable heights and depths, which means that describing this rough ice surface with a few length scales (e.g. H, λ) in order to estimate the aerodynamic roughness will introduce some uncertainty. This is mainly because each individual obstacle has a different contribution to the total drag. Unfortunately, these individual drag contributions cannot be modelled, due to the unknown shape of the wind profile between the roughness elements. Without a universal theory of drag over complex surfaces, several simplifications need to be made.

We choose here to approximate the true surface as an array of f identical obstacles of height H in the profile of length L (Munro, 1989; Smith et al., 2016) (Fig. 4.3). This avoids the use of empirical formulas for the estimation of z_{0m}, and allows us to apply

the bulk drag models. The approach of approximating a natural surface by uniquely shaped obstacles is formally justified by Kean and Smith (2006), as most of the form drag is caused by the largest and steepest obstacles. On the other hand, large natural obstacles also tend to be wide, so their relatively small frontal area index considerably reduces their contribution to the total form drag (Fitzpatrick et al., 2019). To remove the influence of the widest obstacles, the elevation profile of length L is linearly detrended and the power spectral density of the detrended profile is computed in order to filter out all the wavelengths larger than the cutoff wavelength Λ = 35 m. This value is found to give optimal results, which is shown in Appendix 2. In order to avoid spectral leakage when applying Fourier statistics on short and aperiodic signals, we extend each input profile with the identical but mirrored profile before computing the power spectral density. This yields a symmetrical thus periodic profile of length $2L$, which is then high-pass filtered. The final statistics are then computed using the first half of the filtered profile of length L. Typical filtered profiles are shown in Fig. 4.2b and Fig. 4.3. These profiles only contain the ice hummocks, as the high-pass filter removed the influence of the large-scale domes.

The height of the roughness obstacles (H) is taken as :

$$H = 2\widetilde{\sigma_z}, \tag{4.5}$$

in which $\widetilde{\sigma_z}$ is the standard deviation of the filtered elevation profile. This is an arbitrary but convenient choice, as the standard deviation of the topography captures all the scales in the filtered profile but remains insensitive to the height of the small-scale obstacles, which we assume to have a negligible influence on the overall drag. Unfortunately, the variance is sensitive to the height of the largest obstacles, and thus to the chosen value for Λ.

Next, we define an obstacle as a group of consecutive positive values of filtered heights, after Munro (1989) (see also Smith et al. (2016)), which yields f, the number of obstacles. The obstacle frontal area index (λ) in the direction of the elevation profile is then computed as (Fig. 4.3),

$$\lambda = f\frac{Hw}{Lw} = \frac{fH}{L}, \tag{4.6}$$

where w is the width of the profile, set to 15 m. This value was chosen to match the approximate ICESat-2 footprint diameter, yet it is much smaller than the width of the real fetch footprint (Fig. 4.2). We assume that the obstacles and the elevation profile have the same width, which removes all information about the shape of the obstacles in the direction perpendicular to the wind direction. This simplification avoids the additional uncertainty regarding the aggregation of 2D datasets in the process of modelling z_{0m}, and allows us to apply the model to ICESat-2 profiles.

To summarize, a measured elevation profile is now completely defined by the height of the obstacles (H), and the frontal area index (λ), after high-pass filtering (see Fig. 4.3). This now allows us to apply a bulk drag model to estimate one value for z_{0m} per 200 m profile. The exact placement of the obstacles is resolved in the process (Fig. 4.3), but does not serve as input for the drag models. Detailed equations of the bulk drag model can be found in Appendix 1.

4.3   Datasets

4.3.1   Eddy-covariance measurements

Vertical propeller eddy covariance (VPEC, see also T20) measurements are available at sites S5 (67.094°N, 50.069°W, 560 m a.s.l.) and S6 (67.079°N, 49.407°W, 1010 m a.s.l.) since 2016, while AWS observations are available since 1993 and 1995 for each site (Smeets et al., 2018). For this study we use eddy-covariance measurements acquired during September 2019 at site S5 and also site SHR (67.097°N, 49.957°W, 710 m a.s.l.), and from September 2018 to August 2019 at site S6. All these sites are situated in the lower ablation area of the K-transect, which is a 140 km transect of AWS and mass balance observations on the western part of the GrIS (Van de Wal et al., 2012; Smeets et al., 2018). It extends from the ice edge up to 1850 m elevation, and therefore covers many contrasting types of surfaces, ranging from the rough crevassed bare ice close to the ice edge, to the year-round firn-covered surface at the highest locations (see Figs. 4.1 and 4.6). At the end of the melting season, the bare ice surface at S5 and SHR is characterised by densely packed hummocks up to 1.5 m height, while at S6 it is characterised by more sparsely packed hummocks of 0.6 m average height. The datasets include 30-min observations of the friction velocity $u_*(z)$, and wind speed $u(z)$ at the same height above the surface ($z = 3.7$ m). Two independent techniques were used at S5 and SHR. The first technique is the sonic eddy-covariance (SEC) method, which uses measurements from a sonic anemometer (CSAT3B, Campbell scientific, Logan, USA) sampled at 10 Hz. The second technique is VPEC method, that relies on measurements of a vertical propeller, horizontal propeller and fine-wire thermocouple sampled at 5 Hz. At S6, only the VPEC method was used with a sampling interval of 4 s. For both methods, the roughness length (z_{0m}) is calculated using Eq. (4.2).

We only select data taken during near-neutral conditions ($z/L_o < 0.1$), and we assume that the measurements are taken above the roughness layer, i.e. $\widehat{\Psi_m(z)} = 0$. The latter is a reasonable assumption, given that the height of the obstacles (H) at these sites is less than 1.5 m, which means that the roughness layer unlikely exceeds 3 m (Smeets et al., 1999; Harman and Finnigan, 2007). On the other hand, when applying the drag model to estimate z_{0m} (Appendix 1), the correction factor $\widehat{\Psi_m(z)}$ is taken into account. The reason is that the obstacles are located in the roughness layer, where the vertical wind profiles deviate from the inertial sublayer wind profiles, according to Eq. (4.1). Details about the processing steps and further data selection strategies can be found in T20. The data selection strategy removes all data points with wind directions outside the $[80°; 200°]$ interval. In the following sections we average $\ln(z_{0m})$, which is of interest for the determination of the vertical profile of horizontal wind speed (Eq. (4.1)). Additional in situ averaged z_{0m} measurements obtained during different time periods and at several locations along the K-transect are taken from M97 (Meesters et al., 1997), SB08 (Smeets and Van den Broeke, 2008a), L14 (Lenaerts et al., 2014) and T20 and are summarized in Table 4.1.

Table 4.1: Description of z_{0m} in situ datasets on the K-transect. The data from Meesters et al. (1997), Smeets and Van den Broeke (2008a), Lenaerts et al. (2014) and Van Tiggelen et al. (2020) are denoted M97, SB08, L14 and T20 , respectively. The measurement methods are (p) profile, (sec) sonic eddy-covariance or (vpec) vertical propeller eddy covariance.

site (elevation)	season	surface type	z_{0m} range (m)	reference (method)	data averaging period
S5 (550 m)	summer	densely-packed ice hummocks, between 0.5 m and 1.5 m	$6\times10^{-3} - 8\times10^{-2}$	SB08 (p)	Sep 2003 & Aug 2004
			$1.79\times10^{-3} - 3.45\times10^{-2}$	T20 (vpec)	Sep 2016
			$1.05\times10^{-2} - 4.66\times10^{-2}$	this study (sec)	Sep 2019
	winter	snow and exposed ice hummocks	$8\times10^{-5} - 1\times10^{-3}$	SB08 (p)	Dec 2003 to May 2004
			$2.9\times10^{-4} - 1.21\times10^{-2}$	T20 (vpec)	Dec 2016 to May 2017
SHR (710 m)	summer	densely-packed ice hummocks, between 0.5 m an 1 m	$9.1\times10^{-3} - 4.38\times10^{-2}$	this study (sec)	Sep 2019
S6 (1010 m)	summer	sparse ice hummocks, average height 0.6 m	$2\times10^{-3} - 2\times10^{-2}$	SB08 (sec)	Sep 2003 & Aug 2004
			$1.26\times10^{-3} - 7.52\times10^{-3}$	this study (vpec)	Aug 2019
	winter	snow, sastrugi	$5\times10^{-5} - 6\times10^{-4}$	SB08 (sec)	Dec 2003 to May 2004
			$2\times10^{-6} - 1.33\times10^{-4}$	this study (vpec)	Dec 2018 to May 2019
S9 (1520 m)	summer	changing from wet melting snow to large ice crystals	$2\times10^{-6} - 1\times10^{-4}$	SB08 (p)	Sep 2003 & Aug 2004
			$2\times10^{-4} - 5\times10^{-4}$	M97 (sec)	July 1991
	winter	snow, sastrugi	$2\times10^{-5} - 7\times10^{-4}$	SB08 (p)	Dec 2003 to May 2004
S10 (1880 m)	summer	snow, sastrugi	$2\times10^{-4} - 7\times10^{-4}$	L16 (sec)	Sep 2012

4

Table 4.2: Description of DEMs obtained by UAV photogrammetry, and of the corresponding overlapping ICESat-2 laser beams.

Site	Center coordinate	Dimensions (m)	Resolution (m)	UAV survey date)	ICESat-2 track-cycle-beam	ICESat-2 date
A	67.171 N 50.075 W	1500 x 1400	0.3	01-09-2019	1169-04 gt1r	12-09-2019
B	67.126 N 50.075 W	2300 x 1300	0.3	03-09-2019	1344-05-gt1r	23-12-2019
S5	67.093 N 50.065 W	450 x 375	0.025	06-09-2019	1169-02-gt1l	14-03-2019

4.3.2 UAV structure from motion

The high-resolution elevation maps are derived using a structure-from-motion workflow using UAV imagery. Two crevassed areas close to the ice edge were mapped using an eBee fixed-wing UAV from Sensefly, while the area surrounding S5 was mapped using a Mavic Pro quadcopter UAV from DJI. Multiple overlapping true-color images of the surface are processed in Agisoft Photoscan to produce 3D elevation maps. Detailed information about this workflow can be found in Immerzeel et al. (2014), Kraaijenbrink et al. (2016) and references therein. Briefly, the same surface features are identified on different images and are used to reconstruct the 3D geometry between the surface and the camera position. The resulting point cloud of the surface is then gridded and finally geo-referenced using the information of the UAV GPS, which yields a digital elevation model (DEM) of the surface. No additional ground-control points were used for the elevation maps used in this study, which is of little relevance in this study, as we are not interested in the exact absolute elevation but in relative obstacle heights. Details about the UAV DEMs are provided in Table 4.2.

The elevation profiles are then extracted by projecting all the DEM points in a 200 m x 15 m rectangle on the center line, followed by averaging the projected points in 1 m bins (see Fig. 4.3). The aim of this averaging method is to mimic ICESat-2 profiles.

4.3.3 ICESat-2 laser altimeter

Launched in September 2018 by the National Aeronautics and Space Administration (NASA), the ICESat-2 (Ice, Cloud, and Elevation Satellite-2) satellite carries a laser altimeter system in near-polar orbit (Markus et al., 2017). The altimeter relies on a photon-counting system, which in combination with both the spacecraft's position and its pointing orientation, enables the retrieval of 3-D position of individual backscattered photons (Neumann et al., 2019). Our hypothesis is that the small footprint diameter ($\approx$ 15 m) and short along-track spacing between these footprints (0.7 m) allows for an accurate estimation of land ice aerodynamic roughness properties.

A typical geolocated photon measurement ATL03 (Neumann et al., 2019) can be seen in Fig. 4.3 for site S5, and in Fig. 4.4a for area A. Details about which ICESat-2 measurements are compared against the UAV surveys are provided in Table 4.2. Not more than one ICESat-2 measurement exactly overlaps each UAV survey. This is mainly

due to the presence of clouds and due to changes in laser pointing orientations in other ICESat-2 measurements, but also due to changes in the studied locations due to ice flow. The global geolocated photon product ATL03 requires some processing steps before the roughness statistics can be computed. These steps mainly involve the selection of valid photons, aggregating the 3-D photon positions on a regular along-track grid, and finally correcting for remaining biases. The standard algorithm used to derive an accurate estimate of land ice height product from ATL03 to ATL06 is described in detail by Smith et al. (2019). Unfortunately the 20 m along-track resolution of the ATL06 land ice height product is too coarse for aerodynamic roughness calculations for two reasons. First, in the ATL06 product there are only ten points in 200 m sections, which is not enough to apply the high-pass filter. And second, on this scale the amount of roughness obstacles (f) would be greatly underestimated as can be seen in Figs. 4.3 & 4.4. Fortunately, information smaller than the footprint diameter can be extracted from the ATL03 product, as shown by Herzfeld et al. (2020), in which a density-dimension algorithm is used that facilitates surface-height determination at the 0.7 m nominal along-tack resolution. In the following part we describe a method to produce a 1 m resolution along-track surface height estimation from the ATL03 raw photons signal.

The first step involves selecting all the ATL03 photons that have been flagged as either low, medium or high confidence by the ATL03 algorithm. All the selected photons are projected on the along-track segment, and a median absolute difference filter is used to remove all the photon heights which deviate too much from the local ensemble median,

$$\langle z \rangle - \frac{q_{low}}{0.6745}\langle |z - \langle z \rangle| \rangle \le z \le \langle z \rangle + \frac{q_{high}}{0.6745}\langle |z - \langle z \rangle| \rangle, \tag{4.7}$$

where $< z >$ denotes the median of z within a moving window. We choose $q_{low} = 1$ and $q_{high} = 2$, in order to filter more photons below than above the median. We assume that the highest detected photons are more likely to be first surface reflections, while the lower photons are more likely to be delayed by scattering. We set the window length to 50 m. The previous selection strategy could also be applied for retrieving the surface in the case of multiple reflections (e.g. shallow supraglacial lakes), but this was not tested.

The second step involves interpolating the irregular photon locations on a regular, 1 m resolution, along-track grid. The overlap between the individual footprints means that the geolocated photon heights in close vicinity must be correlated to each other, with a correlation diameter similar to twice the footprint diameter (≈ 30 m). We take advantage of this feature to interpolate the ATL03 photons using a k-nearest neighbour, one dimensional, ordinary kriging algorithm, of which details can be found in e.g. Hengl (2009). In essence, the interpolation weights depend on the covariance with the nearby measurements, which is assumed to decrease over distance. A gaussian covariance function with a radius of 15 m is found to fit the experimental semi-variograms best. For computational efficiency, only the 100 closest geolocated photons within a quarter footprint diameter (3.75 m) of each grid point are used for the interpolation. We only choose the high confidence photons, but if there is less than 1 photon per 0.7 m, we also select the medium confidence photons. If there are not enough medium confidence photons, we increase the search radius to half the footprint diameter (7.5 m) or even up to a footprint diameter (15 m). The low confidence photons are only used as a last resort. If in a 15 m footprint diameter there are still not enough photons present, the height
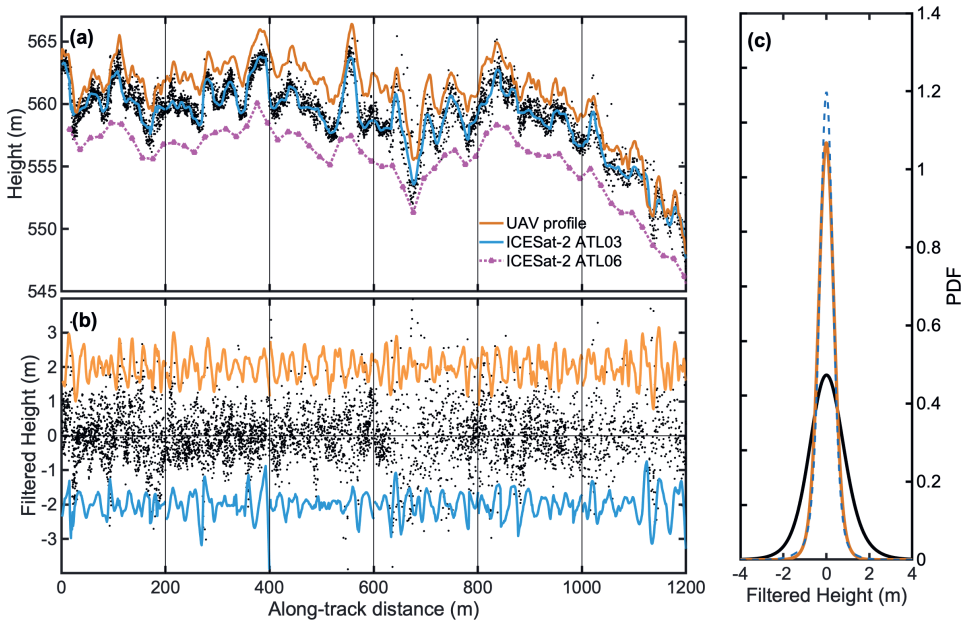
Figure 4.4: (a) Elevation profile at site A measured by the UAV and by ICESat-2 (solid lines), selected ICESat-2 photons (black dots) and ICESat-2 ATL06 height (pink dashed line). The UAV and ATL06 profiles have been vertically offset by 2 m for clarity. (b) Filtered profiles (solid lines) and residual photons elevations after filtering per 200 m windows (black dots), where the UAV and ATL03 filtered profiles have also been vertically offset. (c) Probability density function of the filtered ICEsat-2 profile (blue dashed line), UAV profile (orange solid line) and residual photons elevations (black line).

on that grid point is not estimated, which results in a gap. A sensitivity experiment using different photon selection strategies and different kriging parameters is found in Appendix 2.

The last step involves grouping the interpolated elevation measurements in 200 m along-track windows, and the high-pass filtering using a cut-off wavelength of $\Lambda = 35$ m (Sect. 4.2). The height of the obstacles (H) is defined as twice the standard deviation of the filtered signal (Eq. (4.5)).

Although 1 m resolution is still too coarse to capture all the small-scale obstacles that contribute to form drag, we expect that most of the form drag over rough ice is caused by the larger obstacles that are resolved by the ICESat-2 altimeter. Furthermore, the small-scale information is still indirectly present in the scatter of the surrounding photons to the closest grid point, which is a measure of both the instrumental error and the surface slope, but also of the surface roughness (Gardner, 1982).

An alternative approach that does not require gridding the ATL03 product to 1 m resolution would be to use the standard deviation of the raw photon signal detrended for the resolved 20-m resolution ATL06 data, as in Yi et al. (2005) and Kurtz et al.

(2008). However, as we will see in the following sections, this would overestimate the height of the roughness obstacles. Besides, the frontal area index (λ) would remain unknown.

When working with the 1-m interpolation profile, we model the standard deviation of the unresolved topography (σ_{sub}) according to,

$$\sigma_{sub} = \left(\sigma_{ph,res}^2 - \sigma_i^2\right)^{0.5}/2, \tag{4.8}$$

where $\sigma_{ph,res}$ is the standard deviation of the photon residual elevations, defined as the signal of the selected photons minus the interpolated 1 m resolution profile (Fig. 4.4), $\sigma_i = 0.13$ m is the standard deviation due to the instrumental precision (Brunt et al., 2019). We calculate σ_{sub} for each 200 m profile. The total variance of the surface elevation measured by the laser altimeter in 200 m intervals is the sum of both the resolved and unresolved variance:

$$\sigma_{tot} = \sqrt{\widetilde{\sigma_{res}}^2 + \sigma_{sub}^2} \tag{4.9}$$

in which $\widetilde{\sigma_{res}}$ is the resolved standard deviation of the filtered 1 m resolution profile. The height of the roughness obstacles, corrected for the unresolved topography is then estimated according to:

$$H_{corr} = 2\sigma_{tot} \tag{4.10}$$

The obstacle frontal area index (λ) is finally computed using Eq. (4.6), where the number of obstacles (f) is estimated from the filtered profiles. Both H and λ are then used as input for the bulk drag model (Appendix 1), which results in one value for z_{0m} per 200 m profile.

The filtered ICESat-2 signal and residual photon elevations at site A are shown in Fig. 4.4b, and their probability density functions in Fig. 4.4c. At this site, the filtered ICESat-2 signal at 1 m resolution captures most of the information present in the UAV signal. On the other hand, the residual photon elevations, defined as the selected photons detrended for the interpolated profile under Eq. (4.9) still contain much larger scatter than the UAV elevation profile. This demonstrates that roughness is not the only factor explaining the scatter in the raw altimeter signal. Therefore using the residual scatter (Eq. (4.9)) will overestimate the height of the roughness obstacles. In the next sections, we will analyse the uncorrected height of the obstacles (H), unless stated otherwise.

4.4   Results

4.4.1   Evaluation of the bulk drag model forced with a UAV DEM

Bulk drag models are often used as a convenient way to estimate the aerodynamic properties of natural surfaces. Nevertheless, the number of quantitative evaluations of these models for rough snow and ice surfaces is very limited. Brock et al. (2006) found that z_{0m} modelled using the method by L69 (Eq.(4.23)) agrees well with observations over melting ice on a mountain glacier, although they used shorter profiles, up to 15 m in length, and sampled in the orientation perpendicular to the wind direction. On

the other hand, Van den Broeke (1996) found that L69 overestimates z_{0m} at site S4 at the K-transect (lowest site in Fig. 4.6). The same overestimation was found by Smeets et al. (1999), Fitzpatrick et al. (2019) and Chambers et al. (2019) for rough glacier ice, but also by Miles et al. (2017) for a debris-covered glacier. These studies all use different methods at different sites to estimate H and λ, which illustrates the limited suitability of the model by L69 for realistic snow and ice surfaces.

To verify the suitability of several drag models (see Appendix 1), we use the eddy-covariance observations at site S5 as independent validation (Sect. 4.3). Different values of z_{0m} are calculated for different fetch directions as depicted in Fig. 4.2. Figure 4.5 compares both the estimated z_{0m} from in situ observations and the modelled z_{0m} at the end of the ablation season, as a function of the measured obstacle frontal area index λ. The L69 model (Eq.(4.23)) overestimates z_{0m} for $\lambda < 0.04$ at this location (Fig. 4.5, blue line). In accord with L69, the drag coefficient of an individual obstacle $C_d = 0.25$ is likely too high for naturally streamlined obstacles. Furthermore, L69 does not consider the displacement height, which means that the height of the obstacles (H) relevant for form drag is overestimated. Nevertheless, L69 still yields a reasonable estimate of z_{0m} for $\lambda > 0.04$, which can be explained by the neglect of the displacement that is compensated by too small C_d for these fetch directions. The method by M98 (Eq. (4.24)) does account for the displacement height and, while using the same drag coefficient $C_d = 0.25$, it gives improved results for $\lambda < 0.04$ compared to L69 (Fig. 4.5, green line). The same holds for the model by R92 (Fig. 4.5, red line). M98 is expected to fail for very small λ, due to the absence of skin friction. Using $C_d = 0.1$, all three models perform better for $\lambda < 0.05$ but perform poorly for $\lambda > 0.04$ (Fig. 4.5, dashed lines). This is a strong indication that C_d is not constant, but varies with the wind direction, depending on the exact placement and shape of the obstacles. In Sect. 4.4.3 we estimate the values for C_d required to fit the model to the observations; these values vary between 0.1 and 0.3, and show a weak relationship with H. The parametrization for C_d from Garbrecht et al. (1999) (Eq. (4.12)), for which C_d increases with H, yields the most acceptable results when used in combination with the R92 model (Fig. 4.5). Note that Lüpkes et al. (2012) use a constant value for C_d.

The R92 model with the parametrization for C_d allows for some variability in modelled z_{0m} for the same λ, but is still not able to reproduce the eddy-covariance observations (Fig. 4.5). We attribute this to the parametrization of C_d, that was derived for sea-ice pressure ridges and therefore likely less suitable for rough ice hummocks. Nevertheless, the overall error between model and observation is acceptable, given the simplicity of the bulk drag models that were designed for idealized roughness geometries. As pointed out by L69, realistic modelling of total drag over a complex natural surface should intuitively require a complete variance spectrum of the topography. Linking variance spectra to the total drag has been investigated recently through numerical simulations (Yang et al., 2016; Zhu and Anderson, 2019; Li et al., 2020), but a universal and physically based relationship for complex surfaces is still lacking. In the next sections, we therefore use the model of R92 with a parametrized C_d for mapping z_{0m} using either UAV or ICESat-2 profiles.
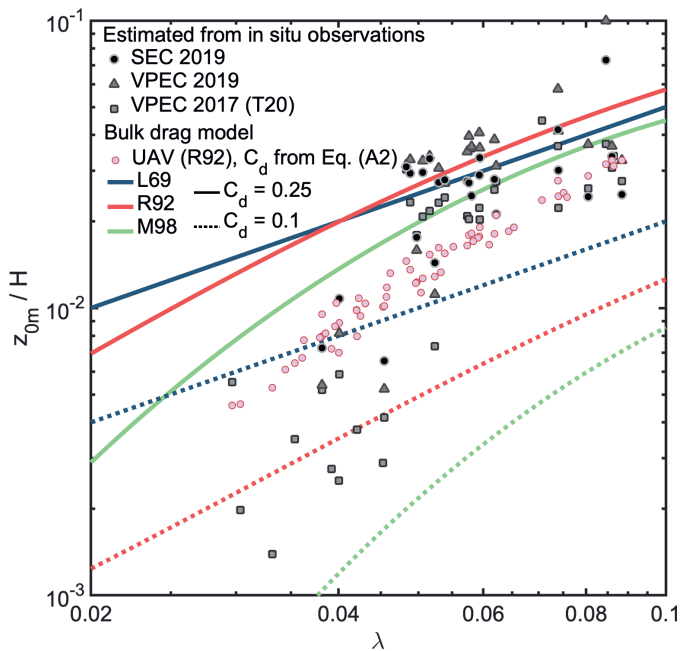
Figure 4.5: Modelled z_{0m} at site S5 using three different bulk drag models: (L69, blue lines Lettau, 1969), (M98, green lines Macdonald et al., 1998), (R92, red lines Raupach, 1992) and using two different values for the drag coefficient for form drag: $C_d = 0.25$ (solid lines) and $C_d = 0.1$ (dashed lines). Solid grey symbols are measurements from sonic eddy-covariance (SEC) or vertical propeller eddy-covariance (VPEC). Additional data are from T20 (Van Tiggelen et al., 2020). Pink circles are the model results forced with H and λ from UAV photogrammetry, using the R92 model and C_d parameterized using Eq. (4.12).
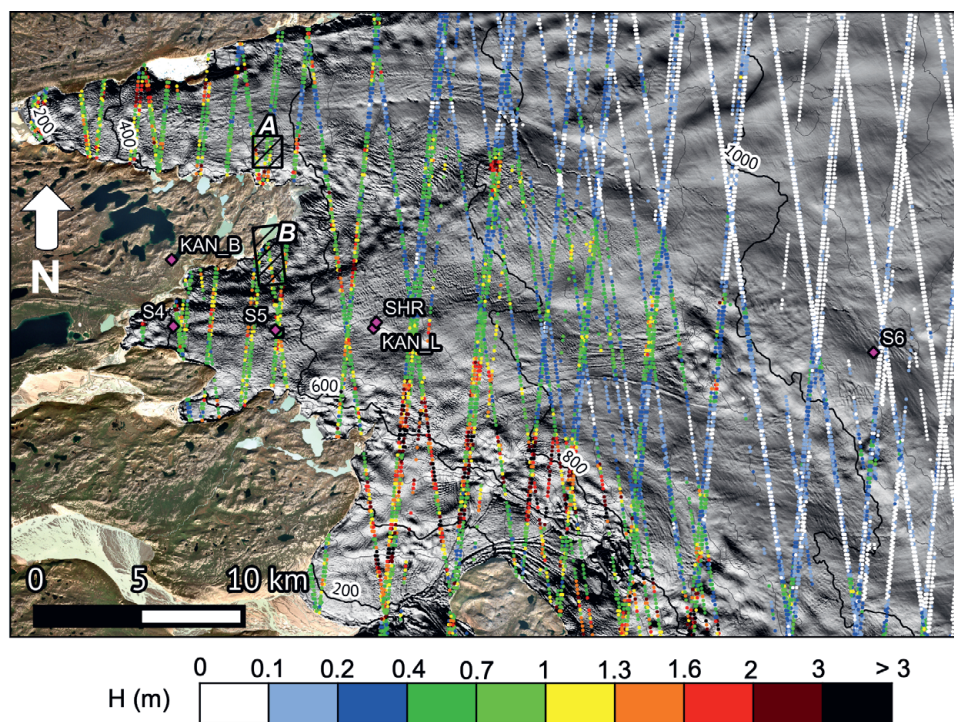
Figure 4.6: Estimated height of the roughness obstacles (*H*) from ICESat-2 between 16 October 2018 and 06 September 2020 in the lower part of the K-transect, West Greenland. The location of the automatic weather stations are given by the pink diamonds. The black boxes A and B delineate the areas mapped by UAV photogrammetry. A hillshade of ArcticDEM (Porter et al., 2018) is shown as background over the ice sheet.

4.4.2   Height of the roughness obstacles (H) estimated from ICESat-2

The estimated height of the obstacles (*H*) using two years of ICESat-2 measurements (16 October 2018 – 06 September 2020) crossing the lower part of the K-transect is shown in Fig. 4.6. *H* ranges between less then 0.1 m at the higher locations, to more than 3 m in rough crevassed areas near the ice edge. At first glance a clear pattern of roughness emerges, in which ice dynamics and elevation seem to be the controlling factors. Low-lying bare ice areas are rougher, while the higher, firn covered areas are smooth. Nevertheless, the roughness is very variable locally due to isolated crevasses and melt channels. Besides, we expect a seasonal variability that is not yet captured in this analysis.

4.4.3   Evaluation of ICESat-2 roughness statistics against UAV DEMs

Climate models and satellite altimeter corrections require information about the larger-scale spatial variability of surface (aerodynamic) roughness. This motivated us to compare the roughness statistics acquired with high-resolution UAV photogrammetry to the

statistics estimated from the ICESat-2 laser altimeter.

The elevation profile from the UAV survey in box A (Fig. 4.6) was already compared to the overlapping ICESat-2 profiles in Fig. 4.4a, while H, λ and z_{0m} are compared in Fig. 4.7. In box A, the UAV and ICESat-2 profiles were taken 11 days apart at the end of the ablation season. The height (H) and frontal area index (λ) of the roughness obstacles is estimated for 200 m intervals, with each interval center separated by 50 m. Overall, the uncorrected 1 m profile from ICESat-2 (Fig. 4.7, solid black line) clearly captures all the largest obstacles and the large-scale variability, but still slightly underestimates both the height (H) and the frontal area index (λ) of the obstacles, compared to the UAV surveys (Fig. 4.7, orange line). This is expected, given the size of the laser footprint and the low-pass filtering properties of the kriging procedure. On the other hand, the correction using the standard deviation of the photons distribution (Eq. (4.9)) overestimates H (Fig. 4.7, dashed black line). This can be explained by additional processes that affect the local photon distribution but that we did not consider, such as the forward scattering in the atmosphere (Kurtz et al., 2008), the penetration of photons in the ice layer (Cooper et al., 2021), or simply the presence of outliers that passed the median absolute difference filter (Eq. (4.7)). Furthermore, the obstacle frontal area index (λ) is underestimated by the ICESat-2 altimeter, since we do not account for unresolved obstacles when counting the number of obstacles (f). In addition, using the standard deviations of the ATL03 product detrended for the 20 m resolution ATL06 signal, results in an even greater overestimation of H (Fig. 4.7, purple line). This is due to the fact that besides the additional processes broadening the altimeter signal, the scatter of this signal also contains the large scale variability at wavelengths larger than $\Lambda = 35$ m. We assumed that such large wavelengths can be neglected in the drag calculations, therefore they are removed in the filtered UAV and ICESat-2 profiles.

Two more UAV surveys were performed in September 2019 in area B and around S5, but the overlapping ICESat-2 profiles were measured during winter (see Table 4.2). The comparison of H, λ and modelled z_{0m} is given in Fig. 4.7. In area B, crevassed and slightly rougher than A, the elevation was measured in December, three months after the UAV survey. The uncorrected ICESat-2 profiles show a slightly more pronounced underestimation of H compared to area A, which we relate to snowfall reducing the height of the roughness obstacles. On the other hand, the corrected ICESat-2 profiles overestimate H by 0.06 m, which translates in an overestimation of z_{0m} by approximately 2.5×10^{-3} m (Fig. 4.7). On average, the uncorrected ICESat-2 values underestimate z_{0m} by 2.9×10^{-3} m for area A and 9×10^{-3} m for area B, which corresponds to $\approx 40\%$ and $\approx 36\%$ of the average z_{0m} estimated by the UAV at these two sites, respectively.

At site S5, UAV elevation profiles and eddy-covariance measurements are available in September 2019, while the ICESat-2 elevation profile was measured in March (Table 4.2). Both the satellite and the UAV profiles are shown in Fig. 4.3. Although the UAV profile is too short to statistically compare H and λ to the ICESat-2 altimeter, the qualitative comparison between the two confirms that the satellite altimeter is very well capable of detecting most of the obstacles that are smaller than 20 m in width. Interestingly, some depressions in the UAV DEM are not captured by ICESat-2, most likely as a result of snow filling them in March. Furthermore, the bending (or 'doming') of the UAV profile is well visible near the edges, which is a consequence of the lack of reference ground
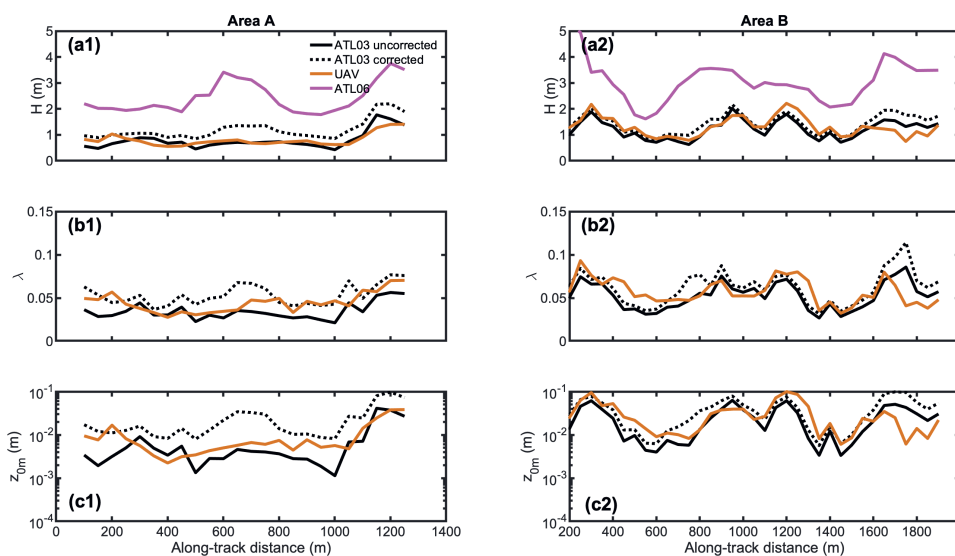
Figure 4.7: (a1) and (a2), estimated height of the roughness obstacles (H). (b1) and (b2), estimated frontal area index. (c1) and (c2), estimated aerodynamic roughness length (z_{0m}). Left panels: area A. Right panels: area B. The black lines denote the roughness statistics estimated from the ATL03 filtered profile, with or without accounting for the residual photons elevations (dashed and solid line, respectively). The orange line denotes estimates using UAV elevation profiles, and the pink line denotes the height of obstacles estimated using the scatter of ATL03 photons detrended for the ATL06 signal.
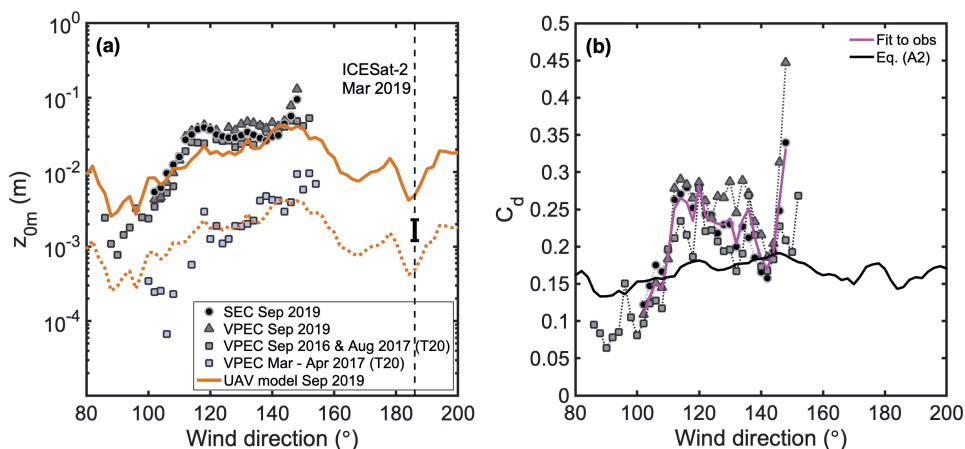
Figure 4.8: (a) Drag model evaluation at site S5. (b): Drag coefficient for form drag (C_d) used in the bulk drag model (black line) or required to fit the observations. The orange solid line is the modelled z_{0m} using the R92 model and UAV photogrammetry on 6 September 2019, while the dashed orange line is the orange line shifted down by a factor 10. Solid symbols are measurements from sonic eddy-covariance (SEC) or vertical propeller eddy-covariance (VPEC). Additional data is from van Tiggelen et al. (2020, T20). The vertical dashed line denotes the direction sampled by the ICESat-2 laser beam on 14 March 2019. The error bar denotes the range between the uncorrected and corrected ICESat-2 measurements.

control points in the UAV data processing, which is a common issue with UAV data processing (James and Robson, 2014). Both H and λ are smaller in the satellite profile than in the UAV profile, but the modelled z_{0m} agrees qualitatively with that estimated using observations from the AWS S5 during March-April. During this time period, z_{0m} is approximately a factor 10 smaller than during the end of the ablation season (Fig. 4.8, dashed orange line). Unfortunately, the track direction of the satellite altimeter rarely coincides with the wind direction measured by the anemometers at this location, due to the katabatic forcing. This prevents a direct comparison of ICESat-2 roughness to in situ observations, as the aerodynamic roughness strongly depends on the wind direction (Van Tiggelen et al., 2020). The z_{0m} value estimated from ICESat-2 profiles must thus be interpreted as the aerodynamic roughness in the wind direction along the direction of the ground laser track.

Only a high-resolution, two-dimensional DEM, e.g. obtained using a UAV, allows for an accurate description of the aerodynamic roughness around a point of interest in multiple directions. An example of such an analysis is shown for site S5 in Fig. 4.8. The R92 model applied to the UAV elevation profiles reproduces the considerable variability of the estimated z_{0m} using in situ observations. Across all the wind directions available in the measurements, z_{0m} using the UAV profiles is underestimated by 7.6×10^{-3} m, or 28% of the average value estimated by the SEC method in September 2019 (2.65×10^{-2} m). The comparison improves when comparing the modelled z_{0m} to VPEC measurements from September 2016 and August 2017 (T20), the model now overestimates the

estimated z_{0m} by in situ observations by 1.1×10^{-3} m, or 9% of the observed value (1.25×10^{-2} m). As these data contain more wind directions, the overestimation of z_{0m} in the southerly fetch directions is compensated by an underestimation in the easterly directions (Fig. 4.8). The difference between different in situ data highlights the variability in z_{0m} in time, but also the uncertainty in the field measurements. The difference in averaged estimated z_{0m} using in situ observations during the overlapping period across all wind directions is 12% between the VPEC and the SEC methods.

The ice hummocks seen in the easterly directions have smaller H and λ, which results in a smaller z_{0m} than in the southerly directions. This is due to the anisotropic nature of the ice hummocks, and is confirmed by the eddy-covariance observations, regardless of the season. The extent of the UAV survey allows the application of the drag model for wind directions that rarely occur during the measurement period. This is particularly useful for the development of z_{0m} parametrizations in atmospheric models. Interestingly, the topography at site S5 translates in a wavy pattern of z_{0m} as function of wind direction, with two local minima at fetch directions of 90 and 180 degrees (Fig. 4.8).

To summarize, three independent but co-located methods, namely UAV photogrammetry, ICESat-2 laser altimetry and in situ eddy-covariance measurements, allow us to estimate the aerodynamic roughness of a rough ice surface at a specific site. The comparison confirms our two initial hypotheses: (1) the variability of estimated z_{0m} using in situ observations as function of wind direction found by T20 is indeed a consequence of the anisotropic topography, and (2) the ICESat-2 data are very well suited to estimate z_{0m} of a rough ice surface in both space and time. Without correcting for the residual scatter in photon elevations, the 1 m resolution ICESat-2 profiles most likely provide a lower bound of roughness, as they underestimate z_{0m} by almost a factor 2 at the two rough ice locations in areas A and B. On the other hand, an attempt to account for this residual scatter may lead to an overestimated z_{0m}, by a factor that depends on the noise in the raw altimeter data. Nevertheless, given the fact that z_{0m} varies over several orders of magnitude, we deem this method useful to understand the spatio-temporal variability of the aerodynamic roughness length over the GrIS.

4.4.4   Results: Mapping the roughness length z_{0m} using ICESat-2

In this section we apply the elevation profile filtering described in Section 4.3 and the R92 model with parameterized C_d (see Appendix 1) to ICESat-2 ATL03 data to model and map the aerodynamic roughness (z_{0m}) over the K-transect. We process nearly two years of ICESat-2 ATL03 measurements, taken between 16 October 2018 and 06 September 2020. The results, without accounting for the unresolved photon scatter, are presented in Fig. 4.9. Within a distance of 10 km from the ice margin, z_{0m} ranges between 10^{-3} m and 10^{-1} m. There is a clear transition of z_{0m} values that separates the rough (S4, S5, KAN_L, SHR) and smooth (S6 and higher) surface in the ablation zone. Within a distance of several km, z_{0m} can vary by more than one order of magnitude, e.g. north of locations S5 and KAN_L (Fig. 4.9). In order to quantify the variability in time, we group the z_{0m} values from ICESat-2 in two groups, July – September and October – June, which corresponds to ICESat-2 cycles 1-3 & 5-8, and 4 & 8 respectively. The average z_{0m} value for the two groups in each 200 m elevation bin is presented in Fig. 4.10. During summer, the average z_{0m} value is 1×10^{-2} m below 600 m asl, while
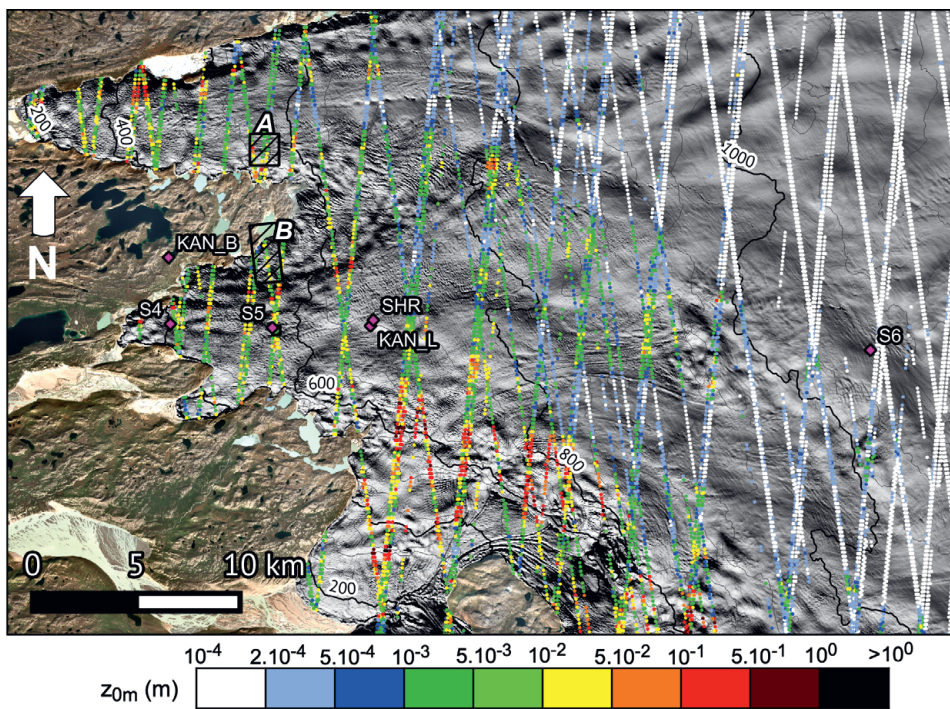
Figure 4.9: Estimated aerodynamic roughness length (z_{0m}), without accounting for the residual photon backscatter, from ICESat-2 between 16 October 2018 and 06 September 2020 in the lower part of the K-transect, West Greenland. The location of the automatic weather stations are given by the pink diamonds. The black boxes A and B delineate the areas mapped by UAV photogrammetry. A hillshade of ArcticDEM (Porter et al., 2018) is shown as background over the ice sheet.

it is around 6×10^{-3} m during the other months. The average roughness approaches its minimum value of 10^{-4} m above 1000 m asl, regardless of the season. When the ICESat-2 altimeter does not detect any obstacle, the bulk drag model only accounts for skin friction, which is prescribed as a constant in the model. Interestingly, z_{0m} decreases very near the ice margin, which might be explained by the decreasing ice velocity at the margin, as most of the glaciers in this area are land-terminating.

The measurements described in Table 4.1 are also included in Fig. 4.10. The comparison indicates that the satellite product captures the overall variability along the K-transect (Fig. 4.10). Especially at lower elevations, the modelled z_{0m} is within the range of in situ observations. The in situ roughness z_{0m} can vary due to changing wind direction, but also due to instrumental uncertainty. Especially the smooth sites where the profile method has been used can exhibit large variability, such as at site S9 (see Table 4.1).

Unfortunately, the ICESat-2 altimeter is not able to detect obstacles that contribute to form drag at sites S6 (1010 m asl) and higher. At S6, the surface is flat during winter, but becomes rough during summer with ice hummocks with 0.6 m average
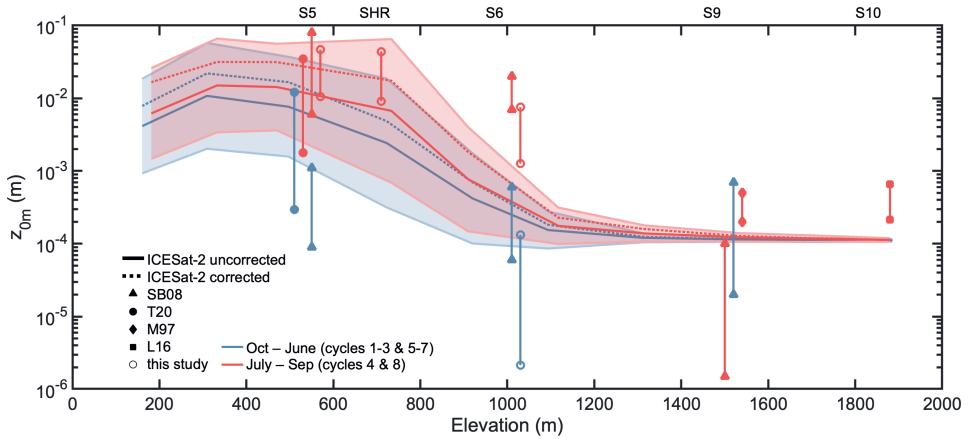
Figure 4.10: Estimated aerodynamic roughness length (z_{0m}) from ICESat-2 between 16 October 2018 until 06 September 2020 along the K-transect. The data were averaged over 200 m elevation bins and two time periods: summer (July – September, red) and winter (October – June, blue). The variability range denotes the two-sided standard deviation within one elevation class. The in situ observations are described in Table 4.1.

height (SB08). Unfortunately the horizontal extent of these obstacles is smaller than the ICESat-2 footprint diameter (≈ 15 m). Higher up, the ice hummocks become even smaller and the surface eventually becomes snow-covered year-round. Nevertheless, snow sastrugi, known to reach up to 0.5 m height at site S10 from photographic evidence, still contribute to form drag. This results in a maximum observed value of $z_{0m} = 7 \times 10^{-4}$ m at sites S9 and S10 (Fig. 4.10). Using a rough estimate for both H and λ at S6 and S10, based on photographs taken during the end of the ablation season, yields more realistic values for z_{0m} (Fig. 4.11) than using H and λ from the ICESat-2 elevation profiles. Therefore we conclude that the roughness obstacles are not properly resolved at these locations in the ATL03 data using the algorithm presented in this study, even when the correction using the residual photons scatter is applied. This is mainly due to the limited footprint of the ICESat-2 measurements, but also due to the orientation of the surface features, which limits the detectability of highly anisotropic features from 1D profile measurements. These limitations in the ICESat-2 measurements result in a uniform prescribed value of $z_{0m} = 1 \times 10^{-4}$ m for elevations above ≈ 1000 m asl. The algorithm described in Sect. 4.3 could be adapted to extract these features from the ATL03 data. For instance, smaller-scale obstacles could be retrieved in multiple directions at cross-over points, using the information from multiple ICESat-2 tracks. However, this is beyond the scope of this study, which is to map the aerodynamic roughness of rough ice at large scales. For now, the implications of these findings for the sensible heat flux, and thus surface ablation, remain to be investigated. The areas with high z_{0m} are in the low-lying ablation zone close to the ice edge, where the highest melt rates are observed. Accounting for the variable roughness might shed light on the drivers of these high melt rates.

4.5 Conclusion

The aerodynamic roughness of a surface (z_{0m}) in part defines the magnitude of the surface turbulent energy fluxes, yet is often poorly known for glaciers and ice sheets. We adapt the bulk drag partitioning model from Raupach (1992) such that it can be applied to 1D elevation profiles. Forcing this model with 1 m resolution elevation profiles taken from the ICESat-2 satellite laser altimeter, z_{0m} becomes a quantifiable and mappable quantity. The model assumes that the surface is composed of regularly spaced, identical obstacles, which all have the same drag coefficient. Despite the fact that the drag coefficient for each individual obstacle remains poorly known, the evaluation in this study against different in situ observations, using different techniques and for different locations and time periods, demonstrates the validity of this model. On the other hand, the use of the model of Lettau (1969) is not recommended over a rough ice surface, as it does not separate the form drag and the skin friction, and neglects both the effects of the displacement height and of inter-obstacle sheltering.

Mapping surface obstacles at 1 m resolution using the ICESat-2 altimeter data proves possible, as long as the roughness obstacles are large enough (e.g. crevasses, ice hummocks). Obstacles that are small compared to the ICESat-2 footprint diameter of ≈ 15 m, such as ice hummocks found above 1000 m elevation in summer, or snow sastrugi expected year-round at even higher locations on the ice sheet from photographic evidence, are not resolved by the ICESat-2 measurements when used in combination with the methods presented in this study. This translates in a lower bound of $z_{0m} \approx 10^{-3}$ m that can realistically be mapped using this method. Furthermore, accounting for the scatter in the unresolved altimeter signal leads to overestimates of the aerodynamic roughness, as this scatter is a consequence of many different processes that must individually be modelled.

The methods presented in this paper can effectively be used to map z_{0m} at ice sheet elevations below 1000 m. This lower ablation area is also where the contribution of turbulent heat fluxes to surface ablation, and thus runoff, is the largest. As a consequence of the orientation of the ICESat-2 orbit, the modelled z_{0m} must be interpreted as the roughness that would be felt by air flowing in the direction parallel to each laser track. Surfaces of glaciers are often anisotropic, and z_{0m} can vary by over one order of magnitude depending on the local wind direction.

The implications of the highly variable aerodynamic roughness for turbulent heat fluxes, and thus surface ablation, remains to be investigated. As current regional climate models typically use constant values for z_{0m}, these implications can be significant, especially in the lower ablation area where most of the surface runoff is generated. This analysis revealed for instance that highly crevassed areas have aerodynamic roughness values over 10^{-1} m, two orders of magnitude larger than typically used in regional climate models over bare ice.

Appendix 1: Bulk drag model

For a single roughness element of height H and frontal area A_f, placed on a horizontal area A_l, R92 (Raupach, 1992) models the form drag as :

$$\lim_{\lambda \to 0} \tau_r = \frac{F_D}{A_l} = \rho C_d \frac{A_f}{A_l} u(H)^2 = \rho C_d \lambda u(H)^2, \tag{4.11}$$

where F_d is the pressure drag force exerted on the obstacle, H is the obstacle height, λ the frontal area index and C_d the drag coefficient of the obstacle. An important uncertainty resides in choosing an accurate value for C_d, due to its dependence on the shape of the obstacles, on the Reynolds number, and on the surface texture. Based on the analysis by Garbrecht et al. (2002) for sea-ice pressure ridges, we choose the following parameterization,

$$C_d = \begin{cases} 0.5(0.185 + 0.147H) & \text{if } H \le 2.5 \text{ m} \\ 0.5\left(0.22\log(\frac{H}{0.2})\right) & \text{if } H > 2.5 \text{ m} \end{cases} \tag{4.12}$$

Note that the factor 0.5 is a consequence of a different definition for C_d in Garbrecht et al. (2002) than Eq. (4.11).

Similarly, R92 models the skin friction for an unobstructed flat surface as:

$$\lim_{\lambda \to 0} \tau_s = \rho C_s(z) u(z)^2 \tag{4.13}$$

where $C_s(z)$ is the drag coefficient of the flat surface, referenced at a height z. Following Andreas (1995), $C_s(z)$ is estimated from the 10-m drag coefficient $C_s(10)$ measured over a flat surface, according to:

$$C_s(z) = \left[C_s(10)^{-0.5} - \frac{1}{\kappa}\left(\ln\left(\frac{10-d}{z-d}\right) - \widehat{\Psi_m}(z) \right) \right]^{-2}, \tag{4.14}$$

with $C_s(10) = 1.2071 \times 10^{-3}$, which yields $z_{0m} = 10^{-4}$ m for a perfectly flat surface in this model. This value was chosen as it is the minimum value estimated using in situ observations by Smeets and Van den Broeke (2008a) during winter over different snow surfaces.

In reality, the total surface shear stress is the sum of both the form drag on each individual obstacle (τ_r), and the skin friction on the underlying surface (τ_s) (Eq. (4.3)). Furthermore, an additional complexity arises at increasing obstacle frontal area index (λ), as the obstacles may effectively shelter a part of the surface and each other, thereby reducing both the skin friction and the form drag. Based on the previous work of Arya (1975), and on scaling arguments of the effective shelter volume, R92 includes sheltering and models the total surface shear stress over multiple obstacles as:

$$\tau(\lambda) = \tau_s(\lambda) + \tau_r(\lambda) \tag{4.15}$$

$$= \rho u(H)^2 \left[C_s(H)\exp\left(-c\lambda\frac{u(H)}{u_*}\right) + \lambda C_d\exp\left(-c\lambda\frac{u(H)}{u_*}\right) \right], \tag{4.16}$$

where $c = 0.25$ is an empirical constant that determines the sheltering efficiency. The latter equation may be written in the form:

$$Xe^{-X} = a, \tag{4.17}$$

with:

$$X = \frac{c\lambda}{2} \frac{u(H)}{u_*}, \tag{4.18}$$

$$a = \frac{c\lambda}{2} (C_s + \lambda C_d)^{-0.5}, \tag{4.19}$$

which is solved iteratively using $X_{i+1} = e^{X_i}$ and $X_0 = a$, after R92. The solution yields $\frac{u(H)}{u_*}$.

The conversion of $\frac{u(H)}{u_*}$ to $z_{0m,R92}$ is finally possible using the semi-logarithmic wind profile Eq. (4.2) and referencing the wind speed at $z = H$. However, an expression for the displacement height d and the roughness sublayer profile function $\widehat{\Psi_m(z)}$ is still required. For the displacement height, the simplified expression by Raupach (1994) is used:

$$d = H \left[1 - \frac{1 - \exp(-\sqrt{c_{d1}\lambda})}{\sqrt{c_{d1}\lambda}} \right] \tag{4.20}$$

with $c_{d1} = 7.5$, which is then used to derive the value for Ψ_r at height $z = H$ using the following expression:

$$\widehat{\Psi_m(H)} = \log(c_w) - 1 + c_w \tag{4.21}$$

where,

$$c_w = \frac{z_* - d}{H - d}, \tag{4.22}$$

in which z_* is the upper height of the roughness layer. Raupach (1994) empirically determined that $c_w = 2$, which yields $\widehat{\Psi_m(H)} = 0.193$.

To summarize, the aerodynamic roughness length z_{0m} of an elevation profile of length L is modelled according to the following steps:

- The elevation profile is high-pass filtered using a cut-off wavelength $\Lambda = 35$ m.

- The obstacle height (H) is set to twice the standard deviation of the filtered profile.

- Each group of consecutive positive heights is defined as a single obstacle, which yields the amount of obstacles (f) per profile length (L).

- The frontal area index (λ) is calculated using Eq. (4.6).

- The displacement height d is estimated with Eq. (4.20).

- $C_s(z)$ is evaluated at $z = H$ using Eq. (4.14), while C_d is parameterized using Eq. (4.12).
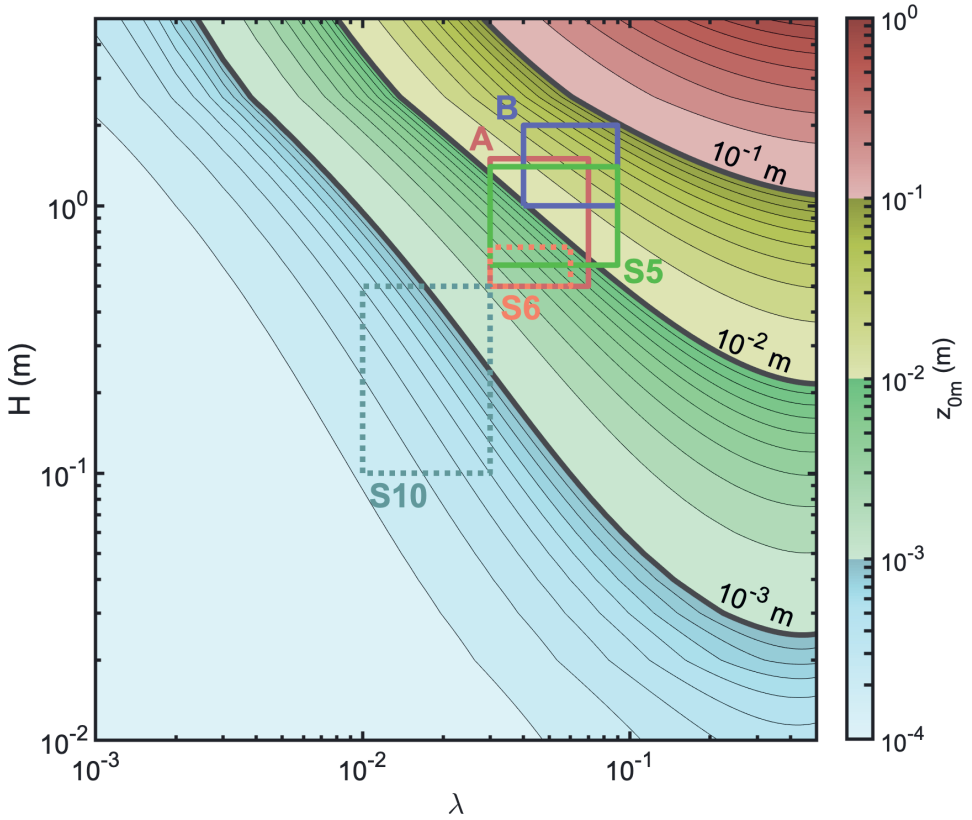
Figure 4.11: Estimated z_{0m} using the R92 model with parameterized C_d (Appendix 1), as function of obstacle height H and frontal area index λ. The solid squares denote the estimated H and λ at three sites using UAV surveys. The dashed squares are estimates based on photographs taken at the end of the ablation season. See Fig. 4.1 for the location of each site.

- $\dfrac{u(H)}{u_*}$ is estimated from Eqs. (4.17) - (4.19).

- z_{0m}/H is estimated by evaluating the logarithmic wind profile at a height $z = H$, using Eq. (4.2)

Following the steps above, z_{0m} can be estimated for any H and λ, which is done in Fig. 4.11. At areas A, B and site S5, H and λ are estimated from the UAV surveys and from ICESat-2 data. At site S6, we assume that $H = 0.6 \pm 0.1$ m and $\lambda = 0.045 \pm 0.015$, based on photographs taken during the end of the ablation season. At the highest site S10, we assume that $H = 0.3 \pm 0.2$ m and $\lambda = 0.02 \pm 0.01$, which are typical values for sastrugi (Andreas, 1995).

Other attempts have been made to relate z_{0m} to the geometry of multiple surface roughness elements. For instance L69 (Lettau, 1969) empirically relate z_{0m} to the average

frontal area index of the roughness obstacles, which has been adapted by Munro (1989) for the surface of a glacier:

$$z_{0m,L69} = 2C_d H \frac{A_f}{A_l} = 2C_d H \lambda.$$

(4.23)

Note that Eq. (4.12) was adapted in order to be consistent with the definition of C_d in Eq. (4.11). In fact, M98 (Macdonald et al., 1998) have shown that Eq. (4.23) can be obtained by assuming that there is only form drag, and by setting $d = 0$, $\widehat{\Psi_m(z)} = 0$ and $C_d = 0.25$. By including the displacement height d, M98 is able to reproduce the non-linear feature of the $\frac{z_{0m}}{H} = f(\lambda)$ curve:

$$z_{0m,M98} = (H - d)\exp\left(-\left[\frac{C_d}{\kappa^2}\lambda\left(1 - \frac{d}{H}\right)\right]^{-0.5}\right).$$

(4.24)

Appendix 2: Sensitivity experiments

Cutoff wavelength Λ

We find that the optimal value of the cutoff wavelength for the high-pass filter is $\Lambda = 35$ m. This may be explained by the fact that the resulting filtered topography using $\Lambda = 35$ m still contains most ($\approx 80\%$) of the total variance of the slope spectrum. The latter is defined as the power spectral density of the first derivative of the elevation profile. A sensitivity experiment using different values for Λ at S5 can be found in Fig. 4.12. Changing the value for Λ strongly impacts the estimated H (Fig. 4.12c), as the elevation profiles considered here contain information at all wavelengths (Fig. 4.12a). On the other hand, increasing the value for Λ above 35 m does not significantly affect the estimate frontal area index λ (Fig. 4.12b). Overall, increasing Λ from 10 m to 50 m increases the modelled z_{0m} from 7.6×10^{-4} m to 2.8×10^{-2} m at S5, in the direction 184° that matches the ICESat-2 track (Fig. 4.12d).

ATL03 kriging parameters

In order to interpolate the geolocated photons product ATL03 in a regular 1-m resolution elevation profile, a fixed set of interpolation parameters was used, referred to as the default set. These are the median filter coefficients in Eq. (4.7) $q_{low} = 1$ and $q_{high} = 2$, the median filter window length of 50 m, the choice of a gaussian covariance function with a radius of 15 m in the kriging equations, and the maximum distance of photon distance to each regular grid point of 15 m.

This default parameter set was found to give robust results, even when only medium or low confidence photons are present in the ATL03 data. A sensitivity experiment by varying each parameter separately in a 200-m portion of areas A and B is given in Fig. 4.13. While the interpolated ATL03 elevation still misses small-scale features present in the UAV data, varying each parameter does not give improved results (Fig 4.13).
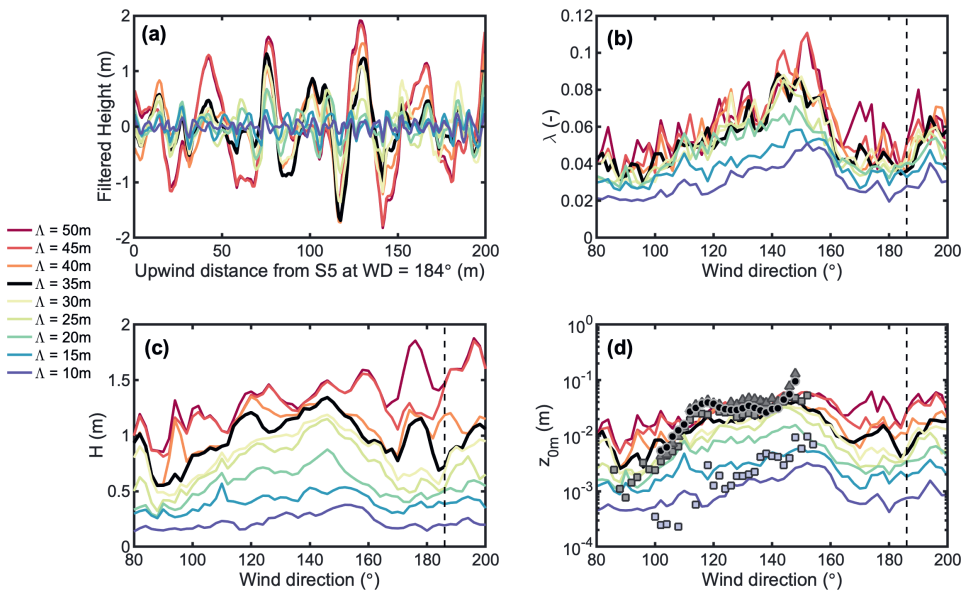
Figure 4.12: (a) Filtered elevation profile in direction 186°, (b) estimated obstacle frontal area index, (c) estimated obstacle height and (d) modelled aerodynamic roughness length at site S5 for different high-pass cutoff wavelengths Λ. See Figure 4.8 in main text for the labels in panel d).
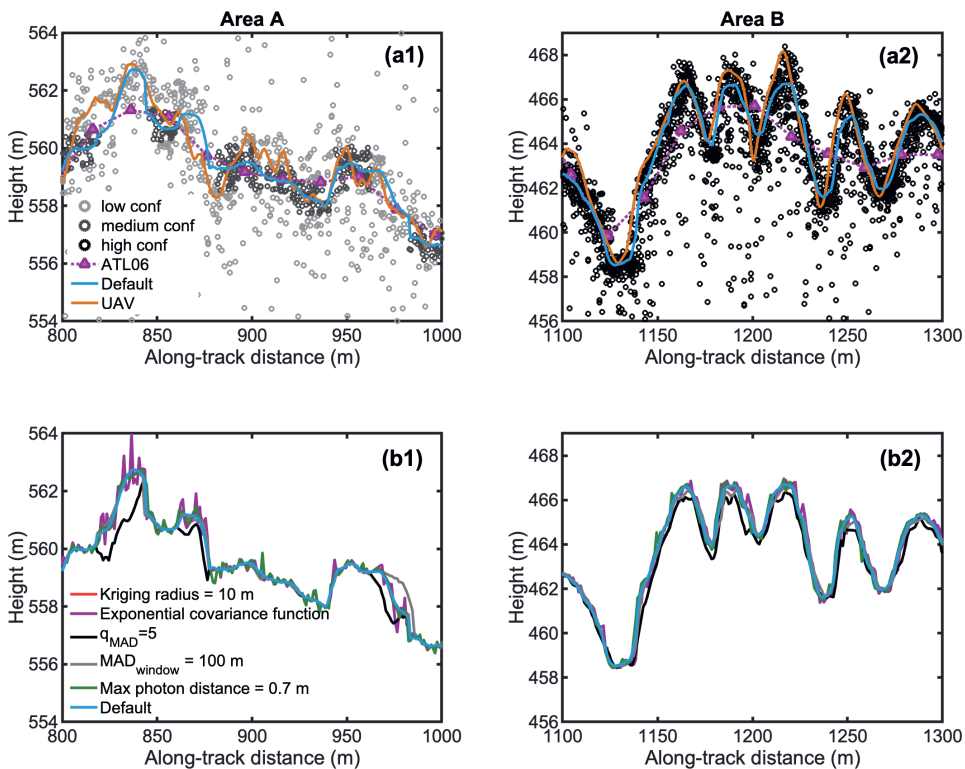
Figure 4.13: Elevation profiles in a 200-m portion of area A (left) and area B (right). The top panels contain the ATL03 data sorted in confidence levels (dots), the ATL06 data (pink triangles), the profiles measured by UAV photogrammetry (orange line) and the 1-m interpolated ATL03 data using the default settings used in the main text (blue line). The bottom panels contain the 1-m interpolated AT03 data using different origins and photon filtering settings.

25 April 2019

29 August 2019

Chapter 5

Observed and parameterised roughness lengths for momentum and heat over rough ice surfaces

Summary

Turbulent heat fluxes, i.e the sensible heat flux and latent heat flux, are important sources/sinks of energy for surface melt over glaciers and ice sheets. Therefore, credible simulations of e.g. future Greenland Ice Sheet mass loss need an accurate description of these fluxes. However, the parameterisation of surface turbulent heat fluxes in climate models requires knowledge about the surface roughness lengths for momentum, heat and moisture, which are currently either unknown or tuned to indirect observations. In this study we take advantage of a large dataset of eddy covariance observations acquired during multiple years and at multiple sites over the Greenland Ice Sheet. These in-situ observations are used to develop an improved parameterisation for the roughness length for momentum, and update the parameterisation for the roughness lengths for heat and moisture over rough ice surfaces. The newly derived parameterisations are implemented in a surface energy balance model that is used to compute surface melt. Sensitivity experiments confirm the high sensitivity of surface melt to the chosen roughness length models. The new parameterisation models the sensible heat flux to within 10 W m^{-2}, and the cumulative ice ablation within 10% at three out of four sites. Two case studies demonstrate the important contribution of the turbulent heat fluxes to surface ablation. The presented roughness parameterisations can be implemented in climate models to improve the physical representation of surface roughness over rough snow and ice surfaces, which is expected to improve the modelled turbulent heat fluxes and thus surface melt.

5.1 Introduction

The Greenland Ice Sheet (hereafter, the ice sheet) is a major contributor to contemporary sea level-rise (Shepherd et al., 2020), and is expected to contribute further during the next century (Goelzer et al., 2020). The recent increase in the ice sheet's mass loss is for an important part caused by a decrease in surface mass balance (SMB), which is explained by an increase in surface melt and subsequent runoff (Van den Broeke et al., 2016; Hanna et al., 2021; Mankoff et al., 2021). Surface melt is known to be correlated to the large-scale atmospheric circulation (Huai et al., 2020; Mattingly et al., 2020). Yet, state-of-the-art regional climate models (RCMs) still show considerable differences in modelled melt in the ablation area (Fettweis et al., 2020), the area where the surface mass balance is negative and bare ice is at the surface during the melting season. In the ablation area, both the interdiurnal and interannual variability in surface melt are strongly influenced by the turbulent exchange of sensible and latent heat at the surface, i.e. the sensible heat flux (SHF) and latent heat flux (LHF) (Van den Broeke et al., 2011; Wang et al., 2021).

Short-lived heat waves can cause anomalous surface melt through turbulent heat fluxes (Fausto et al., 2016a). Such an extreme melt event is illustrated in Figure 5.1a showing modelled SHF from the regional climate model RACMO2.3p2 on 28 July 2021 (Noël et al., 2019). On this day, daily averaged SHF peaked with values up to 150 W m^{-2} over many parts of the ablation area, including the K-transect, a transect of mass balance observations and weather stations located on the western margin of the ice sheet. On this day, the near-surface air temperature was above the melting point hence the SHF was directed towards the surface and contributed to surface melt. A different situation (Figure 5.1b) occurred on 11 September 2020. At this time, large scale conditions led to a daily averaged SHF reaching 100 W m^{-2} over the Q-transect, which is a similar transect of surface observations located on the southern part of the ice sheet. However, sub-zero near-surface air temperatures that are typical for this time of year mean that the SHF heated the surface, but did not contribute to melt, which was zero. Consequently, accurate simulations of future Greenland Ice Sheet mass loss require an accurate representation of the turbulent heat fluxes, during a variety of large scale atmospheric conditions. Both these case studies will be investigated in more detail using in-situ observations in Section 5.4.2.

The focus of this study is on contemporary Greenland Ice Sheet SHF, how it is observed in-situ and calculated in surface energy balance (SEB) and RCM applications. In atmospheric models, the surface turbulent heat fluxes are virtually always parameterised using a bulk turbulence model that relies on knowledge of the roughness lengths for heat, moisture and momentum (Moene and van Dam, 2014). These roughness lengths determine the vertical transport of heat, moisture and momentum at the surface through turbulent diffusion, and as such influence the calculation of melt energy over the ice sheet (Braithwaite, 1995; Herzfeld et al., 2006). The roughness lengths are not well known over the ice sheet, therefore constant values for the roughness length for momentum (z_{0m}) are used in most models. While it is known that z_{0m} for ice and snow can vary over two orders of magnitude in both time and space due to changing surface conditions (Brock et al., 2006; Smeets and Van den Broeke, 2008a; Smith et al., 2016;
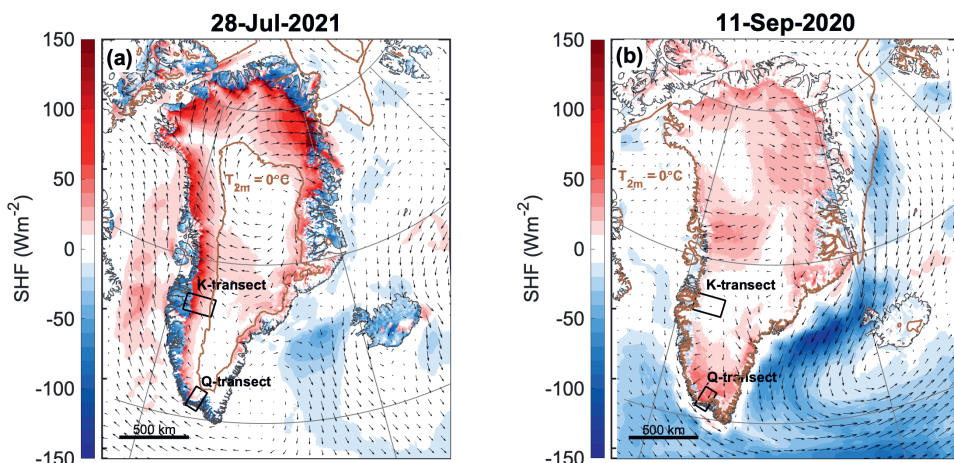
Figure 5.1: Daily averaged modelled SHF on 28 July 2021 (a) and on 11 September 2020 (b) using the regional climate model RACMO2.3p2, with the 10-m wind vectors and 0°C isotherm of 2m air temperature. The locations of the K-transect and of the Q-transect are shown. Site QAS_L is on the Q-transect, and sites S5, KAN_L/SHR and S6 are on the K-transect. Both case studies are investigated further in Section 5.4.1.

Fitzpatrick et al., 2019; Van Tiggelen et al., 2021), a practical parameterisation of z_{0m} over the ice sheet is still lacking. The roughness length for heat (z_{0h}) is commonly set as a constant fraction of z_{0m}. In reality, the fraction z_{0h}/z_{0m} for ice/snow is expected to decrease with increasing roughness Reynolds number, i.e with the turbulent intensity of the flow (Andreas, 1986; Smeets and Van den Broeke, 2008b; Guo et al., 2011; Sicart et al., 2014; Elvidge et al., 2021). The common reason for these simplifications is that direct observations of z_{0m}, z_{0h} and SHF, and therefore the verification of such relationships, are scarce over the ice sheet.

In this study we present a unique dataset of eddy-covariance measurements collected in the ablation area of the Greenland Ice Sheet at four different locations during different time periods. We combine these new measurements with previously published eddy covariance measurements taken over rough melting ice, in order to develop improved parameterisations for both z_{0m} and z_{0h}. In Section 5.2 we describe the observations and the SEB model used in this study. In Section 5.3, we further develop the work of Smeets and Van den Broeke (2008a,b); Van Tiggelen et al. (2021), where we present a new simple parameterisation for the variation in height of ice hummocks, and an updated parameterisation for z_{0h}. In Section 5.4.1 we perform sensitivity tests with the SEB model over a 5 year period (2016-2021), and present the first evaluation of modelled SHF over several rough, melting ice sites on the ice sheet using direct eddy covariance observations. Finally we compare the new SEB model output to a data set of observations, including melt, during two cases studies in Section 5.4.2.

5.2 Methods

5.2.1 Theory

When a snow or ice surface is at the melting point, the energy available for melt (M) is determined by the surface energy balance:

$$M = R_{net} + SHF + LHF + G, \tag{5.1}$$

with R_{net} the net absorbed radiation by the surface, SHF the turbulent sensible heat flux, LHF the turbulent latent heat flux and G the subsurface conductive heat flux, all expressed positive when directed towards the surface in W m^{-2}. The SHF and LHF are defined as the net turbulent transfer of sensible and latent heat from the atmosphere to the surface:

$$SHF = -\rho_a C_p \overline{w'T'},$$
$$LHF = -\rho_a L_{e,s} \overline{w'q'}, \tag{5.2}$$

with ρ_a the air density, $C_p = 1004$ J kg^{-1} K^{-1} the dry air specific heat capacity, $L_{m,s}$ the latent heat for either evaporation (L_e) or sublimation (L_s), w' the turbulent fluctuations of vertical air velocity, T' the turbulent fluctuations of air temperature and q' the turbulent fluctuations of specific humidity. The overbar denotes time averaging. When the sampling rate of the observations is not high enough to capture all near-surface turbulence, or when near-surface turbulence is not explicitly captured in a model (e.g. in RCMs), the surface turbulent heat fluxes are commonly approximated using the time averaged vertical gradients by invoking Monin-Obukhov similarity theory:

$$\overline{w'T'} = -\left(\frac{\kappa u(z)}{\ln(\frac{z}{z_{0m}}) - \Psi_m(\frac{z}{L}) + \Psi_m(\frac{z_{0m}}{L})} \right) \left(\frac{\kappa(T(z) - T_s)}{\ln(\frac{z}{z_{0h}}) - \Psi_h(\frac{z}{L}) + \Psi_h(\frac{z_{0h}}{L})} \right),$$

$$\overline{w'q'} = -\left(\frac{\kappa u(z)}{\ln(\frac{z}{z_{0m}}) - \Psi_m(\frac{z}{L}) + \Psi_m(\frac{z_{0m}}{L})} \right) \left(\frac{\kappa(q(z) - q_s)}{\ln(\frac{z}{z_{0q}}) - \Psi_q(\frac{z}{L}) + \Psi_q(\frac{z_{0q}}{L})} \right), \tag{5.3}$$

in which $u(z)$, $T(z)$ and $q(z)$ are the time averaged horizontal wind speed, air temperature and specific humidity at a height z above the surface, respectively, T_s is the surface temperature and q_s is the surface specific humidity which is assumed at saturation. Ψ_m, Ψ_h and Ψ_q are the vertically integrated stability functions for momentum, heat and moisture, that we take from Holtslag and De Bruin (1988), L is the Obukhov length and $\kappa = 0.4$ the Von Kármán constant. z_{0m}, z_{0h} and z_{0q} are the roughness lengths for momentum, heat and moisture, which are defined as the heights above the surface where the logarithmic vertical profile of wind speed, temperature and specific humidity extrapolate to their surface values, respectively. The two terms $\Psi(\frac{z_0}{L})$ are small compared to $\Psi(\frac{z}{L})$ so we set them to 0. We assume that $\Psi_q = \Psi_h$ and that $z_{0q} = z_{0h}$. The validity of Monin-Obukov similarity over rough, melting ice has been challenged over mountain glaciers by the eddy covariance observations of e.g. Conway and Cullen (2013) and Radić et al. (2017). However, no direct evaluation of SHF has so far been performed over the margin of the ice sheet. In this study we assume that Monin-Obukhov similarity is valid, which allows us to estimate the roughness lengths using the measured

fluxes and vertical gradients according to:

$$z_{0h} \simeq \frac{z}{\exp\left(\kappa \frac{T(z)-Ts}{T_*} + \Psi_h\left(\frac{z}{L}\right)\right)} \qquad (5.4)$$

$$z_{0m} \simeq \frac{z}{\exp\left(\kappa \frac{u(z)}{u_*} + \Psi_m\left(\frac{z}{L}\right)\right)} \qquad (5.5)$$

where $u_* = (\overline{u'w'}^2 + \overline{v'w'}^2)^{1/4}$ is the friction velocity and $T_* = -\overline{w'T'}/u_*$ is the turbulent temperature scale, with u' and v' the turbulent fluctuations of the two components of horizontal wind speed.

5.2.2 Observations

Automatic weather stations (2016 - 2021)

Near-surface meteorological and turbulence observations were performed at four sites (Figures 5.1 and 5.2). QAS_L is the lowest site of the Q-transect on the southern Greenland Ice Sheet (Hermann et al., 2018), while S5, SHR/KAN_L, and S6 are located in the lower ablation area along the K-transect on the western Greenland Ice Sheet (Smeets et al., 2018). At each site, an automatic weather station (AWS) continuously records 30 min averages of wind speed, wind direction, the four broadband radiation components, air temperature, air relative humidity, air pressure and surface height change during the study period (September 2016 - August 2021). Additional details concerning the AWS data and underlying corrections are given by Smeets et al. (2018) for sites S5 and S6, which are part of the IMAU AWS network, and by Fausto et al. (2021) for sites KAN_L and QAS_L, which are part of the PROMICE AWS network. The data include the corrections for incoming direct shortwave radiation for station tilt, the heating of the unventilated air temperature, humidity and longwave radiation sensors, but also the correction of the longwave radiation sensors for the internal sensor temperature and the calibration of the relative humidity sensors with respect to the ice saturation humidity. Different instruments were used to measure the daily ice ablation in addition to the yearly stake measurements: an ablation draw-wire (ADW), a pressure transducer assembly (PTA) or a sonic height ranger mounted on fixed stakes (SR). Details of the ice ablation instruments at each station are given in the Appendix, together with the exact location of each site.

At sites S5 and SHR/KAN_L, the sensor's height above the surface relevant for turbulent flux calculations is not well defined due to the presence of ice hummocks (Figures 5.2b,c). The AWS are typically located on top of an ice hummock, therefore we convert the height of the instruments above the local surface to the true height relevant for the turbulent flux calculations (z in Equation 5.3) according to Van Tiggelen et al. (2020):

$$z = z_m + H - d, \qquad (5.6)$$

with z_m the height of the sensors above the local surface, H the a-priori assumed average height of the hummocks above the surrounding topography and d the displacement height, which is the reference height above the surface relevant for the flux calculations
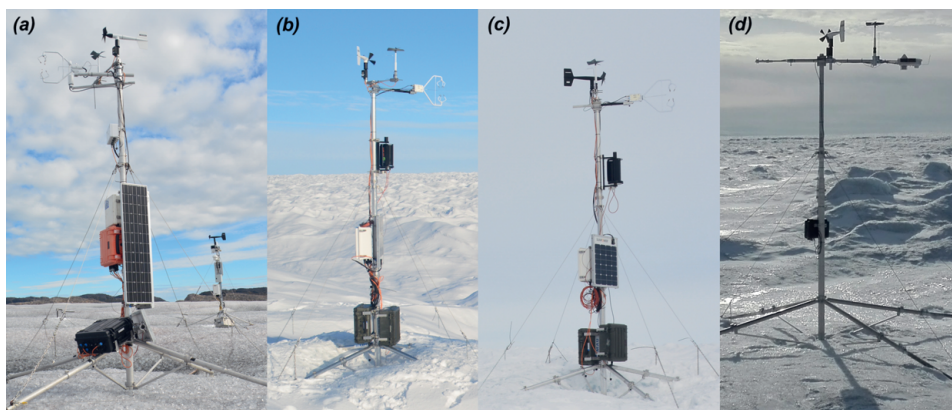
Figure 5.2: Eddy-covariance stations at (a) QAS_L (b) S5 (c) SHR and (d) S6. In (a), (b) and (c), both a SEC and VPEC system were operated. In (d) only a VPEC system was installed.

(Jackson, 1981). Both H and d have a seasonal variability over the ice sheet due to changing surface conditions, but we assume that this seasonal variability in surface conditions only has an influence on the turbulent flux calculations through changes in z_{0m}, as will be shown in Section 5.3.1. For S5 and SHR/KAN_L we assume $H = 1$ m and $d = 0.3$ m to process the AWS and eddy covariance measurements.

Eddy covariance stations

At QAS_L, S5 and SHR, sonic eddy covariance (SEC) systems were installed in September 2019 on a separate mast with a CSAT3 instrument (Campbell Scientific) at 3.9 m height at QAS_L and a CSAT3B instrument (Campbell Scientific) at 3.5 m above the local surface at S5 and SHR (Figure 5.2). The instruments were installed such that the transducer heads point towards the prevailing katabatic wind direction, in order to mitigate for the flow distortion by the instruments as much as possible. The SEC system samples all three wind speed components and air temperature at a rate of 10 Hz, and records the 30-min averages and covariances including $\overline{w'T'}$, $\overline{u'w'}$ and $\overline{v'w'}$. At the same height, air temperature is sampled at 10 Hz with a fine-wire thermocouple (FW3, Campbell scientific). All three masts were also equipped with a vertical propeller eddy covariance (VPEC) system which records the same variables at a rate of 5 Hz (Van Tiggelen et al., 2020). An additional VPEC system was also installed on the AWS mast since September 2016 at sites S5 and S6 that samples at a rate of 0.25 Hz. In addition, we use 2012 SEC data from site S10 (K-transect) from Lenaerts et al. (2014), and 2004 SEC data from S6 and 1996 SEC data from the Vatnajökull icecap (Iceland, Smeets and Van den Broeke (2008a)). These data are complemented with previously unpublished CSAT3 data from site S5 collected during 2006 and 2008. At QAS_L, the SEC system was complemented with an open path gas analyser (LI-7500, LI-COR) in September 2020 that samples the H_2O concentration at 10 Hz. Some SEC systems were not sampling continuously in order to save power. In total, we use 12 different SEC datasets and 2 different VPEC datasets recorded at 7 different locations between

1996 and 2021. An overview of all the available eddy covariance data is given in the Appendix.

The 30-min averages and covariances are rotated in the average flow direction and tilt corrected using a pitch and a yaw rotation. In addition, we remove the influence of humidity on the SHF as measured with a sonic anemometer using the method from Schotanus et al. (1983) with AWS data. We correct for lateral sensor separation and sampling time-lags using the method described in Moore (1986). The 1996 eddy covariance data from Iceland are also corrected for cross-wind using the method described by Schotanus et al. (1983), since an older type of sonic anemometer was used. Finally, for the VPEC data we apply the sensor response time corrections as described by Van Tiggelen et al. (2020). For the CSAT3 data, we apply a transducer shadowing correction on the 30-min averaged data based on Fig 6. in Horst et al. (2015). For the LI-7500 data we correct for air density fluctuations in the measurement volume using the correction from Webb et al. (1980).

The following data selection criteria are applied to the 30-min averaged eddy covariance data. First, we minimise the uncertainty in the stability corrections by selecting near-neutral runs ($0 < z/L < 0.2$) and we remove data with a low signal-to-noise ratio using the criteria $u_* > 0.1$ m s^{-1}, $u > 3$ m s^{-1} and $|SHF| > 20$ W m^{-2}. We remove non-stationary runs by requiring $\partial T/\partial t < 0.6$ K hr^{-1} and $\partial u/\partial t < 2$ m s^{-1} hr^{-1}. We mitigate for possible flow distortion by requiring that $|\overline{v'w'}/\overline{u'w'}| < 0.5$ and $1.1 < \sqrt{\overline{w'^2}}/u_* < 1.5$, and by only selecting wind directions that lie within $\pm45°$ of the orientation of the transducer heads. We remove runs affected by noise by requiring that $u_* < 1.5$ m s^{-1}. The latter value was found to be an optimal threshold to remove runs affected by solid precipitation or blowing snow. For the VPEC data we remove the short gaps due to stalling or freezing of the vertical propeller by selecting runs that verify $\sqrt{\overline{w'^2}} > 0.5$ m s^{-1}. Finally, when computing z_{0h} for all sites except for S10, we remove the uncertainty in determining T_s by only selecting data taken above a melting surface, i.e $T(z) > 275.15$ K, and set the surface temperature to $T_s = 273.15$ K. For the highest site S10 we require $T(z) > 260$ K and compute T_s from the outgoing longwave radiation, otherwise too few data would remain. The amount of data after applying these criteria is significantly reduced (Appendix), but minimises the instrumental uncertainties.

5.2.3 SEB model

The SEB model used in this study is a further developed version of the model used by Reijmer et al. (1999), Kuipers Munneke et al. (2018b), Jakobs et al. (2019) and Huai et al. (2020). The model calculates snow melt and ice ablation by closing the SEB (Equation 5.1). We force the model with 30-min average AWS observations, from 15 September 2016 until 9 August 2021. To compute the turbulent heat fluxes, Monin-Obukhov similarity is assumed (Equation 5.3). The latter requires a value for the roughness lengths z_{0m} and z_{0h}, which are either set as constants or parameterised using the new equations derived in the following section. A 24 hour moving average albedo is used to compute downward shortwave radiation based on the measured upward shortwave radiation (Van den Broeke et al., 2004). Downward longwave radiation is prescribed from observations,

while upward longwave radiation is computed using the calculated surface temperature and assuming emissivity = 1. The latter was chosen to match the measured upward longwave radiation over a melting surface. The surface temperature (T_s) is computed by iteration, then the excess energy is defined as M, and is used for melting either snow or ice.

The SEB model includes a subsurface routine to calculate the conductive heat flux G. The model computes diffusive heat transfer up to a depth of 25 m, with a variable amount of layers of 0.01 m thickness near the surface increasing to 2 m at the bottom. At the bottom we assume that the temperature is unaffected by the air temperature fluctuations in these 5 year simulations, thus we set a zero heat flux. The subsurface temperature is initialised on 15 September 2016 across the whole column with the measured, multi-year average air temperature at each site. Subsurface penetration of shortwave radiation in the ice/snow layers is not taken into account. The latter is known to cause significant internal melt at these locations (Van den Broeke et al., 2008), yet we assume that the total melt energy always interacts at the top layer. The snow has a fixed density of 400 kg m^{-3}, and the snow depth measured by a sonic height ranger is prescribed in the model, and assumed to be zero as soon as ice ablation is recorded by the AWS, in order to accurately represent the start of the ice ablation season.

5.3 Parameterisation of roughness lengths

5.3.1 Roughness length for momentum z_{0m}

Figure 5.3 shows the daily averaged z_{0m} at sites S5 and S6 between 2016 and 2021. These values are calculated from VPEC observations using Equation 5.5, and selecting only data within $20°$ of the prevailing katabatic wind direction. Outside these wind directions, the time-averaged z_{0m} can vary by one order of magnitude (Van Tiggelen et al., 2020). At S5, the z_{0m} values range between $\approx 6 \times 10^{-3}$ m before the start of the ablation season to $\approx 2 \times 10^{-2}$ m at the end of the ablation season, which is consistent with previous studies at this location (Smeets and Van den Broeke, 2008a; Van Tiggelen et al., 2021). At the higher location S6, the same strong seasonal cycle is present but z_{0m} values are lower and do not exceed $\approx 5 \times 10^{-3}$ m.

Based on previous drag modelling work (Raupach, 1992; Van Tiggelen et al., 2021), z_{0m} is known to directly depend on both the average height of the roughness obstacles after high-pass filtering of the topography (H_{mod}), and on the obstacle frontal area index (λ). If we consider the obstacles along a fixed wind fetch direction, and we assume that all the obstacles have the same height, then $\lambda = f H_{mod}/100$, with f the number of obstacles per 100 m profile length, and H_{mod} the modelled height of the ice obstacles. As an approximation, we take $f = 8$ obstacles per 100 m, based on UAV surveys over this rough ice area (Van Tiggelen et al., 2021). We then model the total obstacle height as :

$$H_{mod} = H_{ice} - H_{snow},\tag{5.7}$$

where H_{ice} is the height of the ice obstacles and H_{snow} is the snow depth, either taken from AWS observations or from RCM output. Note that although they represent the same physical quantity, $H \neq H_{mod}$ since the seasonal cycle in obstacle height is not
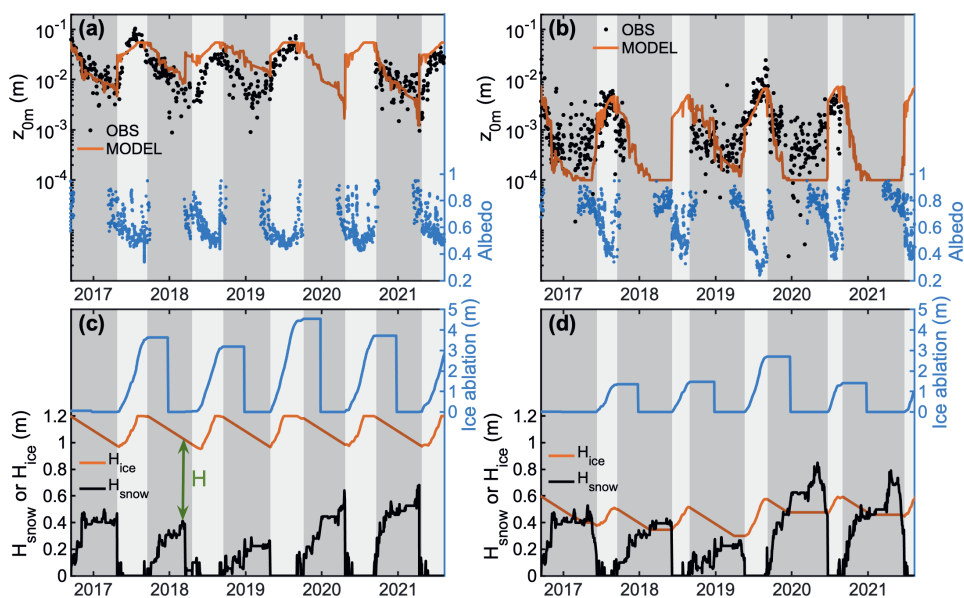
Figure 5.3: Top panels: S5 (a) and S6 (b): daily averaged z_{0m} estimated from observations in a fixed wind direction interval (black dots), modelled z_{0m} using the new parameterisation from this study (orange line), and measured daily averaged albedo (blue dots). Bottom panels: S5 (c) and S6 (d): measured daily snow depth (black line), seasonal ice ablation (blue line) and modelled ice roughness height H_{ice} (orange line). The shaded areas denote time periods when no ice ablation is recorded by the draw wire. The green arrow in (c) denotes the modelled height of the obstacles (H).

known a priori. Varying H at site S5 between 1 ± 1 m in Equation 5.6 translates in at most a factor 2 difference in estimated z_{0m} from observations, or one order of magnitude less than the observed seasonal cycle in z_{0m} (Figure 5.3). Snowfall is assumed to fill in the depressions of the topography, which effectively reduces the apparent height of the obstacles seen by the wind. The latter is confirmed when visiting the stations during the accumulation season. H_{ice} is bounded according to $H_{max}/2 < H_{ice} < H_{max}$ where H_{max} is the prescribed maximum height of the obstacles observed at the end of the ablation season, for a particular wind direction. H_{ice} increases during the ablation season due to differential melting and decreases during the accumulation season due to differential sublimation, only when the ice obstacles are not completely buried by snow, i.e:

$$\Delta H_{ice} = \begin{cases} \Delta H_{melt} + \Delta H_{subl} & \text{if } H_{snow} < H_{ice}, \\ 0 & \text{otherwise.} \end{cases} \tag{5.8}$$

where ΔH_{ice} is used to compute the new ice obstacle height in the next time-step according to:

$$H_{ice,i+1} = H_{ice,i} + \Delta H_{ice}, \tag{5.9}$$

where i is the current time-step iteration. We model the increase in ice obstacle height during each time-step as:

$$\Delta H_{melt} = K_m M_{melt}, \tag{5.10}$$

where M_{melt} is the accumulated ice melt during the same time step in meters, either taken from observations or from model output. The constant was set to $K_m = 0.1$ in order to match the z_{0m} observations during the ablation season. A more precise calibration of K_m would require several repeated surveys of the ice obstacles at a single location using e.g. photogrammetry, as in Van Tiggelen et al. (2021). We assume a fixed decrease in ice obstacle height due to sublimation only when there is no melt:

$$\Delta H_{subl} = \begin{cases} K_s \ (\text{mm day}^{-1}) & \text{if } M_{melt} = 0, \\ 0 \ (\text{mm day}^{-1}) & \text{otherwise.} \end{cases} \tag{5.11}$$

The quantity K_s is fixed to $K_s = 2$ mm day^{-1}, based on short-term height ranger measurements and time-lapse imagery taken during the accumulation season over bare ice at site S5.

The roughness length for momentum (z_{0m}) is then computed using the simplified drag partitioning model from Raupach (1994):

$$z_{0m} = (H - d) \exp(-\kappa \gamma) \exp(\widehat{\Psi_H}), \tag{5.12}$$

with $\widehat{\Psi_H} = 0.193$ the wind profile correction within the roughness sublayer and,

$$\gamma = (C_s + C_d \lambda)^{-0.5}, \tag{5.13}$$

in which the form drag coefficient (C_d) is adapted from Garbrecht et al. (2002) (see also Van Tiggelen et al. (2021)) according to:

$$C_d = \begin{cases} 0.5(0.185 + 0.147H) & \text{if } H \leq 2.5 \text{ m} \\ 0.5\left(0.22\log(\dfrac{H}{0.2})\right) & \text{if } H > 2.5 \text{ m.} \end{cases} \tag{5.14}$$

The skin drag coefficient is modelled as:

$$C_s = \left[C_{s,10}^{-0.5} - \frac{1}{\kappa} \left(\ln\left(\frac{10 - d}{H - d} \right) - \widehat{\Psi}_H \right) \right]^{-2}, \tag{5.15}$$

with $C_{s,10} = 1.2071 \times 10^{-3}$ after Van Tiggelen et al. (2021). The displacement height (d) is calculated as:

$$d = H \left(1 - \frac{(1 - \exp(-(c_1 \lambda)^{0.5}))}{(c_1 \lambda)^{0.5}} \right), \tag{5.16}$$

with $c_1 = 7.5$.

It must be noted at this point that the model from Raupach (1994) (Equation 5.12) is only valid for moderate frontal area densities ($\lambda \leq 0.1$), which corresponds to roughness obstacles not higher than 1.25 m when assuming f = 8 obstacles per 100 m. For larger obstacles, over-sheltering might become important, which may require more sophisticated models (Shao and Yang, 2008). Furthermore, this model yields an unrealistic value of $z_{0m} = 0$ m when $H = 0$ m. This is overcome by setting a lower limit to H of 0.01 m, which then yields $z_{0m} \approx 10^{-4}$ m.

In summary, the height of the roughness obstacles (H) is determined using ice ablation and snow depth, and by prescribing a constant value for H_{max} for each location. Then the corresponding z_{0m} values are computed using the steps above. The model results at S5 and S6 are shown in Figure 5.3, where the only varying parameter across sites is H_{max}. At S5 we set $H_{max} = 1.2$ m and at S6 we set $H_{max} = 0.6$ m, based on photographic evidence. The resulting modelled z_{0m} at S5 and S6 during 2016-2021 is shown in Figure 5.3. The model is able to accurately simulate the yearly z_{0m} cycle at both stations, although differences persist. Interestingly, the logarithmic increase of z_{0m} during summer due to obstacle height increase is coincident with the decrease in albedo due to surface impurities, which is consistent with remote sensing observations (Nolin and Payne, 2007). As such, during a high melt year such as 2019, albedo is lower than usual while z_{0m} is larger than usual, since differential melting is greater. Furthermore, winter z_{0m} value are underestimated at S6 when all the ice obstacles are buried by snow. In contrast, z_{0m} values are overestimated during winter in 2018 and 2019 at S5. This means that additional processes must be considered for a snow surface, such as the development of sastrugi as parameterised by Agosta et al. (2019), or the influence of blowing snow. For a melting snow surface, the development of ablation hollows may also be an important process for z_{0m} (Brock et al., 2006). Nevertheless, the newly developed model better reproduces the seasonal z_{0m} evolution than, e.g, using a constant value for snow and ice (Brock et al., 2006).

5.3.2   Roughness length for heat z_{0h}

The ratio of roughness length for heat (z_{0h}) over z_{0m} for all 12 datasets of SEC observations is shown in Figure 5.4 as function of the roughness Reynolds number $Re_* = u_* z_{0m}/\nu$, where $\nu = \mu/\rho$ is the air kinematic viscosity, ρ the air density and μ the air dynamic viscosity. Both z_{0m} and z_{0h} are estimated from 30-min sonic eddy covariance observations using Equations 5.4 and 5.5, and the ratio z_{0h}/z_{0m} is bin-averaged per dataset and per month for different logarithmically-spaced Re_* classes.
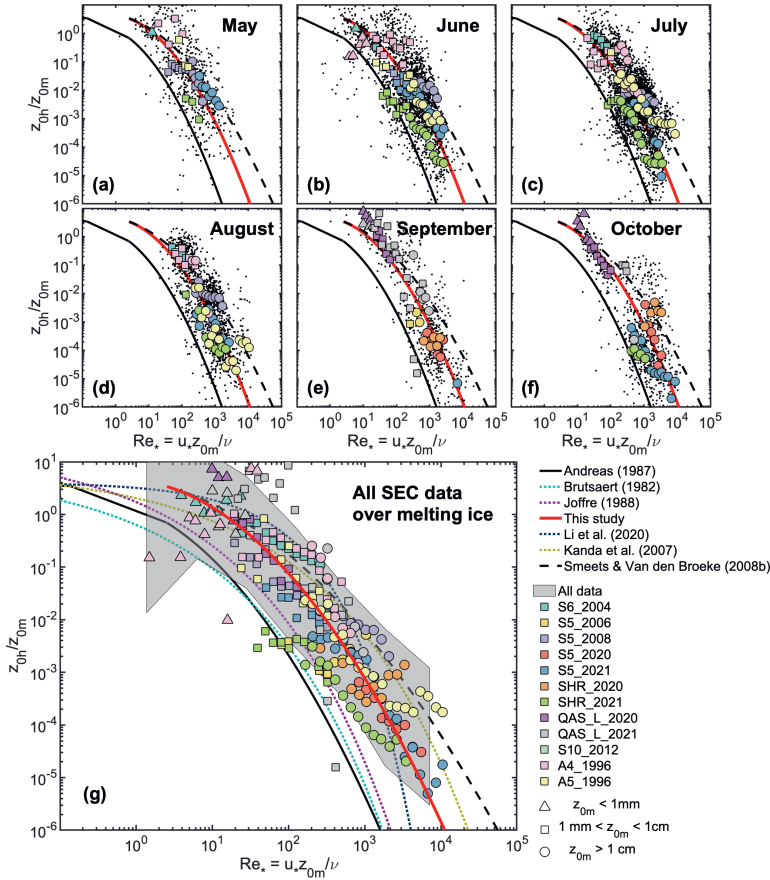
Figure 5.4: Observed z_{0h}/z_{0m} ratio as function of roughness Reynolds number $Re_* = u_* z_{0m}/\nu$ for 12 sonic eddy covariance datasets acquired over melting snow/ice. Top panels (a-f) separate the data in monthly intervals from May to October, while the bottom panel (g) contains all the data averaged in logarithmically spaced bins. The continuous and dashed lines denote the models from Andreas (1986); Brutsaert (1982); Joffre (1988); Kanda et al. (2007); Smeets and Van den Broeke (2008b); Li et al. (2020), and the updated parameterisation (Equation 5.17). Symbols denote the bin-averaged z_{0m} per dataset, and the shaded area in (g) denotes two times the standard deviation of all the data per Re_* bin. The black dots in (a-f) denote all the data used for bin-averaging.

No clear seasonal relationship is visible (Figure 5.4a-f), yet all the datasets confirm that the z_{0h}/z_{0m} ratio strongly decreases for increasing Re_* (Figure 5.4g). This is a consequence of form drag that increases turbulent momentum transfer at higher Re_* values, whereas turbulent heat transfer is controlled by the much less efficient process of molecular diffusion, which occurs in the very thin viscous layer in direct contact with the surface. However, not all the datasets imply the same z_{0h}/z_{0m} relation versus Re_*. At the smoother surface of sites S6, A4 and QAS_L, the observed z_{0h}/z_{0m} ratio generally agrees with the parameterisation of Smeets and Van den Broeke (2008b). At the rougher sites S5, A5 and SHR, the data lie between the model of Andreas (1986) and the parameterisation of Smeets and Van den Broeke (2008b). This means that the modelled sensible heat fluxes using the latter parameterisation will be larger than the observed fluxes, at least when using the same gradients and z_{0m}. The other models (Brutsaert, 1982; Joffre, 1988; Kanda et al., 2007; Li et al., 2020) also fail to reproduce the observed z_{0h}/z_{0m} for the whole range of Re_*.

When bin-averaging all the 12 datasets over all time periods, the following new relation best reproduces the observations, which is an adapted version of the model from Andreas (1986):

$$\ln\left(\frac{z_{0h}}{z_{0m}}\right) = b_0 + b_1 \ln(Re_*) + b_2 (\ln(Re_*))^2 \tag{5.17}$$

with $b_0 = 1.5$, $b_1 = -0.15$ and $b_2 = -0.16$. We propose to use this updated relation for rough snow/ice, i.e $z_{0m} > 10^{-3}$ m. For smooth snow/ice , i.e $z_{0m} \leq 10^{-3}$, the model from Andreas (1986) should be used, as there are insufficient measurements to verify the new relationship for smooth surfaces. Note that only for lower values of Re_*, the updated relationship resembles the relation from Smeets and Van den Broeke (2008b), which was developed using data from S6, A4 and A5 using a comparable data selection strategy.

As demonstrated by Andreas (2002), plots of z_{0h}/z_{0m} versus $Re_* = u_* z_{0m}/\nu$ from empirical data may suffer from self-correlation due to the shared variable z_{0m} in both axes. Using the equations in Andreas (2002) we computed the expected correlation between z_{0h}/z_{0m} and $Re_* = u_* z_{0m}/\nu$ for all the different datasets used in Figure 5.4 (Table 5.2). The largest expected correlation (-0.7183) is found in the S6_2004 data, which is a dataset obtained higher up in the ablation area where the surface is relatively smooth and temperature gradients are smaller, leading to a relatively smaller variability in z_{0m}, z_{0h} and SHF. However, the average self-correlation for all datasets is much lower (-0.3237) due to a large spread in z_{0h} values (Table 5.2). The large spread in z_{0h} values is caused by a larger temporal variability in measured turbulent heat fluxes (T_* in Equation 5.4), which is typical in the lower part of the ablation area of the ice sheet. Hence, using longer datasets from various locations where large SHF values are observed reduces the problem of artificial correlation (Andreas, 2002).

5.4 Results

5.4.1 Sensitivity tests

In order to test the improved parameterisations for both z_{0m} (Section 5.3.1, Equation 5.12) and for z_{0h} (Section 5.3.2, Equation 5.17), we run the SEB model for the four sites with two different settings for z_{0m}, and three different settings for z_{0h}, i.e. six permutations. For z_{0m}, we either use a constant value $z_{0m} = 1.3 \times 10^{-3}$ m for all sites, or use the parameterisation described in Section 5.3. The maximum height of ice roughness obstacles (H_{max}) is the only varying parameter across sites, and set to 0.5 m, 1.2 m, 1 m and 0.6 m for QAS_L, S5, KAN_L and S6, respectively. These values are based on photographs taken during the yearly station maintenance at the end of the ablation season. This value is site specific, and should be adapted to each area of interest. An alternative is to estimate H_{max} using ICESat-2 measurements, or using UAV photogrammetry (Van Tiggelen et al., 2021). For z_{0h}, we test the two different parameterisations from Andreas (1986) and Smeets and Van den Broeke (2008b), in addition to the adjusted parameterisation derived in Section 5.3.2 (Equation 5.17).

Impact on modelled SHF

Figure 5.5 compares daily averaged observed and modelled SHF using the parameterised z_{0m} value. Panels (a) and (b) show the comparison at sites S5 with VPEC data and at QAS_L with SEC data with the updated z_{0h} parameterisation as an example. Panel (c) shows the bias and root-mean-square error (RMS) for all the datasets and modelled z_{0m}. While the RMS is still considerable (20.5 W m^{-2} at S5 and 17.2 W m^{-2} a QAS_L), the bias is close to zero and smaller than when the models from Andreas (1986) and Smeets and Van den Broeke (2008b) are used (figure 5.5c). The RMS ranges between 7.8 and 25.3 W m^{-2}, compared to a mean SHF during melting days of 42 W m^{-2} at S6 to 89 W m^{-2} at S5. When using the model from Andreas (1986), SHF is underestimated by 10.6 W m^{-2} at SHR, and up to 28 W m^{-2} at S5. On average, the model from Smeets and Van den Broeke (2008b) overestimates the SHF by 4.3 W m^{-2} at S5, to 15.2 W m^{-2} at SHR. The revised z_{0h} model from Equation 5.17 yields improved SHF for all stations, with a mean bias of 3.2 W m^{-2}, -4.1 W m^{-2}, -6.7 W m^{-2} and 4.2 W m^{-2} for QAS_L, S5 (VPEC data), S5 (SEC data) and SHR, respectively. At site S6, all the models underestimate the SHF, with a bias between -12.2 W m^{-2} and -21.1 W m^{-2}.

Figure 5.5c also compares average modelled z_{0m} values to the values estimated from in situ observations. At all sites, modelled z_{0m} values are larger than the value (1.3×10^{-3} m) that is typically used over snow or ice, ranging from 7.4×10^{-3} m at S6 to 1.94×10^{-2} m at S5. This means that the modelled SHF using this fixed value for z_{0m} will be smaller than the modelled SHF using the newly parameterised z_{0m}, when using the same model for z_{0h}. Furthermore, the values are also higher than the observations for all sites except at S6. For instance at S5, the average z_{0m} value over the 268 days of selected VPEC data during melting conditions is 4.18×10^{-2} m, versus the observed averaged value of 1.94×10^{-2} m. An optimal set for model parameters (f,K_m,K_s,C_d,C_s,H_{max}) could be used to match the observed z_{0m} at a single site, but this would limit the applicability of the model to sites with eddy covariance observations. Interestingly, using a higher z_{0h} value also results in a larger modelled z_{0m}, since a larger SHF promotes ablation,
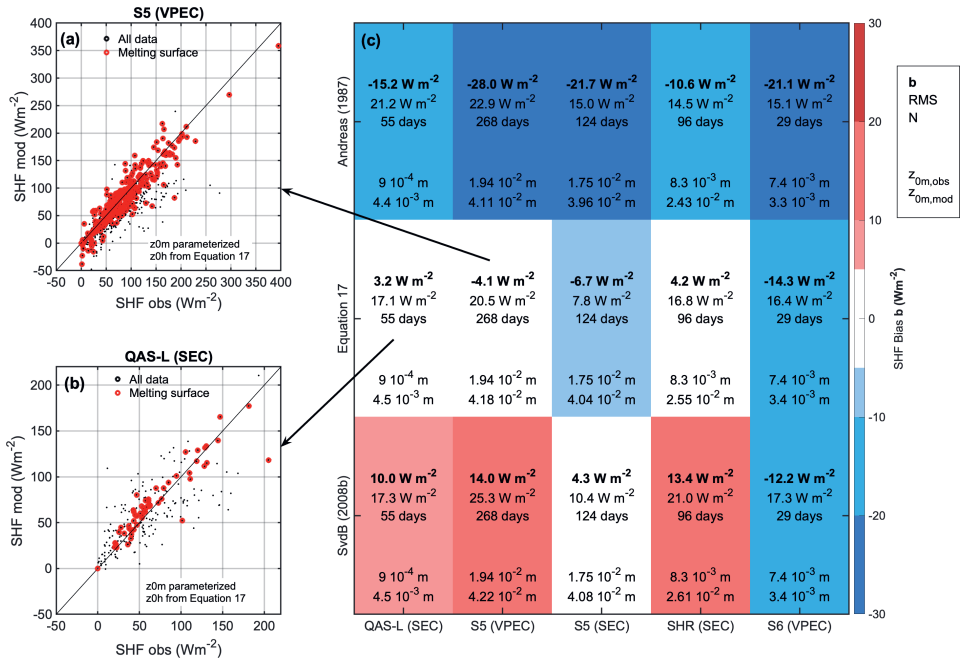
Figure 5.5: Modelled daily averaged sensible heat flux (SHF) versus sonic eddy covariance (SEC) and vertical propeller eddy covariance (VPEC) observations at four sites. Two different datasets are shown for site S5. Panels (a) and (b) compare the modelled SHF using a parameterised z_{0m} and z_{0h} from Equation 5.17 to the observed SHF from eddy covariance observations. Panel (c) contains in each cell from top to bottom: the bias (b), room-mean-square error (RMS), number of observations (N), observed z_{0m}, and modelled z_{0m}. The simulations use a parameterised z_{0m}, and use a parameterised z_{0h} from either Andreas (1986), Equation 5.17 or Smeets and Van den Broeke (2008b) (different rows). The color in (c) indicates the bias. All z_{0m} values are rounded to 10^{-4} m.

therefore a faster growth of roughness obstacles during the ablation season (Equation 5.10). Yet, this effect remains small compared to the difference with the observed values: i.e. a modelled z_{0m} value ranging from 4.11×10^{-2} m to 4.22×10^{-2} m at S5 (VPEC data) depending on the chosen model for z_{0h} (panel c).

Impact on modelled ice ablation

The total 2016-2021 cumulative ice ablation from the SEB model using six combinations for z_{0m} and z_{0h} for all four AWS sites (QAS_L, S5, KAN_L/SHR, S6) are compared to manual stake observations in Figure 5.6. We also compare the differences in modelled ablation to the uncertainty in the AWS forcing by perturbing the optimal model run (z_{0m} modelled, z_{0h} from equation 5.17, red line) with a broadband albedo change of ± 0.02. This uncertainty was quantified as follows. Besides suffering from tilt and window-heating, an unventilated net radiometer reading may contain a so called 'zero offset' bias in the shortwave components due to cooling of the instrument body by infrared radiation. For the pyranometer in the CNR4 instrument, the SW_{up} and SW_{down} biases are reported to be less than 15 W m^{-2} by the manufacturer, and linearly depend on the net infrared radiation (Behrens, 2021). The estimated albedo using AWS data is defined:

$$\alpha = \frac{SW_{up} + b}{SW_{down} + b},$$ (5.18)

with SW_{down} and SW_{up} the true downward and upward shortwave radiation, respectively, and b the bias. Using the maximal reported value for $b = 15$ W m^{-2}, and SW_{down} = 300 W m^{-2}, SW_{up} = 150 W m^{-2}, which are representative for bare ice during summer over the ice sheet, we find $\alpha = 0.524$. The latter is 0.024 higher than the true surface albedo SW_{up}/SW_{down} of 0.500. Therefore a bias of $\pm$ 0.020 in measured albedo was deemed realistic to quantify the propagating error in the SEB model due to radiometer errors.

Overall, the optimal run (red line) agrees best with the independent stake observations (within 10%), except at site S6 where ablation is overestimated (+ 20%). Since the contribution of turbulent heat fluxes to total ablation is smallest at S6 ($\approx$ 20%, Kuipers Munneke et al. (2018b)), using different z_{0m} and z_{0h} models does not explain this bias. Further, SHF and LHF partly compensate each other at this higher elevation near equilibrium line altitude, as demonstrated by Steffen (1995). At the lower sites, different z_{0m} and z_{0h} models considerably affect modelled ablation; e.g. up to 1.13 m ice per year at S5, or 29% of the yearly ablation. The modelled z_{0m} and the z_{0h} from Smeets and Van den Broeke (2008b) yields the largest ablation (green line), while a fixed $z_{0m} = 1.3 \times 10^{-3}$ m and the z_{0h} from Andreas (1986) yields the lowest ablation (brown line). The sensitivity of the modelled ablation to the chosen z_{0h} model is largest at S5, which is a low-lying site (520 m) with ice hummocks higher than 1 m, and where the contribution of SHF to melt energy is large. QAS_L is situated at an even lower elevation (280 m), yet the sensitivity to the choice of z_{0h} is less pronounced than at S5 since the average z_{0m} value is smaller. Also, differences between the modelled ablation using a fixed $z_{0m} = 1.3 \times 10^{-3}$ m are smaller; e.g. 0.28 m of ice per year at S5, or 7% of the yearly ablation; since all z_{0h} parameterisations are similar at lower roughness Reynolds numbers (Figure 5.4).
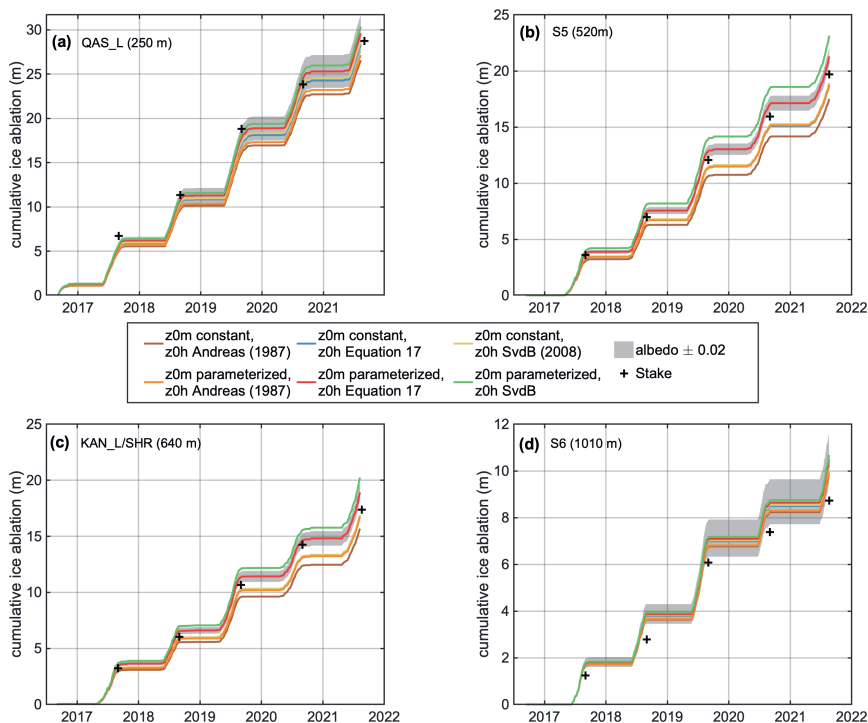
Figure 5.6: Modelled cumulative ice ablation at four sites on the Greenland Ice Sheet with the surface energy balance (SEB) model using 6 possible settings for z_{0m} and z_{0h}. The black squares denote the manual, yearly stake observations. The shaded area denotes the range of modelled ice ablation by perturbing the prescribed albedo to the SEB model by a change of ± 0.02, for the run with a parameterised z_{0m}, and z_{0h} from Equation 5.17.

To summarize, the parameterisation for z_{0h} should be carefully chosen over areas that are both rough and situated at lower elevations. In these areas, the contribution of SHF to ice ablation is the largest, and z_{0h} models differ most. Both an accurate z_{0m} and z_{0h} model are required to correctly model the SHF, although an underestimated z_{0h} can still partly be compensated by an overestimated z_{0m}. Yet the z_{0m} values also affects the momentum fluxes, thereby impacting the wind field in coupled models. Finally, radiation measurement errors lead to a considerable spread in modelled ablation (25% at S6), especially at higher elevation or darker surface sites where the relative contribution of turbulent fluxes to ablation is smaller. We recommend the use of the newly developed z_{0m} model developed in this study with well chosen values for parameters including H_{max}, in combination with the updated parameterisation for z_{0h} (Equation 5.17). The parameters of both the z_{0m} and z_{0h} parameterizations were calibrated with a greatly reduced amount of measurements, due to the strict selection procedure (see Appendix). Yet, the updated parameterizations give the most accurate results when applied in the SEB model forced with 4 years of continuous, meteorological forcing.

5.4.2 Case studies: strong melt events

To demonstrate the important short-term variability of SHF and its impact on melt, we selected two cases with important contributions of the SHF to the melt energy. This enables us to evaluate the SEB model with optimal roughness length settings, but also to highlight the impact of instrumental uncertainties in observing ice ablation during extreme melt episodes (Figures 5.7 & 5.8). The modelled ground heat flux (G) is not shown, since its contribution to the SEB during melting events is usually negligibly small compared to the other fluxes (Van den Broeke et al., 2008).

S5: 25 July - 3 August 2021

At site S5, we analyse the period between 25 July and 3 August 2021, during which an important peak in SHF was observed at S5 and SHR (Figure 5.7b, dots). This peak is explained by a high ($\approx 10 \ m \ s^{-1}$) wind speed (Figure 5.7c), and a large (8 $^\circ C$) surface to air temperature gradient (Figure 5.7e). This peak is realistically modelled (orange line, Figure 5.7b), with accurate representations of both z_{0m} (panel d) and z_{0h} (not shown). In combination with a large net absorbed radiation, the modelled surface lowering during this period is substantial (6.7 cm per day, 60 cm total, panel a). The latter modelled surface lowering agrees well (within 15%) with both the SR and PTA observations from KAN_L (≈ 5 km upslope, 160 m higher), but does not agree with the two ADW measurements at S5. The mismatch is evidence of the considerable spatial variability in ice ablation during short time periods. We expect the net absorbed radiation and the turbulent heat fluxes to be heterogeneous in the rough area surrounding these weather stations. Besides, the ADW masts at S5 are anchored several cm into the ice surface, making them more sensitive to subsurface melt caused by solar insolation, but not to surface melt caused by turbulent heat fluxes. This is visible in the night between 26 and 27 July in Figure 5.7a, during which the SEB model and the observations at KAN_L suggest ablation, but both draw wires at S5 do not. Over longer periods, the ADW masts still record the same cumulative ablation since they sink back in the ice during daytime. At this site, the VPEC and SEC observations of SHF and z_{0m} also do not per-
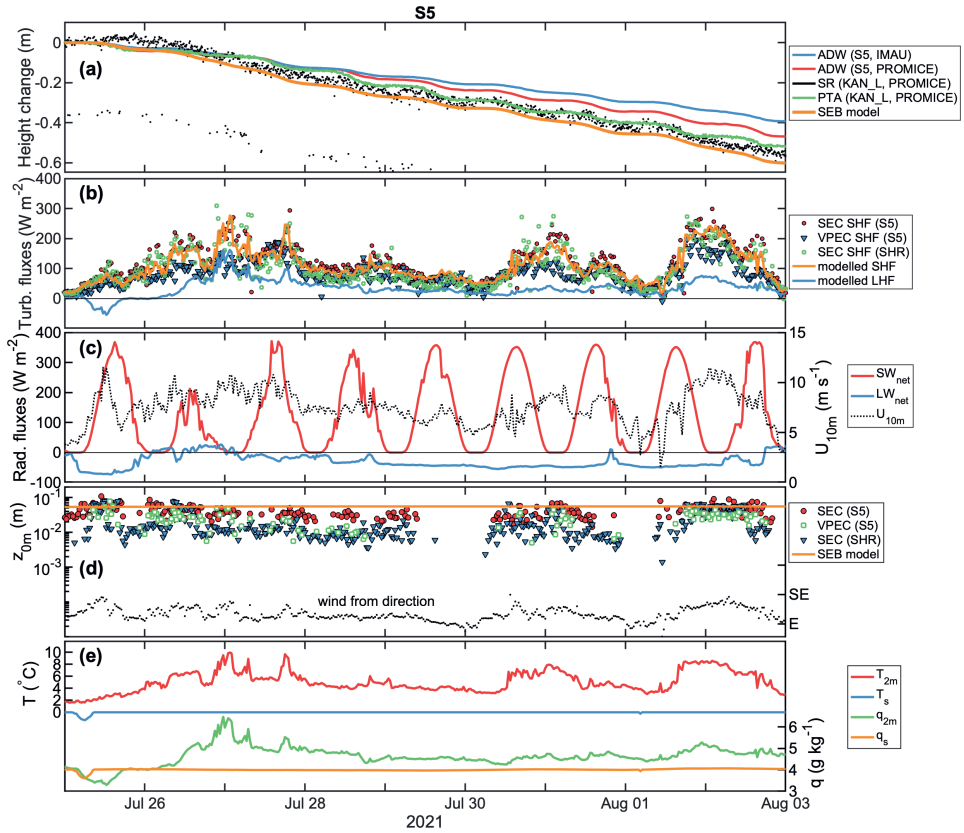
Figure 5.7: Case study at S5. Top panel (a) includes the modelled height change using the surface energy balance model with a parameterised z_{0m} and z_{0h} from Equation 5.17, in addition to the surface height change recorded by an ablation draw wire (ADW), sonic height ranger (SR) and pressure transducer assembly (PTA). Panel (b) illustrates the sensible heat flux (SHF) and latent heat flux (LHF) from both model, sonic eddy covariance (SEC) and vertical propeller eddy covariance (VPEC) observations. Panel (c) contains the observed net surface absorbed fluxes of shortwave (SW_{net}), longwave radiation (LW_{net}), and the 10-m wind speeds. Panel (d) contains estimated z_{0m} values from both SEC and VPEC observations, as well as the modelled z_{0m} value and the observed wind from direction. Bottom panel (e) illustrates the 2m air temperature and specific humidity, and both modelled surface temperature and surface specific humidity.

119
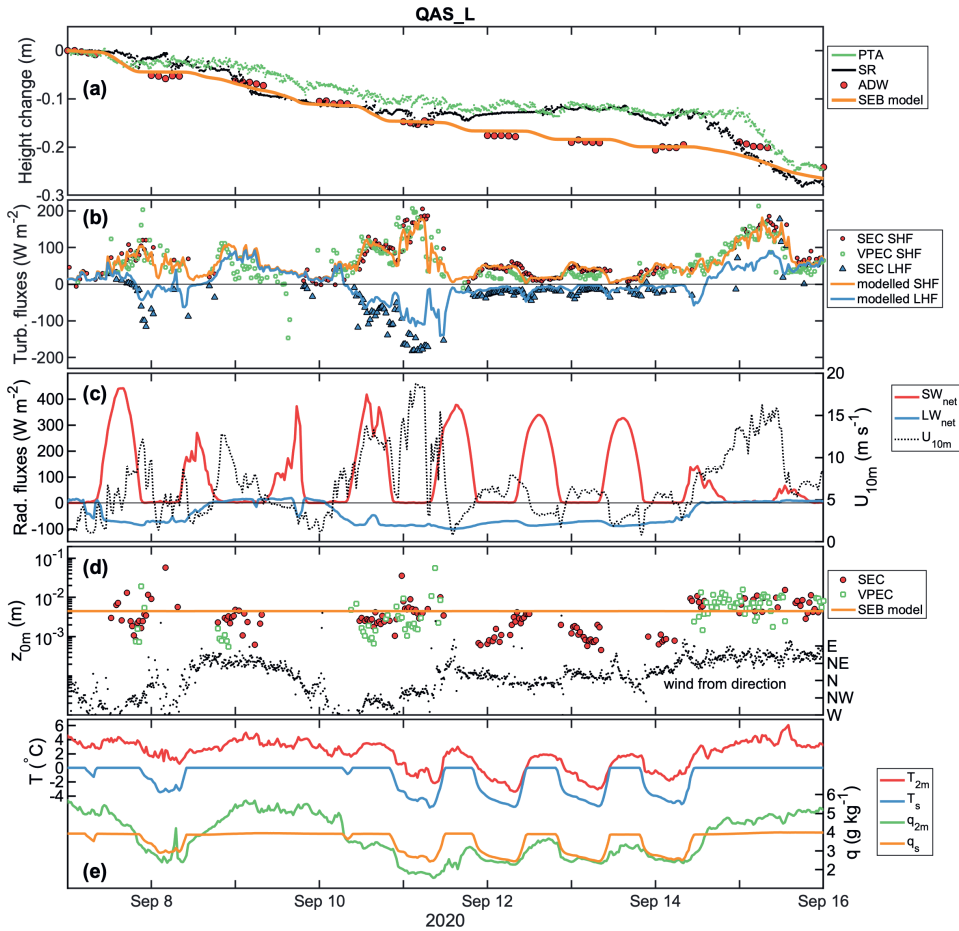
Figure 5.8: Same as Fig 5.7 for QAS_L

fectly match. This is likely explained by the different placement of the masts on the ice hummock (10 m apart), in combination with the uncertainty related to the slow-response correction of the VPEC sensors (Van Tiggelen et al., 2020).

QAS_L: 7 September - 16 September 2020

At QAS_L, we analyse the data between 7 and 16 September 2020, during which both SHF and LHF, and all three types of independent ablation measurements are available. We only consider the nighttime data of the ADW, since daytime internal heating of the logger caused nonphysical values, which was not yet corrected for in this instrument. Overall, the SEB model captures within 3% the 28 cm of ablation that was recorded by all three sensors during this time period (Figure 5.8a). However, day-to-day differences between the ablation measurements also suggest some spatial variability in melt. The SHF is accurately represented by the SEB model (within 10%), although the upward LHF appears to be underestimated (Figure 5.8b). Few LHF measurements are available

when LHF > 0 (downward), since these are often conditions when the air is warm and close to saturation, which negatively affects the measurements with an open path gas analyser. Furthermore, the thick cloud cover during such conditions (Figure 5.8c) reduces the power input from the solar panels, which means that the gas analyser was often switched off to safeguard the batteries. Interestingly, on 10-11 September, the large peak in SHF (Figure 5.8b), explained by a high ($\approx 15~m~s^{-1}$) wind speed (Figure 5.8c), is fully compensated by a negative LHF caused by dry conditions (Figure 5.8e), which prevents nighttime melt (Figure 5.8a). On the other hand, on 9 and 16 September, both a positive SHF and LHF enhance nighttime melt. This is confirmed by the PTA and SR measurements, and to a lesser extent by the ADW (Figure 5.8a). The average z_{0m} during this time period is realistically captured (Figure 5.8d), although sub-daily changes in z_{0m} linked to changing wind directions are not. For instance, wind directions deviating from the prevailing, southerly katabatic wind direction have slightly larger z_{0m} values, which are not represented in the current z_{0m} model formulation. The latter also holds for the westerly (katabatic) wind direction at S5 (panel d).

5.5 Conclusions/Summary

Turbulent heat fluxes, i.e the sensible heat flux (SHF) and the latent heat flux (LHF), are important sources/sinks of energy for the Greenland Ice Sheet. Any atmospheric model, ranging from large eddy simulations to earth system models must therefore accurately represent these turbulent fluxes, which demands accurate estimates of the aerodynamic roughness lengths for momentum (z_{0m}) and heat (z_{0h}), provided that similarity theory is applied between the lowest model level and the surface.

In this study we applied a bulk turbulent drag model to model z_{0m} variations in time using information on ice melt and snow depth. We tested this model at four contrasting sites on the ice sheet for which eddy covariance data are available. The model is able to reproduce the observed seasonal cycle in z_{0m} (Figure 5.3). The z_{0m} values increase during the start of the melting season when the seasonal snow melts, uncovering the rough underlying ice. When the snow is gone, ice hummocks are modelled to gradually increase in height due to differential ablation, which further increases z_{0m} during the ablation season. At the start of the accumulation season, z_{0m} decreases again when the topographic depressions between the ice obstacles are assumed to be gradually filled with fresh snow. The remaining exposed top of the ice hummocks are also modelled to decrease in height due to differential sublimation, which reduces the z_{0m} values further.

Twelve eddy covariance datasets, acquired since 1996 over rough ice and snow surfaces in both Greenland and Iceland, are used to compute z_{0h}. Although the spread between the in situ observations remains large, all data confirm that the z_{0h}/z_{0m} ratio decreases with increasing roughness Reynolds number ($Re_* = u_* z_{0m}/\nu$, Figure 5.4). A new empirical relationship was fitted (Equation 5.17), which improves modelled SHF over rough ice (Figure 5.5), which in turn improves the modelled ice ablation (Figure 5.6).

The methods described in this study can be used to improve the representation of turbulent heat fluxes over rough ice in either SEB models using AWS data as input, or coupled surface-atmosphere models. The impact of the revised parameterisations for both z_{0m} and z_{0h} was found to be particularly large in the lower part of the ablation

area, where the largest vertical gradients of wind speed and temperature are found together with large ice hummocks or crevasses, and where a negative LHF less frequently offsets the SHF. An important uncertainty remains in the representation of the spatial patterns of ice ablation at the scale of the roughness obstacles themselves. Differences between in situ ablation measurements in the same area strongly confirm a spatial variability in surface ablation (Figures 5.7 & 5.8). Yet, neither of the current state-of-the-art SEB models nor regional climate models are able to resolve melt at the meter-scale, complicating the direct comparison of point in situ observations with large scale models over such complex surfaces.

Data description and acronyms

The metadata of all the eddy covariance datasets used in this study are given in Table 5.1. The acronyms used in this study are summarised in Table 5.2.

Table 5.1: Description of eddy covariance datasets

site	location	time period	Instrument (method)	valid runs when Tair >2C / valid 30min runs / total runs	z (m)	z0m (m) 10%-90% quantile (Tair >2C)	SHF (W m^{-2}) 10%-90% quantile (Tair >2C)	Albedo range	Ablation sensor
QAS_L	61.0305 -46.8497 250 m	29 Aug 2019 15 Feb 2020	CSAT3 (SEC)	250 / 786 / 5109	3.75	6 10-4 - 3.0 10-3	51.9 - 172.7	0.16 - 0.81	ADW, PTA, SR, stake
		21 Aug 2020 08 Feb 2021	CSAT3 + LI-7500 (SEC)	103 / 596 / 7869	3.75	9 10-4 -1.11 10-2	53.0 - 193.6	0.20 - 0.92	ADW, PTA, SR, stake
S5	67.09431 -50.07208 520 m	01 Sep 2005 09 Mar 2006	CSAT3 (SEC)	90 / 574 / 4455	4.52	2.5 10-3 - 2.32 10-2	46.3 - 166.2	0.54 - 0.91	SR, stake
		04 Apr 2008 31 Aug 2008	CSAT3 (SEC)	1893 / 2329 / 6852	4.45	5.6 10-3 - 4.28 10 -2	37.7 - 143.9	0.48 - 0.95	SR, stake
		05 Sep 2019 31 Oct 2019	CSAT3B (SEC)	313 / 1020 / 2515	4.45	2.45 10-2 -1.102 10-1	42.2 - 137.9	0.50 - 0.95	ADW, stake
		11 Sep 2020 09 Aug 2021	CSAT3B (SEC)	2418 / 5759 / 11268	4.45	9.6 10-3 - 5.96 10-2	44.1 - 162.9	0.47 - 0.95	ADW, stake
		15 Sep 2016 31 Aug 2021	Propellers & thermocouple (VPEC)	1761 / 4821 / 67235	4.45	6.3 10-3 - 5.98 10-2	45.1 - 182.8	0.45 - 0.95	ADW, stake
SHR/ KAN_L	67.09674 -49.96082 640 m	04 Sep 2019 02 Dec 2019	CSAT3B (SEC)	273 / 1493 / 3779	4.45	1.29 10-2 - 6.91 10-2	39.6 - 122.1	0.43 - 0.90	PTA, SR, stake
		10 Sep 2020 09 Aug 2021	CSAT3B (SEC)	1760 / 2973 / 9375	4.45	3.9 10-3 - 5.04 10-2	33.7 - 113.4	0.41 - 0.92	PTA, SR, stake
S6	67.07941 -49.40981 1010 m	01 Sep 2003 18 Aug 2004	CSAT3 (SEC)	873 / 4578 / 15656	2.75	5 10-4 - 1.05 10-2	23.6 - 73.2	0.45 - 0.95	SR, stake
		15 Sep 2016 08 Sep 2020	Propellers & thermocouple (VPEC)	85 / 1102 / 69311	2.8 - 3.7	1.3 10-3 - 7.6 10-3	37.1 - 124.8	0.24 - 0.95	ADW, stake
S10	66.9999 -47.0199 1880 m	13 Aug 2012 24 Oct 2012	CSAT3 (SEC)	4 / 30 /1603	3.7 - 4.2	3 10-5 - 1 10-4	11.7 - 20.5	0.58 - 0.95	SR, stake
A4	64.09083 -16.32889 279 m	17 May 1996 01 Sep 1996	Solent 1012 R2 (SEC)	844 / 873 / 4379	3 - 3.65	8 10-4 - 1.14 10-2	34.4 - 234.8	-	SR, stake
A5	64.12278 16.36889 381 m	19 May 1996 31 Aug 1996	Solent 1012 R2 (SEC)	679 / 679 /4844	3 - 4.65	5 10-3 -1.221 10-1	30.2 - 163.1	-	SR, stake

5

Table 5.2: Standard deviation (σ) of observed $ln(z_{0m})$, $ln(z_{0m})$ $ln(u_*)$ and estimated expected (or fictitious) correlation (ρ) after Andreas (2002) for all sonic eddy covariance measurements during melting conditions

Dataset	$\sigma ln(z_{0m})$	$\sigma ln(z_{0h})$	$\sigma ln(u_*)$	ρ
S6 2004	1.1424	1.0421	0.2751	-0.7183
S5 2006	0.8024	2.0670	0.2531	-0.3451
S5 2008	0.8113	1.5715	0.2945	-0.4312
S5 2020	0.5590	2.7403	0.3471	-0.1698
S5 2021	0.7623	2.7702	0.3696	-0.2388
SHR 2020	0.6268	2.3241	0.3435	-0.2284
SHR 2021	0.9701	2.4093	0.3325	-0.3533
QAS_L 2020	0.8165	2.0782	0.2981	-0.3435
QAS_L 2021	0.9621	3.6270	0.4199	-0.2350
S10 2012	0.8277	9.6676	0.3942	-0.0770
A4 1996	1.0868	2.5179	0.4907	-0.3612
A5 1996	1.2087	2.6684	0.4811	-0.3834

Table 5.3: Acronyms

Acronym	Definition
ADW	Ablation draw wire
AWS	Automatic weather stations
IMAU	Institute for Marine and Atmospheric research Utrecht
LHF	Latent heat flux
LW	Longwave radiation
PROMICE	Programme for monitoring of the Greenland Ice Sheet
PTA	Pressure transducer assembly
RCM	Regional climate model
RMS	Centred root-mean-square error
SEB	Surface energy balance
SEC	Sonic eddy covariance
SHF	Sensible heat flux
SMB	Surface mass balance
SR	Sonic height ranger
SW	Shortwave radiation
UAV	Uncrewed aerial vehicle
VPEC	Vertical propeller eddy covariance

Chapter 6

Impact of an improved Greenland ice sheet surface roughness description on modelled surface melt in RACMO2.3p2

6.1 Introduction

Between 1992 and 2018, the Greenland ice sheet (hereafter, the ice sheet) contributed 10.8 ± 0.9 mm to the global mean sea-level rise (Shepherd et al., 2020). Approximately half of this cumulative mass loss is attributed to a decrease in surface mass balance (SMB), which is in turn attributed to an increase in surface melt and resulting runoff (Van den Broeke et al., 2016). While regional climate models (RCMs) are used for both the past reconstruction and the future projection of the ice sheet SMB, they are known to underestimate surface melt in the low-lying ablation area of the ice sheet (Fausto et al., 2016a; Noël et al., 2016; Fettweis et al., 2020). A possible explanation is an underestimation of the modelled turbulent heat fluxes (sensible heat flux or SHF, and latent heat flux or LHF), but a proper evaluation across the entire ice sheet is lacking. In this chapter we present a comprehensive database of SEB fluxes using observations from all available IMAU and PROMICE automatic weather stations, 25 in total. We then evaluate the near surface meteorology and SEB fluxes modelled by RACMO2.3p2 to identify model biases. We finally perform sensitivity experiments with RACMO2.3p2 by varying the snow and ice surface aerodynamic roughness parametrisation schemes in order to quantify the associated uncertainties in modelled near-surface temperature, wind speed, but also turbulent heat fluxes and surface melt.

6.2 Methods

6.2.1 Regional climate model RACMO2.3p2

We use the polar version of the Regional Atmospheric Climate Model (RACMO) version 2.3p2, which is described in more detail by Noël et al. (2016). The model combines the

---

This chapter is based on: Van Tiggelen and others (in preparation): Impact of an improved Greenland ice sheet surface roughness description on modelled surface melt in RACMO2.3p2

dynamical core of the High Resolution Limited Area Model (HIRLAM) with the physics from the European Centre for Medium-Range Weather Forecasts–Integrated Forecast System (ECMWF-IFS cycle CY33r1). In addition, a multi-level subsurface snow/ice routine is used over the grounded ice sheet (Ettema et al., 2010) that includes snow drift (Lenaerts et al., 2012), prognostic snow albedo (Kuipers Munneke et al., 2011) and a prescribed albedo for bare ice based on MODIS data. Surface turbulent heat fluxes are parameterized using Monin-Obukhov similarity theory (MOST), in which the correction functions of Holtslag and De Bruin (1988) are used for stable stratification. In the default version of RACMO2.3p2, the roughness length for momentum (z_{0m}) is fixed to 1 mm for snow and 5 mm for ice. For the roughness length for heat (z_{0h}) and moisture (z_{0q}), the parameterization of Andreas (1986) is used for snow, while the parameterization of Smeets and Van den Broeke (2006) is used for bare ice. These parameterizations have the following form:

$$\ln\left(\frac{z_{0h}}{z_{0m}}\right) = b_0 + b_1 \ln(Re_*) + b_2 (\ln(Re_*))^2 \tag{6.1}$$

with b_0, b_1 and b_2 empirically derived parameters.

We initialise the model on 01 September 2016 using the simulation output of Noël et al. (2019), and run it until 31 December 2021 with a 5.5 km horizontal resolution. The model is forced at its lateral boundaries with ERA5 reanalysis every 6 hours. In addition to the default run (run 'DEF') using the aforementioned settings, seven sensitivity experiments are performed using different surface roughness settings. The different combinations of z_{0m} and z_{0h} parameterizations are listed in Table 6.1.

To obtain the roughness length (z_{0m}) associated with bare ice, we test three different parameterizations:

1. A fixed z_{0m} = 5 mm for bare ice, and z_{0m} = 1 mm for snow, as mentioned above.

2. An empirical relationship for bare ice:

$$z_{0m,bare\ ice}(elev) = (z_{0m,max} - z_{0m,min})\left(1 - \frac{1}{1 + e^{a(elev-b)}}\right) + z_{0m,min} \tag{6.2}$$

   with $elev$ the surface elevation of the ice sheet, $z_{0m,max} = 2 \times 10^{-2}$ m, $z_{0m,min} = 10^{-3}$ m, $a = -0.01$ m^{-1} and $b = 900$ m which are empirically derived parameters to match the retrieved z_{0m} using summer ICESat-2 data from chapter 4] (Van Tiggelen et al., 2021).

3. A prognostic z_{0m} based on the method described in chapter 5, which is the relationship proposed by Raupach (1994):

$$z_{0m} = (H - d)\exp(-\kappa\gamma)\exp(\widehat{\Psi_H}), \tag{6.3}$$

   with H the height of the roughness obstacles, $\kappa = 0.4$ the Von Kármán constant, $\widehat{\Psi_H} = 0.193$ the wind profile correction within the roughness sublayer Raupach (1994) and,

$$\gamma = (C_s + C_d\lambda)^{-0.5}, \tag{6.4}$$

with C_s the skin friction coefficient, C_d the form drag coefficient and λ the frontal area density of the roughness obstacles. In this parameterization, the height of the roughness elements (H) is a prognostic quantity in RACMO, and is modelled using snow depth and ice ablation. The quantities d, C_s, C_d and λ are then parameterized as function of H as was done in chapter 5. An important parameter is the maximum height of the ice obstacles (H_{max}), which is regressed as function of elevation as:

$$H_{max}(elev) = (H_2 - H_1)e^{-(elev-b)/a} + H_1. \tag{6.5}$$

Here, H_2 = 3.2 m, H_1 = 0.2 m, b = 100 m and a = 400 m, which are parameters that are empirically derived from ICESat-2 data.

For the roughness lengths for heat and moisture (z_{0h} & z_{0q}) we test four different parameterizations. For snow we always use the model of Andreas (1986), while for bare ice we test the following:

1. Equation 6.1 with b_0 = 0.317 b_1 = -0.565, b_2 = -0.183 (based on A86, Andreas (1986))

2. Equation 6.1 with b_0 = 3.5, b_1 = 0.7, b_2 = -0.15 (SB06, Smeets and Van den Broeke, 2006)

3. Equation 6.1 with b_0 = 1.5, b_1 = 0.15, b_2 = -0.16 (chapter 5)

4. An imposed fixed ratio $z_{0h} = 0.1 \times z_{0m}$.

We choose eight relevant combinations of z_{0m} and z_{0h}, which are summarized in Table 6.1. The combination of z_{0m} modelled with a prognostic ice obstacle height and z_{0h} from chapter 5 is referred to as the new version ('NEW').

Table 6.1: Different RACMO2.3p2 settings for z_{0m} and z_{0h} over bare ice. The acronyms are defined in the text.

Experiment number	z_{0h} A86	z_{0h} CH5	z_{0h} SvdB08	$z_{0h} = 0.1z_{0m}$
z_{0m} fixed	10	20	30 (DEF)	-
z_{0m} prescribed by Equation 6.1	11	21	31	41
z_{0m} parameterised based on chapter 5	-	22 (NEW)	-	-

6.2.2 AWS data and SEB model for evaluation

AWS data

We use the observations from 25 automatic weather stations (AWS) located on the ice sheet. Five stations (S5, S6, S9, S22, S23) are part of the IMAU network, while 20 stations are from the PROMICE network. The name, location and elevation of each station is shown in Figure 6.1 and Table 6.2. All the stations were continuously operational for more than one year, with the exception of TAS_L (Table 6.2). Twelve out of the 25 stations are located below 700 m elevation, distributed across the ice sheet (Figure 1.1). This enables a widespread comparison of meteorological quantities with RACMO in the low-lying ablation area.

Table 6.2: Information about all AWS used for the RACMO evaluation and as forcing for the SEB model. Note that both elevation and coordinates might vary due to melt and glacier flow.

AWS	Elevation (m)	latitude; longitude	H_{max} (m)	Network	Time period used
EGP	2661	75.6247;-35.9748	0.2	PROMICE	01 Sep 2016 - 31 Aug 2021
GITS	1886	77.1378;-61.0411	0.2	PROMICE	25 Jul 2017 - 11 Aug 2021
KAN_U	1840	67.0003;-47.0253	0.3	PROMICE	01 Sep 2016 - 31 Aug 2021
S9	1520	67.0532;-48.2675	0.3	IMAU	01 Sep 2016 - 17 Aug 2021
KAN_M	1270	67.0670;-48.8355	0.5	PROMICE	01 Sep 2016 - 31 Aug 2021
NUK_U	1120	64.5108;-49.2692	0.5	PROMICE	01 Sep 2016 - 01 Jul 2021
S6	1120	67.0793;-49.4069	0.6	IMAU	13 Sep 2016 - 09 Aug 2021
SCO_U	970	72.3933;-27.2333	0.5	PROMICE	01 Sep 2016 - 31 Aug 2021
UPE_U	940	72.8878;-53.5783	0.2	PROMICE	01 Sep 2016 - 31 Aug 2018
QAS_U	900	61.1753;-46.8195	0.3	PROMICE	01 Sep 2016 - 31 Aug 2021
TAS_A	890	65.7790;-38.8995	0.8	PROMICE	01 Sep 2016 - 31 Aug 2021
KPC_U	870	79.8347;-25.1662	0.3	PROMICE	01 Sep 2016 - 31 Aug 2020
THU_U	760	76.4197;-68.1463	0.2	PROMICE	01 Sep 2016 - 31 Jan 2021
KAN_L	670	67.0955;-49.95133	1.0	PROMICE	01 Sep 2016 - 31 Aug 2020
QAS_M	630	61.0998;-46.8330	0.5	PROMICE	01 Sep 2017 - 31 Aug 2020
THU_L	570	76.3998;-68.2665	0.4	PROMICE	01 Sep 2016 - 09 Aug 2021
S5	550	67.0942;-50.0691	1.2	IMAU	13 Sep 2016 - 20 Aug 2021
S22	535	78.9000;-22.3800	0.5	IMAU	01 Sep 2017 - 31 Aug 2020
NUK_L	530	64.4822;-49.5358	1.0	PROMICE	01 Sep 2016 - 09 Aug 2021
SCO_L	460	72.2230;-26.8182	0.6	PROMICE	01 Sep 2016 - 31 Aug 2021
KPC_L	370	79.9108;-24.0828	0.4	PROMICE	01 Sep 2016 - 31 Aug 2021
QAS_L	280	61,0308;-46,8493	0.5	PROMICE	01 Sep 2016 - 09 Aug 2021
TAS_L	250	65.6402;-38.8987	0.8	PROMICE	19 Aug 2020 - 09 Sep 2021
UPE_L	220	72.8932;-54.2955	0.6	PROMICE	01 Sep 2016 - 31 Aug 2021
S23	145	78.9200;-21.4500	1.0	IMAU	01 Sep 2016 - 31 Aug 2019

SEB model

The surface energy balance (SEB) model computes the sensible heat flux, latent heat flux and the subsurface heat flux by imposing energy conservation at the surface. It is described in further detail in chapter 5. The turbulent heat fluxes are computed assuming Monin-Obukhov similarity theory (MOST). The roughness length for momentum is modelled using the parameterization from chapter 5, with a site-specific maximum height of the ice obstacles (H_{max}) based on observations in the field. The value of H_{max} for each station is shown in Table 6.2. For z_{0h} and z_{0q} the updated parameterization also from chapter 5 is used. The model is forced with 30-min AWS data from September 2016 until the latest available AWS data in August 2021. We prescribe both the 24-hourly moving average albedo and the snow height to the model as measured with the sonic height ranger. In case of malfunction of the sonic ranger, the surface is assumed to be bare ice if the albedo is lower than 0.6.
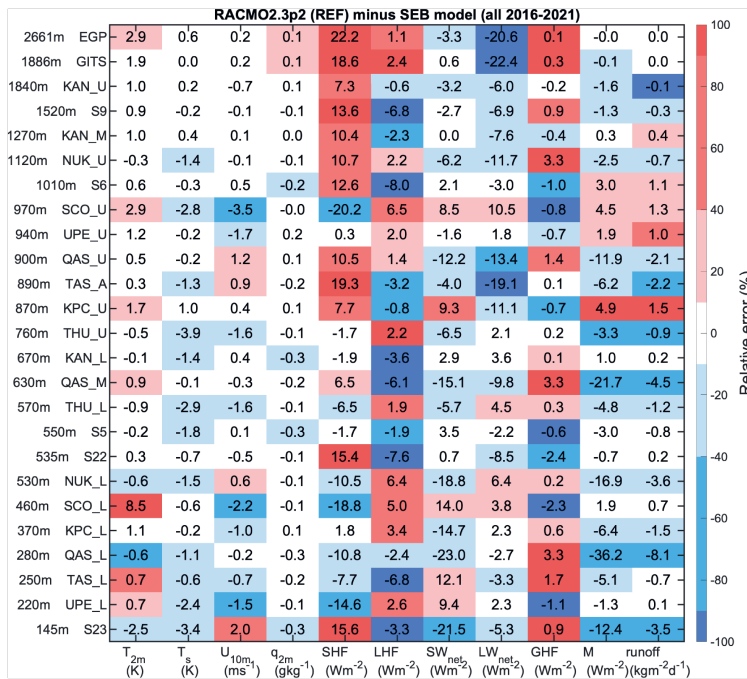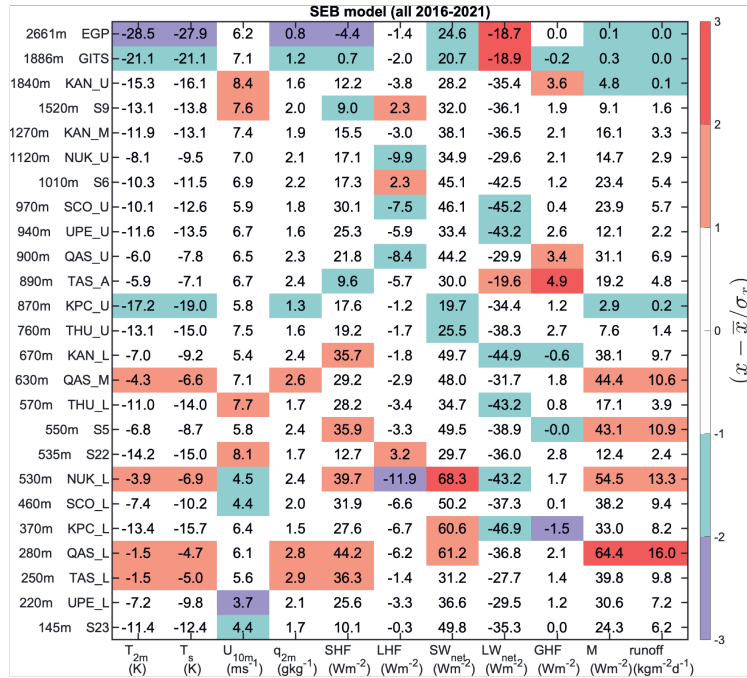
6.3   Evaluation of RACMO with default settings

In this section we compare the output of the default RACMO run ('DEF') with the output of the SEB model at the locations and time periods listed in Table 6.2. For all the variables we extract the value from the RACMO ice sheet pixel that is the closest to each AWS. The comparison of air temperature, wind speed, specific humidity, radiative fluxes, SHF, LHF and surface melt is shown in Figure 6.1, and for the summer months (June-July-August, JJA in Figure 6.2. On average, the default RACMO simulation captures the near surface temperature within 10% (see Figure 6.2 for the definition of the evaluation metric) for 15 out of 25 stations, with an average bias of 0.85 K. The 10 m wind speed is underestimated by on average 0.98 m s^{-1}, with a more pronounced underestimation at the lower stations. The yearly SHF is modelled within ± 20 W m^{-2}, which is the same order of magnitude as the average error in SW_{net} and LW_{net}, and nearly an order of magnitude larger than the errors in LHF and GHF (Figure 6.1). Overall, RACMO underestimates the energy for surface melt by 4.3 W m^{-2}. The largest underestimation in surface melt coincides with either an underestimation in both SHF and SW_{net} (e.g. at QAS_L, NUK_L, THU_L), or an underestimation in SW_{net} and LW_{net} (e.g. at QAS_M, S23). Compensating errors can still lead to an accurate melt, as for instance at SCO_L, UPE_L and S5 where the underestimation in SHF is compensated by a similar overestimation in SW_{net}.

During the summer months (JJA), all the SEB fluxes peak, which may help in identifying the biases in RACMO. The JJA comparison is given in Figure 6.2. At the 7 stations located above 1000 m elevation, the SHF is on average overestimated by 4.9 W m^{-2}, while for the lower stations it is underestimated by on average 10.8 W m^{-2}. In combination with SW_{net} errors ranging from -75.8 W m^{-2} (QAS_L) to 43.3 W m^{-2} (UPE_L), the errors in surface melt range from -115.7 W m^{-2} (QAS_L) to 30.4 W m^{-2} (KAN_L). To summarise, RACMO with the default settings underestimates the summer (JJA) surface melt energy by 14.7 W m^{-2}, or 17.7% of the averaged observed melt from the SEB model (83 W m^{-2}).

The underestimation of surface melt in RACMO was known (Noël et al., 2018), yet this comprehensive comparison reveals that it is for a large part due to a systematic underestimation of the SHF at stations below 1000 m a.s.l. Figure 6.3 presents the same results as function of station elevation. The bias in RACMO surface melt shows a significant (p = 0.0582) linear relationship with surface elevations below 1000 m, ranging from an overestimation of 6.5 W m^{-2} at 1000 m a.s.l up to an underestimation of 53.9 W m^{-2} at sea-level. The bias in SHF (p=0.0576) and LHF (p=0.0394) also demonstrates a significant linear relationship with elevation. The underestimations of both melt, SHF and LHF coincide with a systematic underestimation in both 10 m wind speed of 0.7 m s^{-1}, and surface temperature of 0.19 K for all stations below 1000 m elevation. Above 1000 m elevation, the melt bias is negligibly small due to small errors in SEB components (Figure 6.3).

Figure 6.1: **Top / left:** Observed and SEB modelled quantities at each AWS averaged over the period with observations. The colour denotes the deviation from the mean quantity of all stations, normalised by the standard deviation for all stations. **Bottom / right:** Bias in RACMO modelled quantities nearest to each AWS in the DEF run, compared to the SEB model, and in color the relative percent error. All the data are averaged over the entire 2016-2021 period. AWS locations are sorted by elevation.
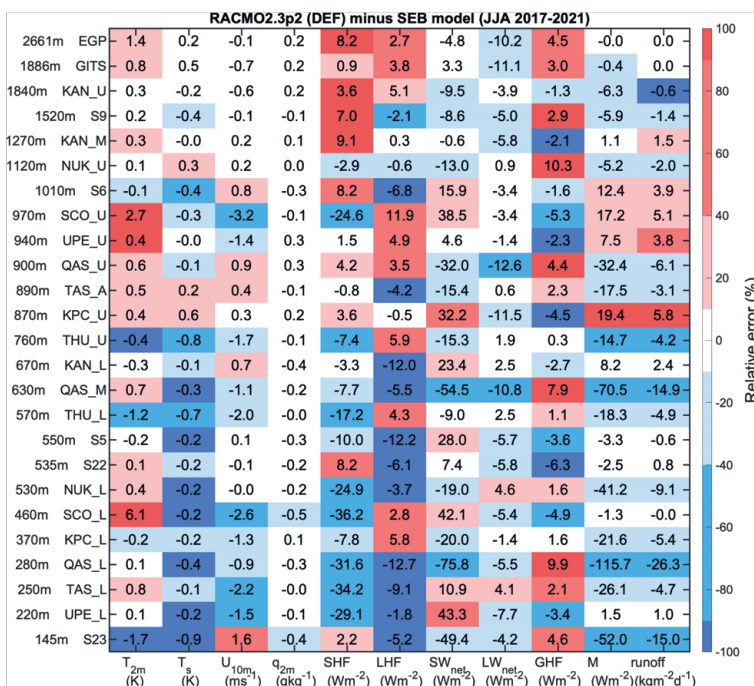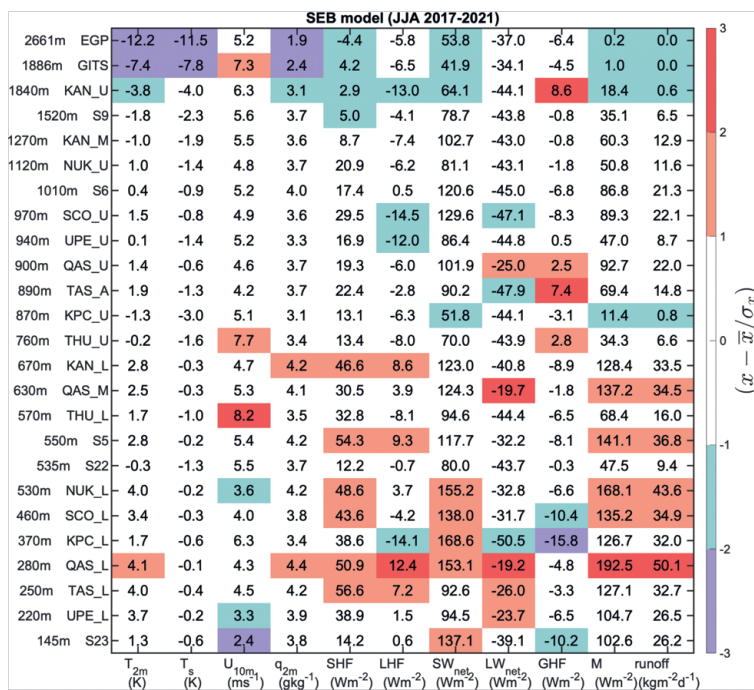
Figure 6.2: Same as Figure 6.1 but for June-July-August (JJA) data only in 2017-2021.
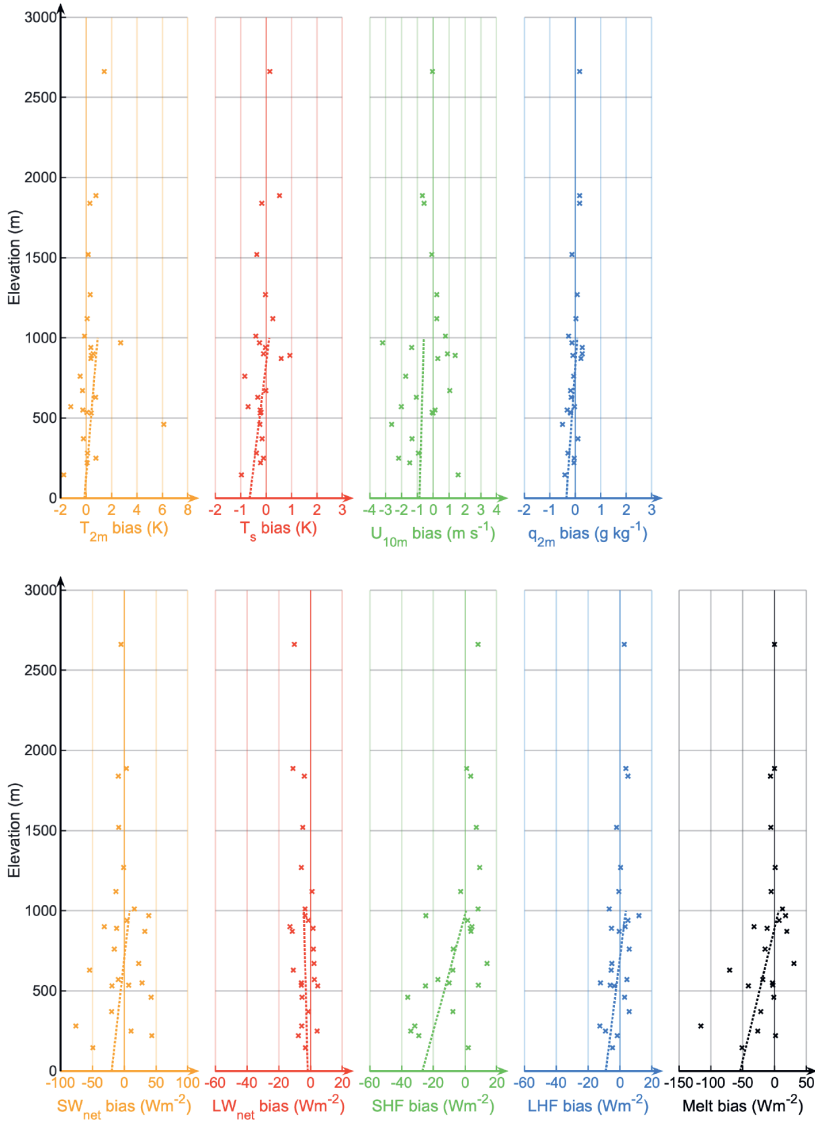
Figure 6.3: June-July-August (JJA) 2017-2021 bias of: **top**: 2m temperature, surface temperature, 10m wind speed, 2m specific humidity and **bottom**: SEB components in RACMO DEF run compared to observed and SEB modelled quantities.

6.4 Impact of improved surface roughness

The sensitivity of modelled SHF in RACMO on the surface roughness parameterization is investigated in this section. We compare the modelled quantities for all eight simulations (Table 6.1) against the twelve stations located below 700 m elevation. We select two time periods: (1) all the available data and (2) only JJA data. The bias for each run for each variable and time period is shown in Table 6.3. The difference in JJA bias between the NEW and DEF runs is shown in Figure 6.4.

When considering all the data, the smallest bias in surface melt (-6.5 W m^{-2}) is for run 41, which uses a prescribed z_{0m} and fixed ratio for z_{0h}/z_{0m}. The difference in bias between all the runs is limited, since the largest bias in M is -7.2 W m^{-2} for run 10, which used a constant z_{0m} and z_{0h} parameterised from A86. However, run 41 has the largest bias in SHF (5.0 W m^{-2}). All runs overestimate T_{2m} between $[0.26 - 0.38]$ K, overestimate U_{10m} between $[0.14 - 0.38]$ m s^{-1} and underestimate q_{2m} between $[0.12 - 0.14]$ g kg^{-1}.

When considering JJA data only, we find that the SHF is slightly improved for most stations in the NEW run compared to the DEF run ($\approx$ 5-15%, Figure 6.4). However, the existing bias in M in the DEF run is only marginally corrected for, since all runs still underestimate M between $[19.2 - 21.9]$ W m^{-2} and the SHF between $[6.4 - 2.5]$ W m^{-2}. Only increasing the z_{0m} values causes a larger underestimation of U_{10m}, ranging from -0.02 m s^{-1} for run 20 with a fixed z_{0m} to -0.30 m s^{-1} for the NEW run with parameterised z_{0m}. The latter has only a marginal effect on modelled SHF and melt. Only increasing z_{0h} values does not affect U_{10m} but improves T_{2m}, with a bias decreasing from 0.53 K to 0.24 K from runs 11 to 41.

To summarise, changing the z_{0h} values improves surface melt, but only if a parameterized z_{0m} is used (runs 11-21-31-41). Furthermore, improving the z_{0m} values over bare ice increases the bias of the modelled JJA values of wind speed in RACMO, since it was already underestimated in the DEF run (Figure 6.1), and the more realistic rougher surface extracts even more momentum from the flow. The lower modelled U_{10m} therefore explains part of the SHF underestimation, which in turn explains the underestimation in surface melt.

6.5 Case study: large melt events

The importance of accurately modelling the SHF is investigated in further detail using a case study from the K-transect for the summer of 2019. Large melt events were observed during this summer and we focus on the entire JJA period and more specifically on the 31st of July. Figure 6.5 presents the measured and modelled SEB components using runs 20 and 22 along the K-transect. For the JJA period, the two runs mainly yield different values of U_{10m}, especially in the bare ice zone below 1000 m elevation. Run 20 reproduces the observations somewhat better while run 22 better reproduces the z_{0m} values parameterised in the SEB model.

On 31 July 2019, which was an extreme melting day on this part of the ice sheet, the SHF equals SW_{net} at the two lowest stations (S5 and KAN_L). The observed SEB components

Table 6.3: Average difference for RACMO runs minus all AWS observations below 700 m elevation. Two values are shown: the bias for the entire dataset (all, $N = 19202$), and for June-July-August (JJA, $N = 4737$)

Bias Run	T_{2m} (K) all / JJA	U_{10m} (ms^{-1}) all / JJA	q_{2m} (gkg^{-1}) all / JJA
10	0.38 / 0.50	0.15 / -0.05	-0.14 / -0.12
11	0.38 / 0.53	0.14 / -0.08	-0.14 / -0.12
20	0.32 / 0.30	0.16 / -0.02	-0.13 / -0.10
21	0.33 / 0.33	0.14 / -0.04	-0.13 / -0.10
22 (NEW)	0.34 / 0.38	0.3 / -0.30	-0.13 / -0.08
30 (DEF)	0.26 / 0.19	0.18 / 0.03	-0.12 / -0.08
31	0.31 / 0.27	0.15 / -0.04	-0.13 / -0.09
41	0.30 / 0.24	0.15 / -0.03	-0.13 / -0.10

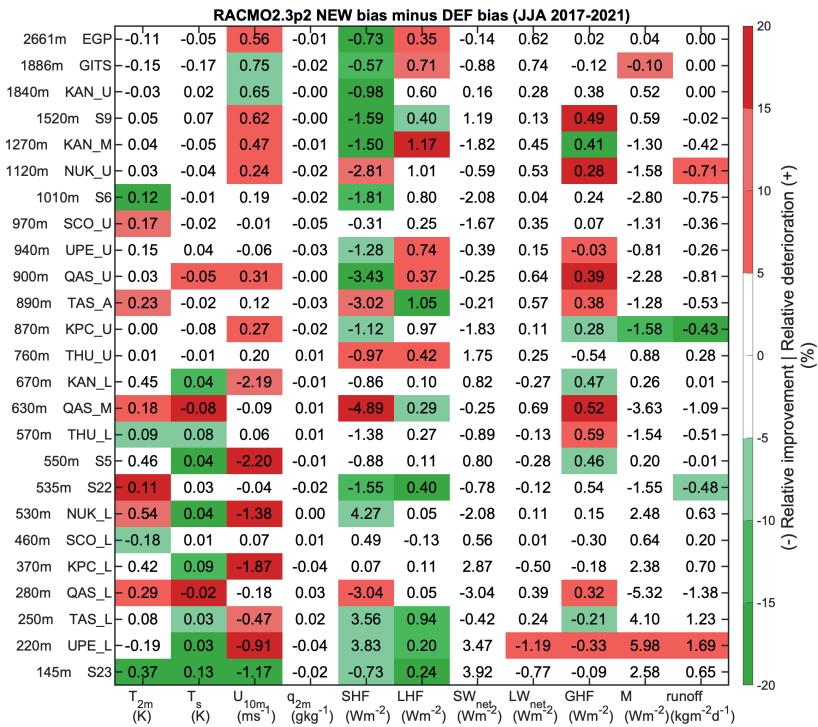| Bias Run	SHF (W m^{-2}) all / JJA	LHF (W m^{-2}) all / JJA	M (W m^{-2}) all / JJA
10	3.7 / -6.4	-1.4 / -3.0	-7.2 / -21.9
11	3.9 / -5.9	-1.3 / -2.9	-7.2 / -22.0
20	4.3 / -4.7	-1.6 / -3.3	-6.9 / -21.0
21	4.4 / -4.1	-1.7 / -3.3	-6.9 / -20.6
22 (NEW)	3.9 / -4.9	-1.4 / -3.1	-7.2 / -21.6
30 (DEF)	5.0 / -3.5	-2.0 / -3.6	-7.1 / -20.6
31	4.7 / -3.3	-1.7 / -3.4	-6.7 / -19.7
41	5.0 / -2.5	-1.8 / -3.4	-6.5 / -19.2

Figure 6.4: Bias of RACMO2.3p2 NEW run minus bias of DEF run, averaged over the JJA 2017-2021 period. The colour denotes the relative improvement (green) or deterioration (red) compared to the observed quantities from Figure 6.1.

are well reproduced for both RACMO simulations, with the exception of the LHF and M at the lowest station (S5) which are underestimated by around 50 W m^{-2}. As for the JJA period, improving z_{0m} in RACMO (run 22) increases/decreases U_{10m} above/below the snowline, while it decreases/increases T_{2m} above/below the snowline. Clearly, U_{10m} is overestimated at all stations above S5 for both runs, which results in an overestimation of SHF. This overestimation is compensated by a similar underestimation of SW_{net}, possibly due to a too high snow albedo in the model. This explains why surface melt is accurately modelled at most sites (within 10 W m^{-2}). Compared to the JJA period, important differences between the models and the observations are found above 1000 m on this day.

6.6   Summary and conclusions

The evaluation of all SEB components modelled by regional climate model RACMO version 2.3p2 against a large database of in-situ observations reveals that surface melt is, on average, underestimated by RACMO. This underestimation is most pronounced at the lowest stations. Although some discrepancies exist in SW_{net}, it appears that this is a consequence of the systematic underestimation of both the SHF and LHF. We hypothesised that the underestimation of the turbulent heat fluxes is caused by the simplified parameterizations for surface roughness in RACMO, yet including an improved parameterization of z_{0m} and z_{0h} does not greatly improve the simulations. A different reason that causes a too low SHF and LHF in RACMO identified during this study is the systematic underestimation of near surface wind speed in RACMO. At this time it remains unclear what causes the underestimation in wind speed. It is possible that the limited horizontal resolution of RACMO (5.5 km) does not accurately resolve the steeper topography around the ice sheet margins that enhances the katabatic forcing. Interestingly, for a case study of an extreme melt event we found that the melt fluxes are still accurately modelled at all the stations along the K-transect, except for the lowest station (S5). At the other stations, a too large modelled SHF and a too low modelled SW_{net} are found to compensate.

For future studies, we recommend a more detailed evaluation of the momentum budget modelled by regional climate models over the Greenland ice sheet. Considering the forthcoming improvements of snow/ice albedo parameterizations, it is possible that discrepancies in modelled SEB components will not always cancel out, possibly causing biases in modelled surface melt. The database and results presented in this study can be used to improve current RCMs. A possible application could be the downscaling of modelled surface melt in RCMs by downscaling the individual SEB components, either statistically, or using a computationally efficient SEB model.
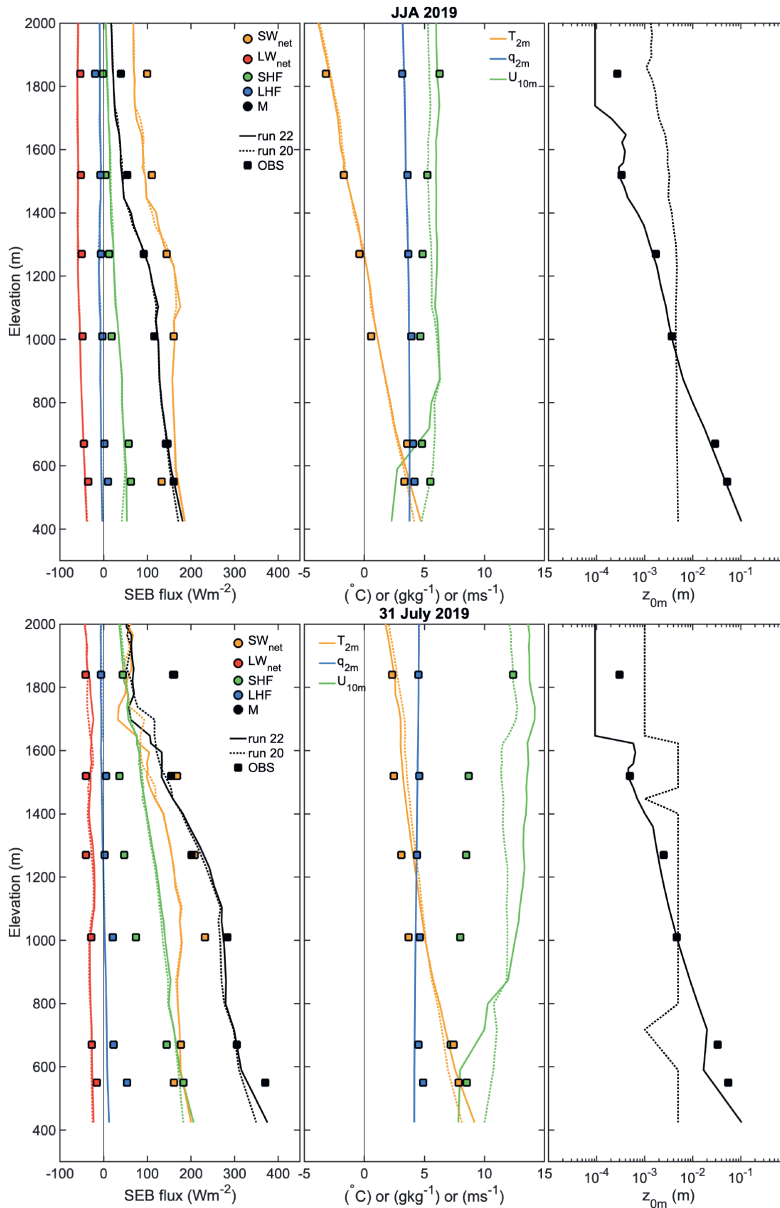
Figure 6.5: Modelled and observed SEB components (left panels), near surface mete-orology (middle panels) and surface aerodynamic roughness (z_{0m}, right panels) for JJA 2019 (top panels) and extreme melt event 31 July 2019 (bottom panels) on the K-transect. Measurements are from stations S5, KAN_L, S6, KAN_M, S9 and KAN_U. Two RACMO simulations are shown: with a fixed z_{0m} (run 20, dotted line) and parameterized z_{0m} (run 22, solid line, see Table 6.1).

Chapter 7

Conclusion and outlook

7.1   General conclusions

The aim of this thesis is to improve our knowledge on modelling surface melt across the Greenland ice sheet. More specifically, four research questions were formulated in the introduction that all address the turbulent heat fluxes, surface roughness, and their impact on surface melt from different perspectives. We answer each question in a different chapter, using field measurements (chapter 3), remote sensing (chapter 4), a surface energy balance model (chapter 5) and finally a regional climate model (chapter 6).

In chapter 3 we show that the vertical propeller eddy covariance (VPEC) method is an adequate method for in situ measurements of turbulent fluxes in the ablation zone of the ice sheet. The flux attenuation due to the limited response times of propellers can be considerable (20% to 40% of the flux), yet it can still be accurately modelled. The application of this robust method yields at the time of writing a unique long-term (2016-2022) dataset of turbulent heat fluxes at sites S5 and S6 in the ablation zone along the K-transect. Thanks to some interesting features in the sensible heat flux (SHF) and surface roughness presented in the chapter, this unique dataset may serve as a starting point for future research.

In chapter 4, we take advantage of the ICESat-2 satellite, launched by NASA just before the start of this thesis (October 2018). The photon-counting mechanism of the laser altimeter, in combination with the very narrow footprint ($\approx$ 15 m) facilitates an unprecedented study of surface topography. The comparison of ICESat-2 data with both UAV and eddy covariance measurements demonstrates that the aerodynamic roughness of a surface (z_{0m}) composed of obstacles wider than the laser footprint can accurately be estimated with ICESat-2. In practice, this results in a lower resolvable bound of $z_{0m} \approx 1$ mm. Therefore, this method can be used to map z_{0m} for crevassed and hummocky terrain up to about 1000 m elevation on the Greenland ice sheet.

In chapter 5, we develop a simple new model for the variation in height of ice hummocks in time, and update the parameterization for the scalar roughness lengths (z_{0h}, z_{0q}). The calibration of all the necessary parameters was possible thanks to combining both eddy

covariance, uncrewed aerial vehicle (UAV) and ICESat-2 data. We implemented these updated parameterizations in a surface energy balance model and used continuous 5-year AWS measurements at 4 locations to simulate ice ablation. We find that using more realistic values for both z_{0m} and z_{0h} results in SHF values with a typical bias less than 5 Wm^{-2} and RMS error of 20 Wm^{-2}. The cumulative ice ablation over 5 years is simulated with an uncertainty of less then 10%.

In chapter 6, the previously derived methods are implemented in the regional climate model RACMO version 2.3p2 and applied to the entire Greenland ice sheet. The measurements from 25 weather stations from both PROMICE and the IMAU are used to evaluate the model. We find that RACMO without any updates underestimates the yearly energy available for surface melt by around 7 Wm^{-2}. We can partly explain this underestimation by discrepancies in modelled SHF and LHF. Including the new and more realistic description of surface roughness parameters (z_{0m} and z_{0h}) in RACMO does however not greatly improve the simulations. Increasing z_{0m} also decreases the modelled wind speed, which was found to be already underestimated in the lower ablation zone by RACMO. Furthermore, improving z_{0h} parameterizations only affect the modelled SHF in situations with large values of z_{0m}.

7.2   Outlook

The contribution of the SHF to surface melt on the Greenland ice sheet is expected to increase in the future, when the ice sheet's surface will be in contact with a warmer atmosphere. Studying the turbulent exchange on the ice sheet thus remains relevant for understanding future changes in Greenland mass balance. Here we provide an outlook on potential future research avenues to model the turbulent exchange on the Greenland ice sheet.

7.2.1   Large eddy simulation over a rough melting ice surface

In chapter 4, the bulk drag model from Raupach (1992) was used to convert the surface topography to aerodynamic properties including the roughness length. This model is based on many assumptions on how to compute e.g. drag coefficients, roughness sublayer, displacement height, etc... But most importantly: it requires extracting one height representative for the roughness elements from realistic topographic profiles. In this thesis the standard deviation of high-pass filtered elevations was used, yet this remains an oversimplification of reality. An alternative to this bulk drag model is to compute the entire 3D wind and temperature fields above a realistic topography in a large-eddy simulation (LES). Such LES simulations have been done for urban-like rectangles (Yang et al., 2016; Zhu and Anderson, 2019; Li et al., 2020), yet most natural surfaces such as rough ice are more fractal than rectangular. Recently, Bonekamp et al. (2020) performed LES simulations over a debris-covered glacier surface measured by UAV photogrammetry, and demonstrate how complicated patterns in surface melt occur over realistic surfaces.

In Figure 7.1 we show some preliminary results from a LES simulation performed for the rough ice surface derived from UAV photogrammetry near S5 in southwest Greenland. These simulations were done on the SURFSARA Cartesius supercomputer with the adaptive-grid, Navier-Stokes solver BASILISK (Popinet, 2009; Van Hooft et al., 2018). This idealised simulation was initialised with a uniform south-westerly wind speed of 10 m s^{-1} and a linear, stable vertical profile of temperature, starting from $0°$C at the surface and increasing by $0.28°$K m^{-1}. The surface temperature is constant and set to $0°$C. The model uses the so-called immersed boundary method, which applies an opposing momentum forcing to the flow such that the wind speed vanishes at the surface. More information about the model can be found in Van Hooft et al. (2018).

A first analysis of the preliminary results reveals a strong horizontal variability in vertical velocity and air temperature. This variability is due to the blocking of the flow by the roughness elements (Figure 7.1), and translates in an explicitly downward modelled SHF of 11.7 ± 87.4 W m^{-2}. Future simulations could use a more realistic initialisation of the wind and temperature gradients close to the surface, and then estimate the roughness lengths z_{0m} and z_{0h} derived from the explicitly modelled vertical profiles. Furthermore, the spatial variability of the SHF at horizontal scales of 10-100m could be quantified. In combination with a cutting-edge ray-tracing model over complex surfaces for computing net absorbed radiation (Larue et al., 2020; Robledano et al., 2022), the spatial variability in the entire SEB could be quantified. Such a modelling framework has the potential to explain the observed 'sub-grid' variability in surface melt, a process that is not yet
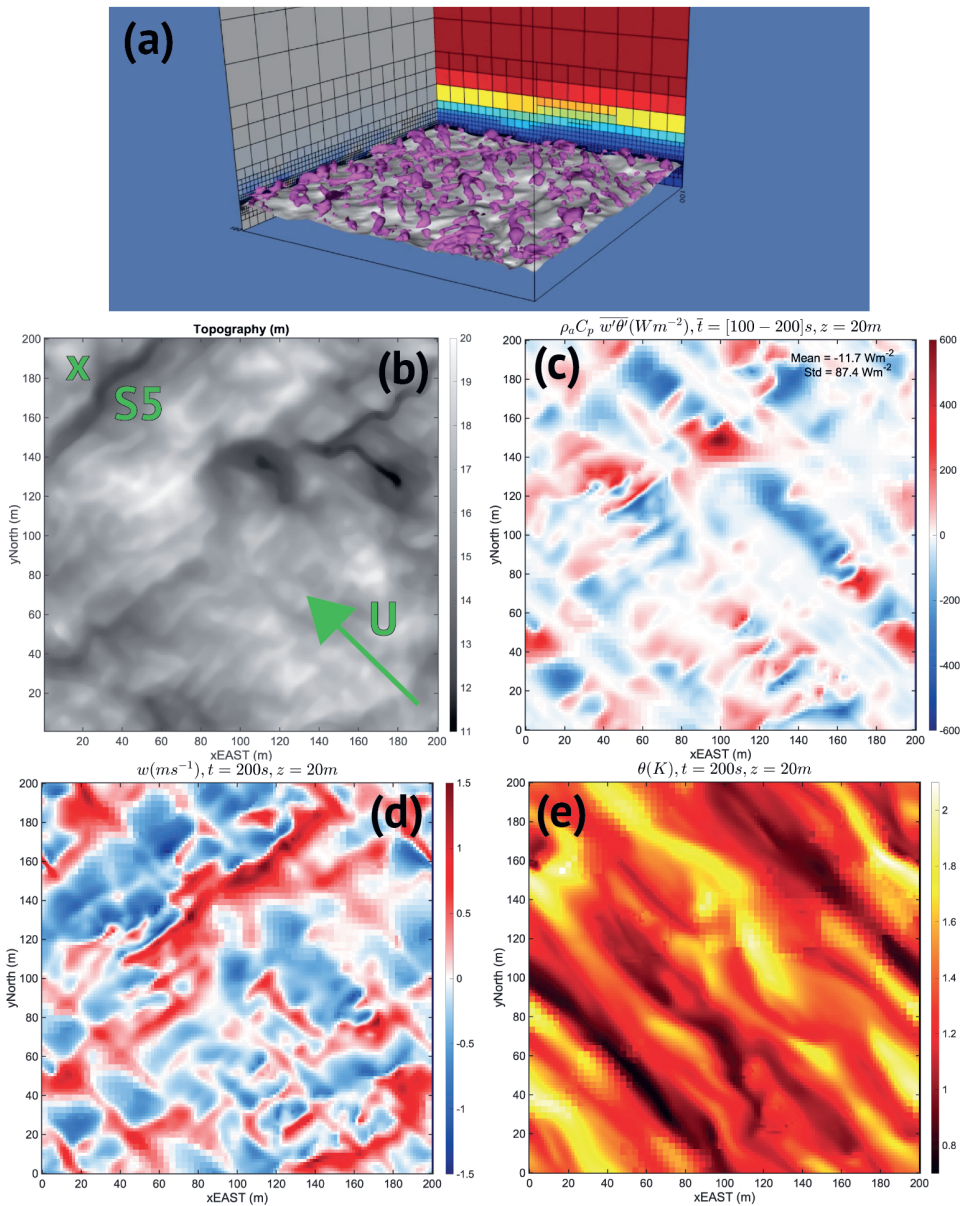
Figure 7.1: (a): snapshot of simulation showing vortex structures (b): Topography used in the model showing the AWS position by the 'x' and the direction of the initial wind speed, (c) SHF at z=20 m averaged between 100-200 s after the start of the simulation, (d) vertical wind speed and (e) potential temperature at t = 100 s after the start taken at z = 20 m.

incorporated in current climate models.

A different application of such a coupled LES-rough melting ice simulation would be to study the effect of basal ice roughness on basal melt. Basal ice features, ranging from small-scale ice scallops (or ice 'ripples') to melt channels and large scale basal crevasses were found to be closely linked to basal melt (Bushuk et al., 2019; Watkins et al., 2021). The potentially amplifying effect of basal ice features is not included in basal melt parameterizations used in ocean - ice sheet/ice shelf models (Favier et al., 2019).

7.2.2   In situ observations

Distinguishing snow sublimation from erosion using timelapse cameras

In chapter 5, it is assumed that during winter solid precipitation gradually fills the topographic depressions between ice hummocks, which is confirmed by wintertime visits and explains the observed decrease in z_{0m}. However, it is not clear whether the snow is simply displaced (eroded), melting, or removed by sublimation. Sublimation occurs when the air is drier than the saturation specific humidity at the surface, i.e. when $LHF < 0$. Cumulative ice surface lowering in a period Δt can thus be calculated from the LHF as: $\Delta h_s = \Delta t \ LHF/(\rho_{i,s}L_s)$, with $\rho_{i,s}$ the density of snow or ice and L_s the latent heat of sublimation, equal to 2.8345×10^6 J kg^{-1} at 0 $^\circ C$. A comparison of modelled surface lowering due to sublimation with data from a sonic height ranger at site S5 is shown in Figure 7.2. On 29 November 2021, around 10 cm of fresh accumulation was observed below the sonic ranger at S5. Two days later, all the snow was removed below the station. This fast removal cannot be explained by sublimation since the LHF was small (≈ -20 W m^{-2}), so this must have been caused by wind erosion. Three weeks later, on 21 December, a large negative peak in LHF is modelled which is estimated to cause between 1 - 5 cm of ablation, depending on the density, while roughly 3 cm of ablation was observed below the sonic ranger. Timelapse imagery reveals that both snow and ice ablation occurred during this period, which raises the question of how much snow sublimated between the ice hummocks. Hence, future investigations could take advantage of both timelapse imagery and AWS observations in order to separate sublimation from snow erosion. This could provide a new dataset to evaluate the LHF and the amount of snow erosion in models.

20 years of observed SEB over the K-transect (2003-2023)

August 2023 will mark the 30th anniversary of meteorological observations at S5 (Smeets et al., 2018), and the 20th anniversary of continuous SEB and SMB observations on the K-transect (Kuipers Munneke et al., 2018b; Van de Wal et al., 2012). The measurements at these sites have been widely used for mass balance investigations, model development, model evaluation, and validation of remote sensing products. Maintaining an up-to-date database is crucial to keep providing independent, in situ observations to the entire research community. An interesting perspective is to extend the time-series provided by Kuipers Munneke et al. (2018b) until today. In Figure 7.3 we show preliminary results from the SEB model forced with 19 years of observations at S5 (2003-2022). This uniquely long SEB record in the ablation zone of the Greenland ice sheet will undoubtedly be an important benchmark for future research.
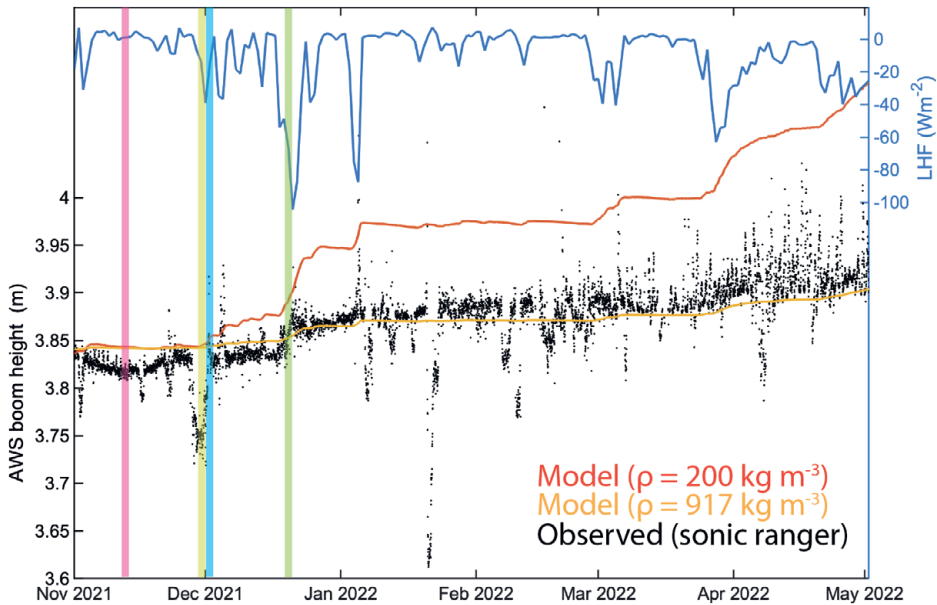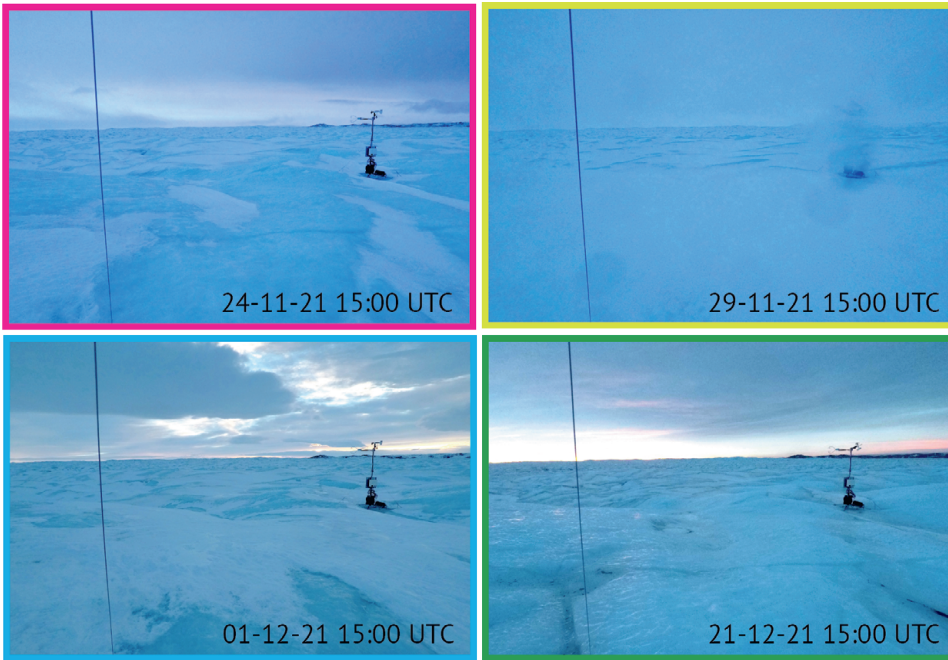
Figure 7.2: **Top four photographs**: screenshots of a timelapse camera showing the eddy covariance station at site S5. **bottom panel**: modelled daily LHF (blue line), observed surface and modelled cumulative surface sublimation using two different values for surface density (ρ). The coloured vertical bars denote the times of the timelapse photographs shown on top.
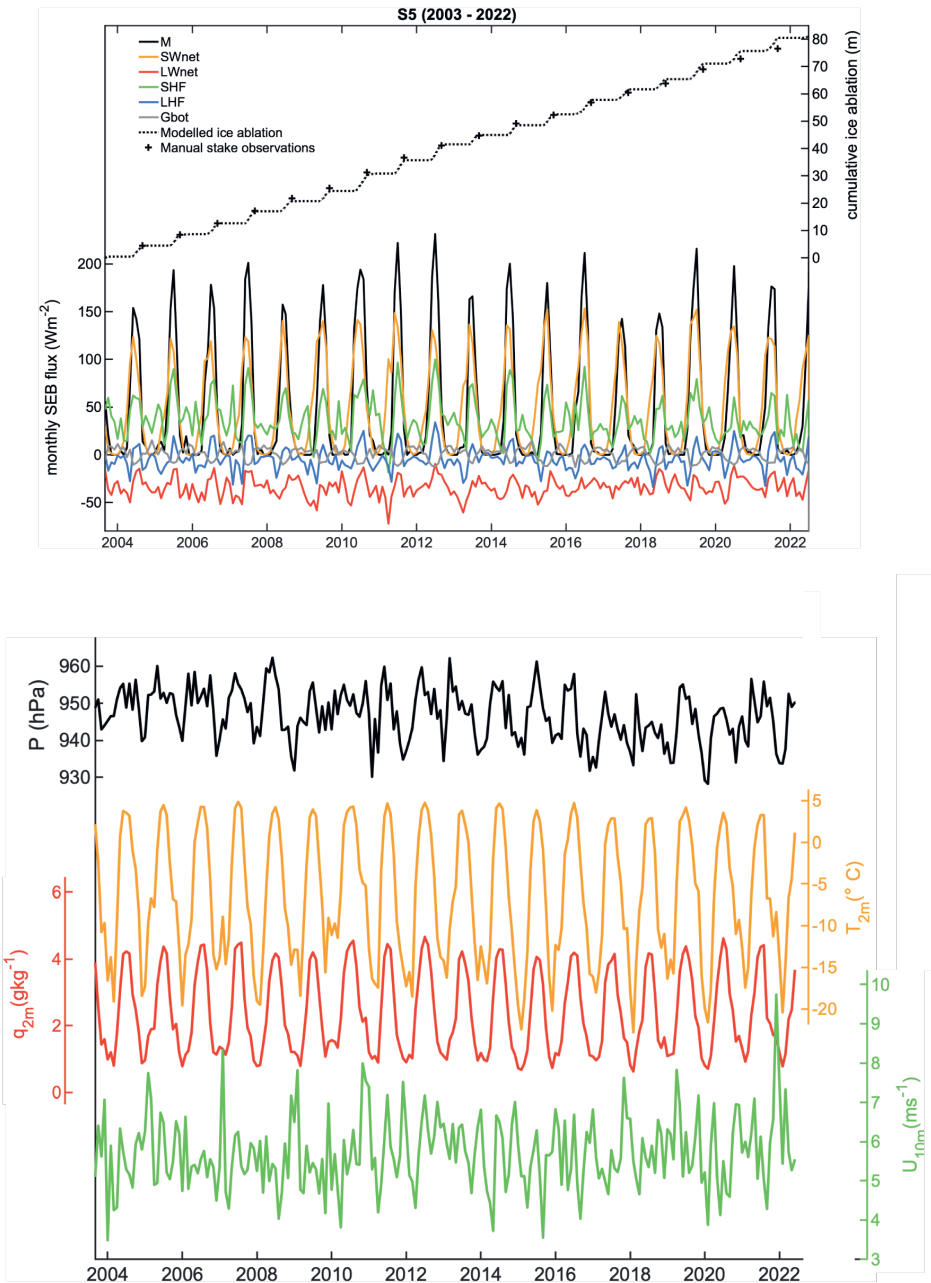
Figure 7.3: **Top**: Monthly SEB fluxes modelled at S5 using AWS observations, and cumulative ice ablation. **Bottom**: Monthly observed air pressure, 2m air temperature, 2m specific humidity and 10 m wind speed at S5.

7.2.3 Remote sensing of surface topography

Map of surface roughness across the entire Greenland ice sheet using ICESat-2

The methods to estimate surface roughness from ICESat-2 data (chapter 4) were extended to the entire Greenland ice sheet in the period October 2018-March 2022. The preliminary resulting map of surface roughness, defined here as the standard deviation of the detrended surface topography in 200-m transects, is shown in Figure 7.4. This map confirms the main finding from chapter 4 that surface roughness mainly decreases with elevation. Yet, some unexpected features are found, such as the relatively rougher northeastern part of the ice sheet. This map can be used for future studies of Greenland ice sheet surface processes. These methods could also be applied to other areas, such as the Antarctic ice sheet.

Repeat UAV surveying

The results of this thesis have raised the question of how variable the surface ablation is in a small area (less than 1 km^2) surrounding a measurement site. This variability explains the variation of aerodynamic surface roughness in time, and the different measured ablation rates, both addressed in chapter 5. Quantifying this subgrid surface melt is possible using repeat UAV surveys. A preliminary comparison of three UAV surveys performed during 2019, 2020 and 2021 at site S5 is shown in Figure 7.5. The elevation profiles are estimated using the methods from chapter 4. The overall variability in topography is similar between the years, yet it appears that the depth of the melt channel decreased from 2019 to 2021. Furthermore, the preliminary data suggest that some hummocks have changed in both height and position between years. Complementing continuous SEB and SMB measurements with repeat UAV surveys will yield a crucial dataset used to either: (1) benchmark SMB and SEB downscaling methods or (2) reduce the measurement uncertainty or (3) close the SEB from measurements only.

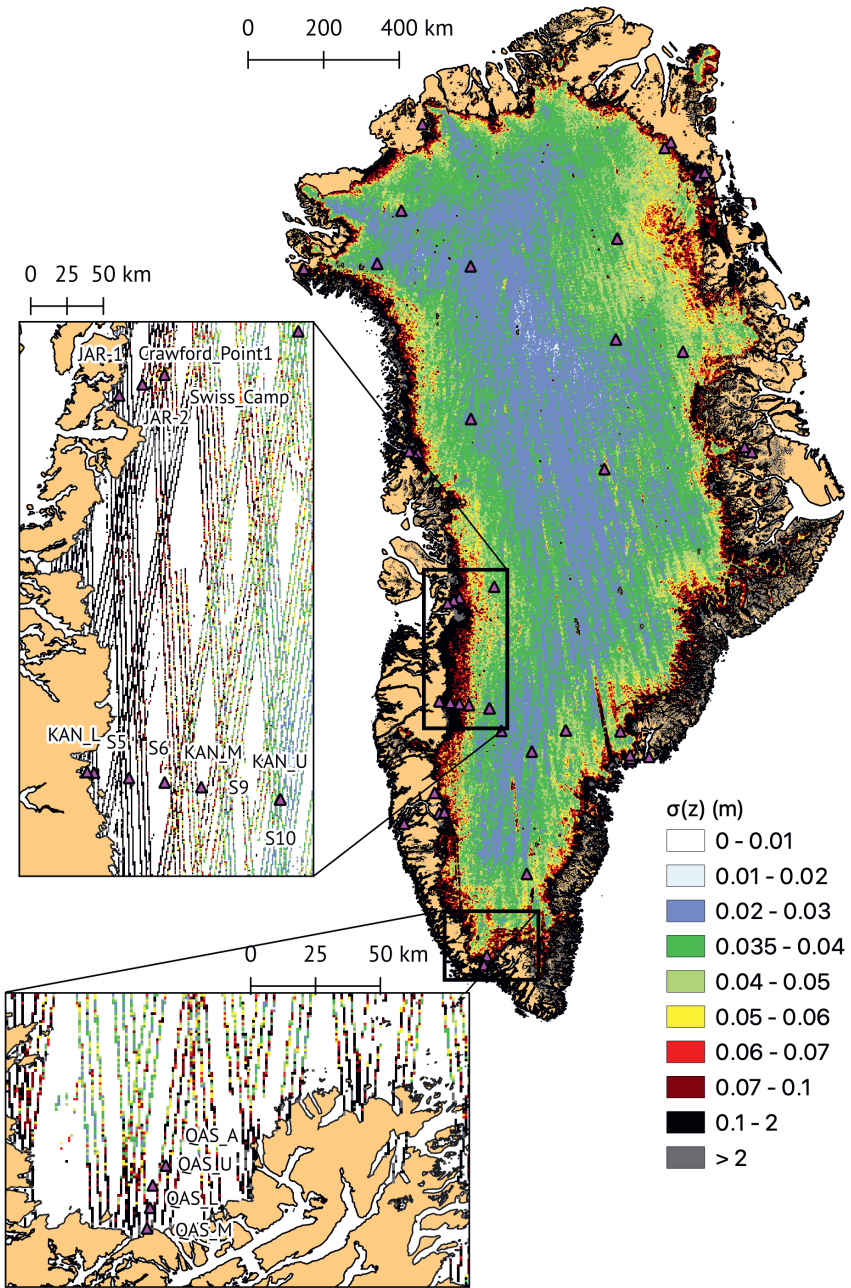Figure 7.4: Estimated standard deviation of elevation over the grounded ice sheet in 200m profiles after linear detrending, using ALT03D data from ICESat-2 during cycles 1-14 (October 2018 - March 2022). The data were gridded, interpolated and smoothed. The insets show the data before interpolation around the K-transect and Q-transect. Pink triangles denote the GC-Net, IMAU & PROMICE AWS locations.
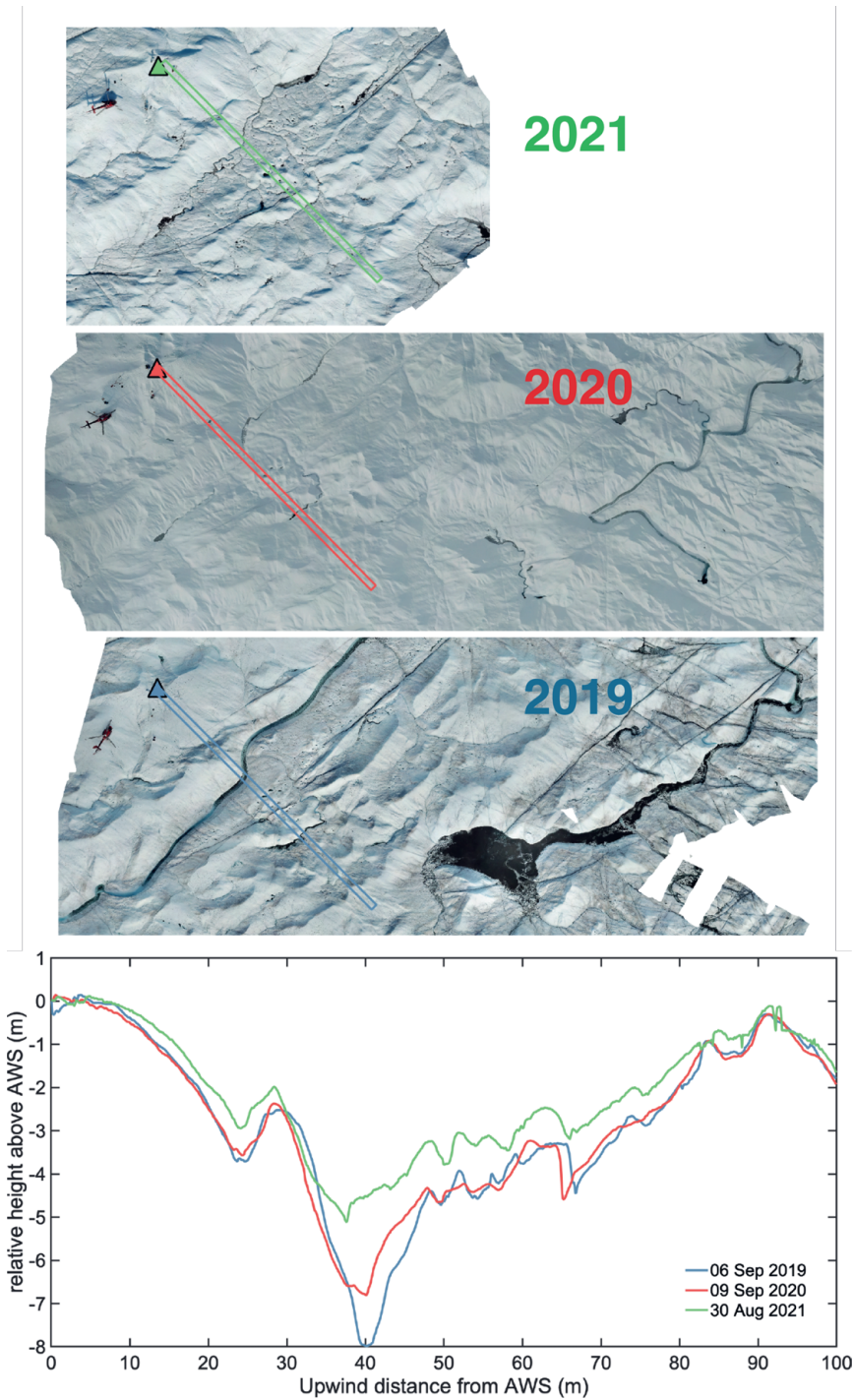
Figure 7.5: Top three images: UAV orthomosaic picture taken during the yearly visit at S5 in 2019 (blue), 2020 (red) and 2021 (green). Bottom panel: Measured relative topography in the katabatic wind direction at S5 using UAV photogrammetry. Triangles denote the location of the AWS at S5 in each picture.

7.3   Final word

Glaciers and ice sheets are powerful indicators of global climate change, and directly impact global sea-level. Therefore, accurately observing the present, and simulating the past and future mass loss of the ice sheets the best we can is crucial for society. We hope that this thesis demonstrates how the combination of simulations, remote sensing and field measurements yields the most complete picture of ice sheet mass loss. The benefit of field measurements should not be underestimated, since all scientific progress is built on observations.

Bibliography

Agosta, C., Amory, C., Kittel, C., Orsi, A., Favier, V., Gallée, H., Van den Broeke, M. R., Lenaerts, J. T., Van Wessem, J. M., Van De Berg, W. J., and Fettweis, X. (2019). Estimation of the Antarctic surface mass balance using the regional climate model MAR (1979-2015) and identification of dominant processes. *Cryosph.*, 13(1):281–296.

Ahlstrøm, A. P., Gravesen, P., Andersen, S. B., van As, D., Citterio, M., Fausto, R. S., Nielsen, S., Jepsen, H. F., Kristensen, S. S., Christensen, E. L., Stenseng, L., Forsberg, R., Hanson, S., and Petersen, D. (2008). A new programme for monitoring the mass loss of the Greenland ice sheet. *Geol. Surv. Denmark Greenl. Bull.*, (15):61–64.

Ambach, W. (1960). Investigations of the heat balance in the area of ablation on the Greenland Ice Cap. *Arch. für Meteorol. Geophys. und Bioklimatologie, Ser. B*, 3(10):279–288.

Andersen, M. L., Stenseng, L., Skourup, H., Colgan, W., Khan, S. A., Kristensen, S. S., Andersen, S. B., Box, J. E., Ahlstrøm, A. P., Fettweis, X., and Forsberg, R. (2015). Basin-scale partitioning of Greenland ice sheet mass balance components (2007-2011). *Earth Planet. Sci. Lett.*, 409:89–95.

Andreas, E. (1986). A theory for the scalar roughness and the scalar transfer coefficients over snow and sea ice. *Boundary-Layer Meteorol.*, 38:159–184.

Andreas, E. (2002). Parameterizing Scalar Transfer over Snow and Ice: A Review. *J. Hydrometeorol.*, 3(4):417–432.

Andreas, E. L. (1995). Air-ice drag coefficients in the western Weddell Sea 2. A model based on form drag and drifting snow. *J. Geophys. Res.*, 100(C3):4833–4843.

Arya, S. P. S. (1975). A Drag Partition Theory for Determining the Large-Scale Roughness Parameter and Wind Stress on the Arctic Pack Ice. *J. Geophys. Res.*, 80(24).

Ataktürk, S. S. and Katsaros, K. B. (1989). The K-Gill: A twin propeller-vane anemometer for measurements of atmospheric turbulence. *J. Atmos. Ocean. Technol.*, 6:509–515.

Aubinet, M., Grelle, A., Ibrom, A., Rannik, U., Moncrieff, J., Foken, T., Kowalski, A., Martin, P., Berbiger, P., Bernhofer, C., Clement, R., Elbers, J., Granier, A., Grünwald, T., Morgenstern, K., Pilegaard, K., Rebmann, C., Snijders, W., Valentini, R., and Vesala, T. (2000). Estimates of the Annual Net Carbon and Water Exchange: The EUROFLUX Methodology. *Adv. Ecol. Res. Vol 30*, 30:113–175.

Bamber, J. L., Westaway, R. M., Marzeion, B., and Wouters, B. (2018). The land ice contribution to sea level during the satellite era. *Environ. Res. Lett.*, 13(6).

Barnes, E. A. and Hartmann, D. L. (2012). Detection of Rossby wave breaking and its response to shifts of the midlatitude jet with climate change. *J. Geophys. Res. Atmos.*, 117(9):1–17.

Barr, W. (2015). Alfred de Quervain's Swiss Greenland expeditions, 1909 and 1912. *Polar Rec. (Gr. Brit).*, 51(4):366–385.

Bauer, A. (1955). The balance of the Greenland Ice Sheet. *J. Glaciol.*, 2(17):456–462.

Bauer, A. (1967). Nouvelle estimation du bilan de masse de l'Indlandsis du Groenland. *Deep. Res. Oceanogr. Abstr.*, 14(1):13–17.

Behrens, K. (2021). *Radiation Sensors*, pages 297–357. Springer International Publishing, Cham.

Blanford, J. H. and Gay, L. W. (1992). Tests of a robust eddy correlation system for sensible heat flux. *Theor. Appl. Climatol.*, 46:53–60.

Bonekamp, P. N., Van Heerwaarden, C. C., Steiner, J. F., and Immerzeel, W. W. (2020). Using 3D turbulence-resolving simulations to understand the impact of surface properties on the energy balance of a debris-covered glacier. *Cryosph.*, 14(5):1611–1632.

Bosveld, F. and Beljaars, A. (2001). The impact of sampling rate on eddy-covariance flux estimates. *Agric. For. Meteorol.*, 109:39–45.

Box, J. E. (2013). Greenland ice sheet mass balance reconstruction. Part II: Surface mass balance (1840-2010). *J. Clim.*, 26(18):6974–6989.

Box, J. E. and Steffen, K. (2001). Sublimation on the Greenland ice sheet from automated weather station observations. *J. Geophys. Res.*, 106(D24):965–981.

Box, J. E., Wehrlé, A., van As, D., Fausto, R. S., Kjeldsen, K. K., Dachauer, A., Ahlstrøm, A. P., and Picard, G. (2022). Greenland Ice Sheet Rainfall, Heat and Albedo Feedback Impacts From the Mid-August 2021 Atmospheric River. *Geophys. Res. Lett.*, 49(11).

Braithwaite, R. (1986). Assessment of mass-balance variations within a sparse stake network, Qamanarssup sermia, West Greenland. *J. Glaciol.*, 32(110):50–53.

Braithwaite, R. J. (1995). Aerodynamic stability and turbulent sensible-heat flux over a melting ice surface, the Greenland ice sheet. *J. Glaciol.*, 41(139).

Braithwaite, R. J., Konzelmann, T., Marty, C., and Ulesen, O. B. (1998). Errors in daily ablation measurements in northern Greenland, 1993-94, and their implications for glacier climate studies. *J. Glaciol.*, 44(148):583–588.

Brock, B. W., Willis, I. C., and Sharp, M. J. (2006). Measurement and parameterization of aerodynamic roughness length variations at Haut Glacier d'Arolla, Switzerland. *J. Glaciol.*, 52(177).

Brunt, K. M., Neumann, T. A., and Smith, B. E. (2019). Assessment of ICESat-2 Ice Sheet Surface Heights, Based on Comparisons Over the Interior of the Antarctic Ice Sheet. *Geophys. Res. Lett.*, 46(22):13072–13078.

Brutsaert, W. (1982). *Evaporation into the atmosphere: theory, history and applications.* Springer, Dordrecht, 1 edition.

Bushuk, M., Holland, D. M., Stanton, T. P., Stern, A., and Gray, C. (2019). Ice scallops: a laboratory investigation of the ice–water interface. *J. Fluid Mech.*, 873:942–976.

Chambers, J. R., Smith, M. W., Quincey, D. J., Carrivick, J. L., Ross, A. N., and James, M. R. (2019). Glacial aerodynamic roughness estimates: uncertainty, sensitivity and precision in field measurements. *J. Geophys. Res. Earth Surf.*

Colgan, W., Mankoff, K. D., Kjeldsen, K. K., Bjørk, A. A., Box, J. E., Simonsen, S. B., Sørensen, L. S., Khan, S. A., Solgaard, A. M., Forsberg, R., Skourup, H., Stenseng, L., Kristensen, S. S., Hvidegaard, S. M., Citterio, M., Karlsson, N., Fettweis, X., Ahlstrøm, A. P., Andersen, S. B., Van As, D., and Fausto, R. S. (2019). Greenland ice sheet mass balance assessed by PROMICE (1995-2015). *Geol. Surv. Denmark Greenl. Bull.*, 43:1–6.

Conway, J. P. and Cullen, N. J. (2013). Constraining turbulent heat flux parameterization over a temperate maritime glacier in New Zealand. *Ann. Glaciol.*, 54(63):41–51.

Cooper, M. G., Smith, L. C., Rennermalm, A. K., Tedesco, M., Muthyala, R., Leidman, S. Z., Moustafa, S. E., and Fayne, J. V. (2021). Spectral attenuation coefficients from measurements of light transmission in bare ice on the Greenland Ice Sheet. *Cryosph.*, 15(4):1931–1953.

Csatho, B. M., Schenk, A. F., van der Veen, C. J., Babonis, G., Duncan, K., Rezvanbehbahani, S., van den Broeke, M. R., Simonsen, S. B., Nagarajan, S., and van Angelen, J. H. (2014). Laser altimetry reveals complex pattern of Greenland Ice Sheet dynamics. *Proc. Natl. Acad. Sci.*, 111(52):18478–18483.

Denby, B. (1999). Second-order modelling of turbulence in katabatic flows. *Boundary-Layer Meteorol.*, 92(1):67–100.

Edwards, T. L., Nowicki, S., Marzeion, B., Hock, R., Goelzer, H., Seroussi, H., Jourdain, N. C., Slater, D. A., Turner, F. E., Smith, C. J., McKenna, C. M., Simon, E., Abe-Ouchi, A., Gregory, J. M., Larour, E., Lipscomb, W. H., Payne, A. J., Shepherd, A., Agosta, C., Alexander, P., Albrecht, T., Anderson, B., Asay-Davis, X., Aschwanden, A., Barthel, A., Bliss, A., Calov, R., Chambers, C., Champollion, N., Choi, Y., Cullather, R., Cuzzone, J., Dumas, C., Felikson, D., Fettweis, X., Fujita, K., Galton-Fenzi, B. K., Gladstone, R., Golledge, N. R., Greve, R., Hattermann, T., Hoffman, M. J., Humbert, A., Huss, M., Huybrechts, P., Immerzeel, W., Kleiner, T., Kraaijenbrink, P., Le clec'h, S., Lee, V., Leguy, G. R., Little, C. M., Lowry, D. P., Malles, J. H., Martin, D. F., Maussion, F., Morlighem, M., O'Neill, J. F., Nias, I., Pattyn, F., Pelle, T., Price, S. F., Quiquet, A., Radić, V., Reese, R., Rounce, D. R., Rückamp, M., Sakai, A., Shafer, C., Schlegel, N. J., Shannon, S., Smith, R. S., Straneo, F., Sun, S., Tarasov, L., Trusel, L. D., Van Breedam, J., van de Wal, R., van den Broeke, M., Winkelmann, R., Zekollari, H., Zhao, C., Zhang, T., and Zwinger, T. (2021). Projected land ice contributions to twenty-first-century sea level rise. *Nature*, 593(7857):74–82.

Elvidge, A. D., Renfrew, I. A., Brooks, I. M., Srivastava, P., Yelland, M., and Prytherch, J. (2021). Surface heat and moisture exchange in the marginal ice zone: Observations and a new parameterization scheme for weather and climate models 1Elvidge,. *J. Geophys. Res. Atmos.*

Ettema, J., Van den Broeke, M. R., Van Meijgaard, E., Van De Berg, W. J., Box, J. E., and Steffen, K. (2010). Climate of the Greenland ice sheet using a high-resolution climate model - Part 1: Evaluation. *Cryosph.*, 4(4):511–527.

Farinotti, D., Huss, M., Fürst, J. J., Landmann, J., Machguth, H., Maussion, F., and Pandit, A. (2019). A consensus estimate for the ice thickness distribution of all glaciers on Earth. *Nat. Geosci.*, 12(3):168–173.

Fausto, R. S., Ahlstrøm, A. P., Van As, D., Bøggild, C. E., and Johnsen, S. J. (2009). A new present-day temperature parameterization for Greenland. *J. Glaciol.*, 55(189):95–105.

Fausto, R. S., Van As, D., Ahlstrøm, A. P., and Citterio, M. (2012). Instruments and methods: Assessing the accuracy of Greenland ice sheet ice ablation measurements by pressure transducer. *J. Glaciol.*, 58(212):1144–1150.

Fausto, R. S., van As, D., Box, J. E., Colgan, W., and Langen, P. L. (2016a). Quantifying the surface energy fluxes in south Greenland during the 2012 high melt episodes using in-situ observations. *Front. Earth Sci.*, 4(82).

Fausto, R. S., van As, D., Box, J. E., Colgan, W., Langen, P. L., and Mottram, R. H. (2016b). The implication of nonradiative energy fluxes dominating Greenland ice sheet exceptional ablation area surface melt in 2012. *Geophys. Res. Lett.*, 43(6):2649–2658.

Fausto, R. S., Van As, D., Mankoff, K. D., Vandecrux, B., Citterio, M., Ahlstrøm, A. P., Andersen, S. B., Colgan, W., Karlsson, N. B., Kjeldsen, K. K., Korsgaard, N. J., Larsen, S. H., Nielsen, S., Pedersen, A., Shields, C. L., Solgaard, A. M., and Box, J. E. (2021). Programme for Monitoring of the Greenland Ice Sheet (PROMICE) automatic weather station data. *Earth Syst. Sci. Data*, 13(8):3819–3845.

Favier, L., Jourdain, N. C., Jenkins, A., Merino, N., Durand, G., Gagliardini, O., Gillet-Chaulet, F., and Mathiot, P. (2019). Assessment of sub-shelf melting parameterisations using the ocean-ice-sheet coupled model NEMO(v3.6)-Elmer/Ice(v8.3). *Geosci. Model Dev.*, 12(6):2255–2283.

Felikson, D., Urban, T. J., Gunter, B. C., Pie, N., Pritchard, H. D., Harpold, R., and Schutz, B. E. (2017). Comparison of Elevation Change Detection Methods from ICESat Altimetry over the Greenland Ice Sheet. *IEEE Trans. Geosci. Remote Sens.*, 55(10):5494–5505.

Fettweis, X., Franco, B., Tedesco, M., Van Angelen, J. H., Lenaerts, J. T., Van den Broeke, M. R., and Gallée, H. (2013). Estimating the Greenland ice sheet surface mass balance contribution to future sea level rise using the regional atmospheric climate model MAR. *Cryosph.*, 7(2):469–489.

Fettweis, X., Hofer, S., Krebs-Kanzow, U., Amory, C., Aoki, T., Berends, C., Born, A., Box, J., Delhasse, A., Fujita, K., Gierz, P., Goelzer, H., Hanna, E., Hashimoto, A., Huybrechts, P., Kapsch, M.-L., King, M., Kittel, C., Lang, C., Langen, P., Lenaerts, J., Liston, G., Lohmann, G., Mernild, S., Mikolajewicz, U., Modali, K., Mottram, R., Niwano, M., Noël, B., Ryan, J., Smith, A., Streffing, J., Tedesco, M., van de Berg, W. J., van den Broeke, M., van de Wal, R., van Kampenhout, L., Wilton, D., Wouters, B., Ziemen, F., and Zolles, T. (2020). GrSMBMIP: Intercomparison of the modelled 1980–2012 surface mass balance over the Greenland Ice sheet. *Cryosph.*, 2020:1–35.

Fichtl, G. H. and Kumar, P. (1974). The response of a propeller anemometer to turbulent flow with the mean wind vector perpendicular to the axis of rotation. *Boundary-Layer Meteorol.*, 6:363–379.

Finnigan, J. J., Clement, R., Malhi, Y., Leuning, R., and Cleugh, H. A. (2003). A Re-Evaluation of Long-Term Flux Measurement Techniques Part I : Averaging and Coordinate Rotation. *Boundary-Layer Meteorol.*, pages 1–48.

Finsterwalder, R. (1959). Expédition glaciologique internationale au groenland 1957–60 (e.g.i.g.). *Journal of Glaciology*, 3(26):542–546.

Fitzpatrick, N., Radić, V., and Menounos, B. (2017). Surface energy balance closure and turbulent flux parameterization on a mid-latitude mountain Glacier, Purcell mountains, Canada. *Front. Earth Sci.*, 5(September):1–20.

Fitzpatrick, N., Radić, V., and Menounos, B. (2019). A multi-season investigation of glacier surface roughness lengths through in situ and remote observation. *Cryosph.*, 13:1051–1071.

Foken, T. (2008). *Micrometeorology*, volume 2. Springer.

Forrer, J. and Rotach, M. W. (1997). On the turbulence structure in the stable boundary layer over the Greenland ice sheet. *Boundary-Layer Meteorol.*, 85(1):111–136.

Frank, J. M., Massman, W. J., Swiatek, E., Zimmerman, H. A., and Ewers, B. E. (2015). All sonic anemometers need to correct for transducer and structural shadowing in their velocity measurements. *J. Atmos. Ocean. Technol.*, 33:149–167.

Garbrecht, T., Lüpkes, C., Augstein, E., and Wamser, C. (1999). Influence of a sea ice ridge on low-level airflow. *J. Geophys. Res. Atmos.*, 104(D20):24499–24507.

Garbrecht, T., Lüpkes, C., Hartmann, J., and Wolff, M. (2002). Atmospheric drag coefficients over sea ice - Validation of a parameterisation concept. *Tellus, Ser. A Dyn. Meteorol. Oceanogr.*, 54(2):205–219.

Gardner, C. S. (1982). Target signatures for laser altimeters: an analysis. *Appl. Opt.*, 21(3):448.

Garratt, J. R. (1975). Limitations of the eddy-correlation technique for the determination of the turbulent fluxes near the surface. *Boundary-Layer Meteorol.*, 8:255–259.

Garratt, J. R. (1980). Surface influence upon vertical profiles in the atmospheric near-surface layer. *Q. J. R. Meteorol. Soc.*, 106(450):803–819.

Garratt, J. R. (1992). *The atmospheric boundary layer.* Cambridge University Press, Cambridge.

Georgi, J., Holzapfel, R., and Kopp, W. (1935). *Wissenschaftliche Ergebnisse der Deutschen Grönland-Expedition Alfred Wegener 1929 und 1930/31. Meteorologie: das Beobachtungsmaterial.* Brockhaus.

Gill, G. C. (1975). Development and use of the Gill UVW anemometer. *Boundary-Layer Meteorol.*, 8:475–495.

Goelzer, H., Nowicki, S., Payne, A., Larour, E., Seroussi, H., Lipscomb, W. H., Gregory, J., Abe-Ouchi, A., Shepherd, A., Simon, E., Agosta, C., Alexander, P., Aschwanden, A., Barthel, A., Calov, R., Chambers, C., Choi, Y., Cuzzone, J., Dumas, C., Edwards, T., Felikson, D., Fettweis, X., Golledge, N. R., Greve, R., Humbert, A., Huybrechts, P., Le Clec'H, S., Lee, V., Leguy, G., Little, C., Lowry, D., Morlighem, M., Nias, I., Quiquet, A., Rückamp, M., Schlegel, N. J., Slater, D. A., Smith, R., Straneo, F., Tarasov, L., Van de Wal, R., and Van den Broeke, M. R. (2020). The future sea-level contribution of the Greenland ice sheet: A multi-model ensemble study of ISMIP6. *Cryosph.*, 14(9):3071–3096.

Gourmelen, N., Escorihuela, M. J., Shepherd, A., Foresta, L., Muir, A., Garcia-Mondéjar, A., Roca, M., Baker, S. G., and Drinkwater, M. R. (2018). CryoSat-2 swath interferometric altimetry for mapping ice elevation and elevation change. *Adv. Sp. Res.*, 62(6):1226–1242.

Groh, A. and Horwath, M. (2021). Antarctic ice mass change products from GRACE/GRACE-fo using tailored sensitivity kernels. *Remote Sens.*, 13(9).

Guo, X., Yang, K., Zhao, L., Yang, W., Li, S., Zhu, M., Yao, T., and Chen, Y. (2011). Critical Evaluation of Scalar Roughness Length Parametrizations Over a Melting Valley Glacier. *Boundary-Layer Meteorol.*, 139(2):307–332.

Hanna, E., Cappelen, J., Fettweis, X., Mernild, S. H., Mote, T. L., Mottram, R., Steffen, K., Ballinger, T. J., and Hall, R. J. (2021). Greenland surface air temperature changes from 1981 to 2019 and implications for ice-sheet melt and mass-balance change. *Int. J. Climatol.*, 41(S1):E1336–E1352.

Hanssen-Bauer, I. and Gjessing, Y. T. (1988). Observations and model calculations of aerodynamic drag on sea ice in the Fram Strait. *Tellus A Dyn. Meteorol. Oceanogr.*, 40(2):151–161.

Harman, I. N. and Finnigan, J. J. (2007). A simple unified theory for flow in the canopy and roughness sublayer. *Boundary-Layer Meteorol.*, 123(2):339–363.

Heinemann, G. (1999). The KABEG'97 field experiment: An aircraft-based study of Katabatic wind dynamics over the Greenland ice sheet. *Boundary-Layer Meteorol.*, 93(1):75–116.

Hengl, T. (2009). *A practical guide to geostatistical mapping.*

Henneken, E. A., Bink, N. J., Vugts, H. F., Cannemeijer, F., and Meesters, A. G. (1994). A case study of the daily energy balance near the equilibrium line on the Greenland ice sheet. *Glob. Planet. Change*, 9(1-2):69–78.

Hermann, M., Box, J. E., Fausto, R. S., Colgan, W. T., Langen, P. L., Mottram, R., Wuite, J., Noël, B., van den Broeke, M. R., and van As, D. (2018). Application of PROMICE Q-Transect in situ accumulation and ablation measurements (2000-2017) to constrain mass balance at the southern tip of the Greenland ice sheet. *J. Geophys. Res. Earth Surf.*, 123(6):1235–1256.

Herzfeld, U. C., Box, J. E., Steffen, K., Mayer, H., Caine, N., and Losleben, M. V. (2006). A Case Study or the Influence of Snow and Ice Surface Roughness on Melt Energy. *Zeitschrift Gletscherkd. Glazialgeol.*, 39:1–42.

Herzfeld, U. C., Trantow, T., Lawson, M., Hans, J., and Medley, G. (2020). Surface heights and crevasse morphologies of surging and fast-moving glaciers from ICESat-2 laser altimeter data - Application of the density-dimension algorithm (DDA- ice) and evaluation using airborne altimeter and Planet SkySat data. *Sci. Remote Sens.*, page 104743.

Hicks, B. B. (1972). Propeller anemometers as sensors of atmospheric turbulence. *Boundary-Layer Meteorol.*, 3:214–228.

Holtslag, A. A. M. and De Bruin, H. A. R. (1988). Applied modeling of the nighttime surface energy balance over land. *J. Appl. Meteorol.*, 27:689–704.

Hori, M., Aoki, T., Tanikawa, T., Motoyoshi, H., Hachikubo, A., Sugiura, K., Yasunari, T. J., Eide, H., Storvold, R., Nakajima, Y., and Takahashi, F. (2006). In-situ measured spectral directional emissivity of snow and ice in the 8-14 μm atmospheric window. *Remote Sens. Environ.*, 100(4):486–502.

Horst, T. W. (1973). Corrections for response errors in a three-component propeller anemometer. *J. Appl. Meteorol.*, 12:716–725.

Horst, T. W. (1997). A simple formula for attenuation of eddy fluxes measured with first-order-response scalar sensors. *Boundary-Layer Meteorol.*, 82:219–233.

Horst, T. W. (2000). On frequency response corrections for eddy covariance flux measurements. *Boundary-Layer Meteorol.*, 94(3):517–520.

Horst, T. W., Kleissl, J., Lenschow, D. H., Meneveau, C., Moeng, C. H., Parlange, M. B., Sullivan, P. P., and Weil, J. C. (2004). HATS: Field observations to obtain spatially filtered turbulence fields from crosswind arrays of sonic anemometers in the atmospheric surface layer. *J. Atmos. Sci.*, 61:1566–1581.

Horst, T. W., Semmer, S. R., and Maclean, G. (2015). Correction of a non-orthogonal, three-component sonic anemometer for flow distortion by transducer shadowing. *Boundary-Layer Meteorol.*, 155:371–395.

Howat, I. M., Negrete, A., and Smith, B. E. (2014). The Greenland Ice Mapping Project (GIMP) land classification and surface elevation data sets. *Cryosph.*, 8(4):1509–1518.

Huai, B., Van den Broeke, M. R., and Reijmer, C. H. (2020). Long-term surface energy balance of the western Greenland Ice Sheet and the role of large-scale circulation variability. *Cryosph.*, 14(11):4181–4199.

Hulth, J. (2010). Using a draw-wire sensor to continuously monitor glacier melt. *J. Glaciol.*, 56(199):922–924.

Ibrom, A., Dellwik, E., Flyvbjerg, H., Jensen, N. O., and Pilegaard, K. (2007). Strong low-pass filtering effects on water vapour flux measurements with closed-path eddy correlation systems. *Agric. For. Meteorol.*, 147:140–156.

Immerzeel, W. W., Kraaijenbrink, P. D. A., Shea, J. M., Shrestha, A. B., Pellicciotti, F., Bierkens, M. F. P., and Jong, S. M. D. (2014). Remote Sensing of Environment High-resolution monitoring of Himalayan glacier dynamics using unmanned aerial vehicles. *Remote Sens. Environ.*, 150:93–103.

IPCC (1990). *Climate change: the IPCC scientific assessment*, volume 80. Cambridge, MA (United States); Cambridge University Press.

IPCC (2021). *Climate Change 2021: The Physical Science Basis. Contribution of Working Group I to the Sixth Assessment Report of the Intergovernmental Panel on Climate Change*, volume In Press. Cambridge University Press, Cambridge, United Kingdom and New York, NY, USA.

Jackson, P. (1981). On the displacement height in the logarithmic velocity profile. *J. Fluid Mech.*, 111(1981):15–25.

Jakobs, C. L., Reijmer, C. H., Kuipers Munneke, P., König-Langlo, G., and Van den Broeke, M. R. (2019). Quantifying the snowmelt-albedo feedback at Neumayer Station, East Antarctica. *Cryosph.*, 13(5):1473–1485.

James, M. R. and Robson, S. (2014). Mitigating systematic error in topographic models derived from UAV and ground-based image networks. *Earth Surf. Process. Landforms*, 39(10):1413–1420.

Joffre, S. M. (1988). Modelling the dry deposition velocity of highly soluble gases to the sea surface. *Atmos. Environ.*, 22(6):1137–1146.

Jouzel, J. (2013). A brief history of ice core science over the last 50 yr. *Clim. Past*, 9(6):2525–2547.

Kaimal, J., Wyngaard, J. C., Izumi, Y., and Coté, O. R. (1972). Spectral characteristics of surface-layer turbulence. *Q. J. R. Meteorol. Soc.*, 98(417):563–589.

Kaimal, J. C. and Finnigan, J. J. (1994). *Atmospheric boundary layer flows: their structure and measurement.* Oxford University Press, New York.

Kanda, M., Kanega, M., Kawai, T., Moriwaki, R., and Sugawara, H. (2007). Roughness lengths for momentum and heat derived from outdoor urban scale models. *J. Appl. Meteorol. Climatol.*, 46(7):1067–1079.

Karlsson, N. B., Solgaard, A. M., Mankoff, K. D., Gillet-Chaulet, F., MacGregor, J. A., Box, J. E., Citterio, M., Colgan, W. T., Larsen, S. H., Kjeldsen, K. K., Korsgaard, N. J., Benn, D. I., Hewitt, I. J., and Fausto, R. S. (2021). A first constraint on basal melt-water production of the Greenland ice sheet. *Nat. Commun.*, 12(1):1–10.

Kean, J. W. and Smith, J. D. (2006). Form drag in rivers due to small-scale natural topographic features: 2. Irregular sequences. *J. Geophys. Res. Earth Surf.*, 111(4):1–15.

King, M. D., Howat, I. M., Candela, S. G., Noh, M. J., Jeong, S., Noël, B. P., van den Broeke, M. R., Wouters, B., and Negrete, A. (2020). Dynamic ice loss from the Greenland Ice Sheet driven by sustained glacier retreat. *Commun. Earth Environ.*, 1(1):1–7.

Kjeldsen, K. K., Korsgaard, N. J., Bjørk, A. A., Khan, S. A., Box, J. E., Funder, S., Larsen, N. K., Bamber, J. L., Colgan, W., Van den Broeke, M., Siggaard-Andersen, M. L., Nuth, C., Schomacker, A., Andresen, C. S., Willerslev, E., and Kjær, K. H. (2015). Spatial and temporal distribution of mass loss from the Greenland Ice Sheet since AD 1900. *Nature*, 528(7582):396–400.

Klein, T. and Heinemann, G. (2002). Interaction of katabatic winds and mesocyclones near the eastern coast of Greenland. *Meteorol. Appl.*, 9(4):407–422.

Kljun, N., Calanca, P., Rotach, M. W., and Schmid, H. P. (2015). A simple two-dimensional parameterisation for Flux Footprint Prediction (FFP). *Geosci. Model Dev.*, 8(11):3695–3713.

Kraaijenbrink, P. D., Shea, J. M., Pellicciotti, F., Jong, S. M., and Immerzeel, W. W. (2016). Object-based analysis of unmanned aerial vehicle imagery to map and characterise surface features on a debris-covered glacier. *Remote Sens. Environ.*, 186:581–595.

Kuipers Munneke, P., Luckman, A. J., Bevan, S. L., Smeets, C. J. P. P., Gilbert, E., van den Broeke, M. R., Wang, W., Zender, C., Hubbard, B., Ashmore, D., Orr, A., King, J. C., and Kulessa, B. (2018a). Intense winter surface melt on an Antarctic ice shelf. *Geophys. Res. Lett.*, 45(15):7615–7623.

Kuipers Munneke, P., Smeets, C. J. P. P., Reijmer, C. H., Oerlemans, J., van de Wal, R. S. W., and van den Broeke, M. R. (2018b). The K-transect on the western Greenland Ice Sheet: Surface energy balance (2003–2016). *Arctic, Antarct. Alp. Res.*, 50(1):S100003.

Kuipers Munneke, P., Van den Broeke, M. R., Lenaerts, J. T., Flanner, M. G., Gardner, A. S., and Van De Berg, W. J. (2011). A new albedo parameterization for use in climate models over the Antarctic ice sheet. *J. Geophys. Res. Atmos.*, 116(5):1–10.

Kurtz, N. T., Markus, T., Cavalieri, D. J., Krabill, W., Sonntag, J. G., and Miller, J. (2008). Comparison of ICESat data with airborne laser altimeter measurements over arctic sea ice. *IEEE Trans. Geosci. Remote Sens.*, 46(7):1913–1924.

Larue, F., Picard, G., Arnaud, L., Ollivier, I., Delcourt, C., Lamare, M., Tuzet, F., Revuelto, J., and Dumont, M. (2020). Snow albedo sensitivity to macroscopic surface roughness using a new ray-tracing model. *Cryosph.*, 14(5):1651–1672.

Lee, X., Massman, W., and Law, B. (2004). *Handbook of micrometeorology: a guide for surface flux measurement and analysis*, volume 29. Springer Science & Business Media.

Lenaerts, J. T. M., Smeets, C. J. P. P., Nishimura, K., Eijkelboom, M., Boot, W., van den Broeke, M. R., and van de Berg, W. J. (2014). Drifting snow measurements on the Greenland ice sheet and their application for model evaluation. *Cryosph.*, 8:801–814.

Lenaerts, J. T. M., van den Broeke, M. R., Déry, S. J., van Meijgaard, E., van de Berg, W. J., Palm, S. P., and Sanz Rodrigo, J. (2012). Modeling drifting snow in Antarctica with a regional climate model: 1. Methods and model evaluation. *J. Geophys. Res. Atmos.*, 117(D5):n/a–n/a.

Lettau, H. (1969). Note on Aerodynamic Roughness-Parameter Estimation on the Basis of Roughness-Element Description.

Li, Q., Bou-Zeid, E., Grimmond, S., Zilitinkevich, S., and Katul, G. (2020). Revisiting the Relation Between Momentum and Scalar Roughness Lengths of Urban Surfaces. *Q. J. R. Meteorol. Soc.*, pages 1–31.

Liu, C. and Barnes, E. A. (2015). Extreme moisture transport into the Arctic linked to Rossby wave breaking. *J. Geophys. Res.*, 120(9):3774–3788.

Loewe, F. (1964). Das grönländische Inlandeis nach neuen Feststellungen (New Light on the Greenland Ice Sheet). *Erdkunde*, 18(3):189–202.

Lucas-Picher, P., Wulff-Nielsen, M., Christensen, J. H., Aoalgeirsdóttir, G., Mottram, R., and Simonsen, S. B. (2012). Very high resolution regional climate model simulations over Greenland: Identifying added value. *J. Geophys. Res. Atmos.*, 117(2):1–16.

Lunt, D. J., Foster, G. L., Haywood, A. M., and Stone, E. J. (2008). Late Pliocene Greenland glaciation controlled by a decline in atmospheric CO2 levels. *Nature*, 454(7208):1102–1105.

Lüpkes, C. and Gryanik, V. M. (2015). A stability-dependent parametrization of transfer coefficients for momentum and heat over polar sea ice to be used in climate models. *J. Geophys. Res.*, 120(2):552–581.

Lüpkes, C., Gryanik, V. M., Hartmann, J., and Andreas, E. L. (2012). A parametrization, based on sea ice morphology, of the neutral atmospheric drag coefficients for weather prediction and climate models. *J. Geophys. Res. Atmos.*, 117(13):1–18.

Lüpkes, C., Gryanik, V. M., Rösel, A., Birnbaum, G., and Kaleschke, L. (2013). Effect of sea ice morphology during Arctic summer on atmospheric drag coefficients used in climate models. *Geophys. Res. Lett.*, 40(2):446–451.

MacCready Jr., P. B. and Jex, H. R. (1964). Response characteristics and meteorological utilization of propeller and vane wind sensors. *J. Appl. Meteorol.*, 3:182–193.

Macdonald, R. W., Griffiths, R. F., and Hall, D. J. (1998). An improved method for the estimation of surface roughness of obstacle arrays. *Atmos. Environ.*, 32(11):1857–1864.

Machguth, H., Thomsen, H. H., Weidick, A., Ahlstrøm, A. P., Abermann, J., Andersen, M. L., Andersen, S. B., Bjørk, A. A., Box, J. E., Braithwaite, R. J., Bøggild, C. E., Citterio, M., Clement, P., Colgan, W., Fausto, R. S., Gleie, K., Gubler, S., Hasholt, B., Hynek, B., Knudsen, N. T., Larsen, S. H., Mernild, S. H., Oerlemans, J., Oerter, H., Olesen, O. B., Smeets, C. J., Steffen, K., Stober, M., Sugiyama, S., Van As, D., Van den Broeke, M. R., and Van de Wal, R. S. (2016). Greenland surface mass-balance observations from the ice-sheet ablation area and local glaciers. *J. Glaciol.*, 62(235):861–887.

Madsen, M. V., Steen-Larsen, H. C., Hörhold, M., Box, J., Berben, S. M., Capron, E., Faber, A. K., Hubbard, A., Jensen, M. F., Jones, T. R., Kipfstuhl, S., Koldtoft, I., Pillar, H. R., Vaughn, B. H., Vladimirova, D., and Dahl-Jensen, D. (2019). Evidence of isotopic fractionation during vapor exchange between the atmosphere and the snow surface in Greenland. *J. Geophys. Res. Atmos.*, 124:2932–2945.

Mankoff, K., Fettweis, X., Langen, P., Stendel, M., Kjledsen, K., Karlsson, N., Noël, B., van den Broeke, M. R., Colgan, W., Simonsen, S., Box, J., Solgaard, A., Ahlstrøm, A., Andersen, S. B., and Fausto, R. (2021). Greenland ice sheet mass balance from 1840 through next week. *Earth Syst. Sci. Data Discuss.*, pages 1–37.

Mankoff, K. D., Solgaard, A., Colgan, W., Ahlstrøm, A. P., Abbas Khan, S., and Fausto, R. S. (2020). Greenland Ice Sheet solid ice discharge from 1986 through March 2020. *Earth Syst. Sci. Data*, 12(2):1367–1383.

Markus, T., Neumann, T., Martino, A., Abdalati, W., Brunt, K., Csatho, B., Farrell, S., Fricker, H., Gardner, A., Harding, D., Jasinski, M., Kwok, R., Magruder, L., Lubin, D., Luthcke, S., Morison, J., Nelson, R., Neuenschwander, A., Palm, S., Popescu, S., Shum, C. K., Schutz, B. E., Smith, B., Yang, Y., and Zwally, J. (2017). The Ice, Cloud, and land Elevation Satellite-2 (ICESat-2): Science requirements, concept, and implementation. *Remote Sens. Environ.*, 190:260–273.

Massman, W. and Clement, R. (2005). Uncertainty in eddy covariance flux estimates resulting from spectral attenuation. In Lee, X., Massman, W., and Law, B., editors, *Handbook of Micrometeorology: A Guide for Surface Flux Measurement and Analysis*, pages 67–99. Springer Netherlands.

Massman, W. J. (2000). A simple method for estimating frequency response corrections for eddy covariance systems. *Agric. For. Meteorol.*, 104:185–198.

Mattingly, K. S., Mote, T. L., and Fettweis, X. (2018). Atmospheric River Impacts on Greenland Ice Sheet Surface Mass Balance. *J. Geophys. Res. Atmos.*, 123(16):8538–8560.

Mattingly, K. S., Mote, T. L., Fettweis, X., As, D. V., Tricht, K. V., Lhermitte, S., Pettersen, C., and Fausto, R. S. (2020). Strong summer atmospheric rivers trigger Greenland ice sheet melt through spatially varying surface energy balance and cloud regimes. *J. Clim.*, 33(16):6809–6832.

Mauder, M., Cuntz, M., Drüe, C., Graf, A., Rebmann, C., Schmid, H. P., Schmidt, M., and Steinbrecher, R. (2013). A strategy for quality and uncertainty assessment of long-term eddy-covariance measurements. *Agric. For. Meteorol.*, 169:122–135.

Mauder, M. and Zeeman, M. J. (2018). Field intercomparison of prevailing sonic anemometers. *Atmos. Meas. Tech.*, 11:249–263.

McBean, G. A. (1972). Instrument requirements for eddy correlation measurements. *J. Appl. Meteorol.*, 11:1078–1084.

McMillan, M., Leeson, A., Shepherd, A., Briggs, K., Armitage, T. W., Hogg, A., Kuipers Munneke, P., van den Broeke, M., Noël, B., van de Berg, W. J., Ligtenberg, S., Horwath, M., Groh, A., Muir, A., and Gilbert, L. (2016). A high-resolution record of Greenland mass balance. *Geophys. Res. Lett.*, 43(13):7002–7010.

Meesters, A. G., Bink, N. J., Vugts, H. F., Cannemeijer, F., and Henneken, E. A. (1997). Turbulence observations above a smooth melting surface on the Greenland ice sheet. *Boundary-Layer Meteorol.*, 85(1):81–110.

Miles, E. S., Steiner, J. F., and Brun, F. (2017). Highly variable aerodynamic roughness length (z0) for a hummocky debris-covered glacier. *J. Geophys. Res. Atmos.*, 122:8447–8466.

Miller, N. B., Shupe, M. D., Cox, C. J., Noone, D., Persson, P. O. G., and Steffen, K. (2017). Surface energy budget responses to radiative forcing at Summit, Greenland. *Cryosph.*, 11:497–516.

Moene, A. and van Dam, J. (2014). *Transport in the Atmosphere-Vegetation-Soil Continuum.* Cambridge University Press.

Moncrieff, J., Clement, R., Finnigan, J., and Meyers, T. (2005). Averaging, detrending, and filtering of eddy covariance time series. In Lee, X., Massman, W., and Law, B., editors, *Handbook of Micrometeorology: A Guide for Surface Flux Measurement and Analysis*, pages 7–31. Springer Netherlands, Dordrecht.

Monna, W. and Bosveld, F. (2013). In Higher Spheres: 40 years of observations at the Cabauw Site. *KNMI Publ.*, 232.

Moore, C. J. (1986). Frequency response corrections for eddy correlation systems. *Boundary-Layer Meteorol.*, 37:17–35.

Morlighem, M., Rignot, E., Binder, T., Blankenship, D., Drews, R., Eagles, G., Eisen, O., Ferraccioli, F., Forsberg, R., Fretwell, P., Goel, V., Greenbaum, J. S., Gudmundsson, H., Guo, J., Helm, V., Hofstede, C., Howat, I., Humbert, A., Jokat, W., Karlsson, N. B., Lee, W. S., Matsuoka, K., Millan, R., Mouginot, J., Paden, J., Pattyn, F., Roberts, J., Rosier, S., Ruppel, A., Seroussi, H., Smith, E. C., Steinhage, D., Sun, B., den Broeke, M. R., Ommen, T. D., van Wessem, M., and Young, D. A. (2020). Deep glacial troughs and stabilizing ridges unveiled beneath the margins of the Antarctic ice sheet. *Nat. Geosci.*, 13(2):132–137.

Morlighem, M., Williams, C. N., Rignot, E., An, L., Arndt, J. E., Bamber, J. L., Catania, G., Chauché, N., Dowdeswell, J. A., Dorschel, B., Fenty, I., Hogan, K., Howat, I., Hubbard, A., Jakobsson, M., Jordan, T. M., Kjeldsen, K. K., Millan, R., Mayer, L., Mouginot, J., Noël, B. P., O'Cofaigh, C., Palmer, S., Rysgaard, S., Seroussi, H., Siegert, M. J., Slabon, P., Straneo, F., van den Broeke, M. R., Weinrebe, W., Wood, M., and Zinglersen, K. B. (2017). BedMachine v3: Complete Bed Topography and Ocean Bathymetry Mapping of Greenland From Multibeam Echo Sounding Combined With Mass Conservation. *Geophys. Res. Lett.*, 44(21):11,051–11,061.

Mott, R., Egli, L., Grünewald, T., Dawes, N., Manes, C., Bavay, M., and Lehning, M. (2011). Micrometeorological processes driving snow ablation in an Alpine catchment. *Cryosph.*, 5:1083–1098.

Mouginot, J., Rignot, E., Bjørk, A. A., van den Broeke, M., Millan, R., Morlighem, M., Noël, B., Scheuchl, B., and Wood, M. (2019). Forty-six years of Greenland Ice Sheet mass balance from 1972 to 2018. *Proc. Natl. Acad. Sci. U. S. A.*, 116(19):9239–9244.

Munro, D. S. (1989). Surface roughness and bulk heat transfer on a glacier: comparison with Eddy correlation. *J. Glaciol.*, 35(121):343–348.

Murphy, D. M. and Koop, T. (2005). Review of the vapour pressures of ice and supercooled water for atmospheric applications. *Q. J. R. Meteorol. Soc.*, 131(608):1539–1565.

Nansen, F. (1890). *The First Crossing of Greenland.* Number v. 2 in Silver library. Longmans, Green, and Company. Translated by H.M. Gepp.

Neumann, T. A., Martino, A. J., Markus, T., Bae, S., Bock, M. R., Brenner, A. C., Brunt, K. M., Cavanaugh, J., Fernandes, S. T., Hancock, D. W., Harbeck, K., Lee, J., Kurtz, N. T., Luers, P. J., Luthcke, S. B., Magruder, L., Pennington, T. A., Ramos-Izquierdo, L., Rebold, T., Skoog, J., and Thomas, T. C. (2019). The Ice, Cloud, and Land Elevation Satellite – 2 mission: A global geolocated photon product derived from the Aadvanced Ttopographic Llaser Aaltimeter Ssystem. *Remote Sens. Environ.*, 233(September):111325.

Nilsson, J., Gardner, A., Sørensen, L. S., and Forsberg, R. (2016). Improved retrieval of land ice topography from CryoSat-2 data and its impact for volume-change estimation of the Greenland Ice Sheet. *Cryosph.*, 10(6):2953–2969.

Niwano, M., Aoki, T., Hashimoto, A., Matoba, S., Yamaguchi, S., Tanikawa, T., Fujita, K., Tsushima, A., Iizuka, Y., Shimada, R., and Hori, M. (2018). NHM-SMAP: Spatially and temporally high-resolution nonhydrostatic atmospheric model coupled with detailed snow process model for Greenland Ice Sheet. *Cryosph.*, 12(2):635–655.

Noël, B., van de Berg, W. J., Lhermitte, S., and van den Broeke, M. R. (2019). Rapid ablation zone expansion amplifies north Greenland mass loss. *Sci. Adv.*, 5(9):eaaw0123.

Noël, B., van de Berg, W. J., Machguth, H., Lhermitte, S., Howat, I., Fettweis, X., and van den Broeke, M. R. (2016). A daily, 1 km resolution data set of downscaled Greenland ice sheet surface mass balance (1958–2015). *Cryosph.*, 10(5):2361–2377.

Noël, B., van de Berg, W. J., van Wessem, J. M., van Meijgaard, E., van As, D., Lenaerts, J. T. M., Lhermitte, S., Kuipers Munneke, P., Smeets, C. J. P. P., van Ulft, L. H., van de Wal, R. S. W., and van den Broeke, M. R. (2018). Modelling the climate and surface mass balance of polar ice sheets using RACMO2 – Part 1: Greenland (1958–2016). *Cryosph.*, 12(3):811–831.

Noël, B., van Kampenhout, L., Lenaerts, J. T., van de Berg, W. J., and van den Broeke, M. R. (2021). A 21st Century Warming Threshold for Sustained Greenland Ice Sheet Mass Loss. *Geophys. Res. Lett.*, 48(5):1–9.

Nolin, A. W. and Mar, E. (2019). Arctic sea ice surface roughness estimated from multi-angular reflectance satellite imagery. *Remote Sens.*, 11(1):1–12.

Nolin, A. W. and Payne, M. C. (2007). Classification of glacier zones in western Greenland using albedo and surface roughness from the Multi-angle Imaging SpectroRadiometer (MISR). *Remote Sens. Environ.*, 107(1-2):264–275.

Nordenskjöld, A. E. (1883). Nordenskjöld's greenland expedition. *Nature*, 29(732):39–42.

Oerlemans, J. (1991). The role of ice sheets in the Pleistocene climate. *Nor. Geol. Tidsskr.*, 71(3):155–161.

Oerlemans, J. and Vugts, H. F. (1993). A Meteorological Experiment in the Melting Zone of the Greenland Ice Sheet. *Bull. Am. Meteorol. Soc.*, 74(3):355–366.

Ohmura, A., Konzelmann, T., Rotach, M., Forrer, J., Wild, M., Abe-Ouchi, A., and Toritani, H. (1994). Energy balance for the Greenland ice sheet by observation and model computation. *Snow ice Cover. Interact. with Atmos. Ecosyst. Proc. Symp. Yokohama, 1993*, (223):85–94.

Olesen, O. (1986). Fourth year of glaciological field work at Tasersiaq and Qapiarfiup sermia, West Greenland. *Rapp. Grønlands Geol. Undersøgelse*, 130:121–126.

Peary, R. (1887). A Reconnoissance of the Greenland Inland Ice. *J. Am. Geogr. Soc. New York*, 19:261–289.

Peltola, O., Mammarella, I., Haapanala, S., Burba, G., and Vesala, T. (2013). Field intercomparison of four methane gas analyzers suitable for eddy covariance flux measurements. *Biogeosciences*, 10:3749–3765.

Petty, A. A., Tsamados, M. C., and Kurtz, N. T. (2017). Atmospheric form drag coefficients over Arctic sea ice using remotely sensed ice topography data, spring 2009–2015. *J. Geophys. Res. Earth Surf.*, 122(8):1472–1490.

Pohl, S., Marsh, P., and Liston, G. E. (2006). Spatial-temporal variability in turbulent fluxes during spring snowmelt. *Arctic, Antarct. Alp. Res.*, 38(1):136–146.

Popinet, S. (2009). An accurate adaptive solver for surface-tension-driven interfacial flows. *J. Comput. Phys.*, 228(16):5838–5866.

Porter, C., Morin, P., Howat, I., Noh, M.-J., Bates, B., Peterman, K., Keesey, S., Schlenk, M., Gardiner, J., Tomko, K., Willis, M., Kelleher, C., Cloutier, M., Husby, E., Foga, S., Nakamura, H., Platson, M., Wethington, Michael, J., Williamson, C., Bauer, G., Enos, J., Arnold, G., Kramer, W., Becker, P., Doshi, A., D'Souza, C., Cummens, P., Laurier, F., and Bojesen, M. (2018). ArcticDEM.

Prandtl, L. (1925). 7. bericht über untersuchungen zur ausgebildeten turbulenz. *ZAMM - Journal of Applied Mathematics and Mechanics / Zeitschrift für Angewandte Mathematik und Mechanik*, 5(2):136–139.

Radić, V., Menounos, B., Shea, J., Fitzpatrick, N., Tessema, M. A., and Déry, S. J. (2017). Evaluation of different methods to model near-surface turbulent fluxes for a mountain glacier in the Cariboo Mountains, BC, Canada. *Cryosph.*, 11:2897–2918.

Raupach, M. (1992). Drag and drag partition on rough surfaces. *Boundary-Layer Meteorol.*, 60:375–395.

Raupach, M. R. (1994). Simplified expressions for vegetation roughness length and zero-plane displacement as functions of canopy height and area index. *Boundary-Layer Meteorol.*, 71(1-2):211–216.

Reijmer, C., Greuell, W., and Oerlemans, J. (1999). The annual cycle of meteorological variables and the surface energy balance on Berkner Island, Antarctica. *Ann. Glaciol.*, 29:49–54.

Robledano, A., Picard, G., Arnaud, L., Larue, F., and Ollivier, I. (2022). Modelling surface temperature and radiation budget of snow-covered complex terrain. *Cryosph.*, 16(2):559–579.

Ryan, J. C., Smith, L. C., Van As, D., Cooley, S. W., Cooper, M. G., Pitcher, L. H., and Hubbard, A. (2019). Greenland Ice Sheet surface melt amplified by snowline migration and bare ice exposure. *Sci. Adv.*, 5(3):1–11.

Schotanus, P., Nieuwstadt, F. T., and De Bruin, H. A. (1983). Temperature measurement with a sonic anemometer and its application to heat and moisture fluxes. *Boundary-Layer Meteorol.*, 26:81–93.

Shao, Y. and Yang, Y. (2008). A theory for drag partition over rough surfaces. *J. Geophys. Res. Earth Surf.*, 113(2):1–9.

Shepherd, A., Ivins, E., Rignot, E., Smith, B., van den Broeke, M., Velicogna, I., Whitehouse, P., Briggs, K., Joughin, I., Krinner, G., Nowicki, S., Payne, T., Scambos, T., Schlegel, N., A, G., Agosta, C., Ahlstrøm, A., Babonis, G., Barletta, V. R., Bjørk, A. A., Blazquez, A., Bonin, J., Colgan, W., Csatho, B., Cullather, R., Engdahl, M. E., Felikson, D., Fettweis, X., Forsberg, R., Hogg, A. E., Gallee, H., Gardner, A., Gilbert, L., Gourmelen, N., Groh, A., Gunter, B., Hanna, E., Harig, C., Helm, V., Horvath, A., Horwath, M., Khan, S., Kjeldsen, K. K., Konrad, H., Langen, P. L., Lecavalier, B., Loomis, B., Luthcke, S., McMillan, M., Melini, D., Mernild, S., Mohajerani, Y., Moore, P., Mottram, R., Mouginot, J., Moyano, G., Muir, A., Nagler, T., Nield, G., Nilsson, J., Noël, B., Otosaka, I., Pattle, M. E., Peltier, W. R., Pie, N., Rietbroek, R., Rott, H., Sandberg Sørensen, L., Sasgen, I., Save, H., Scheuchl, B., Schrama, E., Schröder, L., Seo, K. W., Simonsen, S. B., Slater, T., Spada, G., Sutterley, T., Talpe, M., Tarasov, L., van de Berg, W. J., van der Wal, W., van Wessem, M., Vishwakarma, B. D., Wiese, D., Wilton, D., Wagner, T., Wouters, B., and Wuite, J. (2020). Mass balance of the Greenland Ice Sheet from 1992 to 2018. *Nature*, 579(7798):233–239.

Sicart, J. E., Litt, M., Helgason, W., Ben Tahar, V., and Chaperon, T. (2014). A study of the atmospheric surface layer and roughness lengths on the high-altitude tropical Zongo glacier, Bolivia. *J. Geophys. Res.*, 119(10):6196–6206.

Smeets, C. and Van den Broeke, M. (2006). Parameterizing scalar transfer over a rough ice surface. *The Mass Budget of Arctic Glaciers (Extended abstracts). Workshop and GLACIODYN planning meeting, 29 January - 3 February 2006, Obergugl (Austria). IASC - Working Group Arctic Glaciology*, pages 94–98.

Smeets, C. J., Duynkerke, P. G., and Vugts, H. F. (1998). Turbulence characteristics of the stable boundary layer over a mid-latitude glacier. Part I: a combination of katabatic and large-scale forcing. *Boundary-Layer Meteorol.*, 87:117–145.

Smeets, C. J. P. P., Duynkerke, P. G., and Vugts, H. F. (1999). Observed Wind Profiles and Turbulence Fluxes over an ice Surface with Changing Surface Roughness. *Boundary-Layer Meteorol.*, 92(1):99–121.

Smeets, P. C. J. P., Kuipers Munneke, P., van As, D., van den Broeke, M. R., Boot, W., Oerlemans, H., Snellen, H., Reijmer, C. H., and van de Wal, R. S. W. (2018). The K-transect in west Greenland: Automatic weather station (1993–2016). *Arctic, Antarct. Alp. Res.*, 50(1):S100002.

Smeets, P. C. J. P. and Van den Broeke, M. R. (2008a). Temporal and spatial variations of the aerodynamic roughness length in the ablation zone of the Greenland ice sheet. *Boundary-Layer Meteorol.*, 128:315–338.

Smeets, P. C. J. P. and Van den Broeke, M. R. (2008b). The parameterisation of scalar transfer over rough ice. *Boundary-Layer Meteorol.*, 128:339–355.

Smith, B., Fricker, H. A., Gardner, A. S., Medley, B., Nilsson, J., Paolo Nicholas Holschuh, F. S., Adusumilli, S., Brunt, K., Csatho, B., Harbeck, K., Markus, T., Neumann, T., Siegfried, M. R., and Jay Zwally, H. (2020). Pervasive ice sheet mass loss reflects competing ocean and atmosphere processes. *Science (80-.).*, 368(6496):1239–1242.

Smith, B., Fricker, H. A., Holschuh, N., Gardner, A. S., Adusumilli, S., Brunt, K. M., Csatho, B., Harbeck, K., Huth, A., Neumann, T., Nilsson, J., and Siegfried, M. R. (2019). Land ice height-retrieval algorithm for NASA's ICESat-2 photon-counting laser altimeter. *Remote Sens. Environ.*, 233(September):111352.

Smith, M. W., Quincey, D. J., Dixon, T., Bingham, R. G., Carrivick, J. L., Irvine-Fynn, T. D. L., and Rippin, D. M. (2016). Aerodynamic roughness of glacial ice surfaces derived from high-resolution topographic data. *J. Geophys. Res. Earth Surf.*, 121:748–766.

Sørensen, L. S., Simonsen, S. B., Nielsen, K., Lucas-Picher, P., Spada, G., Adalgeirsdottir, G., Forsberg, R., and Hvidberg, C. S. (2011). Mass balance of the Greenland ice sheet (2003-2008) from ICESat data - The impact of interpolation, sampling and firn density. *Cryosph.*, 5(1):173–186.

Steffen, K. (1995). Surface energy exchange during the onset of melt at the equilibrium line altitude of the Greenland ice sheet. *Ann. Glaciol.*, 21:13–18.

Steffen, K. and Box, J. (2001). Surface climatology of the Greenland ice sheet : Greenland Climate Network 1995-1999. *J. Geophys. Res.*, 106(12):33951–33964.

Stull, R. B. (1988). *An introduction to boundary layer meteorology*, volume 13. Springer Science & Business Media.

Tedstone, A. J., Cook, J. M., Williamson, C. J., Hofer, S., McCutcheon, J., Irvine-Fynn, T., Gribbin, T., and Tranter, M. (2020). Algal growth and weathering crust state drive variability in western Greenland Ice Sheet ice albedo. *Cryosph.*, 14(2):521–538.

Tedstone, A. J. and Machguth, H. (2022). Increasing surface runoff from Greenland's firn areas. *Nat. Clim. Chang.*, 12(7):672–676.

Tjernström, M., Shupe, M. D., Brooks, I. M., Persson, P. O. G., Prytherch, J., Salisbury, D. J., Sedlar, J., Achtert, P., Brooks, B. J., Johnston, P. E., Sotiropoulou, G., and Wolfe, D. (2015). Warm-air advection, air mass transformation and fog causes rapid ice melt. *Geophys. Res. Lett.*, 42:5594–5602.

Van Angelen, J. H., van den Broeke, M. R., and van de Berg, W. J. (2011). Momentum budget of the atmospheric boundary layer over the Greenland ice sheet and its surrounding seas. *J. Geophys. Res.*, 116(D10).

Van Angelen, J. H., van den Broeke, M. R., Wouters, B., and Lenaerts, J. T. (2014). Contemporary (1960–2012) Evolution of the Climate and Surface Mass Balance of the Greenland Ice Sheet. *Surv. Geophys.*, 35(5):1155–1174.

Van As, D., Fausto, R. S., Ahlstrøm, A. P., Andersen, S. B., Andersen, M. L., Citterio, M., Edelvang, K., Gravesen, P., Machguth, H., Nick, F. M., Nielsen, S., and Weidick, A. (2011). Programme for monitoring of the Greenland Ice sheet (PROMICE): first temperature and ablation records. *Geol. Surv. Denmark Greenl. Bull.*, 23:73–76.

Van Dalum, C. T., Jan Van De Berg, W., Lhermitte, S., and Van den Broeke, M. R. (2020). Evaluation of a new snow albedo scheme for the greenland ice sheet in the regional atmospheric climate model (RACMO2). *Cryosph.*, 14(11):3645–3662.

Van Dalum, C. T., Jan Van De Berg, W., and Van den Broeke, M. R. (2021). Impact of updated radiative transfer scheme in snow and ice in RACMO2.3p3 on the surface mass and energy budget of the Greenland ice sheet. *Cryosph.*, 15(4):1823–1844.

Van de Berg, W. J., van Meijgaard, E., and van Ulft, L. (2020). The added value of high resolution in estimating the surface mass balance in southern Greenland. *Cryosph.*

Van de Wal, R., Boot, W., Smeets, C., Snellen, H., van den Broeke, M., and Oerlemans, J. (2012). Twenty-one years of mass balance observations along the K-transect, West Greenland. *Earth Syst. Sci. data Discuss.*, 5:351–363.

Van den Broeke, M., Enderlin, E., Howat, I., Kuipers Munneke, P., Noël, B., van de Berg, W. J., van Meijgaard, E., and Wouters, B. (2016). On the recent contribution of the Greenland ice sheet to sea level change. *Cryosph.*, 10:1933–1946.

Van den Broeke, M., van As, D., Reijmer, C., and van de Wal, R. (2004). Assessing and Improving the Quality of Unattended Radiation Observations in Antarctica. *J. Atmos. Ocean. Technol.*, 21(9):1417–1431.

Van den Broeke, M. R. (1996). Characteristics of the lower ablation zone of the West Greenland ice sheet for energy-balance modelling. *Ann. Glaciol.*, 23:7–13.

Van den Broeke, M. R. and Gallée, H. (1996). Observation and simulation of barrier winds at the western margin of the Greenland ice sheet. *Q. J. R. Meteorol. Soc.*, 122:1365–1383.

Van den Broeke, M. R., Smeets, P. C. J. P., Ettema, J., Van Der Veen, C., Van De Wal, R., and Oerlemans, J. (2008). Partitioning of melt energy and meltwater fluxes in the ablation zone of the west Greenland ice sheet. *Cryosph.*, 2(2):179–189.

Van den Broeke, M. R., Smeets, P. C. J. P., and van de Wal, R. S. W. (2011). The seasonal cycle and interannual variability of surface energy balance and melt in the ablation zone of the west Greenland ice sheet. *Cryosph.*, 5(2):377–390.

Van Hooft, J. A., Popinet, S., van Heerwaarden, C. C., van der Linden, S. J., de Roode, S. R., and van de Wiel, B. J. (2018). Towards Adaptive Grids for Atmospheric Boundary-Layer Simulations. *Boundary-Layer Meteorol.*, 167(3):421–443.

Van Tiggelen, M., Smeets, P. C., Reijmer, C. H., and van den Broeke, M. R. (2020). A Vertical Propeller Eddy-Covariance Method and Its Application to Long-term Monitoring of Surface Turbulent Fluxes on the Greenland Ice Sheet. *Boundary-Layer Meteorol.*

Van Tiggelen, M., Smeets, P. C., Reijmer, C. H., Wouters, B., Steiner, J. F., Nieuwstraten, E. J., Immerzeel, W. W., and van den Broeke, M. R. (2021). Mapping the aerodynamic roughness of the Greenland ice sheet surface using ICESat-2: Evaluation over the K-transect. *Cryosph.*, pages 1–28.

Vignon, E., Genthon, C., Barral, H., Amory, C., Picard, G., Gallée, H., Casasanta, G., and Argentini, S. (2017). Momentum- and heat-flux parametrization at Dome C, Antarctica: a sensitivity study. *Boundary-Layer Meteorol.*, 162:341–367.

Wang, W., Zender, C. S., As, D. V., Fausto, R. S., and Laffin, M. K. (2021). Greenland surface melt dominated by solar and sensible heating. *Geophys. Res. Lett.*, pages 1–16.

Wang, W., Zender, C. S., van As, D., Smeets, P. C. J. P., and van den Broeke, M. R. (2016). A retrospective, iterative, geometry-based (RIGB) tilt-correction method for radiation observed by automatic weather stations on snow-covered surfaces: application to Greenland. *Cryosph.*, 10:727–741.

Watkins, R. H., Bassis, J. N., and Thouless, M. D. (2021). Roughness of Ice Shelves Is Correlated With Basal Melt Rates. *Geophys. Res. Lett.*, 48(21):1–8.

Webb, E. K., Pearman, G., and Leuning, R. (1980). Correction of flux measurements for density effects due to heat and water vapour transfer. *Q. J. R. Meteorol. Soc.*, 106(447):85–100.

Weidner, G., King, J., Box, J. E., Colwell, S., Jones, P., Lazzara, M., Cappelen, J., Brunet, M., and Cerveny, R. S. (2021). WMO evaluation of northern hemispheric coldest temperature: 69,6C at Klinck, Greenland, 22 December 1991. *Q. J. R. Meteorol. Soc.*, 147(734):21–29.

Wilczak, J. M., Oncley, S. P., and Stage, S. A. (2001). Sonic anemometer tilt correction algorithms. *Boundary-Layer Meteorol.*, 99:127–150.

Wouters, B., Chambers, D., and Schrama, E. J. (2008). GRACE observes small-scale mass loss in Greenland. *Geophys. Res. Lett.*, 35(20):1–5.

Wyngaard, J. C. (1981). Cup, propeller, vane, and sonic anemometers in turbulence research. *Annu. Rev. Fluid Mech.*, 13:399–423.

Yang, X. I., Sadique, J., Mittal, R., and Meneveau, C. (2016). Exponential roughness layer and analytical model for turbulent boundary layer flow over rectangular-prism roughness elements. *J. Fluid Mech.*, 789:127–165.

Yi, D., Zwally, H. J., and Sun, X. (2005). ICESat measurement of Greenland ice sheet surface slope and roughness. *Ann. Glaciol.*, 42:83–89.

Zhu, X. and Anderson, W. (2019). Turbulent flow over urban-like fractals: Prognostic roughness model for unresolved generations. *J. Turbul.*, 19(11):995–1016.

List of photographs

Acknowledgements

As I attempt to write down the last words of this book and look back at the last 4 years, I realise how privileged I have been. I find myself immensely grateful to all the people that have led me to where I am now, studying the fascinating sciences of snow, ice, and meteorology. I am especially grateful to the team at IMAU for giving me this opportunity. To Michiel, Carleen, and Paul for their guidance and supporting me all these years. I look forward keeping working with you on these topics!

During my master's in Delft, I found a great interest in studying land-atmosphere interactions, but I was looking for more field experience. My TU Delft advisor Bas asked me after my graduation what kind of a PhD I was looking for and I said, "Something with fieldwork in Antarctica". A few months later, after working on a campsite in France, a new position opened at IMAU. I received a mail from Bas saying something like: "this includes fieldwork in Greenland. It's not Antarctica but also a very nice place I believe". Thank you Bas, you were absolutely right! I thank my TU Delft supervisor Stephan for his good advice: "Maurice, jij moet lekker gaan promoveren".

When I started in 2018, I directly felt welcome at IMAU. Thanks to all the colleagues for their patience when explaining me what "firn", "ISMIP", "IMBIE", "RACMO", "SMB", etc ... means. I now also apologise to those who read the thesis for all the acronyms...

"IMAU is a good place for a PhD" said a reliable source in 2018. After more than 4 years here I agree. Thanks to all the great colleagues at IMAU for the good ambience, the regular Thursday evening drinks (before the Corona lockdowns), the long evening talks with Brice and Bas over Belgium beers, the IJsbeercelona futsal games that we sometimes won, the HOEMBA meetings that still need to have a new name. Thanks to Sharon, Leo, Tijn, Christiaan, Stan for making me feel welcome in the Ice & Climate PhD group, and thanks to Kat, Max, Meike, Sanne, Ann-Sofie, Tim, Caroline, Anneke and Franka for keeping the group alive. And no, I will not forget the postdocs, but I can't list all of you. So many have come and left. All I can say is that I am grateful to the all the friendly and experienced postdocs at IMAU that make the work more enjoyable. I am also very grateful to the technical support at IMAU, and especially Giorgio. Without you we wouldn't have so much data!

During this project I have been privileged to go to Greenland a few times. For this I am especially grateful to Paul, Jason and Dirk for bringing me along and sharing their

extensive field experience with me. And thanks for the enjoyable time! Special thanks to Paul for trusting me on my own with the helicopter pilot the first time in South Greenland. And thanks to Jason for lending me a yoga mattress to sleep on the ice, when the only thing I had was a sleeping bag. Only then I realised how rough the ice really is. I also would like to thank all the persons in Greenland for helping me out. From carrying heavy boxes, to giving me boat lifts, sponsoring me with beers, helping me setup the stations in the field, to lending me their car to bring the equipment to the heliport. I am immensely grateful to all the very friendly and helpful locals I had the pleasure to meet. Especially Niels from Narsaq for sharing hunted caribou meat on the barbecue, Isaac for showing me the secrets of brewing QajaQ beers, Jacky and all his colleagues from Blue Ice Explorer for the fresh mussels and for lending me a hiking map which turned out to be very useful!

I've also had the pleasure to work with some great people from other institutes these years. I would like to thank the colleagues at GEUS and especially Robert for their hospitality and for the great discussions. Thanks to Jakob, Walter and Philip for sharing their experience with UAVs. Thanks to Ghislain for the great discussions about 3D modelling over rough ice. And thanks to Antoon for his patience and time when we were working on Basilisk simulations. I realised during the lockdowns how much science depends on good discussions and collaborations.

Yet life is not just your work. This is also something I realised more and more. In between lockdowns, moves between several small rooms in Utrecht, I was lucky to have some good friends close to me. Thank you Thijs for carrying all my heavy stuff over the glacier in Chamonix when I had only one arm, and for pulling me from work to help you with renovating your house! And Jorjan for organising Ajax games, for biking so fast that I managed to crash while mountainbiking in the flatlands, and for closely investigating the inside of a crevasse in the Vallée Blanche. Turns out they are very deep indeed! Antoine, Cédric, Manu, Thomas, Ryan, Audrey, Christophe, Laurie et tous les autres de la Dream Team, merci à vous pour les bons moments, les nouvel ans, les mariages (à venir) ! Ce n'est pas facile de garder le contact mais j'espère tous vous voir bientôt !
I am also privileged to have a loving family. Thanks to my parents for all their love and support, and for reviewing this thesis before sending it to the committee. To my sisters that I wish would visit more often to the Netherlands. To my uncle Paul and aunt Annemiek for supporting me in the flatlands. To my loving and proud grandparents. And to Lotte: bedankt voor alle prachtige momenten.

Sooo what's next? I find myself grateful again that I was given the opportunity to keep working on the meteorology of the poles. As I am writing these lines, I already started working on a new project at IMAU that involves field measurement from Antarctica. But it seems someone will need to go there at some point to get all the data...

Publications

First author

Van Tiggelen M., Smeets C.J.P.P., Reijmer C.H., van den Broeke M.R., A Vertical Propeller Eddy-Covariance Method and Its Application to Long-term Monitoring of Surface Turbulent Fluxes on the Greenland Ice Sheet, *Boundary-Layer Meteorology* 176:441–463. https://doi.org/10.1007/s10546-020-00536-7, 2020

Van Tiggelen M., Smeets C.J.P.P., Reijmer C.H., Wouters B., Steiner J.F.,Nieuwstraten E.J., Immerzeel W.W., van den Broeke M.R., Mapping the aerodynamic roughness of the Greenland Ice Sheet surface using ICESat-2: Evaluation over the K-transect, *The Cryosphere* 15:2601–2621. https://doi.org/10.5194/tc-15-2601-2021, 2021

Van Tiggelen M., Smeets C.J.P.P., Reijmer C.H., van den Broeke M.R., van As D., Box J.E., Fausto R.S., Observed and parameterised roughness lengths for momentum and heat over rough ice surfaces, *Journal of Geophysical Research: Atmospheres*, 128, e2022JD036970. https://doi.org/10.1029/2022JD036970, 2023

Van Tiggelen M. and others, Impact of an improved Greenland ice sheet surface roughness description on modelled surface melt in RACMO2.3p2, in preparation, 2023

Co-author

Van Hooft A.J, Baas P., van Tiggelen M., Ansorge C., van de Wiel B.J.H., An idealized description for the diurnal cycle of the dry atmospheric boundary layer, *Journal of the Atmospheric Sciences* 76:3717–3736. https://doi.org/10.1175/JAS-D-19-0023.1, 2019

Curriculum Vitae

Maurice van Tiggelen

20-07-1994	Born in Saint-Martin-d'Hères (France)
2008 - 2011	Baccalauréat général scientifique, Lycée Edouard Herriot, Voiron (France)
2011 - 2012	Classe préparatoire aux grandes écoles, Physique Chimie Sciences de l'Ingénieur (PCSI), Lycée Vaugelas, Chambéry (France)
2012 - 2013	Classe préparatoire aux grandes écoles, Physique Chimie (PC), Lycée Champollion, Grenoble (France)
2013 - 2018	Diplôme national d'ingénieur (MSc), Hydraulics, Civil & Environmental Engineering, Ense³, Grenoble INP, Grenoble (France)
2015 - 2018	MSc. Applied Earth Sciences, Geoscience and Remote Sensing, TU Delft. Master thesis title: *Towards improving the land-surface-atmosphere coupling in the Dutch Atmospheric Large-Eddy Simulation model (DALES)* Cum Laude
2018 - 2023	PhD at the Institute for Marine and Atmospheric research Utrecht (IMAU), Utrecht University. Thesis title: *Roughish ice, snow and turbulent heat fluxes on the Greenland ice sheet* Promotor: prof. dr. M.R. van den Broeke Co-promotor: dr. C.J.P.P. Smeets Co-promotor: dr. C.H. Tijm-Reijmer
2023 -	Postdoctoral researcher at IMAU, Utrecht University